Search for Chargino-Neutralino Production in $p\bar{p}$ Collinsions at $\sqrt{s} = 1.8\mathrm{TeV}$

June 1996

Yukihiro Kato

Submitted in partial fulfillment of the requirements for the degree of Doctor of Science
in Osaka City University

Abstract

We have searched for the existence of the chargino-neutralino $(\tilde{\chi}_1^\pm\tilde{\chi}_2^0)$ pair production predicted by the Minimal Supersymmetric Standard Model(MSSM). The MSSM is the most preferable model as the extension to Standard Model(SM); it solves the difficulties of the SM. The MSSM predicts supersymmetric partner for the SM particles. The chargino and neutralino are the supersymmetric partners for the mixing of the Higgs boson and the gauge boson. They are predicted to be pair-produced in $p\bar{p}$ collisions and both have the leptonic decay modes. The search was done for $\tilde{\chi}_1^\pm\tilde{\chi}_2^0 \to \ell^\pm\ell^+\ell^- + X$ events ($\ell = e$ or μ), which we call "trilepton" events, using the 19.11 pb^{-1} data from $p\bar{p}$ collisions at $\sqrt{s}$ = 1.8 TeV, collected by the Collider Detector at Fermilab(CDF) during the 1992-1993 Tevatron run.

In all possible combinations of electron and muon channels, we observed no candidate event using our trilepton selection criteria. The expected SM background for the trilepton events was estimated to be 1.9 events. From these results and the 15.6% systematic uncertainty for this analysis, we obtained the 95% confidence lower limits for the chargino and neutralino mass and obtained the upper limit on $\sigma(p\bar{p} \to \tilde{\chi}_1^\pm\tilde{\chi}_2^0)\cdot BR(\tilde{\chi}_1^\pm\tilde{\chi}_2^0 \to 3\ell+X)$. Assuming the GUT hypothesis within the framework of the MSSM, our analysis excluded $M_{\tilde{\chi}_1^\pm} < 47$ GeV/c^2 for $-600 < \mu < -200$ GeV at $\tan\beta = 2.0$ and $M_{\tilde{q}} = 1.2 \times M_{\tilde{g}}$ (which is the region of maximum experimental sensitivity). Though LEP measurements rule out a similar mass region in e^+e^- collisions, the results should be presented in parallel since the searched channels are different. In addition, we obtained $M_{\tilde{\chi}_2^0} < 49$ GeV/c^2 (46 GeV/c^2) for $-600 < \mu < -200$ GeV at $M_{\tilde{q}} = 1.2 \times M_{\tilde{g}}$ ($2.0 \times M_{\tilde{g}}$) and $\tan\beta = 2.0$, with improved the LEP limit (40 GeV/c^2).

Acknowledgements

Many people have helped me to write this thesis. I'm very grateful to them for their guidance and help.

I would like to thank my advisor, Professor Tamotsu Takahashi, for his support throughout my graduate student career and gave me the opportunity to work at CDF. I would also like to thank Assistant professor Yoshiki Teramoto who gave me the precise advises on the physics research. It was a great fortune for me that I had a chance to work with them. Their enthusiasm for physics has always encouraged me. I would like to thank Professor Toru Okusawa and Assistant professor Takuo Yoshida, who are members of the CDF group in Osaka City University, for encouraging me to be a good scientist of physics.

I would like to thank Professor Shoji Mikamo who conducted this analysis. He has a profound knowledge of the supersymmetric theory and provided me a lot of suggestions for the supersymmetric theory. His suggestions are very precise and help me to understand the supersymmetric theory. I could not have finished this analysis without his suggestions. I would also like to thank Teruki Kamon. He knew the way of CDF analysis very much and guided me during the course of this analysis. Though he was very busy for his duty in his university, he devoted much time with me to discuss about and check out this analysis. Especially, I appreciate that he worked and discussed with me over midnight. I could not have finished this work and gotten good results without his continuous help.

I'm very grateful to Jeff Wolinski, Stephan Lammel, Jay Hauser, and Ben Tannenbaum for their supports and discussions on this analysis. They gave me various suggestions to get the great results and helped me to scan the SUSY parameter space efficiently. And they arranged my poor English expressions to excellent expressions on the transparencies and the physics papers. The time I discussed and worked with them was a good experience for my research career. I want to thank other SUSY working group members who helped me to perform this analysis. I also want to thank Philip Schlabach and Fotios Ptohos who worked with me during the time of the CMX detector constructions.

Conversations with the members of the cosmic ray and high energy physics group were unforgettable memories. They encouraged me to finish this analysis as soon as possible. In my staying at Fermilab, discussions on physics and other various things with the members of the Tsukuba high energy physics group and the KEK group were very beneficial for me. I also want to thank Kunitaka Kondo who is a representative of the CDF-Japanese group and got me a chance to work at CDF. I want thank to other CDF collaborators who worked to get the collision data and provided the good analysis environment. This thesis would not have been possible without their great works.

This work was supported by the Ministry of Science, Culture and Education of Japan; the U.S Department of Energy and National Science Foundation; the Italian Istituto Nazionale di Fisica Nucleare; the National Sciences and Engineering Research Council of Canada; the National Science Council of the Republic of China; and the A.P.Sloan Foundation.

CDF Collaboration

F. Abe,[13] M. G. Albrow,[7] S. R. Amendolia,[23] D. Amidei,[16] J. Antos,[28] C. Anway-Wiese,[4] G. Apollinari,[26] H. Areti,[7] M. Atac,[7] P. Auchincloss,[25] F. Azfar,[21] P. Azzi,[20] N. Bacchetta,[18] W. Badgett,[16] M. W. Bailey,[18] J. Bao,[35] P. de Barbaro,[25] A. Barbaro-Galtieri,[14] V. E. Barnes,[24] B. A. Barnett,[12] P. Bartalini,[23] G. Bauer,[15] T. Baumann,[9] F. Bedeschi,[23] S. Behrends,[3] S. Belforte,[23] G. Bellettini,[23] J. Bellinger,[34] D. Benjamin,[31] J. Benlloch,[15] J. Bensinger,[3] D. Benton,[21] A. Beretvas,[7] J. P. Berge,[7] S. Bertolucci,[8] A. Bhatti,[26] K. Biery,[11] M. Binkley,[7] F. Bird,[29] D. Bisello,[20] R. E. Blair,[1] C. Blocker,[29] A. Bodek,[25] W. Bokhari,[15] V. Bolognesi,[23] D. Bortoletto,[24] C. Boswell,[12] T. Boulos,[14] G. Brandenburg,[9] C. Bromberg,[17] E. Buckley-Geer,[7] H. S. Budd,[25] K. Burkett,[16] G. Busetto,[20] A. Byon-Wagner,[7] K. L. Byrum,[1] J. Cammerata,[12] C. Campagnari,[7] M. Campbell,[16] A. Caner,[7] W. Carithers,[14] D. Carlsmith,[34] A. Castro,[20] Y. Cen,[21] F. Cervelli,[23] H. Y. Chao,[28] J. Chapman,[16] M.-T. Cheng,[28] G. Chiarelli,[8] T. Chikamatsu,[32] C. N. Chiou,[28] S. Cihangir,[7] A. G. Clark,[23] M. Cobal,[23] M. Contreras,[5] J. Conway,[27] J. Cooper,[7] M. Cordelli,[8] C. Couyoumtzelis,[23] D. Crane,[1] J. D. Cunningham,[3] T. Daniels,[15] F. DeJongh,[7] S. Delchamps,[7] S. Dell'Agnello,[23] M. Dell'Orso,[23] L. Demortier,[26] B. Denby,[23] M. Deninno,[2] P. F. Derwent,[16] T. Devlin,[27] M. Dickson,[25] J. R. Dittmann,[6] S. Donati,[23] R. B. Drucker,[14] A. Dunn,[16] K. Einsweiler,[14] J. E. Elias,[7] R. Ely,[14] E. Engels, Jr.,[22] S. Eno,[5] D. Errede,[10] S. Errede,[10] Q. Fan,[25] B. Farhat,[15] I. Fiori,[2] B. Flaugher,[7] G. W. Foster,[7] M. Franklin,[9] M. Frautschi,[18] J. Freeman,[7] J. Friedman,[15] H. Frisch,[5] A. Fry,[29] T. A. Fuess,[1] Y. Fukui,[13] S. Funaki,[32] G. Gagliardi,[23] S. Galeotti,[23] M. Gallinaro,[20] A. F. Garfinkel,[24] S. Geer,[7] D. W. Gerdes,[16] P. Giannetti,[23] N. Giokaris,[26] P. Giromini,[8] L. Gladney,[21] D. Glenzinski,[12] M. Gold,[18] J. Gonzalez,[21] A. Gordon,[9] A. T. Goshaw,[6] K. Goulianos,[26] H. Grassmann,[6] A. Grewal,[21] G. Grieco,[23] L. Groer,[27] C. Grosso-Pilcher,[5] C. Haber,[14] S. R. Hahn,[7] R. Hamilton,[9] R. Handler,[34] R. M. Hans,[35] K. Hara,[32] B. Harral,[21] R. M. Harris,[7] S. A. Hauger,[6] J. Hauser,[4] C. Hawk,[27] J. Heinrich,[21] D. Cronin-Hennessy,[6] R. Hollebeek,[21] L. Holloway,[10] A. Hölscher,[11]

S. Hong,[16] G. Houk,[21] P. Hu,[22] B. T. Huffman,[22] R. Hughes,[25] P. Hurst,[9] J. Huston,[17] J. Huth,[9] J. Hylen,[7] M. Incagli,[23] J. Incandela,[7] H. Iso,[32] H. Jensen,[7] C. P. Jessop,[9] U. Joshi,[7] R. W. Kadel,[14] E. Kajfasz,[7a] T. Kamon,[30] T. Kaneko,[32] D. A. Kardelis,[10] H. Kasha,[35] Y. Kato,[19] L. Keeble,[8] R. D. Kennedy,[27] R. Kephart,[7] P. Kesten,[14] D. Kestenbaum,[9] R. M. Keup,[10] H. Keutelian,[7] F. Keyvan,[4] D. H. Kim,[7] H. S. Kim,[11] S. B. Kim,[16] S. H. Kim,[32] Y. K. Kim,[14] L. Kirsch,[3] P. Koehn,[25] K. Kondo,[32] J. Konigsberg,[9] S. Kopp,[5] K. Kordas,[11] W. Koska,[7] E. Kovacs,[7a] W. Kowald,[6] M. Krasberg,[16] J. Kroll,[7] M. Kruse,[24] S. E. Kuhlmann,[1] E. Kuns,[27] A. T. Laasanen,[24] N. Labanca,[23] S. Lammel,[4] J. I. Lamoureux,[3] T. LeCompte,[10] S. Leone,[23] J. D. Lewis,[7] P. Limon,[7] M. Lindgren,[4] T. M. Liss,[10] N. Lockyer,[21] C. Loomis,[27] O. Long,[21] M. Loreti,[20] E. H. Low,[21] J. Lu,[30] D. Lucchesi,[23] C. B. Luchini,[10] P. Lukens,[7] P. Maas,[34] K. Maeshima,[7] A. Maghakian,[26] P. Maksimovic,[15] M. Mangano,[23] J. Mansour,[17] M. Mariotti,[23] J. P. Marriner,[7] A. Martin,[10] J. A. J. Matthews,[18] R. Mattingly,[15] P. McIntyre,[30] P. Melese,[26] A. Menzione,[23] E. Meschi,[23] G. Michail,[9] S. Mikamo,[13] M. Miller,[5] R. Miller,[17] T. Mimashi,[32] S. Miscetti,[8] M. Mishina,[13] H. Mitsushio,[32] S. Miyashita,[32] Y. Morita,[13] S. Moulding,[26] J. Mueller,[27] A. Mukherjee,[7] T. Muller,[4] P. Musgrave,[11] L. F. Nakae,[29] I. Nakano,[32] C. Nelson,[7] D. Neuberger,[4] C. Newman-Holmes,[7] L. Nodulman,[1] S. Ogawa,[32] S. H. Oh,[6] K. E. Ohl,[35] R. Oishi,[32] T. Okusawa,[19] C. Pagliarone,[23] R. Paoletti,[23] V. Papadimitriou,[31] S. Park,[7] J. Patrick,[7] G. Pauletta,[23] M. Paulini,[14] L. Pescara,[20] M. D. Peters,[14] T. J. Phillips,[6] G. Piacentino,[2] M. Pillai,[25] R. Plunkett,[7] L. Pondrom,[34] N. Produit,[14] J. Proudfoot,[1] F. Ptohos,[9] G. Punzi,[23] K. Ragan,[11] F. Rimondi,[2] L. Ristori,[23] M. Roach-Bellino,[33] W. J. Robertson,[6] T. Rodrigo,[7] J. Romano,[5] L. Rosenson,[15] W. K. Sakumoto,[25] D. Saltzberg,[5] A. Sansoni,[8] V. Scarpine,[30] A. Schindler,[14] P. Schlabach,[9] E. E. Schmidt,[7] M. P. Schmidt,[35] O. Schneider,[14] G. F. Sciacca,[23] A. Scribano,[23] S. Segler,[7] S. Seidel,[18] Y. Seiya,[32] G. Sganos,[11] A. Sgolacchia,[2] M. Shapiro,[14] N. M. Shaw,[24] Q. Shen,[24] P. F. Shepard,[22] M. Shimojima,[32] M. Shochet,[5] J. Siegrist,[29] A. Sill,[31] P. Sinervo,[11] P. Singh,[22] J. Skarha,[12] K. Sliwa,[33] D. A. Smith,[23] F. D. Snider,[12] L. Song,[7] T. Song,[16] J. Spalding,[7] L. Spiegel,[7] P. Sphicas,[15] A. Spies,[12] L. Stanco,[20] J. Steele,[34] A. Stefanini,[23] K. Strahl,[11] J. Strait,[7] D. Stuart,[7]

G. Sullivan,[5] K. Sumorok,[15] R. L. Swartz, Jr.,[10] T. Takahashi,[19] K. Takikawa,[32] F. Tartarelli,[23] W. Taylor,[11] P. K. Teng,[28] Y. Teramoto,[19] S. Tether,[15] D. Theriot,[7] J. Thomas,[29] T. L. Thomas,[18] R. Thun,[16] M. Timko,[33] P. Tipton,[25] A. Titov,[26] S. Tkaczyk,[7] K. Tollefson,[25] A. Tollestrup,[7] J. Tonnison,[24] J. F. de Troconiz,[9] J. Tseng,[12] M. Turcotte,[29] N. Turini,[2] N. Uemura,[32] F. Ukegawa,[21] G. Unal,[21] S. van den Brink,[22] S. Vejcik, III,[16] R. Vidal,[7] M. Vondracek,[10] R. G. Wagner,[1] R. L. Wagner,[7] N. Wainer,[7] R. C. Walker,[25] C. H. Wang,[28] G. Wang,[23] J. Wang,[5] M. J. Wang,[28] Q. F. Wang,[26] A. Warburton,[11] G. Watts,[25] T. Watts,[27] R. Webb,[30] C. Wendt,[34] H. Wenzel,[14] W. C. Wester, III,[14] T. Westhusing,[10] A. B. Wicklund,[1] E. Wicklund,[7] R. Wilkinson,[21] H. H. Williams,[21] P. Wilson,[5] B. L. Winer,[25] J. Wolinski,[30] D. Y. Wu,[16] X. Wu,[23] J. Wyss,[20] A. Yagil,[7] W. Yao,[14] K. Yasuoka,[32] Y. Ye,[11] G. P. Yeh,[7] P. Yeh,[28] M. Yin,[6] J. Yoh,[7] T. Yoshida,[19] D. Yovanovitch,[7] I. Yu,[35] J. C. Yun,[7] A. Zanetti,[23] F. Zetti,[23] L. Zhang,[34] S. Zhang,[16] W. Zhang,[21] and S. Zucchelli[2]

[1] *Argonne National Laboratory, Argonne, Illinois 60439*

[2] *Istituto Nazionale di Fisica Nucleare, University of Bologna, I-40126 Bologna, Italy*

[3] *Brandeis University, Waltham, Massachusetts 02254*

[4] *University of California at Los Angeles, Los Angeles, California 90024*

[5] *University of Chicago, Chicago, Illinois 60637*

[6] *Duke University, Durham, North Carolina 27708*

[7] *Fermi National Accelerator Laboratory, Batavia, Illinois 60510*

[8] *Laboratori Nazionali di Frascati, Istituto Nazionale di Fisica Nucleare, I-00044 Frascati, Italy*

[9] *Harvard University, Cambridge, Massachusetts 02138*

[10] *University of Illinois, Urbana, Illinois 61801*

[11] *Institute of Particle Physics, McGill University, Montreal H3A 2T8, and University of Toronto,*
Toronto M5S 1A7, Canada

[12] *The Johns Hopkins University, Baltimore, Maryland 21218*

[13] *National Laboratory for High Energy Physics (KEK), Tsukuba, Ibaraki 305, Japan*

[14] *Lawrence Berkeley Laboratory, Berkeley, California 94720*

[15] *Massachusetts Institute of Technology, Cambridge, Massachusetts 02139*

[16] *University of Michigan, Ann Arbor, Michigan 48109*

[17] *Michigan State University, East Lansing, Michigan 48824*

[18] *University of New Mexico, Albuquerque, New Mexico 87131*

[19] *Osaka City University, Osaka 588, Japan*

[20] *Universita di Padova, Instituto Nazionale di Fisica Nucleare, Sezione di Padova, I-35131 Padova, Italy*

[21] *University of Pennsylvania, Philadelphia, Pennsylvania 19104*

[22] *University of Pittsburgh, Pittsburgh, Pennsylvania 15260*

[23] *Istituto Nazionale di Fisica Nucleare, University and Scuola Normale Superiore of Pisa, I-56100 Pisa, Italy*

[24] *Purdue University, West Lafayette, Indiana 47907*

[25] *University of Rochester, Rochester, New York 14627*

[26] *Rockefeller University, New York, New York 10021*

[27] *Rutgers University, Piscataway, New Jersey 08854*

[28] *Academia Sinica, Taiwan 11529, Republic of China*

[29] *Superconducting Super Collider Laboratory, Dallas, Texas 75237*

[30] *Texas A&M University, College Station, Texas 77843*

[31] *Texas Tech University, Lubbock, Texas 79409*

[32] *University of Tsukuba, Tsukuba, Ibaraki 305, Japan*

[33] *Tufts University, Medford, Massachusetts 02155*

[34] *University of Wisconsin, Madison, Wisconsin 53706*

[35] *Yale University, New Haven, Connecticut 06511*

Contents

List of Tables

List of Figures

Chapter 1

Introduction

The Standard Model[1] has been successful to explain all experimental observations in particle physics for two decades. In 1974, J/Ψ particles were discovered. This was the first experimental evidence of existence of charm quark which was required by the GIM mechanism[2]. Later in 1970's, τ lepton and bottom quark were also discovered. In 1980's the trijet phenomena were observed, which were the first clear signature of gluon's existence and strong evidences to support QCD. In 1983, $W^{\pm}, Z^{0}$ bosons were discovered at CERN's $Sp\overline{p}S$ collider with the mass predicted by the theory. In 1994, CDF presented the evidence of top quark at the Fermilab Tevatron $p\overline{p}$ collider. The experimentally unobserved particles which form the Standard Model are τ-neutrino and Higgs particle. The τ-neutrino has been studied only as an un-detected final state particle in decays of $\tau^{\pm}$, which behave in a manner completely consistent with the Standard Model properties for the ν_{τ}. The Higgs boson is a remnant of the mechanism that breaks the SU(2) $\times$ U(1) symmetry and generates the $W^{\pm}$ and Z^{0} boson masses. The Higgs couples to quarks and leptons of mass m_f with a strength $gm_f/2M_W$. Its coupling to $W^{\pm}$ and Z^{0} bosons is strength g, where g is the coupling constant of the SU(2) gauge theory. Consequently its coupling to stable matter is very small, and its production and detection in experiments is very difficult. LEP showed the mass limit of the Higgs boson above 48 GeV/c^2[3].

In spite of the impressive success of the Standard Model in correlating all observed low-energy data in terms of a very few parameters, it is still very unsatisfactory since it builds on many assumptions and leaves many fundamental questions unanswered. Most of the successes of the Standard Model pertain only to the gauge sector of the theory where, with the help of only one free parameter, $\sin^2 \theta_W$, numerous neutral current data are successfully understood. But in the fermionic sector, all masses and mixing are unexplained. There are some questions about the Standard Model. (1) The Standard Model has three different gauge groups postulated from phenomenological considerations. They are associated with three different gauge coupling constants. (2) All observed electric charges appear in quantized units which are multiples of the electric charge of positron. (3) The fermion masses and mixing have to be decided by experiments and seem to exhibit a hierarchical pattern. (4) Einstein's gravity is totally outside the framework of gauge theories. In fact, adding gravity to gauge theories destroys the attractive property of renomalizability. (5) Higgs scalar mass is a free parameter not fixed by the theory. The many theorists are thinking the new physics to give the answers for these questions. But no new physics has been established by experimental results.

One of the solutions to the Standard Model questions is supersymmetry, a symmetry proposed between fermions and bosons. Supersymmetry introduces spin 0 partners of the quarks and leptons - called squarks and sleptons - and spin 1/2 partners of the gauge bosons and Higgs particles - called gauginos and Higgsinos. Since these predicted particles have not been observed so far, these supersymmetric particles must be heavier than the known particles, implying that supersymmetry must be broken. However, from the unification condition a first estimate of the supersymmetry breaking scale could be made: it was found to be of the order of 1 TeV, or more precisely $10^{3\pm1}$ GeV[4]. If we find any supersymmetric particles experimentally, this is the evidence that supersymmetry is existed.

CDF has been looking for the signatures of pair-produced gluinos ($\tilde{g}\tilde{g}$), squarks ($\tilde{q}\tilde{q}$), and gluino-squark ($\tilde{g}\tilde{q}$). CDF presented the mass limit for squarks and gluinos, $m_{\tilde{q}} > 126$ GeV/c^2 and $m_{\tilde{g}} > 141$ GeV/c^2[5].

In the Minimal Supersymmetric Standard Model (MSSM)[6], the three-lepton(trilepton) event signature has long been suggested as a promising SUSY discovery channel at hadron colliders[7]. The trilepton final state in a $p\overline{p}$ collision originates from chargino-neutralino

($\tilde{\chi}_1^{\pm}\tilde{\chi}_2^0$) pair production (via a virtual W in the s-channel and virtual squarks in the t-channel) with subsequent decays into leptons ($\tilde{\chi}_1^{\pm} \rightarrow \tilde{\chi}_1^0 \ell\nu$ and $\tilde{\chi}_2^0 \rightarrow \tilde{\chi}_1^0 \ell\ell$). The chargino is the mass eigenstates of the charged wino-Higgsino sector. The neutralino is the neutral mass eigenstate of photino-zino-Higgsino sector. These trilepton events are quiet in hadronically and only have three isolated leptons.

This paper describes the search for supersymmetric particles with searching for trilepton events in CDF data. Chapter 2 reviews about the theory of supersymmetry. Chapter 3 through Chapter 7 describe the analysis and results. Chapter 8 describes the summary.

Chapter 2

Minimal Supersymmetric Standard Model

Supersymmetry is an attractive theoretical framework that can permit the consistent unification of particle physics and gravity, which takes place around the Plank scale ($\approx 10^{19}$ GeV). There are many supersymmetric models. Among then, Minimal Supersymmetric Standard Model (MSSM) is the most promising model. Since $\tilde{\chi}_1^{\pm}\tilde{\chi}_2^0$ production is based on MSSM, understanding the MSSM is necessary for the search for $\tilde{\chi}_1^{\pm}\tilde{\chi}_2^0$ production using trilepton event analysis. This chapter describes the MSSM theory and $\tilde{\chi}_1^{\pm}\tilde{\chi}_2^0$ production.

2.1 Theoretical Concept

The Standard Model has been enormously successful in explaining a wide variety of physics. Its principles appear to be valid over remarkable range, from cosmological phenomena in the very early universe, to all microscopic phenomena up to the electroweak energy of about 100 GeV. At present, the Standard Model is in agreement with all current experimental data. In spite of this, there are a number of "structural"defects in the Standard Model, related mainly to the Higgs phenomenon. The Standard Model gives no explanation for the breaking of $SU(2) \times U(1)$, but merely accommodates it by giving an unphysical negative value to the square of Higgs mass (M_H^2). Further, the Higgs, being a spin zero particle, possesses a quadratic self mass divergence. It leads to large quantum corrections ($\mathcal{O}(M_X^2/M_W^2)$) if one assumes that the Standard Model governs physical behavior from the electroweak scale M_W up to the ultra-high energy scale M_X (*e.g.*, the

GUT or Plank scales). These corrections require the specification of Standard Model parameters to a precision of 23 decimal places. Supersymmetry is one of the solutions for these problems.

2.1.1 The Concept of Supersymmetry

Supersymmetry(SUSY) was invented in 1973 by Wess and Zumino[8] and earlier in nonlinear realization by Volkov and Akulov[9]. One of the first requirements of SUSY is an equal number of bosonic and fermionic degrees of freedom in one multiplet. We demonstrate this with a simple example. Consider two pairs of creation and annihilation operators: $(a, a^\dagger)$ and $(b, b^\dagger)$ with a being bosonic and b being fermionic. They satisfy the following commutation and anticommutation relations, respectively,

$$[a, a^\dagger] = \{b, b^\dagger\} = 1 \tag{2.1}$$

The Hamiltonian for this system can be written in general as

$$H = \omega_a a^\dagger a + \omega_b b^\dagger b \tag{2.2}$$

If we define a fermionic operator

$$Q = b^\dagger a + a^\dagger b, \tag{2.3}$$

then

$$\begin{aligned} [Q, a^\dagger] &= b^\dagger, \\ \{Q, b^\dagger\} &= a^\dagger. \end{aligned} \tag{2.4}$$

Thus, if $a^\dagger|0>$ and $b^\dagger|0>$ represent bosonic and fermionic states, respectively, Q will take bosons to fermions and vice versa. Moreover

$$[Q, H] = (\omega_a - \omega_b)Q. \tag{2.5}$$

So, for $\omega_a = \omega_b$ (i.e., equal energy for the bosonic and fermionic states), H is supersymmetric. Furthermore, in this case

$$\{Q, Q^\dagger\} = \frac{2}{\omega}H. \tag{2.6}$$

Thus, the algebra of $Q, Q^\dagger$, and H closes under anticommutation. If there is more than one a and b, then there must be an equal number of them, otherwise eqs.2.5 and 2.6 cannot be satisfied together.

2.1.2 Minimal Supersymmetric Standard Model

The minimal supersymmetric standard model (MSSM) consists of taking the Standard Model as it is known today and adding corresponding supersymmetric partners. The MSSM is the simplest supersymmetric extension of the SM in that it contains the fewest number of fields and superpotential interactions. In addition, the MSSM contains two Higgs doublets, which is minimal for the Higgs sector of the MSSM that generates mass for both "up"-type and "down"-type quarks and charged leptons. Supersymmetric interactions consistent with B - L conservation ($B=$ barion number and $L=$ lepton number) are included. Finally, the most general soft-supersymmetric-breaking terms are added. Table 2.1 shows the supersymmetric particles spectrum. For each standard particle the superpartner is shown in this table. The main subtlety is needed for column 3 of table 2.1; the weak eigenstates will mix, giving mass eigenstates that are linear combinations of weak eigenstates, and that requires separate names for them because they have different properties. For the partners of bosons, mixing generally occurs among the weak eigenstates. Couplings of weak eigenstates are determined by the theory, but couplings of mass eigenstates depend on the amount of mixing; for mass eigenstates the names and symbols are either generic ($\tilde{\chi}_i$) or reflect the couplings. As always, Z^0 and γ are linear combinations of $W^3, B[\gamma = \cos\theta_W B + \sin\theta_W W^3, Z = -\sin\theta_W B + \cos\theta_W W^3]$, with the same combination of $\tilde{W}^3, \tilde{B}$ giving $\tilde{Z}^0, \tilde{\gamma}$. In the table we have not made explicit chiralities of the fermions and their partners. To be fully explicit, two have all weak eigenstates; the usual left-handed electron e_L (in an SU(2) doublet) and right-handed electron e_R (an SU(2) singlet), the left-handed up quark u_L, u_R, d_L, d_R, etc.

As a consequence of $B-L$ invariance, the MSSM possesses a strict R-parity invariance, where $R = (-1)^{3(B-L)+2S}$ for a particle spin S[10]. Note that this formula implies that all the ordinary Standard Model particles have even R-parity, whereas the corresponding

Table 2.1: The supersymmetric particles spectrum

Normal particles	Weak interaction eigenstates		Mass eigenstates	
	Symbol	Name	Symbol	Name
q=u,d,s, c,b,t	$\tilde{q}_L, \tilde{q}_R$	scaler-quark	$\tilde{q}_1, \tilde{q}_2$	scaler-quark
$\ell = e, \mu, \tau$	$\tilde{\ell}_L, \tilde{\ell}_R$	scaler-lepton	$\tilde{\ell}_1, \tilde{\ell}_2$	scaler-lepton
$\nu = \nu_e, \nu_\mu, \nu_\tau$	$\tilde{\nu}$	scaler-neutrino	$\tilde{\nu}$	scaler-neutrino
g	$\tilde{g}$	gluino	$\tilde{g}$	gluino
$W^\pm$	$\tilde{W}^\pm$	wino		
H_1^+	$\tilde{H}_1^+$	higgsino	$\tilde{\chi}_{1,2}^\pm$	charginos
H_2^-	$\tilde{H}_2^-$	higgsino		
γ	$\tilde{\gamma}$	photino		
Z^0	$\tilde{Z}^0$	zino		
H_1^0	$\tilde{H}_1^0$	higgsino	$\tilde{\chi}_{1,2,3,4}^0$	neutralinos
H_2^0	$\tilde{H}_2^0$	higgsino		
$\begin{pmatrix} W^3 \\ B \end{pmatrix}$	$\begin{pmatrix} \tilde{W}^3 \\ \tilde{B} \end{pmatrix}$	wino bino		

supersymmetric partners have odd R-parity. The conservation of R-parity in scattering and decay processes has a crucial impact on supersymmetric phenomenology. For example, starting from an initial state involving ordinary (R-even) particles, it follows that supersymmetric particles must be produced in pairs. In general, these particles are highly unstable and decay quickly into lighter states. However, R-parity invariance also implies that the lightest supersymmetric particle(LSP) is absolutely stable, and must eventually be produced at the end of a decay chain of a heavy unstable supersymmetric particle. In order to be consistent with cosmological constraints, the LSP is almost certainly electrically and color neutral.[11] Consequently, the LSP is weakly-interacting in ordinary matter. LSP behaves like a neutrino and will escape detectors without being directly observed.

The parameters of the MSSM fall into two classes; a supersymmetry-conserving sector and a supersymmetry-breaking sector. Among the parameters of the supersymmetry-conserving sector are; (1) gauge couplings: g_s, g and g', corresponding to the Standard

Model gauge group SU(3)×SU(2)×U(1) respectively; (2) Higgs Yukawa couplings: λ_e, λ_μ, and λ_d (which are 3×3 matrices in flavor space); (3) a supersymmetry-conserving Higgs mass parameter μ. The supersymmetry-breaking sector contains the following set of parameters; (1) gaugino Majorana masses M_3, M_2, and M_1 associated with the SU(3), SU(2), and U(1) subgroups of the Standard Model; (2) scalar mass matrices for the squarks and sleptons; (3) Higgs-squark-squark trilinear interaction terms (the so-called "A-parameters") and corresponding terms involving the sleptons; (4) three scalar Higgs mass parameters - two diagonal and one off-diagonal mass terms for the two Higgs doublets. These three parameters can be re-expressed in terms of the two Higgs vacuum expectation values, v_1 and v_2, and one physical Higgs mass. Here, $v_1(v_2)$ is the vacuum expectation value of the Higgs field which couples exclusively to down-type(up-type) quarks and leptons. The ratio of the two vacuum expectation values,

$$\tan\beta = v_2/v_1 \tag{2.7}$$

is a free parameter of the model.

The SUSY breaking masses for each SM multiplet can be independent. This results in a proliferation of free parameters that makes any phenomenological analysis intractable. Motivated by supergravity models, where supersymmetry breaking effects in a hidden sector are communicated to the observable sector by universal gravitational interactions, we assume here that all the matter sfermions have a common mass at the unification scale. Thus, supersymmetry fixes the Lagrangian at the unification scale in terms of just a few parameters. In order for us to use this Lagrangian for perturbative calculations at the 100 GeV scale relevant to the experiments today, these have to be evolved down to the low energy scale using renormalization group's techniques [12]. The $SU(2)_L$ and $U(1)_Y$ gaugino masses are then fixed by the gluino mass by the well known unification condition [13]. The renormalization group evolution also splits the degeneracy between the various sfermions. The biggest effect is due to color interactions so that the largest splitting occurs between squarks and sleptons, with smaller splitting between the doublet and singlet sfermions.

In our analysis, we have ignored mass splitting between the various squarks. This is a good approximation except for the third generation sfermions where the corresponding Yukawa interactions (which, for instance, cause $\tilde{t}_L - \tilde{t}_R$ mixing) can be important. The slepton masses are also determined by the common scalar mass, and so are fixed in terms of $m_{\tilde{q}}$. Since light sleptons can have a significant impact on neutralino decay patterns, the D-terms responsible for mass splitting can play an important role. The Higgs sector of the MSSM is strongly constrained so that it can be specified by just one additional parameter (which we take to be the mass of H_p) which, we will assume, is independent of the sfermion mass. And we assume that requiring unification of the coupling constants at the GUT scale ("the GUT hypothesis") leads to the following relationship at any scale:

$$\left.\begin{array}{rcl} M_{\tilde{W}} & = & \dfrac{\alpha_2}{\alpha_3}\, M_{\tilde{g}} \\ M_{\tilde{B}} & = & \dfrac{5\alpha_1}{3\alpha_2}\, M_{\tilde{W}} \end{array}\right\} \tag{2.8}$$

2.2 $\tilde{\chi}_1^\pm \tilde{\chi}_2^0 \rightarrow \ell^\pm \ell^\mp \ell^\pm$ production

2.2.1 Charginos and Neutralinos

charginos

The $W^\pm$ bosons, and the charged Higgs bosons H_1^+, H_2^- from the two weak doublets needed in the MSSM, have supersymmetric partners $\tilde{W}^\pm, \tilde{H}_1^+, \tilde{H}_2^-$. These are weak eigenstates - $\tilde{W}^\pm$ are in an SU(2) triplet, and $H^\pm$ are in SU(2) doublets. A term $g_2 \tilde{W}^+ \tilde{H}^- \tilde{H}^0$ is allowed by SU(2)×U(1), and when H^0 gets a vacuum expectation value v, an off-diagonal mass term is generated in the $\tilde{W}^+ \tilde{H}^-$ mass matrix.

Supersymmetry breaking can generate diagonal $\tilde{W}^+ \tilde{W}^-$ or $\tilde{H}^+ \tilde{H}^-$ masses as well, so the full mass matrix, for the left-handed charginos[6] is,

$$(\tilde{W}^- \tilde{H}_1^-) \begin{pmatrix} M & \frac{1}{\sqrt{2}} g v_2 \\ \frac{1}{\sqrt{2}} g v_1 & \mu \end{pmatrix} \begin{pmatrix} \tilde{W}^+ \\ \tilde{H}_2^+ \end{pmatrix} \tag{2.9}$$

If $M = \mu = 0$, then the matrix is diagonalize by adding and subtracting the weak eigenstates, so there are two Dirac spinors

$$\tilde{\chi}_1^+ = \begin{pmatrix} \tilde{W}_L^+ \\ \tilde{H}_{1R}^- \end{pmatrix} \tag{2.10}$$

$$\tilde{\chi}_2^+ = \begin{pmatrix} \tilde{H}_{2L}^+ \\ \tilde{W}_R^- \end{pmatrix} \tag{2.11}$$

with masses $gv_1/\sqrt{2}$ and $gv_2/\sqrt{2}$, respectively. If M or μ is zero, or $M\mu \ll \frac{g^2 v_1 v_2}{2}$, then the product of the eigenvalues $\tilde{M}_1, \tilde{M}_2$ is $\frac{g^2 v_1 v_2}{2}$. Then

$$m_W^2 - m_1 m_2 = \frac{g^2(v_1 - v_2)^2}{4} \geq 0 \tag{2.12}$$

so one of the eigenstates $\tilde{M}_1$ or $\tilde{M}_2$ must have mass less than m_W[14]. However, it can happen that M and μ are large, in which case there is no need for one chargino to be lighter than m_W.

Charginos have many allowed decay modes, as shown in fig 2.1. The relative rates depend on the superpartner masses, and on the mixing coefficients that determine the mass eigenstates (the mixing coefficients are themselves determined by the mass matrix). In the case of charginos, this uncertainty of dominate decay modes considerably complicates the experimental search, and may effectively prevent setting general limits.

neutralinos

The minimal set of the particles W^3, B^0, H_1^0, H_2^0 give supersymmetry partners $\tilde{W}^3, \tilde{B}^0, \tilde{H}_1^0, \tilde{H}_2^0$. These are weak (SU(2)×U(1)) eigenstates. [$(W^\pm, W^3)$ is in an SU(2) triplet, B^0 is an SU(2) singlet, and H_1, H_2 are SU(2) doublets. One could equally well consider $\tilde{Z}^0, \tilde{\gamma}$, the partners of Z^0, γ, instead of $\tilde{W}^3, \tilde{B}^0$]. The partners are all spin 1/2, uncolored and electrically neutral particles, differing only in their SU(2)×U(1) quantum numbers.

When SU(2)×U(1) is spontaneously broken by the Higgs mechanism, these states get off-diagonal contributions to their mass matrix. For example, a term in the Lagrangian $g\tilde{W}^0\tilde{H}_1^0 H_1^0$ would give a $\tilde{W}^0\tilde{H}_1^0$ mass term gv_1 when H_1^0 gets a vacuum expectation value v_1. Another term arises when H_2^0 gets a vacuum expectation value v_2. Additional mass terms may arise from SUSY breaking; if those terms do not break SU(2)×U(1), the resulting mass matrix has the form[6]

$$(\tilde{B}^0, \tilde{W}^3, \tilde{H}_1^0, \tilde{H}_2^0) \begin{pmatrix} M' & 0 & -g'v_1/2 & g'v_2/2 \\ 0 & M & gv_1/2 & -gv_2/2 \\ -g'v_1/2 & gv_1/2 & 0 & -\mu \\ g'v_2/2 & -gv_2/2 & -\mu & 0 \end{pmatrix} \begin{pmatrix} \tilde{B} \\ \tilde{W}^3 \\ \tilde{H}_1^0 \\ \tilde{H}_2^0 \end{pmatrix} \tag{2.13}$$

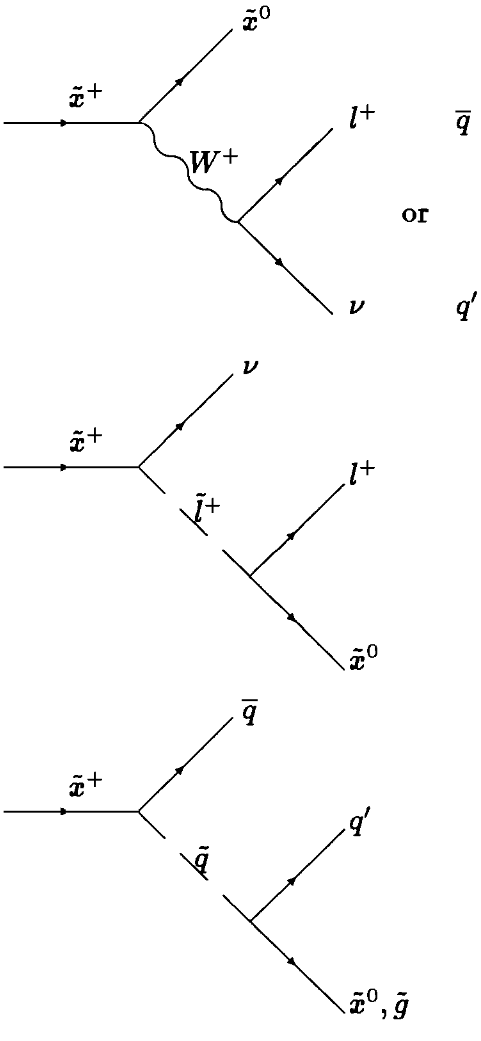

Figure 2.1: Chargino($\tilde{\chi}^+$) decay modes. The notation here is: q and q' are quarks of different charge and $\tilde{\chi}^0$ is any neutralino which is kinematically allowed.

where M, M', μ arise from supersymmetry breaking. The SU(2)×U(1) invariance requires that M and μ above are the same quantities as in the chargino mass matrix, so only one new parameter (M') is introduced above. Nothing definite is known about M, M, μ. The vacuum expectation values v_1 and v_2 are constrained by $m_W = gv/2, v^2 = v_1^2 + v_2^2$, but $\frac{v_2}{v_1}$is a free parameter. Thus there are basically three parameters needed to describe the neutralino mixing.

The mass eigenstates will be different from the weak eigenstates. When mixing occurs, the amount of mixing is determined by the mass matrix, and so the coupling of the mass eigenstates are not fully known. The mass eigenstates are described by $\tilde{\chi}_i^0$,

$$\begin{pmatrix} \tilde{\chi}_1^0 \\ \tilde{\chi}_2^0 \\ \tilde{\chi}_3^0 \\ \tilde{\chi}_4^0 \end{pmatrix} = (N_{ij}) \begin{pmatrix} \tilde{B}^0 \\ \tilde{W}^3 \\ \tilde{H}_1^0 \\ \tilde{H}_2^0 \end{pmatrix} \tag{2.14}$$

The weak eigenstates are neutral Majorana spinors. The mass eigenstates can arrange themselves as Majorana states also, or if two particles are degenerate in mass, the pair can combine to make a Dirac spinor (this depending on the values of $M, \mu, v_2/v_1$).

Neutralino decays can proceed through one of the channels in fig 2.2. The dominant decay channel depends on their masses.

2.2.2 Trilepton Event by Chargino-Neutralino production

Nath and Arnowitt have noted[7] that decays of *off-shell* W and Z bosons can lead to substantial rates for chargino and neutralino production. Chargino decays as $\tilde{\chi}_1 \to \ell\nu\tilde{\chi}_1^0$ and neutralino decays as $\tilde{\chi}_2^0 \to \ell\ell\tilde{\chi}_1^0$. These reactions can lead to the clean final states with three leptons without no hard QCD process. In the tevatron energy range, the Chargino-Neutralino is produced via off-shell s-channel W-exchange and t-channel squark-exchange processes. The squark exchange graphs can lead to negative interference for $\tilde{\chi}_1^\pm\tilde{\chi}_2^0$ production. Fig 2.3 show the Feynman diagrams of the trilepton event from $\tilde{\chi}_1^\pm\tilde{\chi}_2^0$ productions.

The production cross section is determined by a few parameters[15], (1)the supersymmetric Higgsino mass $\mu = -2m_1$, (2)the soft SUSY breaking gluino mass, $m_{\tilde{g}}$, which we

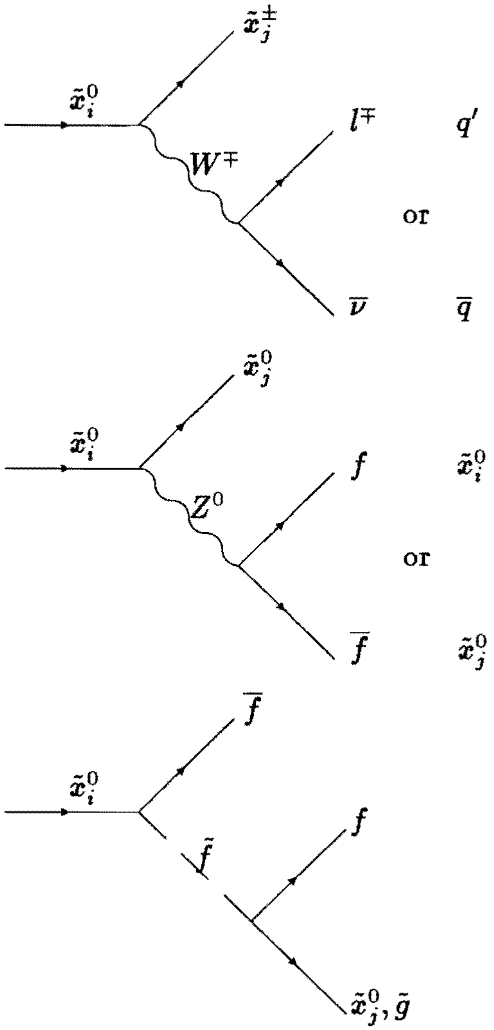

Figure 2.2: Neutralino decay modes. The index i (or j) labels different neutralino or chargino states.

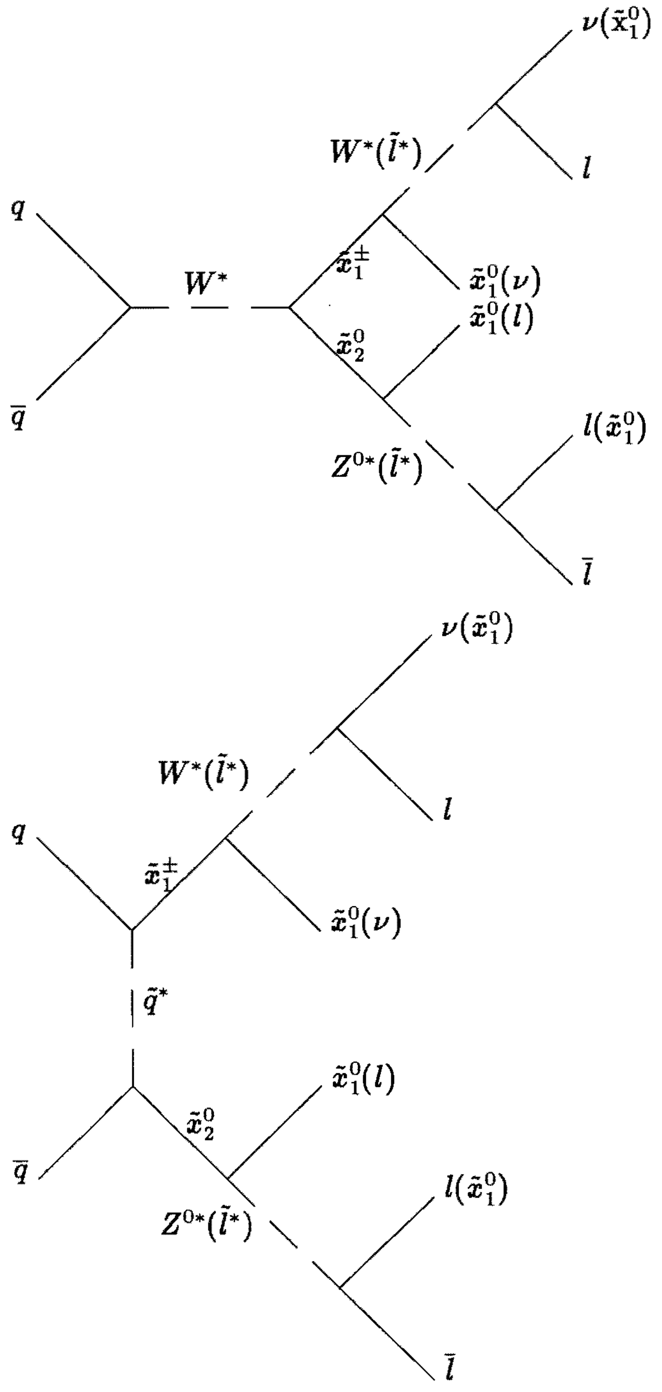

Figure 2.3: The Feynman diagram of the trilepton event from $\tilde{\chi}_1\tilde{\chi}_2^0$ productions.

assume also fixes the SU(2) and U(1) gaugino masses, (3)tan β, the ratio of the vacuum expectation values of the two Higgs fields of the model, (4)the squark mass, $m_{\tilde{q}}$, which, together with the gluino mass, fixes the slepton mass via a unification condition, and (5)the pseudo-scalar Higgs boson mass, m_{H_p}, which fixes the Higgs sector. And the mass and coupling of the $\tilde{\chi}_1$ and $\tilde{\chi}_2^0$ are also determined by these parameters.

The branching fraction for the trilepton events is determined by the leptonic decays of the $\tilde{\chi}_1^\pm$ and $\tilde{\chi}_2^0$. The $\tilde{\chi}_1^\pm$ decays to $\ell\nu\tilde{\chi}_1^0$ via virtual W or virtual sleptons. Since sleptons masses are much higher than W mass, $\tilde{\chi}_1^\pm$ decays are dominated by the virtual W and the branching fraction for the decay $\tilde{\chi}_1^\pm \rightarrow \ell\nu\tilde{\chi}_1^0$ is insensitive to model parameters. The $\tilde{\chi}_2^0$ decays to $\ell\ell\tilde{\chi}_1^0$ via the virtual Z or the virtual sleptons. But, since the $Z\tilde{\chi}_1\tilde{\chi}_2$ coupling can be strongly suppressed, decay amplitudes mediated by sleptons can be important and this branching fraction is sensitive to model parameters. The slepton masses can be written as[16],

$$m_{\tilde{\ell}_L}^2 = m_{\tilde{q}}^2 - 0.73m_{\tilde{g}}^2 - 0.27M_Z^2 \cos 2\beta \tag{2.15}$$

$$m_{\tilde{\ell}_R}^2 = m_{\tilde{q}}^2 - 0.78m_{\tilde{g}}^2 - 0.23M_Z^2 \cos 2\beta \tag{2.16}$$

$$m_{\tilde{\nu}_L}^2 = m_{\tilde{q}}^2 - 0.73m_{\tilde{g}}^2 + 0.5M_Z^2 \cos 2\beta \tag{2.17}$$

where $m_{\tilde{q}}^2$ is the squarks mass squared averaged over all the flavour's. From the above equations, squark masses are same or heavier than the gluinos mass, and sleptons can be considerably lighter than squarks if gluinos and squarks are rather close in mass.

Fig 2.4 shows a production cross section of the $p\bar{p} \rightarrow \tilde{\chi}_1^\pm\tilde{\chi}_2^0$ process. And fig 2.5 shows a total production cross section of the $p\bar{p} \rightarrow \tilde{\chi}_1^\pm\tilde{\chi}_2^0 \rightarrow 3\ell + X$ process.

The value of the production cross section is dominated by the gluino mass. The cross section at the positive μ region for all parameter sets are higher than the negative μ region. Because $\tilde{\chi}_1^\pm$ and $\tilde{\chi}_2^0$ mass at the positive μ region are higher than the negative μ region. For example, the $\tilde{\chi}_1^\pm$ mass at $\tan\beta = 4.0, \mu = 400$GeV, and $M_{\tilde{g}} = 200$GeV/c^2 is 46.2 GeV/c^2. The gluino mass corresponds to $M_{\tilde{\chi}_1^\pm} = 46.2$GeV/c^2 at $\tan\beta = 4.0, \mu = -400$GeV is

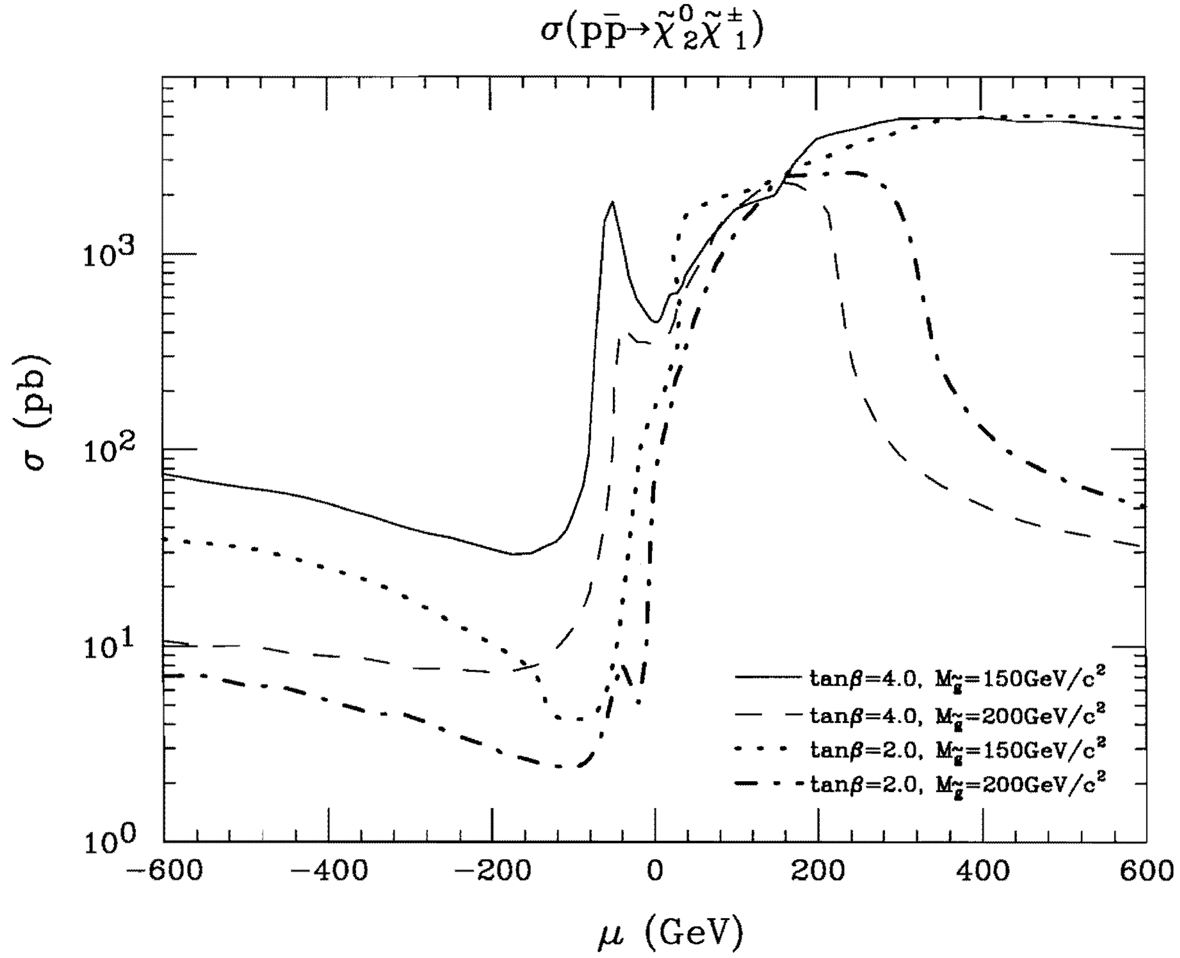

Figure 2.4: Total cross section for $p\bar{p} \rightarrow \tilde{\chi}_1^{\pm}\tilde{\chi}_2^0$ process.

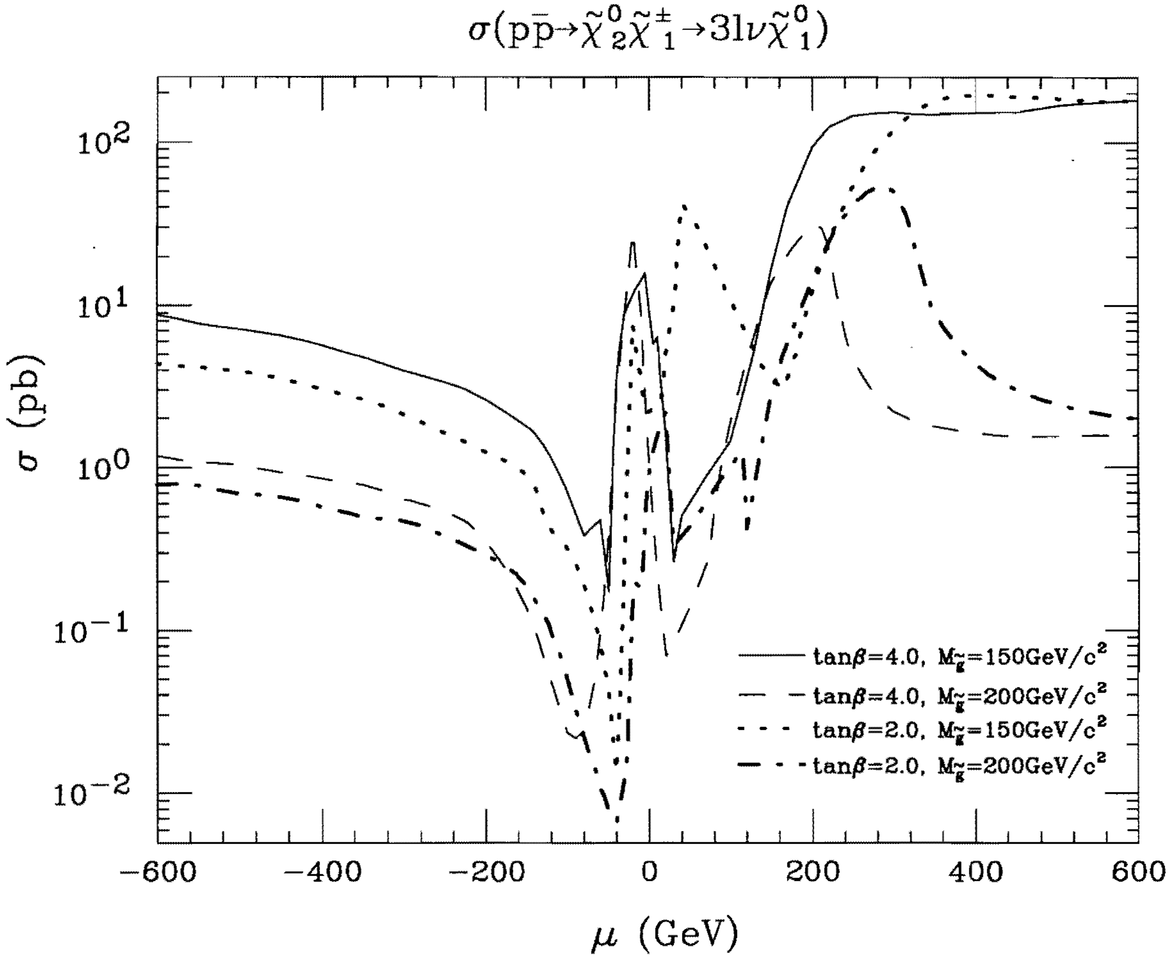

Figure 2.5: Total cross section for $p\bar{p} \rightarrow \tilde{\chi}_1^\pm \tilde{\chi}_2^0 \rightarrow 3\ell + X$ process.

approximately 150 GeV/c^2. Then we can estimate the production cross section of a SUSY parameter set to be dominated by the chargino and neutralino mass.

The $\sigma \cdot BR(p\bar{p} \rightarrow \tilde{\chi}_1^{\pm}\tilde{\chi}_2^0 \rightarrow 3\ell + X)$ at $|\mu| > 200$GeV in all the parameter sets have the same shape as the production cross section. It shows that the branching ratio of the trilepton is constant in this region. Comparing with fig 2.4 and fig 2.5, the branching ratio at $\mu < -200$GeV is higher than at $\mu > -200$GeV. If we have event acceptance of 5% for these trilepton events, we should collect about 100 pb^{-1} data to search up to $M_{\tilde{g}} = 200$GeV/c^2 in the $\mu < -200$GeV region. Since we will collect more than 100 pb^{-1} data on Run 1A and 1B in CDF, we can search to the level of $M_{\tilde{g}} = 200$GeV/c^2, which corresponds to $M_{\tilde{\chi}_1^{\pm}} = 60$GeV/c^2.

2.3 Monte Carlo Simulation of Supersymmetry

The Monte Carlo simulation was one of the most important part of our analysis. The event acceptance for SUSY trilepton events were obtained by the Monte Carlo simulation. We used ISAJET 7.0/ISASUSY 1.0 [17] event generator for SUSY event generation. The ISAJET simulates fundamental processes within the framework of the MSSM for $p\bar{p}$ and pp colliders. And ISAJET is sufficiently flexible that some non-minimal supersymmetry scenarios can be also simulated. Much of the simulation is based upon perturbative leading-log QCD, along with phenomenological models for non-perturbative aspects such as hadronization and beam jet evolution. Event simulation is carried out by the following steps:

- Calculation of hard scattering subprocess (Feynman diagrams)
- Convolution with Q^2 dependent parton distribution functions
- Implementation of all order QCD corrections in approximate forms via final and initial sate parton showers [18]
- Implementation of particle and sparticle decays, along with parton radiation and independent quark and gluon hadronization [19]

- Suitable modeling of the underlying event structure and beam jet evolution

To incorporating supersymmetric processes into ISAJET, the appropriate sparticle subprocess production cross-sections must be incorporated into ISAJET, as well as the corresponding sparticle decay modes as predicted within the MSSM framework. Both production and decay processes depend in general on the parameter set $(m_{\tilde{g}}, m_{\tilde{q}}, \mu, \tan\beta, m_{H_p}, m_t)$. Other elements of the simulation are essentially unchanged. To incorporate supersymmetry into ISAJET, the complete spectrum of MSSM particle states have been defined within ISAJET, with accompanying identification codes.

2.3.1 Production and decay processes for SUSY in ISAJET

The $\mathcal{O}(\alpha_s^2)$ hard scattering subprocesses included in ISAJET are, $(1) gg \to \tilde{g}\tilde{g}$, $(2) q\bar{q} \to \tilde{g}\tilde{g}$, $(3) gq \to \tilde{g}\tilde{q}_i$, $(4) gg \to \tilde{q}_i\tilde{q}_j$, $(5) q\bar{q} \to \tilde{q}_i\bar{\tilde{q}}_j$, $(6) qq \to \tilde{q}_i\tilde{q}_j$. Since the decay patterns of left- and right- squark types are different, ISAJET keeps track of squark flavour and type (denoted by the subscribes i and j). All squark types are currently assumed to be degenerate in mass. The $\mathcal{O}(\alpha\alpha_s)$ subprocesses which generate squarks or gluinos in association with charginos or neutralinos are also included. The subprocesses, which occur via squark exchange, are $(1) gq \to \tilde{q}\tilde{W}_i$, $(2) gq \to \tilde{q}\tilde{Z}_i$, $(3) q\bar{q} \to \tilde{g}\tilde{W}_i$, $(4) q\bar{q} \to \tilde{g}\tilde{Z}_i$. Both the pair production of chargino with neutralino and the chargino pair production are included. These subprocesses contain only W or γ/Z s-channel graphs, which should be the most important ones. The subprocesses are, $(1) q\bar{q} \to \tilde{W}_i\tilde{Z}_j$, $(2) q\bar{q} \to \tilde{W}_i\tilde{W}_j$. Trilepton events are made via the pair production of chargino with neutralino.

Signals for the production of supersymmetric particles obviously depend on how these particles decay. The heavy sparticles generically decay into lighter sparticles with the decay cascade, terminating in the (stable) LSP. The branching ratios for the various sparticles decays, as given by the MSSM, are computed in the set of routines labeled ISASUSY.

Since all the sfermions (squarks and sleptons) have non-trivial gauge interactions, they can decay into all the neutralinos that are kinematically accessible in the decays, $\tilde{f} \to f + \tilde{Z}_i$. The SU(2) doublet sfermions, $\tilde{f}_L$ can also decay via, $\tilde{f}_L \to f' + \tilde{W}_i$. These decays are forbidden for the singlet sfermions in the limit that their Yukawa interactions are negligible. The squarks can also decay by strong interactions via $\tilde{q} \to q + \tilde{g}$. This decay dominates if it is not kinematically suppressed. Since the LSP is assumed to be the lightest neutralino, the two body decay, $\tilde{f} \to f + \tilde{Z}_1$ is always accessible.

The gluinos, being electroweak singlet, can only decay via, $\tilde{g} \to \tilde{q} + q$ and this decay is kinematically allowed. Otherwise, the gluino decays via a virtual squark into 3-body mode, $\tilde{g} \to q\overline{q} + \tilde{Z}_i$, or $\tilde{g} \to q\overline{q'} + \tilde{W}_i$. Note that the decay $\tilde{g} \to q\overline{q} + \tilde{Z}_1$ is always allowed. ISAJET also includes the two boy decay, $\tilde{g} \to g + \tilde{Z}_i$ which can be important in certain regions of the parameter space.

The charginos and neutralinos, if they are heavy enough, can decay via two body modes,

$$\begin{aligned} \tilde{W}_i &\to \tilde{Z}_j + (W, H^{\pm}) \\ \tilde{W}_2 &\to \tilde{W}_1 + (Z, H_l, H_h, H_p) \\ \tilde{Z}_i &\to \tilde{Z}_j + (Z, H_l, H_h, H_p) \\ \tilde{Z}_i &\to \tilde{W}_j + (W, H^{\pm}) \end{aligned}$$

If sfermions are light enough, the decays

$$\begin{aligned} \tilde{Z}_i &\to \tilde{f}_j + \overline{f} \\ \tilde{W}_i &\to \tilde{f}_L + \overline{f}' \end{aligned}$$

may also be kinematically accessible. Here, we have, as before, assumed that Yukawa interactions are negligible; otherwise chargino decays to $\tilde{f}_R$ would also be possible to decays to Higgs bosons. Charginos and neutralinos will also decay via a variety of three body modes,

$$\begin{aligned} \tilde{W}_i &\to f\overline{f}'\tilde{Z}_j \\ \tilde{Z}_i &\to f\overline{f}\tilde{Z}_j \end{aligned}$$

that are mediated by virtual W or Z bosons and virtual sfermions. It is worth nothing that the inclusion of sfermion mediated neutralino decay amplitudes including mass splitting between squarks and sleptons can be very important, in neutralino decays, because the

$Z\tilde{Z}_i\tilde{Z}_j$ coupling can be dynamically suppressed. Finally, we have also incorporated the decays,

$$\tilde{Z}_i \rightarrow \tilde{W}_1 f\overline{f'}$$

into the program.

Chapter 3

Collider Detector at Fermilab

The CDF detector is located at Fermi National Accelerator Laboratory (Fermilab) and it is a general purpose detector to study the physics of $p\bar{p}$ collisions. The Tevatron is the highest energy proton-antiproton accelerator machine, which accelerates proton and antiproton up to 900 GeV and makes them head-on collisions at a center-of mass energy of 1.8 TeV. This chapter provides a brief description of the accelerator and the CDF detector's elements.

3.1 Accelerator

The accelerator complex at Fermilab consists of seven separate accelerator and storage ring components. Figure 3.1 shows an overhead view of the Fermilab accelerator complex. A Cockroft-Walton generator (not shown in Figure 3.1) produces a bunch of 750 KeV H^- ions, which is then injected into a linear accelerator. The liner accelerator accelerates the H^- ions to approximately 200 MeV, and injects them into the circular Booster ring. The Booster accelerates the beam of ions to 8 GeV, strips both electrons off of the H^- ions to leave bare protons, and injects the protons into the Main Ring. The Main Ring is a proton synchrotron of 2 kilometers in diameter. It serves as an injector for the Tevatron ring and as a source of 150 GeV protons for antiproton production. The Tevatron accelerator uses a ring of superconducting magnets, and is housed in the same 2 km diameter tunnel as the Main Ring. The Tevatron accepts 150 GeV particles from the Main Ring and accelerates them to 900 GeV.

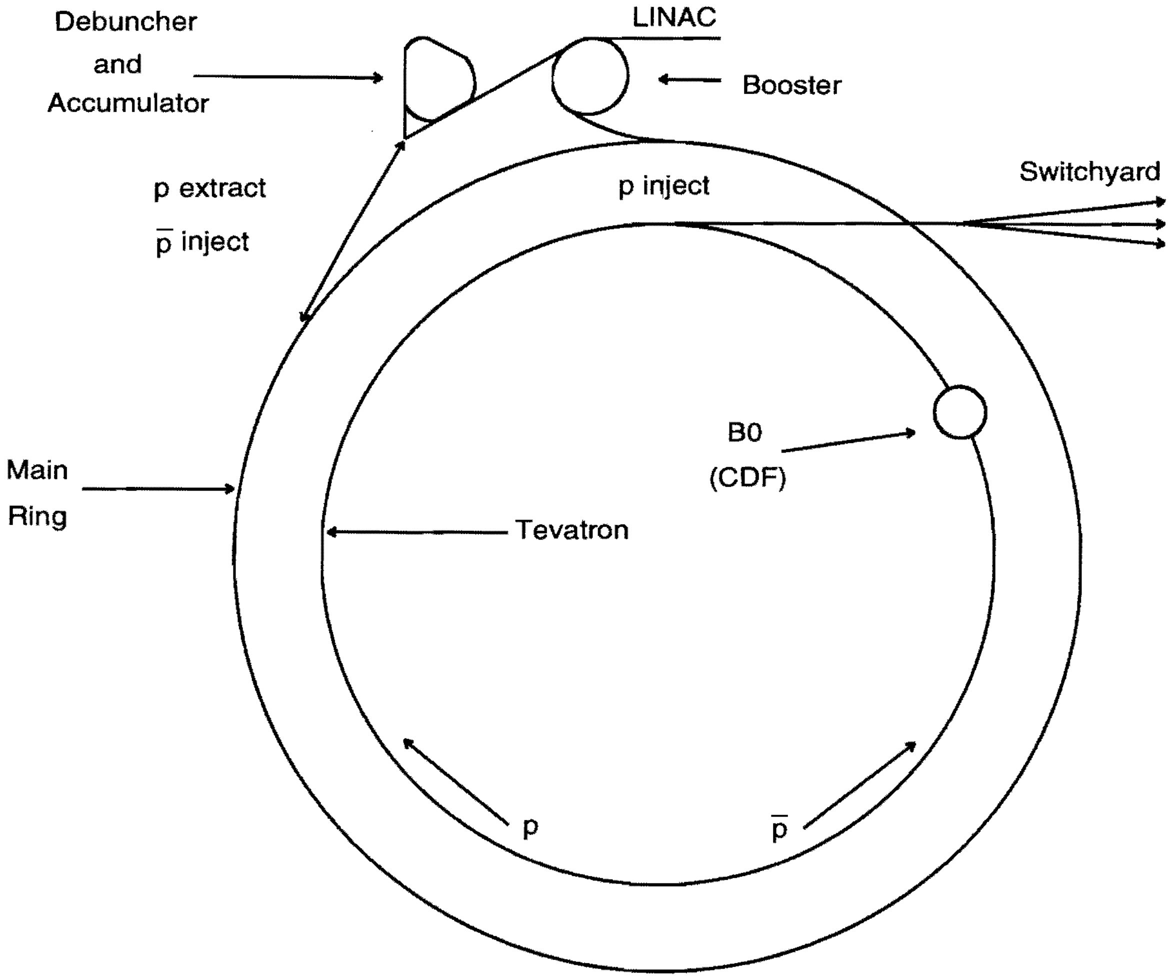

Figure 3.1: An overhead view of the Fermilab accelerator complex.

The antiproton production system produces antiprotons with a large initial energy spread, and then uses two storage rings to reduce this energy spread and store a nearly monoenergetic beam of antiprotons. Antiprotons are produced when 150 GeV protons from the Main Ring hit a beryllium target. The antiprotons are directed into a storage ring called the debuncher. The antiprotons enter the Debuncher in a short time pulse, and have energies of approximately 8.5 GeV with a large energy spread and the transverse motion of the beam where bunch rotation and stochastic cooling[20] take place. Bunch rotation is a radio frequency technique in which the energy spread of an antiproton pulse is reduced by increasing its time spread. In stochastic cooling, a probe senses the position of the beam, and sends a signal across a chord of the accelerator ring to a kicker. The kicker then applies a correction to the beam as it passes by. After two second in the Debuncher, the beam is directed into the Accumulator, where it undergoes further stochastic cooling. The Accumulator is used both to cool the antiprotons and to store them, and accepts a new antiproton pulse from the Debuncher in every two seconds. After several hours in the Accumulator, the antiprotons are accumulated in a tight core with a very narrow energy distribution.

When a sufficient number of antiprotons have been collected, 6 bunches of antiprotons are extracted from the core in the Accumulator, and injected into the Main Ring. There they are accelerated to 150 GeV and injected into the Tevatron, where 6 bunches of protons are already circulating. Since protons and antiprotons have opposite charges, the proton and antiproton bunches will circulate in opposite directions inside the same accelerator ring. The 6 antiproton bunches will intersect with the 6 proton bunches at 12 points around the accelerator ring. A radio frequency process called "cogging" moves intersection points around the ring so that one of the 12 intersections is located at the B0 intersection. Finally the proton and antiproton bunches are simultaneously accelerated to 900 GeV in the Tevatron.

The rate of the collisions with protons and antiproton is measured by the quantity called luminosity. The luminosity $\mathcal{L}$ is defined as,

$$N = \mathcal{L}\sigma$$

where N is the number of produced events for a given process, σ is the production cross section for that given process. For the proton-antiproton colliding system in the Tevatron, the luminosity is given by,

$$\mathcal{L} = \frac{f_r n_{bunch} N_p N_{\overline{p}}}{A}$$

where f_r is the bunch crossing rate, $N_p(N_{\overline{p}})$ is the number of the protons(antiprotons) in each bunch., n_{bunch} is the number of bunches, and A is the effective cross sectional area of beam overlap. The Tevatron provided an instantaneous luminosity of $\mathcal{L} \leq 9.5 \times 10^{30}$ cm^{-2} s^{-1} during the 1992-1993 run.

3.2 The CDF detector

The CDF detector is a large multipurpose solenoidal detector designed to measure the leptons and jets produced in $p\overline{p}$ collisions. A detailed description is given in [20]. It is divided into central, plug, and forward region along the beam axis. Figure 3.2 shows a perspective view of the CDF detector and figure 3.3 shows a side cross sectional view of the CDF detector.

The CDF coordinate system uses a right handed coordinate system. The direction of the proton beam defines the z axis and the horizontal direction defines the x axis and the vertical direction defines the y axis. The azimuthal angle ϕ starts from the positive x-axis and increases from positive x to positive y. The polar angle θ is measured from the proton beam direction. We use the pseudorapidity, η, instead of θ. The pseudorapidity is defined as, $\eta \equiv -\ln(\tan\frac{\theta}{2})$. For high P_T and low mass particles, pseudorapidity is a good approximation of the particle's true rapidity:

$$y = \frac{1}{2}\ln\frac{E+P_z}{E-P_z}$$

Because rapidity transforms additively under Lorentz transformations, the detector geometry is approximately invariant for the z-boosts that are an in-escapable consequence of $p\overline{p}$ collisions. In minimum bias events, the average number of particles per unit pseudorapidity is approximately constant.

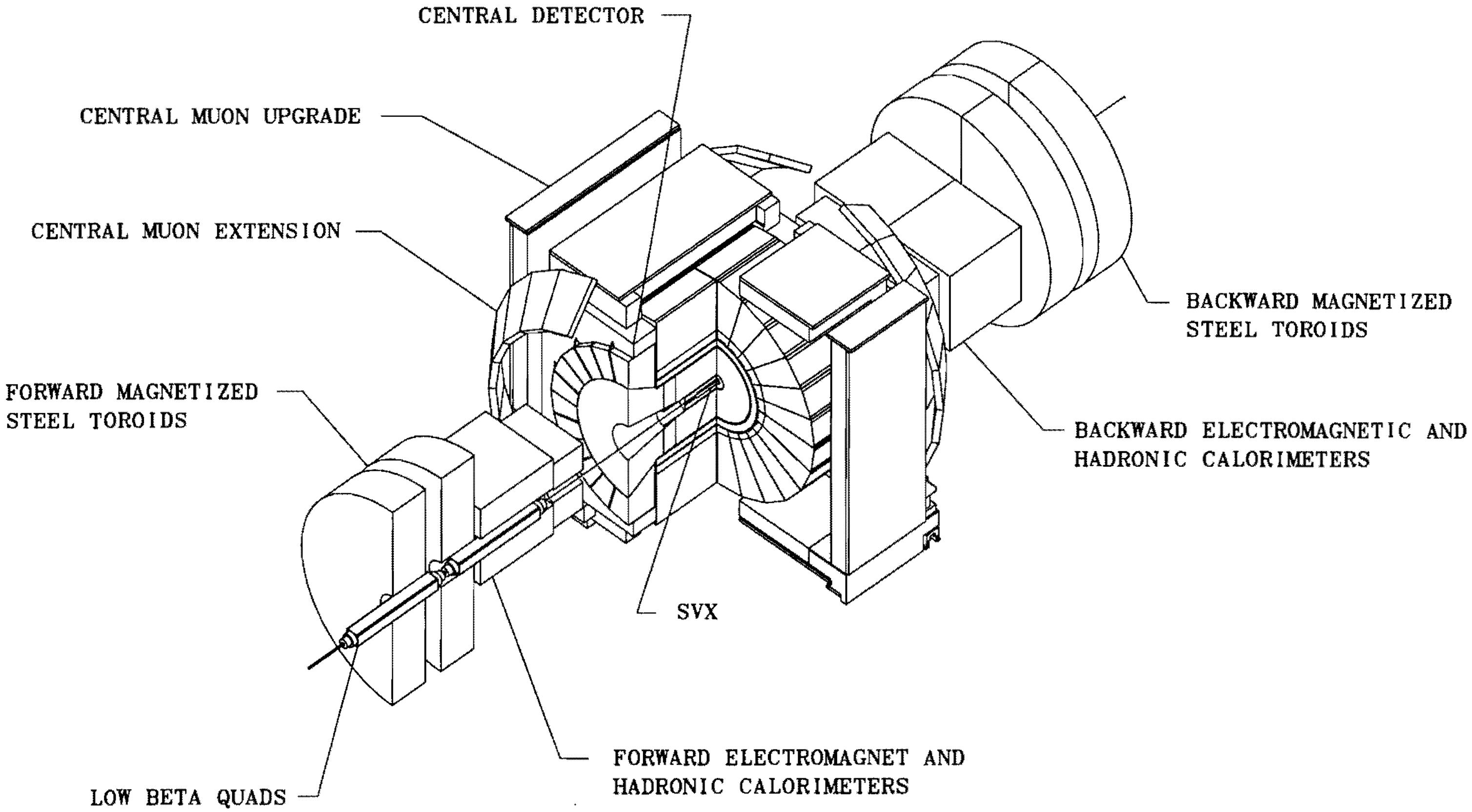

Figure 3.2: A perspective view of the CDF detector

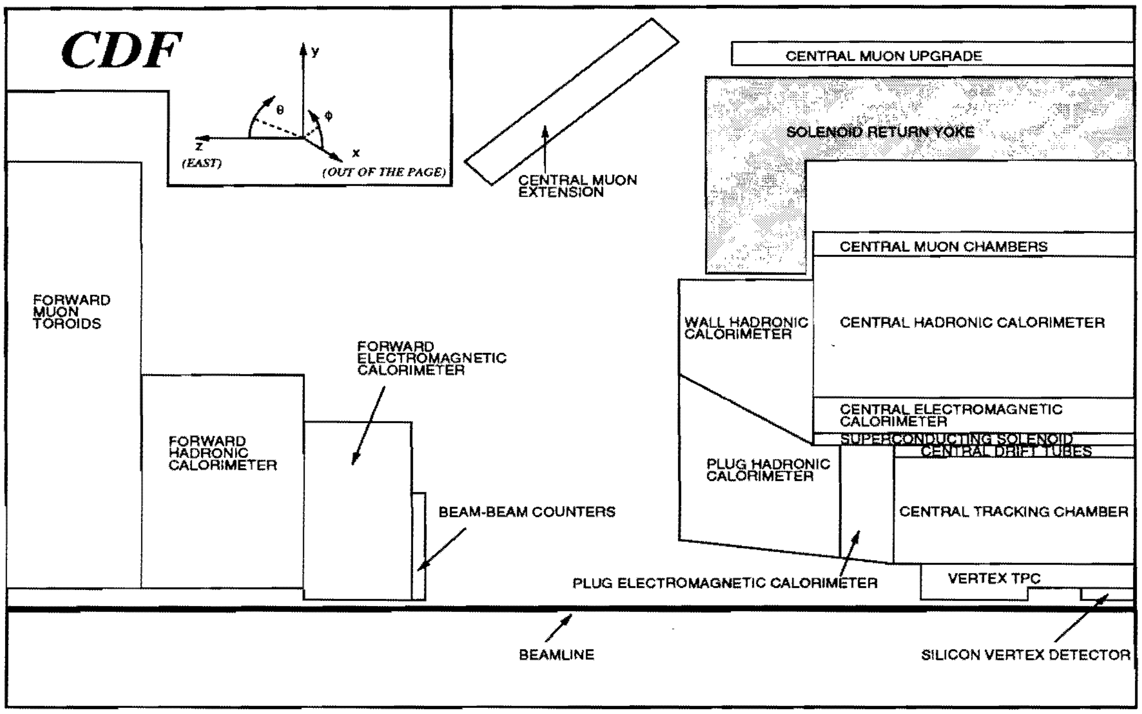

Figure 3.3: Side cross sectional view of the CDF detector

3.2.1 Beam-Beam Counters

The Beam-Beam Counters consists of two planes of scintillation counters covering the angular range of 0.32° to 4.47° in both the forward and backward directions ($3.24 < |\eta| < 5.88$) [20]. Each scintillator plane consists of 16 scintillator paddles arranged in a square around the beam pipe. Two phototubes, one at each end of every scintillator, detect light from charged particles transversing the counter.

Coincident hits in both counters, in time with the passage of the bunches through the detector, serve as both a minimum bias trigger and the primary luminosity monitor. The rate (number) of coincidences in these counters, divided by the effective cross section of the counters, is what gives the instantaneous (integrated) luminosity.

3.2.2 Tracking System

The CDF tracking system consists of three separate systems: silicon vertex detector(SVX), vertex tracking chamber(VTX), and central tracking chamber(CTC). The three tracking

Table 3.1: Description of the Tracking Chambers

	Silicon Vertex Detector (SVX)	Vertex Tracking Chamber (VTX)	Central Tracking Chamber (CTC)
Polar Angle Coverage	$\|\eta\| < 1.0$	$\|\eta\| < 3.25$	$\|\eta\| < 1.5$
Inner, Outer Tracking Radii (cm)	2.7, 7.9	8,[a)] 22	30.9, 132.0
Length (cm)	26	280	320
Layers	4	24	60 axial 24 stereo
Strip or Wire Spacing	60 μm (inner 3 lay.) 55 μm (outer layer)	6.3mm	10 mm
Spatial Resolution	15 μm $(r-\phi)$	200-500 μm $(r-z)$	200 μm $(r-\phi)$ 4 mm $(r-z)$
Momentum Resolution	$\delta P_T/P_T = 0.001 \times P_T^{b)}$	-	$\delta P_T/P_T = 0.002 \times P_T$
Thickness ($\theta = 90^\circ$)	$\approx 0.035X_0$	$\approx 0.045X_0$	$\approx 0.015X_0$

a) For inner 2 modules. Outer 6 modules are 3 cm inner radius.
b) With both CTC and SVX hits incorporated into track fit.

systems are summarized in Table 3.1

Silicon Vertex Detector

Surrounding the 1.9 cm radius beryllium beampipe is a 4 layer silicon microstrip vertex detector(SVX)[21], which was installed in CDF in 1992. The SVX is 51 cm long and consists of two identical cylindrical modules which meet at $z = 0$. Because $p\overline{p}$ interactions are spread along the beamline with standard deviation $\sigma \sim 30$ cm, the geometrical acceptance of the SVX is about 60% for $p\overline{p}$ interactions. The four layers of the SVX are at distances of 3.0, 4.2, 6.8 and 7.9 cm from the beamline. Axial microstrips with 60 μm pitch on the three inner-most layers and 55 μm pitch on the outermost layer provide precision track reconstruction in the plane transverse to the beam. The SVX's single hit resolution is measured in data to be $\sigma = 13\mu$m, and the impact parameter resolution at high momentum is measured to be $\sigma = 17\mu$m. Due to the radiation damage to the SVX readout chip, the performance of the SVX deteriorated over the course of the data taking period [21]. On the inner-most layer, the ratio of the average analog pulse size from a particle to the noise level(S/N) decreased from approximately 9 to 6 from the beginning to the end of the data taking period.

Vertex Tracking Chamber

Outside the SVX is a vertex drift chamber(VTX), installed in 1992, which provides tracking information up to a radius of 22 cm and $|\eta| < 3.25$. The VTX is a time projection chamber in 8 modules with a maximum drift distance of 10 cm. The old VTX was replaced by the current VTX for withstanding the higher luminosity and making space for the SVX. The VTX measure the $p\bar{p}$ interaction vertices along the z axis with a resolution of 1 mm, by finding the point of convergence of all the reconstructed tracks in the event. The VTX is also used to detect the photon conversion.

Central Tracking Chamber

The central tracking chamber(CTC) [22] is a main detector to detect a charged particle in CDF. The CTC is a 3.2 m long cylindrical drift chamber surrounding VTX and SVX. CTC reconstructs a charged particle track in the $r - \phi$ plane and measures their momentum with a 1.4 tesla axial magnetic field generated by a superconducting solenoid of length 4.8 m and radius of 1.5 m. It covers to $|\eta| < 1.5$, but the best momentum measurement is possible in $|\eta| < 1.0$. The CTC has 84 layers of wires and the wires are grouped into 9 "superlayers". The sense wires in each superlayers are organized into $r - \phi$ cells, which are tilted 45° with respect to the radial direction. Five of the superlayers have 12 sense wires that run parallel to the beam and magnetic field. Between each of these axial layers are four stereo superlayers of 6 sense wires each. The stereo wires are strung at a 3° angle from the beam; this yields a z-position resolution of 3 mm, comparable to the position resolution of the central calorimeter. A stiff track that passes through the outer radius of the CTC will have 84 hits spread over a path of at least 1 m.

The CTC has a momentum resolution $\delta P_T/P_T = 0.002P_T$ for isolated tracks intersect with the beam at the beam position point(beam constraint fits). For isolated high P_T tracks, typical of electroweak boson decay, the track finding efficiency is indistinguishable from 100%.

Outside the CTC are three layers of drift tubes(CDT) which use drift times and charge division to measure the $r-\phi$ and z positions of tracks, respectively. Typical resolutions are 2.5 mm in the z direction and 200 μm in $r-\phi$.

3.2.3 Calorimeter

The solenoid and tracking volume of CDF is surrounded by calorimeters which cover 2π in azimuth and in pseudorapidity, η, from -4.2 to 4.2. The calorimeter are segmented in azimuth and pseudorapidity to form a projective tower geometry which points back to the nominal interaction point. There are three separate η regions of calorimeters, the central, end-plug, and forward. Each region has an electromagnetic calorimeter (CEM,PEM,FEM) and behind it an hadronic calorimeter (CHA/WHA,PHA,FHA). This segmentation aids electron identification on a tower-by-tower basis using the ratio of electromagnetic to hadronic energies. In all cases, the absorber in the hadronic compartments is lead. Table 3.2 summarizes the calorimeter subsystems at CDF.

Central Calorimeter

The central region ($|\eta| < 1.1$) system is made up of lead-scintillator shower counters(CEM) [23] followed by an iron-scintillator calorimeter(CHA/WHA) [24]. The central calorimeter is divided into 15° segments("wedges") in ϕ and 0.1 segments in η. These modules are grouped into four removable "arches" which surround the solenoid. The boundaries between wedges and arches produce gaps in calorimeter coverage. The CEM is a sandwich of 31 layers of 5 mm thick polystyrene scintillator and 30 layers of $\frac{1}{8}$ inch thick aluminum clad lead sheets. The scintillator's light is collected through wavelength shifters on the

Table 3.2: Description of the CDF Calorimeter Subsystems

Subsystem	CEM	CHA/WHA	PEM	PHA	FEM	FHA
Energy Resolution ($\%/\sqrt{E}$)	13.5	80	28	130	25	141
Angular Coverage (in $\lvert\eta\rvert$)	< 1.1	< 1.3	$1.1 - 2.4$	$1.3 - 2.4$	$2.2 - 4.2$	$2.3 - 4.2$
Segmentation ($\Delta\eta \times \Delta\phi$)	$0.1 \times 15\cdot$	$0.1 \times 15\cdot$	$0.1 \times 5\cdot$	$0.1 \times 5\cdot$	$0.1 \times 5\cdot$	$0.1 \times 5\cdot$
Active Medium	lead, scintillator	iron, scintillator	lead, proportional tube	iron, proportional tube	lead, proportional tube	iron, proportional tube
Position Resolution ($r - \phi \times z$)	0.2 cm × 0.2 cm[a]	10 cm × 5 cm	0.2cm × 0.2 cm	2 cm × 2 cm	0.2 cm × 0.2 cm	3 cm × 3 cm
Longitudinal Depth	$18X_0$[b], $1.0\Lambda_{abs}$	$4.7\Lambda_{abs}$	$19X_0$, $1.0\Lambda_{abs}$	$5.7\Lambda_{abs}$	$25X_0$, $0.8\Lambda_{abs}$	$7.7\Lambda_{abs}$

[a] Using the CES chambers

[b] Including the $1X_0$ solenoidal coil

Table 3.3: Description of the Shower Max Detector (CES) and Pre-Shower Detector (CPR).

	CES Chamber		CPR Chamber
	Wires	Strips	Wires
	($r - \phi$ view)	(z view)	($r - \phi$ view)
Number of Channels	32	$69^{a)}$, $59^{b)}$	16
Spacing (cm)	1.45	$1.67^{a)}$, $2.07^{b)}$	2.2
Spatial Resolution (cm)	0.2	0.2	–
Saturation Energy (GeV)	150	150	>150
Chamber length in z (cm)	234		103
Chamber Width in ϕ(°)	14.0		12.1

$^{a)}$ for CES segment between 6 cm $< z <$ 115 cm

$^{b)}$ for CES segment between 115 cm $< z <$ 240 cm

both sides of the wedge. The wavelength shifters transmit the light to acrylic light guides which are attached to photomultiplier tubes located at the rear of each wedge.

Proportional chambers are embedded near shower maximum, 6 radiation lengths (X_0) within the CEM. These chambers, called Central Electron Strip (CES) chambers [23], have wires in the $r - \phi$ view and cathode strips in the z view. The CES is summarized in Table 3.3. A second set of proportional chambers, the Central Pre-Radiator (CPR), are placed in between the front face of the CEM and the magnet coil, act as a shower pre-sampler. Both the CES and CPR are split into two separate readout segments in the z direction, so that the wires do not run along the full length of the calorimeter, but are read out in two divisions.

The CHA are located in the wedges just behind the CEM. The CHA are constructed from a sandwich of 32 layers of 1.0 cm scintillator and 2.5 cm steel. The WHA calorimeter occupies the transition region between the central barrel and the plug. Because the particle energies here are greater for the same transverse energy, the steel of the WHA is thicker than that of the CHA. The WHA is a sandwich of 15 layers of 1.0 cm scintillator and 5.0 cm steel. Pions from a test beam are used to calibrate both the CHA and the WHA, and the calibration is maintained with C_s^{137} sources.

Plug Calorimeter

The plug region ($1.1 < |\eta| < 2.4$) is made up of the plug electromagnetic (PEM) [25] and the plug hadronic(PHA) calorimeters. The plug calorimeter is divided into 5° segments in ϕ and 0.09 segments in η. The PEM calorimeters are divided into 4 quadrant, and consist of 34 layers of proportional tubes alternating with 2.7 mm lead sheets. One quadrant is segmentated into 18 towers in azimuthal angle and 14 towers in pseudorapidity. Each tower is subdivided into 3 depth segments. The depth segmentation provides information about the longitudinal development of electron showers.

The PHA calorimeters are divided into twelve 30° stacks, and consist of 20 layers of proportional tubes separated by 5 cm of steel. Each stack is segmented into 6 towers in azimuthal angle and 14 towers in pseudorapidity.

Forward/Backward Calorimeter

The forward/backward electromagnetic calorimeter (FEM) [26] consists of 30 sampling layers of proportional tube chambers with cathode pad readout separated by lead sheets for a total thickness of $25X_0$. The forward/backward hadron calorimeter (FHA) [27] is composed of proportional tube chambers and steel plates. These calorimeters are not used in this analysis.

3.2.4 Muon Detector

The CDF muon system consists of four subsystems: the central muon chambers (CMU), the central muon upgrade chambers (CMP), and the central muon extension chambers (CMX) in the central region and the forward muon chambers (FMU) in the forward region.

The central muon chambers (CMU) [28] are located behind the central calorimeters at 3.47 m from the beam line and cover $|\eta| < 0.6$ for the pseudorapidity region. The central muon upgrade chambers(CMP) [29] are located on outside the solenoid return yoke and cover the same pseudorapidity region for CMU. The central muon extension chambers (CMX) [29] stand by itself near the central components and cover $0.6 < |\eta| < 1.0$ for the pseudorapidity region. The CMP and CMX were installed in 1992 for extending the muon detection region. Approximately 84% of the solid angle for $|\eta| < 0.6$ is covered by CMU, 63% by CMP and 53% by both. And approximately 71% of the solid angle for $0.6 < |\eta| < 1.0$ is covered by CMX. Figure 3.4 shows the muon detector coverage map in $\eta - \phi$ view.

The CMU are operated in the limited-streamer mode, flowing 50%/50% argon/ethane with 0.7% ethanol. Approximately 5 hadronic absorption lengths of the CDF central calorimeter separate the CMU from the interaction region. The four layers of drift cells in CMU provide 3-dimensional reconstruction of tracks via single-hit TDCs in the transverse direction and charge division in the longitudinal direction. The muon chambers are grouped in 15° wedges in ϕ at the outer edge of the calorimeter wedges. Only 12.6° of the wedge is covered by the chambers, leaving a 2.4° gap between adjacent wedges. Each wedge consists of three muon chambers. In addition to the gap in coverage in ϕ, there is a 1.5° gap in θ between the arches (at $\theta = 90°$). A muon chamber has 16 drift cells divided into 4 layers and 4 towers. To reduce the number of electronic channels needed for chamber readout, sense wires from alternate cells in each layer are ganged at $\theta = 90°$. The sense wires from alternate layers in a muon tower lie on a radial line with the nominal $p\bar{p}$ interaction point. The other 2 are offset from this line by 2 mm at the radial chamber's midpoint to resolve the ambiguity of on which side(in ϕ) of the sense wire the particle passed.

The CMP consists of an additional 60 cm of steel absorber behind the CMU, followed by a second set of muon chambers. The return yoke of the CDF solenoid already provides the necessary steel at the top and bottom of the central detector so that it is only necessary to add more steel on the two sides, where two movable steel walls were installed. The CMP chambers have single wire drift cells. Four chamber layers are required, with one pair of chambers half-cell staggered relative to the other pair. The CMP reduces the punch-through rate by a factor of ~ 10 which allows us to lower the P_T thresholds without the trigger rates becoming unmanageable.

The CMX consists of "pinwheels" of drift cells around each end of the detector. In the region $-45^\circ < \phi < 225^\circ$ the cells lie on a conical surface to maximize the acceptance. In the region $225^\circ < \phi < 315^\circ$ the cells have been assembled in a flat pinwheel-like structure to minimize the space occupied. Because of the angle at which particles transverse the calorimeter, the amount of steel is higher here than in CMU and no new steel is added. We have 8 layers of drift cells between 2 layers of scintillator which provide three-dimensional tracking. The scintillators(CSX) provide the timing of the muon track. The cell dimensions are 1" × 6" × 72" and we have a single wire per cell. The resolution is 250 μm(1 cm) perpendicular to (along) the wire. Forty-eight cells are glued into a module covering 15° in ϕ. Two arches with 8 modules each were installed on each side of the detector for this run. The CMX covers currently $\frac{2}{3}$ of ϕ ; 30° at the top of the detector have no coverage due to interference with the main ring shielding and the cryogenics. 90° in the bottom region not instrumented either.

The CDF forward muon chambers (FMU) [30] consist of two muon spectrometers measuring muon momentum and position for polar angles $3^\circ - 16^\circ$ (forward) and $164^\circ - 177^\circ$ (backward). The FMU consists of a pair of magnetized iron toroid instrumented with three sets of drift chambers and two planes of scintillation trigger counters. We have an average of 17 pion interaction lengths in FMU and therefore there should be no pion punch-through background. The main source of background in FMU is decays of pions and kaons in the space between the interaction point and the detector. FMU is not used in this analysis.

3.3 Trigger System

The CDF trigger is itself a four-level combined hardware and software system. The first level trigger, level 0, uses BBC. The analog signal from BBC phototubes feed into fixed threshold discriminators. All discriminator outputs from a single BBC plane are then combined in a logical "OR", and the result are tested for a coincidence of east and west planes within a 15 ns gate around the time of the beam crossing. The coincidence signal opens a gate of the first detector trigger, level 1 trigger.

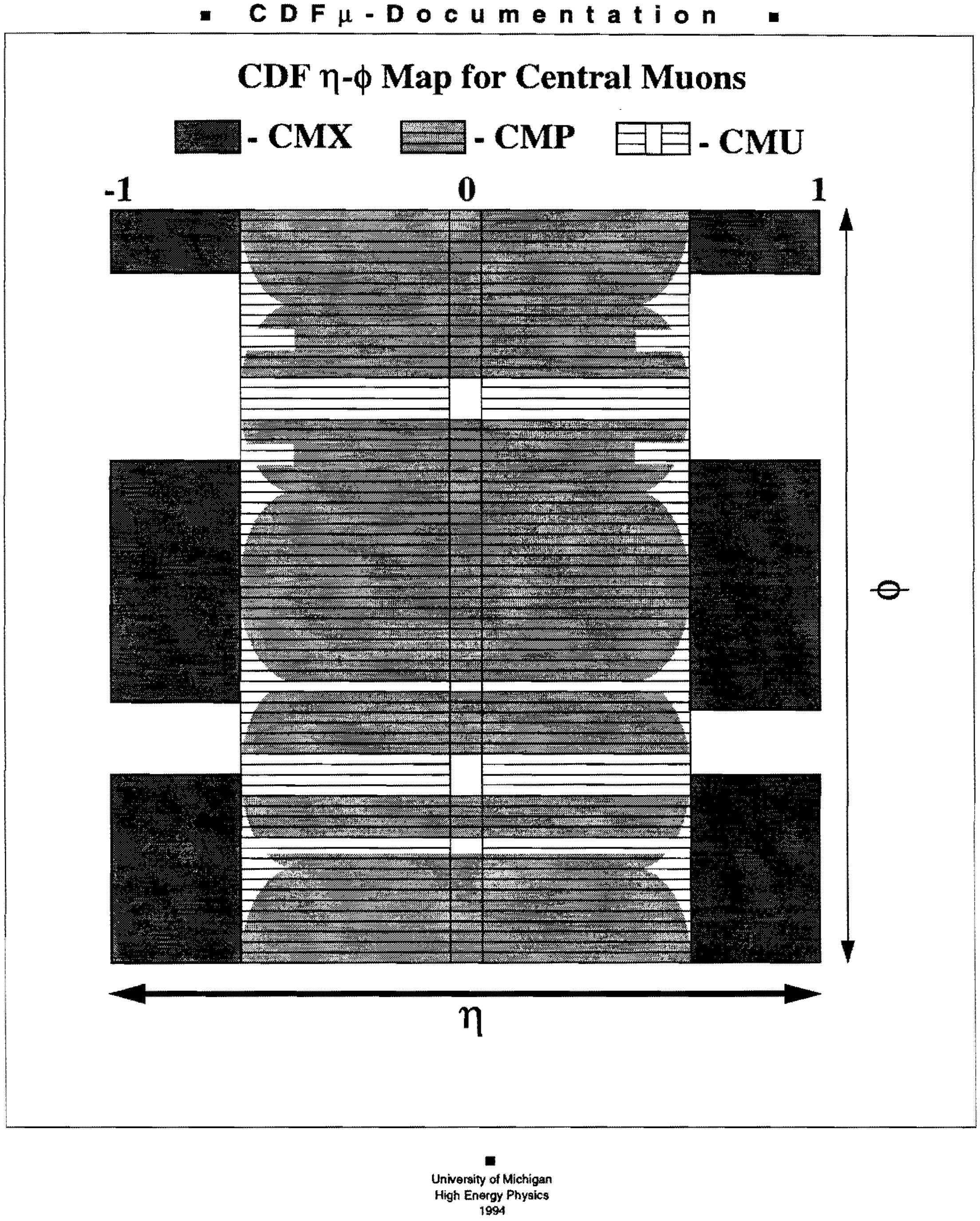

Figure 3.4: Central Muon Detectors Coverage Map

The level 1-3 triggers reduce high rate of $p\overline{p}$ interactions to a rate which could be recorded on a tape. The level 1-3 triggers consist of a logical OR of several requirements which are defined to detect electrons, muons, photons, missing energy, jets, and taus and select events based on physics interests. The level 1 has an input rate of 300kHz, to match the 3.5 μs, crossing time. The level 2 has a maximum input rate of approximately 2.5 kHz, and an output rate of about 20 Hz. The level 3 is a farm of computers that runs a slightly streamlined version of the offline reconstruction code, and can write data on the tape with about 6 Hz. The farm computers of level 3 are made up of 48 Silicon Graphics computers, each containing two event buffers, plus an array of service hardware to push the data into and out of 96 buffers. Each events is sent to a single buffer, so that level 3 can be processed up to 48 separate events in parallel, with another 48 events meanwhile being loaded to secondary buffers.

Many trigger schemes are embeded in the level 1, 2, and 3 triggers to collect the events for all the interesting physics. We use the inclusive muon and electron triggers in this analysis, which we will describe in detail.

3.3.1 CFT

The level 2 muon and electron triggers use 2 dimensional tracks found by Central Fast Tracker (CFT), a hardware track processor which uses fast timing information from the CTC to find high-transverse momentum tracks. The track finder is a 19 stage digital pipeline which analyze "prompt" hits from the 4392 axial sense wires of the CTC to identify tracks. Tracks are found by comparing the hits in the CTC to predetermined hit patterns for the range of transverse momenta allowed by the CFT trigger threshold [31]. The processor has 8 P_T bins covering the range from 2.5 to 15 GeV/c. In an average of 2.5 μs/event, the identification of all high P_T tracks in the CTC is complete, and the list of found tracks is presented to the rest of the CDF trigger system for use in level 2 decisions. The momentum resolution is $\frac{\delta P_T}{P_T} = 3.5 \cdot P_T$

3.3.2 Inclusive Muon Triggers

level 1

The level 1 central muon trigger requires a pair of hits on the radially aligned wires in the CMU or CMP chambers. The transverse momentum, P_T, of the muon track segment is measured by using the arrival times of the drift electrons at the sense wires to determine the deflection angle due to the magnetic field. The muon trigger requires a track segment in the CMU with $P_T > 6$ GeV/c in coincidence with hits in the CMP, or a track segment in the CMX with $P_T > 10$ GeV/c in coincidence with hits on scintillators placed on both sides of the chambers. The scintillator's coincidence is required to occur in a narrow time window centered at the interaction time, in order to reduce the rate from particles not associated with the primary interaction.

level 2

In level 2 central single muon trigger, CTC tracking information in the $r - \phi$ plane is used. The trigger requires the existence of a CFT track with $P_T > 9.2$ GeV/c. The track with $P_T > 9.2$ GeV/c in CFT is required to match within 5 degrees of the muon stub. The central single muon trigger consists of five sets of triggers according to the locations of the hits in the muon chambers.

level 3

The level 3 trigger is also called an offline trigger, because of reconstructing the CTC track using the same code as the offline analysis but only in 2-dimension. For each track the associations of the muon chamber's hit is determined the track P_T and the ϕ of the track at the radius of the muon chambers with a fast 2-dimensional reconstruction algorithm. The momentum resolution of this fast reconstruction is $\delta P_T/P_T \sim 0.0077 \cdot P_T$. If a track has P_T above the P_T threshold and within a position match threshold in the azimuthal direction with a track segment in the muon chamber, the event is picked up.

3.3.3 Inclusive Electron Triggers

level 1

The level 1 electron trigger system is designed to use the projective geometry of the calorimeter towers. The signals from each calorimeter are ganged into trigger towers measuring $\Delta\eta \times \Delta\phi = 0.2 \times 15^\circ$, and are weighted by $\sin\theta$ to provide a crude estimate of transverse energy. The trigger requires that a trigger tower has the transverse electromagnetic energy greater than 6 GeV.

level 2

The level 2 central electron trigger uses the calorimeter information and tracking information. A hardware cluster finder searches the electromagnetic tower array to form clusters. The clusters are formed around seed towers, which at least 4 GeV of transverse energy is required, assuming the vertex position to be at $Z = 0$. The 4 adjacent towers of the each seed tower are searched and included in the cluster if they have $E_T > 3.6$ GeV. The particle's track momentum is measured by CFT. The trigger requires that the seed tower in the region of $|\eta| < 1.19$ transverse energy and track P_T by CFT have to be above the each trigger threshold.

level 3

The level 3 trigger uses the same clustering algorithm and track finding algorithm as used in the offline analysis, except for CTC track reconstruction. The offline clustering makes use of the fine segmentation of the calorimeter. The level 3 trigger requirements are basically the same as the offline electron requirement.

Chapter 4

Event Selection

The range of $\tilde{\chi}_1^\pm$ and $\tilde{\chi}_2^0$ masses which are accessible with the present integrated luminosity is 40 - 60 GeV/c^2. Therefore, the three-way split of the energies of each of the $\tilde{\chi}_1^\pm$ and $\tilde{\chi}_2^0$ between two leptons and the lightest neutralino ($\tilde{\chi}_1^0$) leads to the lepton transverse momenta which are typically lower than the transverse momenta of leptons from W and Z^0 decays. Since the end products are ether electrons or muons, our analysis begins with the inclusive electron and muon data samples. Trilepton events from $\tilde{\chi}_1^\pm\tilde{\chi}_2^0$ production are similar to the WZ^0 events and they don't have any hadronic jet. In addition, the each lepton in this process is well isolated to each other. Therefore, we searched for the events with three isolated leptons in the CDF data sample.

4.1 Outline of the Event Selection

The number of events CDF took during the 1992-1993 run are very large and include the various event types. Since the data are taken with the various event triggers, we classified all the data with the triggers that the event passed. They are called data sample. We use the stream1 inclusive muon and electron data samples. These data samples are passed with the inclusive muon and electron triggers described in section 3.3.2 and 3.3.3. These triggers require at least one lepton with the transverse momentum(P_T) of more than 9.2 GeV/c. This requirement should be satisfied by the trilepton events from $\tilde{\chi}_1^\pm\tilde{\chi}_2^0$ production. Figure 4.1 shows the P_T distribution of the lepton from $\tilde{\chi}_1^\pm\tilde{\chi}_2^0$ production($\mu = -400$GeV, $\tan\beta = 4.0$, M($\tilde{g}$)=150GeV/c^2, M($\tilde{q}$)=1.2M($\tilde{g}$), M($\tilde{\chi}_1^\pm$)=46.2GeV/c^2). From these figures, the stream1 inclusive muon and electron triggers are expected to pick up the most of trilepton events.

Next, we select the events with at least three leptons(muon or electron) from these data sample. Then we put various cuts on the three lepton events to reduce the backgrounds. At the end, we apply the event topology cuts. The different topologies of the trilepton events in $\tilde{\chi}_1^\pm \tilde{\chi}_2^0$ production from the Standard Model processes determine these cuts criteria. We describe the lepton selections and event selections in the following sections.

4.2 Lepton Selection

In our analysis, the most important things are identification of muons and electrons in the event. In CDF, electrons and muons are identified using tracking, calorimeter and muon chamber informations. The transverse momentum(P_T) range of the leptons from $\tilde{\chi}_1^\pm$ or $\tilde{\chi}_2^0$ are 5 GeV/c to 30 GeV/c and they are between the range of the leptons from $b\bar{b}$ production and W, Z^0 production. Since the features of the leptons from $\tilde{\chi}_1^\pm$ or $\tilde{\chi}_2^0$ are similar to the leptons from W, Z^0 production, we use the lepton selection criteria which is similar to the criteria for W and Z^0 in our $\tilde{\chi}_1^\pm \tilde{\chi}_2^0$ search.

4.2.1 Electron Identification

CDF has three categories of electrons based on their detection area: central electrons, plug electrons, and forward electrons. The central electrons are located in the central region ($|\eta| < 1.1$). The plug electrons are located in the plug region ($1.1 < |\eta| < 2.4$). The forward electrons are located in the forward region ($2.2 < |\eta| < 4.2$). The used electrons in this analysis are the central and the plug electrons. The electron identification begins with a clustering algorithm to identify electron showers. An electron cluster consists of a seed tower (the tower in the cluster with the largest energy) and shoulder towers (adjacent towers incorporated into the cluster). Towers with electromagnetic (EM) transverse energy $E_T > 3$GeV are eligible to be seed towers. Hereafter, when the magnitude of the transverse momentum is measured using the calorimeter, we refer to this quantity

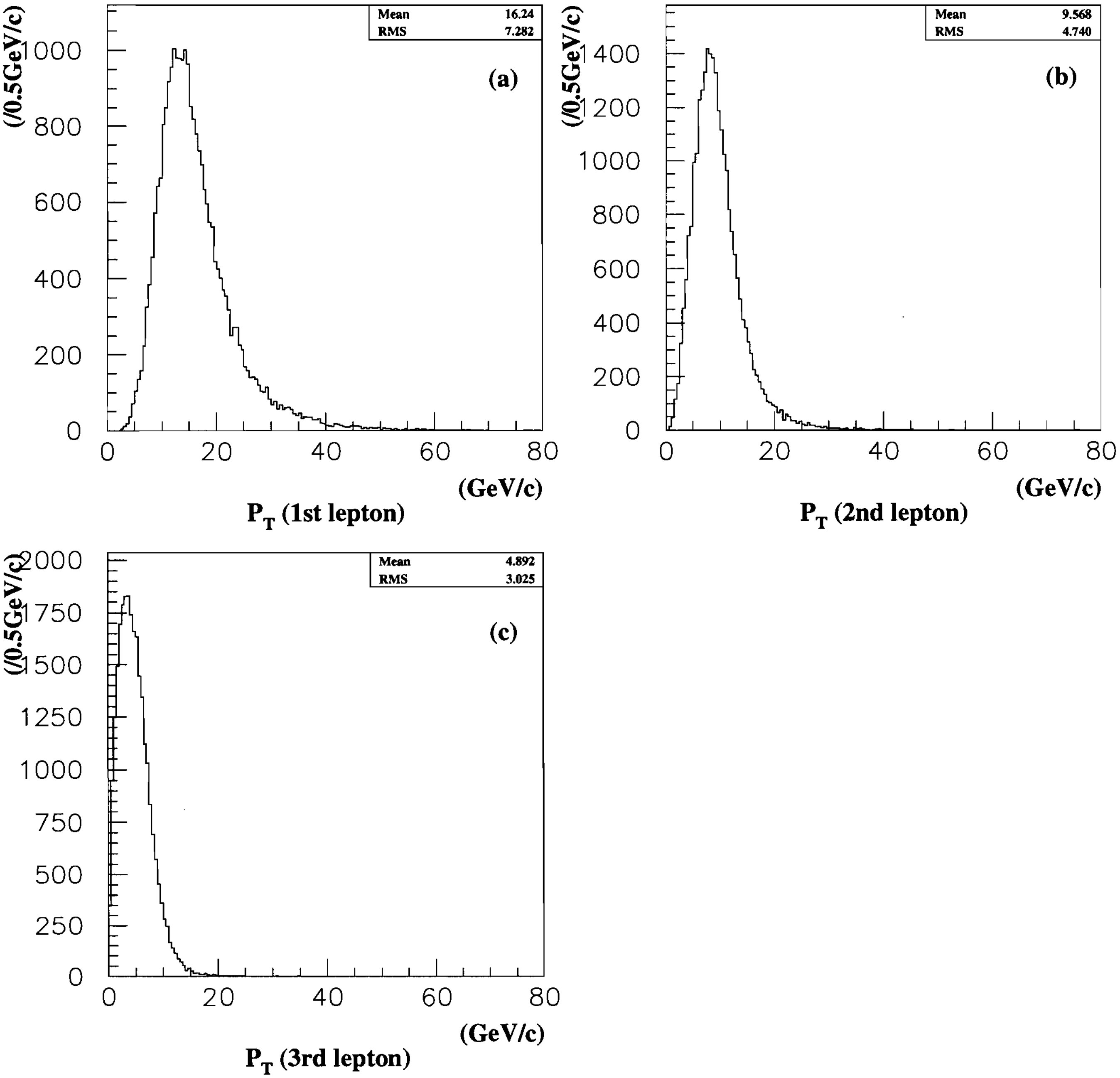

Figure 4.1: P_T distributions of the leptons from $\tilde{\chi}_1^{\pm}\tilde{\chi}_2^0$ production. (a) is 1st, (b) is 2nd, and(c) is 3rd lepton's distributions.

as the particle's "transverse energy", E_T. When the transverse momentum is measured using the tracking chamber, we denote this quantity as the prticle's P_T. Towers with EM $E_T > 0.1$GeV are eligible to be shoulder towers. Beginning with each seed tower, a cluster is formed by incorporating neighboring shoulder towers until either no further adjacent towers can be incorporated or until the maximum cluster size is reached. The maximum cluster size is restricted to three towers in pseudorapidity ($\Delta\eta \approx 0.3$) by one tower in azimuth ($\Delta\phi \approx 15°$) in the central region, five towers in pseudorapidity ($\Delta\eta \approx 0.5$) by five towers in azimuth ($\Delta\phi \approx 25°$) in the plug region, and seven towers in pseudorapidity ($\Delta\eta \approx 0.6$) by seven towers in azimuth ($\Delta\phi \approx 35°$) in the forward region. Finally, it is required that the EM E_T of the cluster be greater than 5GeV and that the ratio of hadronic E_T to electromagnetic E_T be less than 0.125.

The reconstructed event data in the electron bank have contaminations. Two requirements, removal of the electron from a photon conversion and the electrons in outside the fiducial region, have to be made for picking up good electron candidates. Electrons from converted photons ($\gamma \rightarrow e^+e^-$) and Dalitz decays ($\pi^0 \rightarrow e^+e^-\gamma$) have to be removed from the electron sample. These conversion electrons can be identified with a high efficiency, $(88 \pm 4)\%$, using tracking information[32]. A photon conversion can occur before entering the VTX, in the beam pipe or in the inner wall of the VTX. Or converting after exiting the VTX, in the wall of the VTX or in the inner wall of the CTC. The two parameters, $VTX_{\rm OCC}$ and M_{ee}, are useful for rejecting the converted electrons. $VTX_{\rm OCC}$ is the ratio of the number of VTX wire hits to the number of wires which are supposed to be transvered by the particles. The converted electrons have a low value of $VTX_{\rm OCC}$. The two electrons from these processes are expected to form a low invariant mass. Therefore, selection criteria for removing the converted electrons from electron sample are,

- $VTX_{\rm OCC} > 0.2$
- $M_{ee} > 0.5$ GeV/c^2

Fiducial cuts on the shower position, as measured in the CES, are applied to ensure that the electron candidate is away from calorimeter boundaries and that the energy is well measured. For central electrons, the fiducial region is given by bellows,

- A seed tower for the cluster must have a tower number of 0-8. Tower 9 does not have enough depth coverage for the EM calorimeter. Tower 7 of chimney module is rejected.
- An absolute value of Z coordinate of a track, propagated to the CES, must be > 9 cm. This is meant to avoid the $\theta = 90^\circ$ crack.
- A track must be located within 21 cm from the tower center at ϕ coordinate of the local wedge.

The fiducial volume for electrons covers 78.9% of the solid angle in the central region. For plug electrons, the fiducial region is given by bellows,

- A seed tower must not be in inner 2 pads nor outer 1 pad. This region has not enough depth coverage.
- A seed tower must not be a pad along the quadrant edge. This requirement is approximately same as the one that the cluster centroid be at least 5 cm away from the border of each quadrant.

The "electrons" passed with these selections are considered as electron candidates. We apply further the some selection criteria for picking up good quality electrons in each regions.

Central Electron Identification

A central (CEM) electron candidate has a CTC track extrapolating to a CEM electron cluster with CES informations. The CEM electron selection criteria are applied to the CEM candidates to discriminate against charged hadrons and neutral particles using,

1. The transverse energy: E_T
2. The ratio of cluster energy to track momentum: E/P

3. The ratio of hadronic energy to electromagnetic energy of the cluster: HAD/EM
4. A comparison of the lateral shower profile in the calorimeter cluster with that of the test-beam electrons: $LSHR$
5. The distance between the position of the extrapolated track and the CES shower position measured in the $r - \phi$ and z views: Δx and Δz
6. A χ^2 comparison of the CES shower profiles with those of test beam electrons: χ^2_{strip}

$LSHR$ describes the energy sharing among adjacent towers in a wedge. $LSHR$ is defined as follows:

$$LSHR \equiv 0.14 \times \sum_i \frac{E_i^{meas} - E_i^{pred}}{\sqrt{0.14^2 \times E^{cl} + (\Delta E_i^{pred})^2}}$$

where the sum runs over the two towers adjacent to the seed tower in the same azimuthal wedge, E_i^{meas} is the energy deposition in tower i, E_i^{pred} is the energy expected in tower i, and E^{cl} is the cluster energy. The expected energy is calculated from the test-beam measurements. $LSHR$ depends on the seed tower energy and the shower impact point in the strip chamber. $LSHR$ gives a measurement of the lateral shower development and is different for electrons and jets.

χ^2_{strip} shows the difference of the shower shape in the Z view of CES between the data and the expected shower shape from electrons in the test-beam data. The fit is calculated to 11 points with 2 parameters and is rescaled by a factor which gave the χ^2 from test-beam data to be a mean of 1. CES has a position resolution of 0.2 cm in both the Z view and azimuthal view. The strip cluster position is used in the definition of the good fiducial regions. Table 4.1 shows the central electron selection criteria.

We define two categories,"GOLD" and "Ordinary", for a central electron. The ordinary electron isn't satisfied with the inclusive electron trigger conditions and the GOLD electron is satisfied with them. The inclusive electron trigger conditions are tight for the electrons from $\tilde{\chi}_1^{\pm}\tilde{\chi}_2^0$ production. The E_T range of electrons from $\tilde{\chi}_1^{\pm}\tilde{\chi}_2^0$ is between 6 GeV and 30 GeV. Therefore we require that at least one electron from $\tilde{\chi}_1^{\pm}\tilde{\chi}_2^0$ should passe the

Table 4.1: Selection criteria for central electrons

Cut	Gold	Ordinary
E_T	> 11 GeV	> 5 GeV
Conversion removal	Yes	Yes
Fiducial area	Yes	Yes
E/P	< 2.0	< 2.0
HAD/EM	< 0.05	$< 0.055 + 0.045 \times \frac{E}{100}$
LSHR	< 0.2	< 0.2
$\|\delta x\|$	< 3 cm	< 3 cm
$\|\delta z\|$	< 5 cm	< 5 cm
χ^2_{strip}	< 10	< 15

trigger conditions. Figure 4.2 shows the distributions of the variables used in the selection for the $Z \rightarrow e^+e^-$ events. The arrows in the figures show the cut values for the ordinary electrons. Since the cut value of HAD/EM for the ordinary electrons is depend on electron's energy, the figure doesn't show the cut value.

Plug Electron Identification

None of the plug electron can use CTC tracking information because the CTC tracking volume doesn't cover the plug region of the calorimeter. Therefore, the calorimeter and the VTX information are used to identify the plug electrons. The effective coverage for plug electrons is $1.2 < |\eta| < 1.35$. Fiducial cuts reduce the solid angle coverage in this region by an additional 11%. The following are selection variables for the plug electron:

1. The transverse energy: E_T
2. The ratio of hadronic energy to electromagnetic energy of the cluster: HAD/EM
3. A comparison of the lateral shower profile in the calorimeter cluster with that of test beam electrons: $\chi^2_{3\times3}$
4. The ratio of the number of VTX hits pointing to the calorimeter cluster to the predicted number: $VTX_{\rm OCC}$

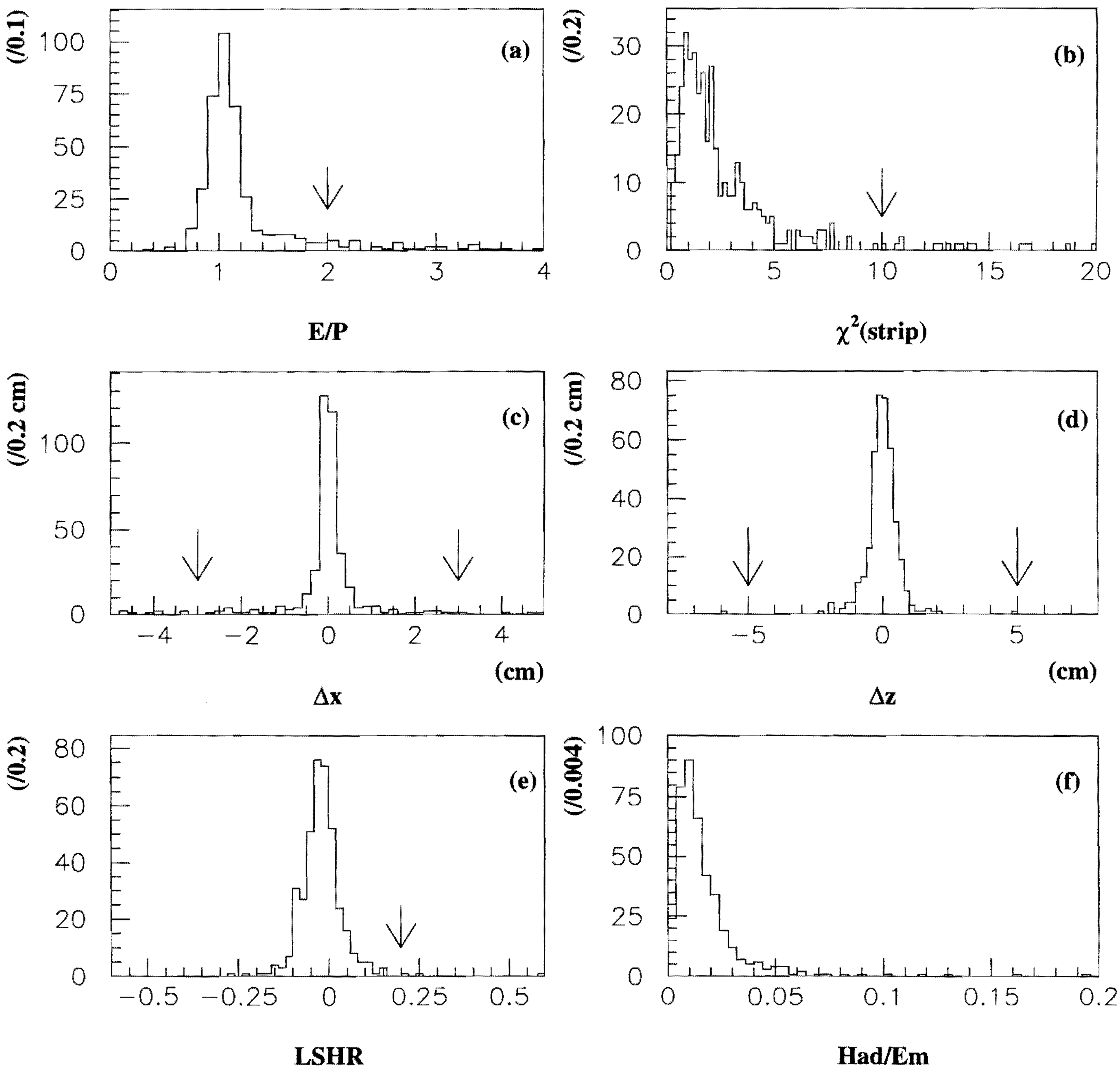

Figure 4.2: Distributions of the central ordinary electron selection variables. The cut value of HAD/EM doesn't show because its value is depend on electron's energy.

Table 4.2: Selection criteria for plug electrons

Cut	Ordinary
E_T	> 5 GeV
Conversion removal	Yes
Fiducial area	Yes
$\chi^2_{3\times3}$	< 3.0
$VTX_{\rm OCC}$	> 0.5

$\chi^2_{3\times3}$ is performed in 2 dimension within total 9 pads ($\Delta\eta \times \Delta\phi = 3 \times 3$) in which most of the EM shower energy is contained. $VTX_{\rm occ}$ can be used to discriminate charged particles from neutral particles in the VTX. This is used to make sure the existence of a VTX track associated with a plug EM cluster. The electrons from photon conversion have a low value of $VTX_{\rm OCC}$. By requiring this value be high, π^0's, γ's and photon conversions are removed. Table 4.2 shows selection criteria for the plug electrons. Figure 4.3 shows the distributions of the selection variables in the $Z \to e^+e^-$ events. The arrows in the figures show the cut values. Since the cut value of HAD/EM is depend on electron's energy, the figure doesn't show the cut value.

The plug electron doesn't have a "Gold" category because there is no reasonable plug electron trigger for $\tilde{\chi}_1^\pm\tilde{\chi}_2^0 \to 3\ell + X$ production in the CDF trigger scheme.

4.2.2 Muon Identification

Muons are identified with CTC, muon chamber tracking information and calorimeter information. Muon leaves a track in CTC and the muon chamber and deposits energy in the calorimeter as a minimum ionizing particle. In this analysis, we use the muon system in the central region, the central muon chambers (CMU), the central muon upgrade chambers (CMP), and the central muon extension chambers (CMX). The total coverage of these muon chambers is the pseudorapidity $|\eta| \leq 1.0$. Another way of muon identifications is to use the CTC and the calorimeters without using the muon chambers. These muon candidates are called "central minimum ionizing particles (CMIO)". Hence we have two types of identified muons in the central region.

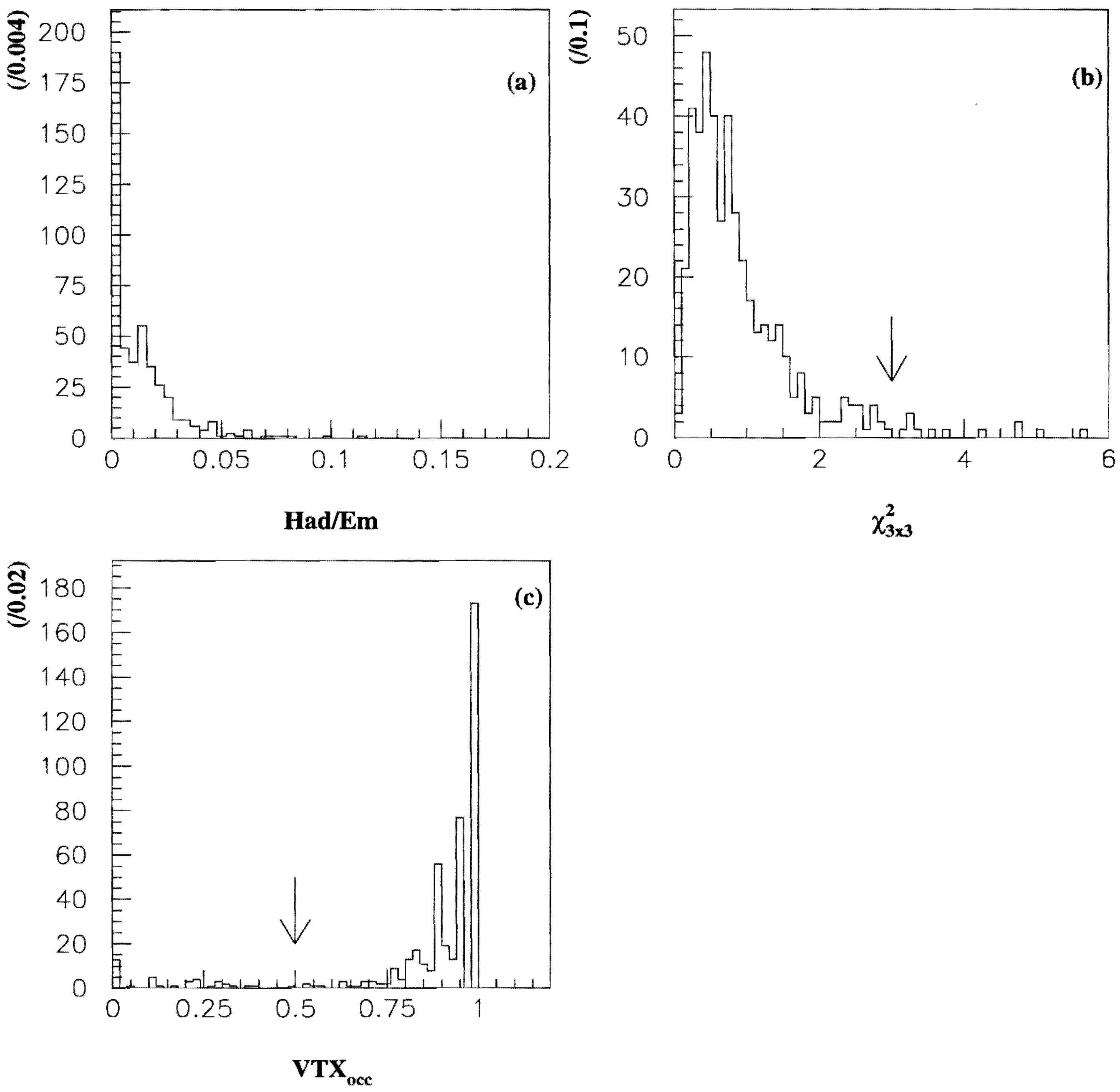

Figure 4.3: Distributions of the plug electron selection variables.

Central muon (CMUO muon)

We identify a muon as a CMUO muon in the pseudo-rapidity region $|\eta| \leq 1.0$ by requiring a match between a CTC track and a track segment in the muon chambers of CMU, CMP, or CMX. The following are the selection variables to separate muons from hadrons that interact in the calorimeters, and from cosmic rays:

1. The transverse momentum: P_T
2. An energy deposition in the electromagnetic or hadronic calorimeter, which is characteristic to minimum ionizing particles: EM or HAD energy
3. The closest approach of the reconstructed track to the beam line: Impact parameter
4. The matching distance and χ^2 matching between the extrapolated track and the track segment in the muon chambers: $|\Delta x|$ or $\chi^2(\Delta x)$
5. Fiducial volume requirement.

The EM+HAD selection is required because there was a bug in an offline muon reconstruction code which picks up a wrong tower where no track actually passes through. The fiducial volume requirement apply to the muon position with propagating the track, starting at the interaction vertex, to the appropriate muon chamber using the beam-constrained (P_X, P_Y, P_Z) and (x,y,z). The following are the fiducial volume for each chamber:

- CMU:
    - $1.27° \leq |\phi_W| \leq 13.73°$
    - $13.0\text{cm} \leq |\text{z}| \leq 225.0$ cm
    - Wedge 5, $80° \leq |\phi| \leq 90°$ cut chimney: $z \geq 205.06$cm
    - Cut dead Wedge: 17 East, 6 West
- CMP:

Table 4.3: Selection criteria for CMUO muons

Cut	Gold CMU/CMP	Ordinary CMU/CMP/CMX
P_T	> 11 GeV/c	> 4 GeV/c
Fiducial area	Yes	Yes
E(EM Tower)	< 2 GeV	< 2 GeV
E(HAD Tower)	< 6 GeV	< 6 GeV
E(EM+HAD Tower)	> 0.1 GeV	> 0.1 GeV
Impact parameter δ_0	< 0.2 cm	< 0.5 cm
CMU $\|\Delta x\|$ or $\chi^2(\Delta x)$	< 2 cm or < 9	< 2 cm or < 9
CMP $\|\Delta x\|$ or $\chi^2(\Delta x)$	< 5 cm or < 9	< 5 cm or < 9
CMX $\|\Delta x\|$ or $\chi^2(\Delta x)$	N/A	< 5 cm or < 9

  - $|z| \leq 315.0$cm
  - $|z| \leq 306.3$cm Shorter Bottom Chambers
  - $|z| \leq 235.0$cm Shortest Bottom Chambers

- CMX:
  - $379.0 \leq |z| \leq 509.0$cm
  - Cut no coverage: $75° \leq \phi \leq 105°$ Top and $225° \leq \phi \leq 315°$ Bottom
  - Cut dead region: West $105° \leq \phi < 108°$

Where ϕ_W is the phi angle within a wedge. CMU wedges 17 east and 6 west were completely dead throughout the run, so this cut removes no muon candidate. Table 4.3 shows the CMUO muon selection criteria. Figure 4.4 and figure 4.5 are the distributions of the selection variables for CMUO muons in the $Z \to \mu^+\mu^-$ events.

In these figures, the arrow show the selection criteria. The hatched area in the figure 4.5 are rejected region of these selections.

CMUO muon is defined two categories, "GOLD" and "Ordinary", same as the central electron's category. The "GOLD" muon is required to leave the hits in CMU or CMP. The inclusive muon trigger schemes that we use for this analysis don't include the CMX trigger scheme.

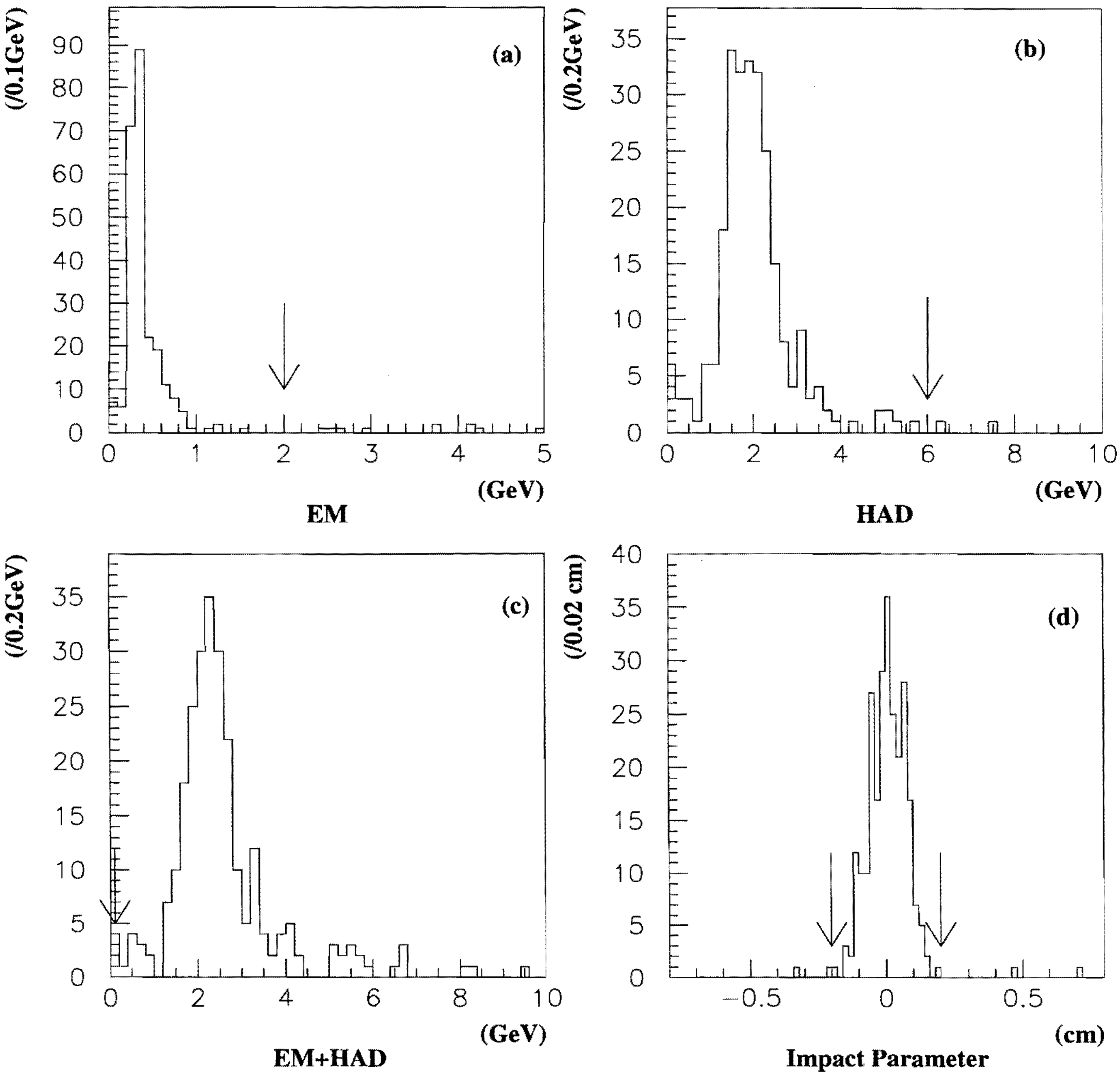

Figure 4.4: Distributions of the CMUO muons selection variables (1)

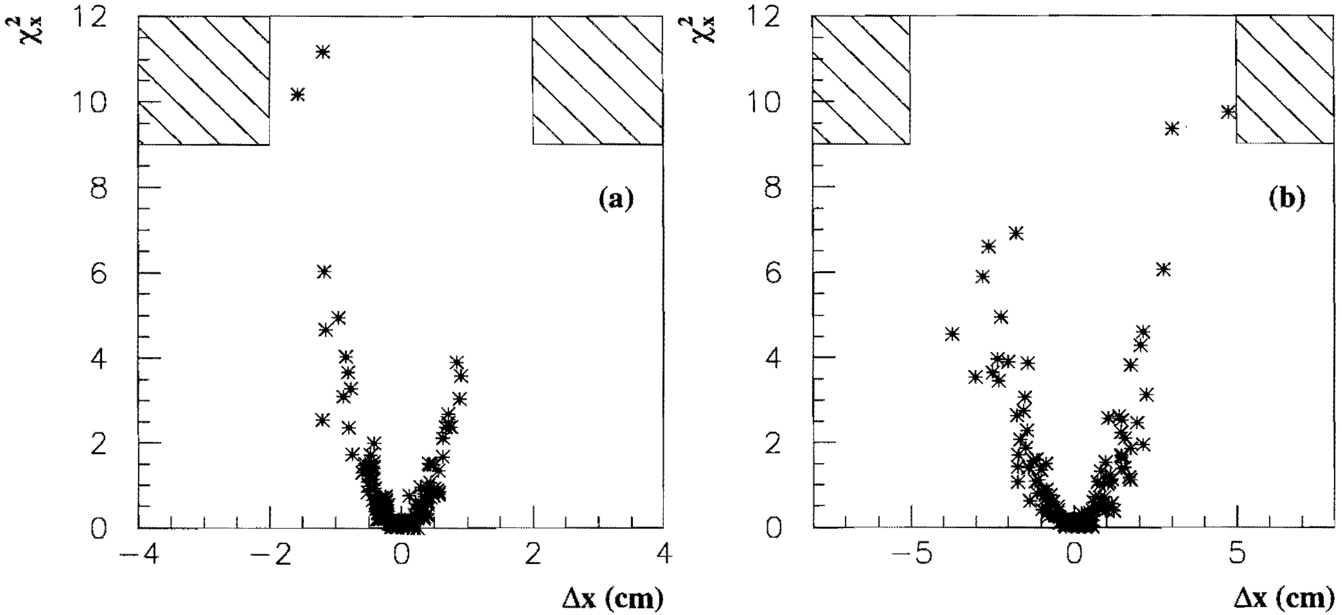

CMU matching

CMP matching

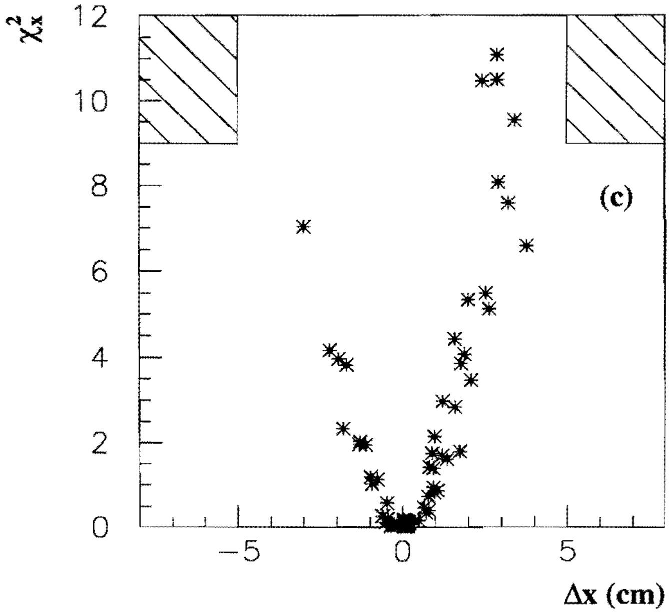

CMX matching

Figure 4.5: Distributions of the CMUO muons selection variables (2). The hatched area are rejected region of these selections.

Table 4.4: Selection criteria for CMIO muons

Cut	Ordinary CMIO
P_T	> 10 GeV/c
E(EM Tower)	< 2 GeV
E(HAD Tower)	< 6 GeV
E(EM+HAD Tower)	> 0.1 GeV
Impact parameter δ_0	< 0.5 cm

Central Minimum Ionizing particle (CMIO muon)

There is a muon identified by requiring the energy in the calorimeter tower in the path of the extrapolated track to be consistent with that for a minimum ionizing particle. This muon is called "Central Minimum Ionizing Particle (CMIO)" and doesn't have any associate hits in the muon chamber. This extends muon identification to $|\eta| < 1.2$ as well as covering azimuthal holes in the region $|\eta| < 1.0$. CMIO dose not generate triggers. The following are the selection variables for CMIO muons.

1. The transverse momentum: P_T
2. An energy deposition in the electromagnetic or hadronic calorimeter, which is characteristic to minimum ionizing particles: EM or HAD energy
3. The closest approach of the reconstructed track to the beam line: Impact parameter
4. Fiducial volume requirement.

The difference of the selection variables between CMUO and CMIO is only the track matching of CTC with the hits in the muon chambers. CMIO requires a CTC track to measure the track momentum. The fiducial volume for a CMIO muon is the same as the fiducial volume for a central electron. Since the CMIO muon uses the CTC track and the energy deposit in the calorimeters, a good calorimeter region becomes the CMIO fiducial volume. Table 4.4 shows the CMIO muon selection criteria.

CMIO's P_T threshold is higher than the ordinary CMUO. Because the energy resolution of the calorimeter is higher with higher the particle momentum, high P_T threshold is set to guarantee the accuracy of the energy resolution of the calorimeter. Other criteria are same as the ordinary CMUO.

4.3 Event Selection

From the inclusive Stream1 electron and muon samples, we made a multilepton sample by requiring events to contain as least two leptons, of which one must be 'GOLD' with $P_T > 10$ GeV/c. The ninety 8mm tapes of stream1 electron data set were available, containing 3.68 million events, and one hundred 8mm tapes of stream1 muon data set, containing 2.71 million events. The integrated luminosity of the data set is 19.11 pb^{-1}. We selected 34,055 dilepton candidate events in the stream1 electron data set and 28,474 dilepton candidate events in the stream1 muon data set. These events were stored in the disk for further analysis. Some events were overlapped in the two data sample, if they have at least one 'Gold' muon and 'Gold' electron. Therefore, combined number of two data sets is not equal to the total number of the dilepton events. We rejected events in the run which has problems in CTC, calorimeter, or muon chambers using the run condition's list. After this rejection, 31,081 events were left for the inclusive electron data sample and 26,069 events for the inclusive muon data sample. Within these samples, there were 94 (electron stream1) and 136 (muon stream1) trilepton events which have at least one 'Gold' lepton with $P_T > 11$ GeV/c. To select the trilepton events from $\tilde{\chi}_1^{\pm}\tilde{\chi}_2^0$ production from these events, we set the additional selection criteria.

1. Isolation: $ISO(R < 0.4)$
2. Event vertex: $|Z_{vertex}|$
3. Separation of the leptons in $\eta - \phi$ space: $\Delta R_{\ell\ell}$
4. Separation of the two highest P_T leptons in ϕ: $\Delta\phi_{\ell_1\ell_2}$
5. Sum of the three lepton's charge
6. Requirement of electron pair(s) or muon pair(s) in an event

7. Invariant mass of lepton pair

The event that passed all the above criteria were considered as SUSY trilepton candidates.

Isolation Cut

One would expect the leptons in SUSY trilepton events to be well-isolated, because they are not expected to be produced in association with other particles. As mentioned above, leptons from other physics processes are produced associated with jets of other particles nearby in $\eta - \phi$ space. The Monte Carlo simulation confirms this. Figure 4.6 show the sum of the EM and HAD transverse energies in a cone of $R = \sqrt{(\Delta\eta)^2 + (\Delta\phi)^2} = 0.4$ around each lepton to be quite small. In figure 4.6(d), a solid line shows the distribution of a lepton from $\tilde{\chi}_1^{\pm}\tilde{\chi}_2^0$ production and a dash line shows the distribution of a lepton in the inclusive lepton sample of the data.

The isolation variable, *ISO*, is defined as,

$$ISO = E_T(\text{EM}) + E_T(\text{HAD}) - E_T^{\ell}(\text{EM}) - E_T^{\ell}(\text{HAD}) \tag{4.1}$$

where $E_T(\text{EM}) + E_T(\text{HAD})$ is the total E_T of EM and HAD towers within a cone of $R = 0.4$, $E_T^{\ell}(\text{EM})$ and $E_T^{\ell}(\text{HAD})$ are the EM and HAD transverse energies of an electron or a muon cluster. In W and Z analysis, isolation is typically defined as,

$$ISO(W or Z) = \frac{E_T(\text{EM}) + E_T(\text{HAD}) - E_T^{\ell}(\text{EM}) - E_T^{\ell}(\text{HAD})}{E_T^{\ell}(\text{EM}) + E_T^{\ell}(\text{HAD})} \tag{4.2}$$

However, because our leptons are expected to have much lower momentum than the leptons from W Z production, we found it better to define isolation simply as above. And we defined the $ISO < 2.0$GeV as the cut threshold.

Event Vertex Cut

The position in z of the primary event vertex is measured by the VTX. Figure 4.7 shows the z position of event vertex in the include lepton sample.

We required the event vertex fall within $|Z_{vertex}| < 60$cm of the center of the detector, inside the fiducial volume of the VTX.

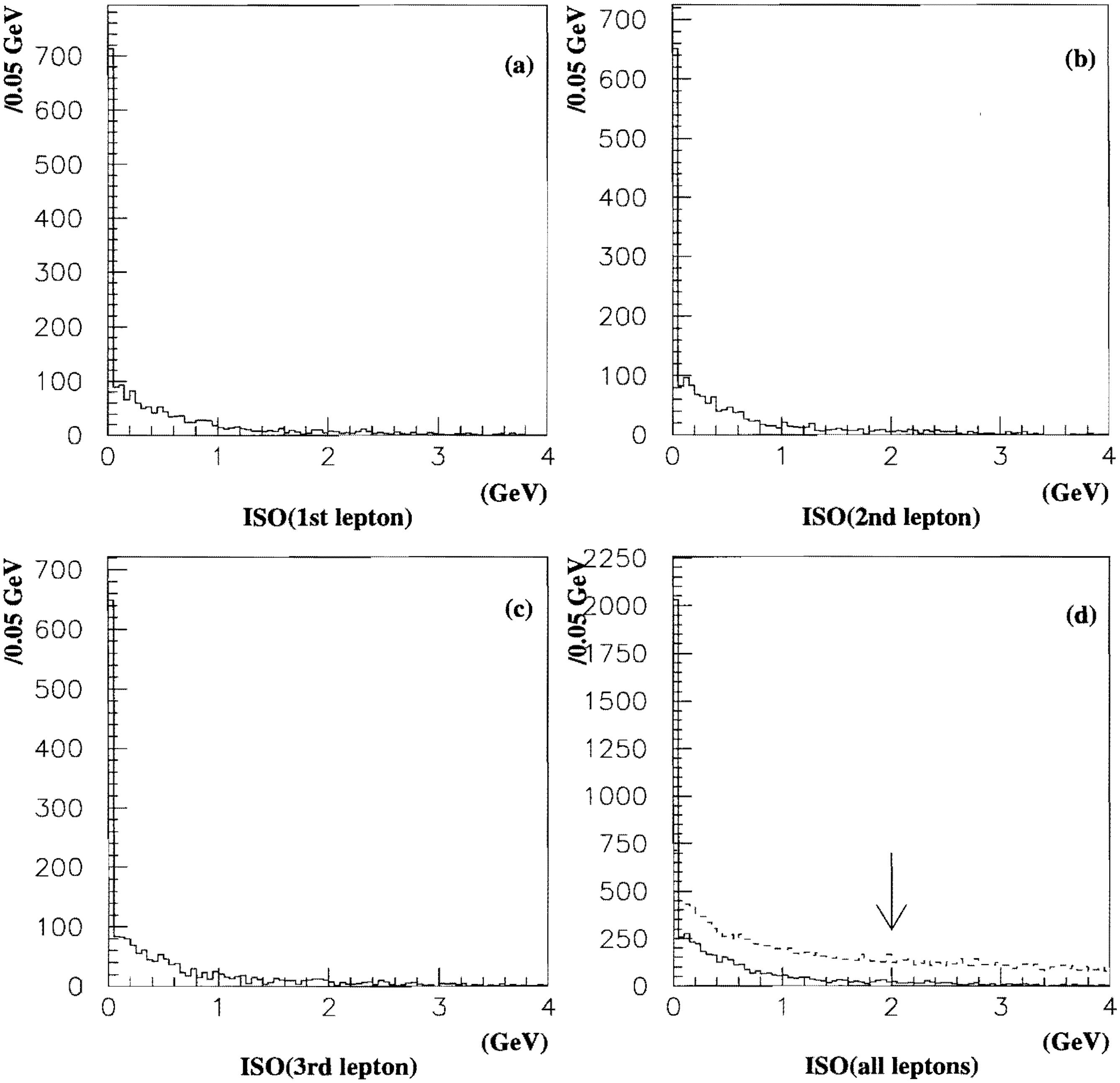

Figure 4.6: Distribution of the EM+HAD transverse energies in a cone of $R < 0.4$ in $\tilde{\chi}_1^\pm \tilde{\chi}_2^0$ productions using ISAJET. In (d), the dash line shows the distribution of the data sample.

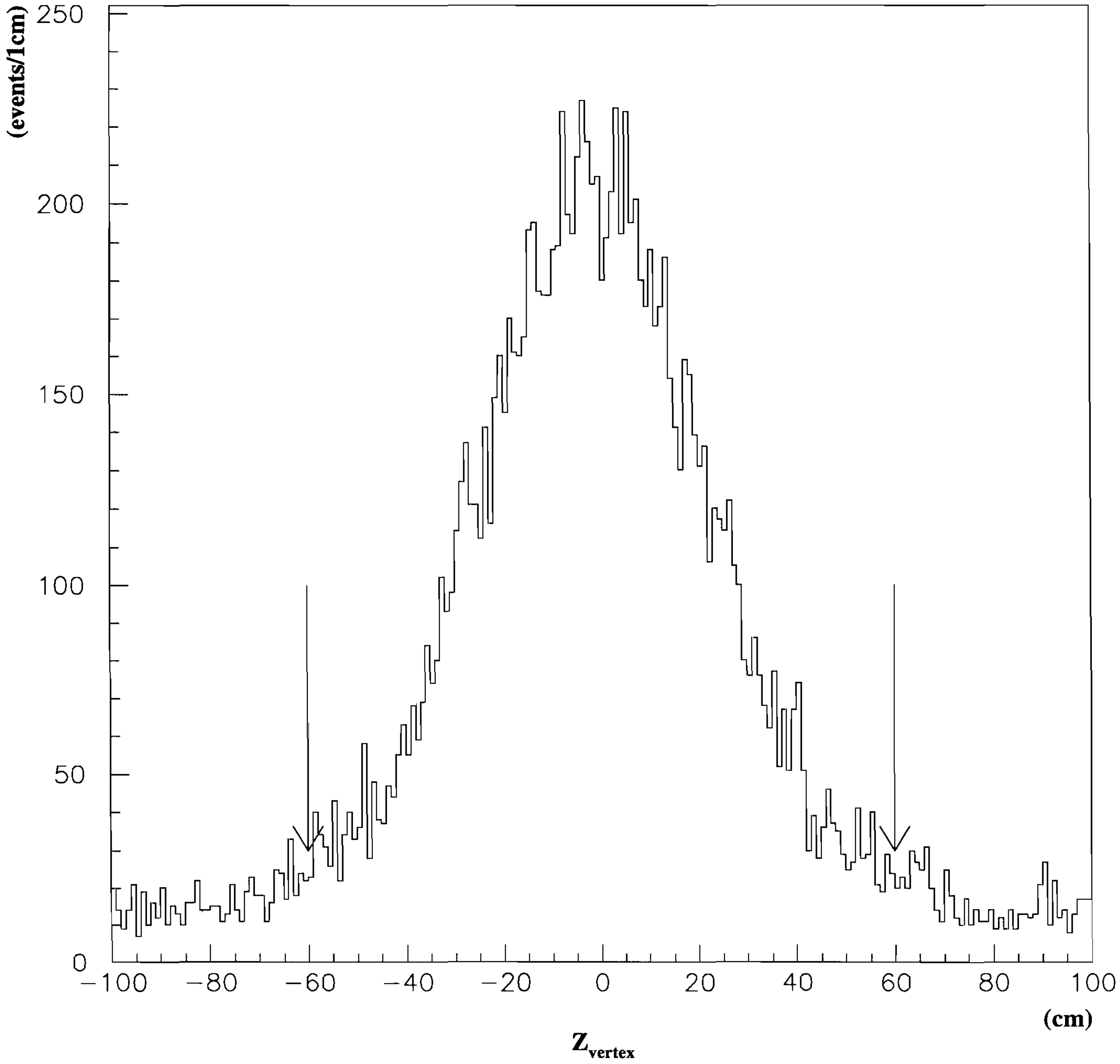

Figure 4.7: The z position of event vertex in the include lepton sample.

ΔR Cut

It was noticed that a large fraction of the multilepton events appear to have two leptons close to each other in $\eta - \phi$ space. This may be because some of the multilepton events come from $b\bar{b}$, or photon conversions not removed by the photon conversion filter, or J/Ψ decays, tracking mistakes, and so on. However, the Monte Carlo simulation shows that, for SUSY trilepton topologies, the leptons do not typically come very close to each other. We defined the ΔR to be the separation between the two leptons in $\eta - \phi$ space. Figure 4.8(a) and (b) show the ΔR distributions of the dilepton events in the data and the trilepton events in $\tilde{\chi}_1^{\pm}\tilde{\chi}_2^0$ production. The distribution of the $\tilde{\chi}_1^{\pm}\tilde{\chi}_2^0$ production is different from the dilepton events in the data. Therefore, to reduce these backgrounds, we required a minimum separation in $\eta - \phi$ space between leptons, $\Delta R > 0.4$.

$\Delta\phi$ Cut

One of the dominant background comes from Drell-Yan events with additional leptons. The lepton pairs from Drell-Yan process make back-to-back lepton events. Figure 4.8(c) and (d) show the $\Delta\phi$ distributions of the dilepton events in the data and the trilepton events in $\tilde{\chi}_1^{\pm}\tilde{\chi}_2^0$ production. The distribution for the dilepton events has two peaks around 170°(0.17rad and 2.97rad). We required $\Delta\phi$ of the highest two $P_T(E_T)$ leptons to be less than 170°. We didn't require that the two lepton's types were same. We have not optimized the back-to-back cut, but we estimated that a cut of 170° will reduce Drell-Yan yield by 50%, while cutting our signal by only $\sim 15\%$.

Cut on the Sum of Three Lepton's Charge and Requiring Lepton pair

In a SUSY trilepton event, $\tilde{\chi}_1^{\pm}$ decays into $\ell^{\pm}, \nu, \tilde{\chi}_1^0$ and $\tilde{\chi}_2^0$ decays into $\ell^+, \ell^-, \tilde{\chi}_1^0$. Then the event must have one lepton pair and the sum of the three lepton's charge must be ± 1. But in some case the charge of plug electrons can't be identified because CTC doesn't cover the full plug region. Therefore we required the event to have one lepton pair and the sum of the three lepton's charge should be less than three.

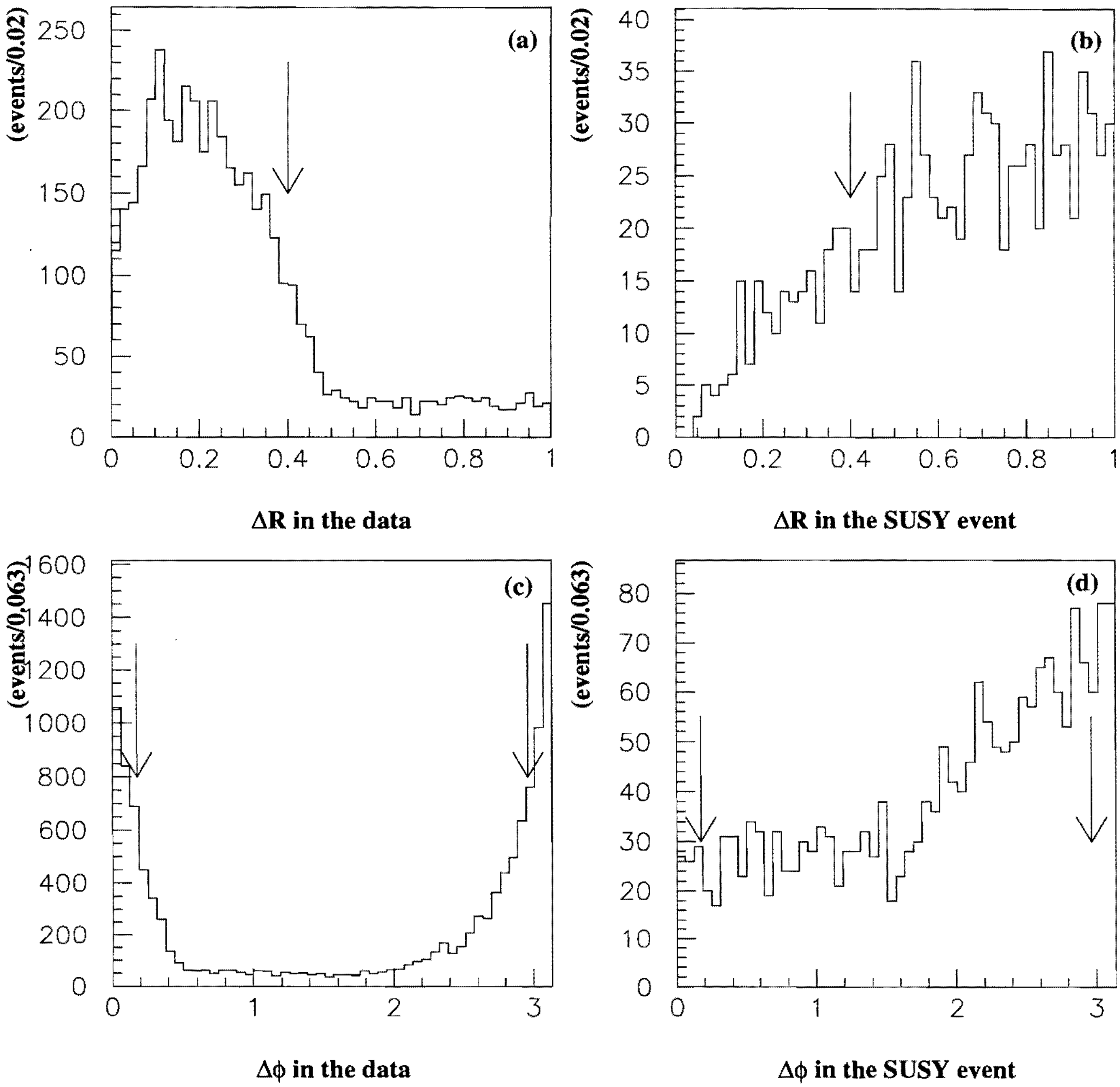

Figure 4.8: Distributions of ΔR and $\Delta\phi$ for dilepton data sample and for SUSY event with $\tilde{\chi}_1^{\pm}\tilde{\chi}_2^0$ production.

Invariant Mass of Lepton Pair Cuts

Figure 4.9 shows the invariant mass distribution of SUSY trilepton events. Figure 4.9 has only a peak around 20 GeV/c^2. This peak can move according to the $\tilde{\chi}_1^\pm$ mass or $\tilde{\chi}_2^0$ mass. For the $\tilde{\chi}_1^\pm$ and $\tilde{\chi}_2^0$ mass in this analysis, this peak will be located between 20GeV/c^2 and 40GeV/c^2. Figure 4.10 shows the invariant mass of our dilepton event data sample with a vertex and beam-constraint fits. Figure 4.10 (b) shows the J/Ψ's peak at 3.1GeV/c^2 and (c) shows two Υ's state peaks around 10 GeV/c^2 and (d) shows the Z^0 peak at 91GeV/c^2. From these data, we removed the background from these known particles. We set the invariant mass cuts according with these mass windows. The mass windows are 75–105 GeV/c^2 for Z^0, 9–11GeV^2 for Υ, and 2.9–3.3 GeV/c^2 for J/Ψ.

Results of the event selection

We apply the above cuts to the dilepton data sample to find the SUSY trilepton event candidates. Using the entire Run 1A data sample, we found no trilepton events that survived all of our cuts. Table 4.5 summarizes the number of events remains after each cut. Since we have no trilepton event candidate, we will set a mass limit of $\tilde{\chi}_1^\pm$ and $\tilde{\chi}_2^0$ in the following chapters.

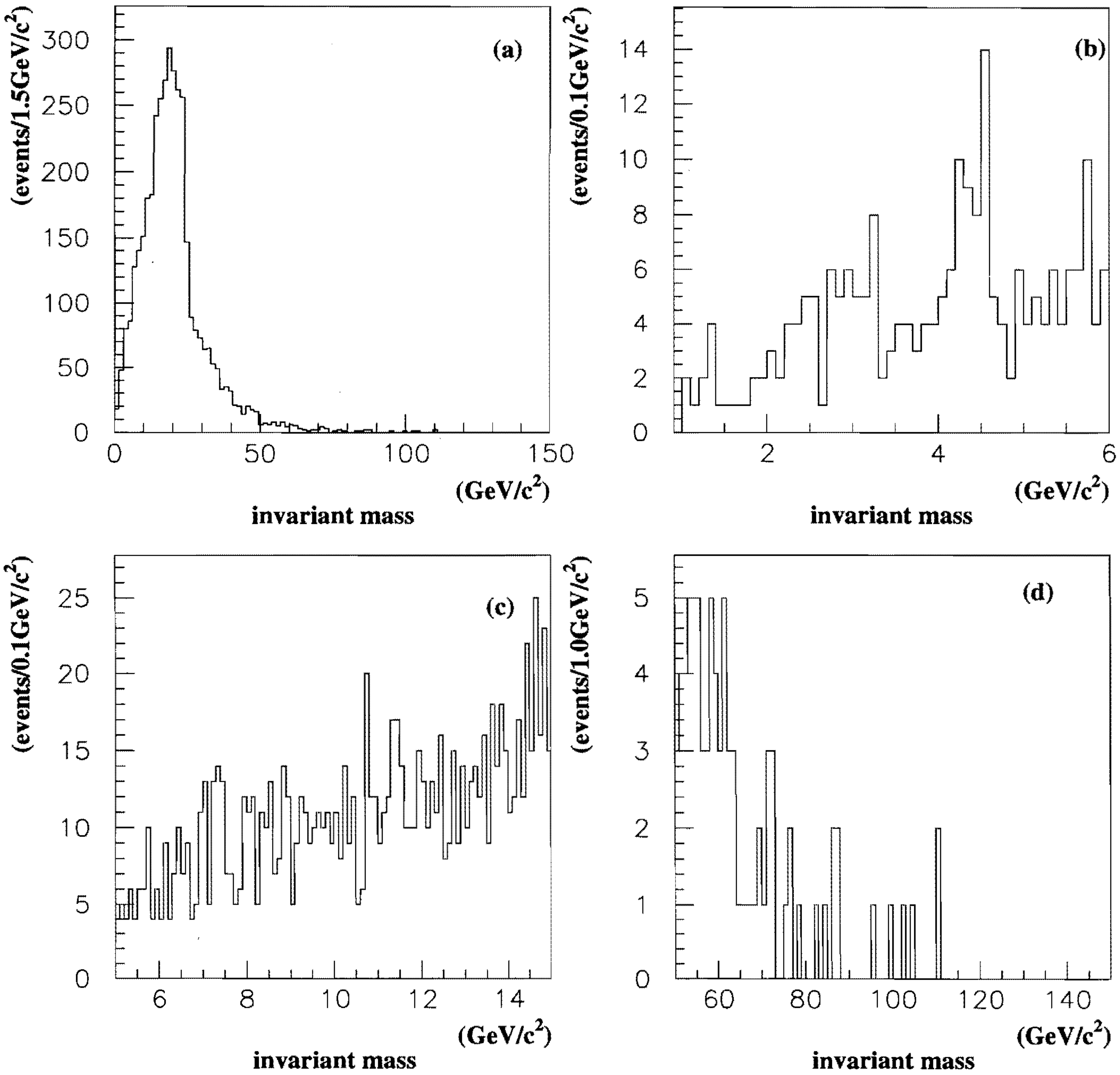

Figure 4.9: Distribution of $M_{\ell^+\ell^-}$ of the trilepton event in the $\tilde{\chi}_1^{\pm}\tilde{\chi}_2^0$ production: (a)all mass region, (b)J/Ψ mass region, (c)Υ mass region, (d)Z^0 mass region.

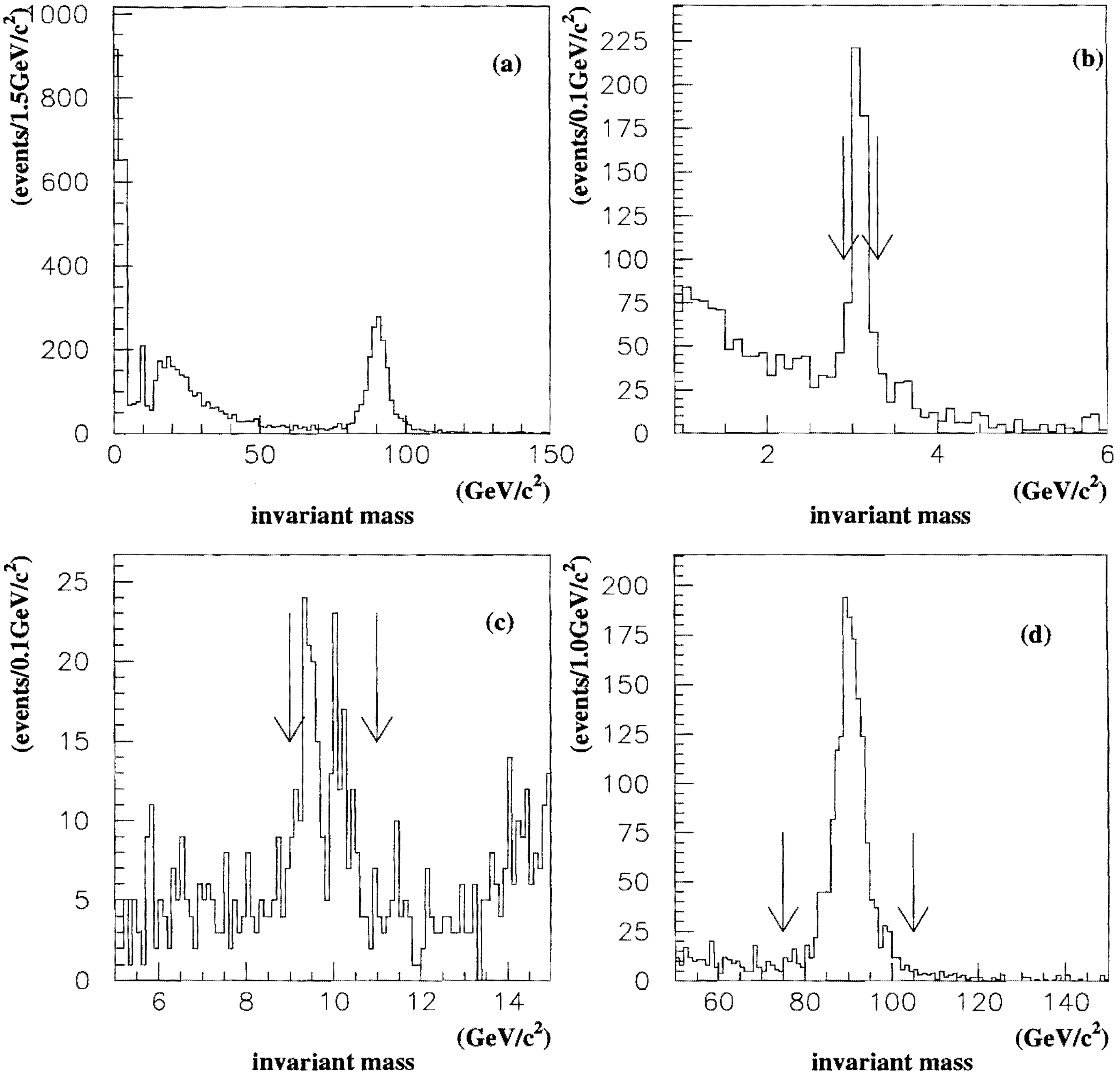

Figure 4.10: Distribution of $M_{\ell^+\ell^-}$ of the dilepton event in the CDF Run 1A 19.11pb^{-1} data sample: (a)all mass region, (b)J/Ψ mass region, (c)Υ mass region, (d)Z^0 mass region.

Table 4.5: Events remaining after trilepton cuts in 19.11 pb^{-1} data.

Cut	muon	electron
Original sample	2,707,852	3,677,903
Dilepton data sample	28,474	34,055
Dilepton data sample (removing bad runs)	26,069	31,081
Dilepton selection without ISO cuts	6,606	5,472
Trilepton selection without ISO cuts	136	94
Trilepton selection with $ISO < 4$	33	14
Trilepton Event Selection		
∘ $ISO(R < 0.4) < 2$ GeV	21	5
∘ $\|Z_{vertex}\| < 60$ cm	21	5
∘ $\Delta R_{\ell\ell} > 0.4$	2	3
∘ $\Delta\phi_{\ell\ell} < 170°$	2	2
∘ $\|Q_1+Q_2+Q_3\| < 3$	2	2
∘ Require e^+e^- or $\mu^+\mu^-$	2	2
∘ Z^0 removal (75-105 GeV/c^2)	1	0
∘ J/Ψ removal (2.9-3.3 GeV/c^2)	1	0
∘ Υ removal (9-11 GeV/c^2)	0	0

Chapter 5

Detection Efficiency

We used Monte Carlo simulation to derive physical quantities of the trilepton events from $\tilde{\chi}_1^\pm \tilde{\chi}_2^0$ production. Since there are possible differences between the Monte Carlo simulation and the actual detector's performance, we estimated the detection efficiency of the CDF detector using the real data. Uncertainties in the estimates of the detection efficiencies will be treated as systematic errors. We estimated the detection efficiencies using the CDF 1992-1993 data and compare values with the other CDF analysis results.

The total detection efficiency, ϵ^{tot}, can be expressed as

$$\epsilon^{tot} = \frac{\sum_x w_x \mathcal{A}_x^{MC}}{N_{gen}}, \tag{5.1}$$

where

$$\begin{aligned} w_x &= \text{Weight for } x\text{-th event}, \\ \mathcal{A}_x^{MC} &= \text{1 if three-lepton event is accepted (otherwise 0)}, \\ N_{gen} &= \text{Number of events generated.} \end{aligned}$$

In order for the event to be accepted, it must pass the kinematic/geometric, the isolation ($ISO < 4$ GeV), $|z_{vertex}|$, and the event topology ($\Delta R_{\ell\ell}$, $\Delta\phi_{\ell_1\ell_2}$) cuts.

The weight for each trilepton event x ($= \ell_1\, \ell_2\, \ell_3$) is defined as

$$w_x = \underbrace{\left[\alpha_{\ell_1}^{MC} \alpha_{\ell_2}^{MC} \alpha_{\ell_3}^{MC}\right]}_{\alpha_{3\ell}^{MC}} \cdot \epsilon_{3\ell}^{trig} \cdot \underbrace{\left[\epsilon_{\ell_1}^{ISO} \epsilon_{\ell_2}^{ISO} \epsilon_{\ell_3}^{ISO}\right]}_{\epsilon_{3\ell}^{ISO}} \cdot \underbrace{\left[\epsilon_{\ell_1}^{ID} \epsilon_{\ell_2}^{ID} \epsilon_{\ell_3}^{ID}\right]}_{\epsilon_{3\ell}^{ID}}, \tag{5.2}$$

where

ℓ_1, ℓ_2, ℓ_3 = Possible combinations of three leptons;

α_ℓ^{MC} = Acceptance correction factor for MC simulation of lepton type ℓ;

$\epsilon_{3\ell}^{trig}$ = P_T dependent trilepton trigger efficiency;

ϵ_ℓ^{ISO} = $\frac{\epsilon_\ell^{ISO<2\text{ GeV}}}{\epsilon_\ell^{ISO<4\text{ GeV}}}$;

ϵ_ℓ^{ID} = Lepton ID efficiency for ℓ (including conversion removal if ℓ = CEM or PEM) ;

Here, ℓ = CEM, PEM, CMU/CMP, CMX, or CMIO. It should be noted that:

- $\epsilon_{3\ell}^{trig}$, ϵ_ℓ^{ISO}, and ϵ_ℓ^{ID} are determined from real data.
- $\epsilon_{3\ell}^{trig}$ is calculated event by event, depending on the number of trigger leptons (n_{trig}), using the CEM and CMU/CMP trigger efficiency curves:

$$\epsilon_{3\ell}^{trig} = \begin{cases} \epsilon_{\ell_1}^{trig} & (n_{trig} = 1) \\ 1 - (1 - \epsilon_{\ell_1}^{trig}) \cdot (1 - \epsilon_{\ell_2}^{trig}) & (n_{trig} = 2) \\ 1 - (1 - \epsilon_{\ell_1}^{trig}) \cdot (1 - \epsilon_{\ell_2}^{trig}) \cdot (1 - \epsilon_{\ell_3}^{trig}) & (n_{trig} = 3) \end{cases} \tag{5.3}$$

This formula is implemented in the SUSY trilepton analysis program.

5.1 Lepton Isolation Efficiency

The isolation requirement for lepton is a powerful tool in reducing the background from $b\bar{b}$ events. We found that ϵ_ℓ^{ISO} is detector-dependent: PEM electrons in the data have smaller efficiency for $ISO < 2$ GeV due to detector noise. Therefore, we study the isolation efficiencies individually for CEM, PEM, and CMUO/CMIO leptons using the real data.

The ISO cut efficiency deviates from unity due to fluctuations of the underlying event (assuming detector noise is negligible). In estimating the ISO efficiency, we would prefer to use a large sample of diboson (*e.g.*, WZ) events, since these events exhibit an underlying-event energy flow similar to that in the $\tilde{\chi}_1^\pm \tilde{\chi}_2^0$ events. However, we do not have a large sample of diboson events. Thus, we chose Z events as the next best sample for this study. We should note that the underlying-event energy flow in minimum bias events is smaller in Z events by approximately 35%, hence, minimum bias events can not be used for this determination. Furthermore, we can assume ϵ_ℓ^{ISO} to be P_T^ℓ-independent.

The selection of Z^0 events was made by requiring two leptons (one with tight ID cuts, the other with loose ID cuts) giving an invariant mass between 86 and 96 GeV/c^2. The tight cut criteria are the same as our gold lepton cuts with E_T^e (P_T^μ) $\geq$ 20 GeV (20 GeV/c) and $ISO \leq 2.0$ GeV. The loose cut criteria are the same as our ordinary lepton cuts without the isolation requirement. We estimated the isolation efficiencies for various categories of leptons by looking at the loose-cut leptons.

Figure 5.1 shows lepton isolation distributions from the Z^0 sample and from the Monte Carlo simulation. The results are summarized in Table 5.1. The results from the data and the Monte Carlo simulation agreed well for the efficiency for a cut at $ISO < 4$ GeV. However, some disagreements were seen for the efficiency for a cut at $ISO < 2$ GeV, especially for PEM electrons, because the simulation doesn't work well for the underlying-event energy flow and multiple interactions. The large difference of PEM electron is due to a larger leakage of showers in the lateral direction than is modeled by the simulation.

Table 5.1: Efficiencies for lepton isolation requirements ($ISO < 4$ GeV and $ISO < 2$ GeV) in $Z^0 \to \ell\ell$ events. CMUO = CMU/CMP/CMX muons.

	Data		QFL Simulation	
	$\leq$ 4.0 GeV (%)	$\leq$ 2.0 GeV (%)	$\leq$ 4.0 GeV (%)	$\leq$ 2.0 GeV (%)
CEM	99.0±0.4	93.2±1.0	98.8±0.3	96.1±0.4
PEM	99.2±0.6	79.2±2.6	99.2±0.3	97.8±0.4
CMUO/CMIO	98.2±0.8	95.7±1.2	98.3±0.4	95.0±0.5

In summary, the lepton isolation efficiencies for CMUO/CMIO, CEM, and PEM are:

$$\begin{aligned} \epsilon_\ell^{ISO} &= \frac{\epsilon_\ell^{ISO<2\,\mathrm{GeV}}}{\epsilon_\ell^{ISO<4\mathrm{GeV}}} = \begin{cases} 0.941 \pm 0.011 & \text{(for CEM)} \\ 0.798 \pm 0.027 & \text{(for PEM)} \\ 0.975 \pm 0.015 & \text{(for CMUO/CMIO)} \end{cases} \\ &= \begin{cases} 0.953 \pm 0.009 & \text{(for CEM/CMUO/CMIO)} \\ 0.798 \pm 0.027 & \text{(for PEM)} \end{cases} \end{aligned} \tag{5.4}$$

Here, we combined the CEM and CMUO/CMIO numbers, because in the CDF calorimeter both are measurements of the same quantity (*i.e.*, underlying event energy flow in Z

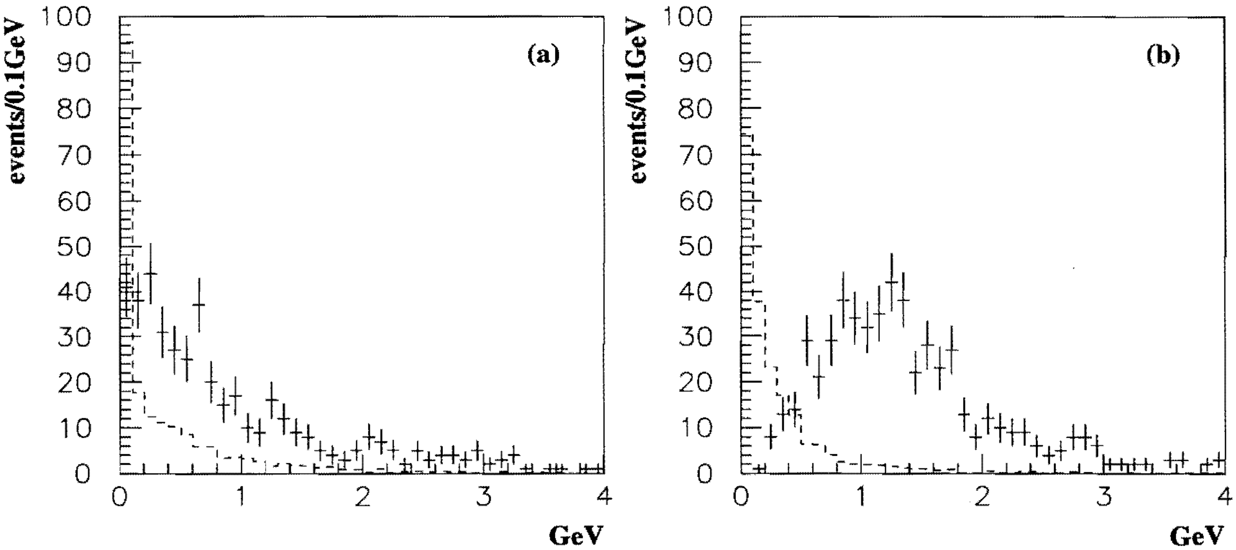

Central electron **Plug electron**

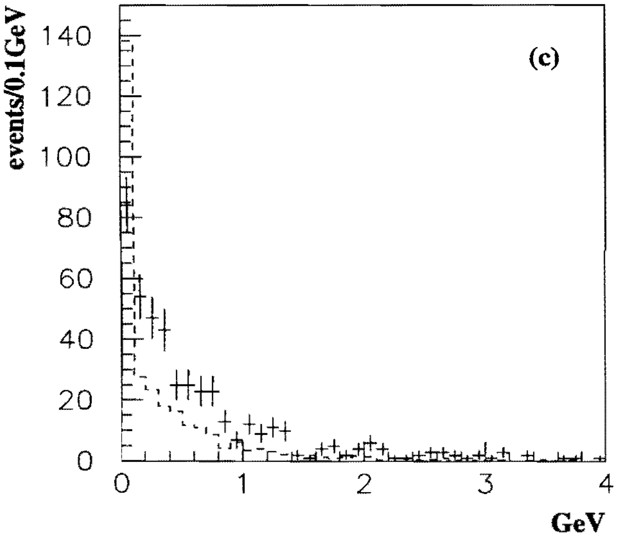

μ

Figure 5.1: Lepton isolation(*ISO*) distributions for (a) CEM, (b) PEM, and (c) CMUO/CMIO in Z events. The points (dashed line) show the data (ISAJET V7.06 + QFL V3.48 simulation).

events).

5.2 Lepton ID Efficiency

In the trilepton analysis, we have to identify leptons with P_T's as low as 4 GeV/c. Therefore, it is important to know the lepton identification efficiency as a function of lepton momentum.

Two data samples are available: $Z^0 \rightarrow \ell\ell$ events for high P_T leptons and $J/\Psi \rightarrow \ell\ell$ events for low P_T leptons. First, dilepton events are selected to have one leg-lepton with tight ID cuts (T) and the second leg-lepton without any ID cuts. Then, some looser cut or set of looser cuts (L) are imposed for the second leg. The formula for the efficiency of the looser ID cuts is given [33] by :

$$\epsilon_L = \frac{N_L + N_{TT}}{N_{tot} + N_{TT}} \pm \sqrt{\frac{(N_L + N_{TT})(N_{tot} - N_L)}{(N_{tot} + N_{TT})^3}} \tag{5.5}$$

where, N_{tot} = the total number of events in the sample, N_{TT} = the subset in which both leptons pass the tight cuts, and N_L = the subset in which the second-leg leptons pass some looser cut or set of looser cuts. The looser cut L is assumed to be included in the tight cuts, *i.e.*, if a lepton passes the tight cuts then it is also guaranteed to pass L.

5.2.1 Electron ID Efficiency

Using $Z^0 \rightarrow ee$ Events

Z^0 events were selected by requiring one CEM electron ($E_T \geq 20$ GeV) to pass the tight cuts defined below. The other electron does not need to pass any ID cuts from the inclusive electron data sets [34]. Both electrons must pass $ISO \leq 2.0$ GeV. The invariant mass of the two electrons must be between 86 and 96 GeV/c^2. The selection criteria for the tight cuts are : (1) $P_T \geq 13$ GeV/c, (2) $E/p \leq 2.0$, (3) $LSHR \leq 0.2$, (4) HAD/EM ≤ 0.05, (5) $\chi^2_{strip} \leq 8.0$, (6) $|\Delta x| \leq 1.5$ cm, (7) $|\Delta z| \leq 2.5$ cm, (8) $E_T(0.4)/E_T \leq 0.2$.

The obtained ID efficiencies for gold CEM, ordinary CEM, and ordinary PEM electrons are listed in Tables 5.2, 5.3, and 5.4, respectively.

Table 5.2: ID efficiency for gold CEM electrons obtained by using the Z^0 sample.

	# of events	Efficiency (%)
N_{tot}	427	
N_{TT}	303	
#3D Tracks ≥ 1	427	100
$P_T \geq 2.0$ GeV/c	427	100
$E/p \leq 2.0$	387	94.5±0.9
$LSHR \leq 0.2$	414	98.2±0.5
HAD/EM ≤ 0.05	406	97.1±0.6
$\chi^2_{strip} \leq 10.0$	394	95.5±0.8
$\lvert\Delta x\rvert \leq 3$ cm	404	96.9±0.7
$\lvert\Delta z\rvert \leq 5$ cm	413	98.1±0.5
Total (Gold CEM)	328	86.4±1.3

Table 5.3: ID efficiency for ordinary CEM electrons obtained by using the Z^0 sample.

	# of events	Efficiency (%)
N_{tot}	427	
N_{TT}	303	
#3D Tracks ≥ 1	427	100
$P_T \geq 2.0$ GeV/c	427	100
$E/p \leq 2.0$	387	94.5±0.8
$LSHR \leq 0.2$	414	98.2±0.5
HAD/EM $\leq 0.055 + 0.045 \times \frac{E}{100}$	423	99.5±0.3
$\chi^2_{strip} \leq 15.0$	401	96.4±0.7
$\lvert\Delta x\rvert \leq 3$ cm	404	96.9±0.7
$\lvert\Delta z\rvert \leq 5$ cm	413	98.1±0.5
Total (Ordinary CEM)	347	89.0±1.2

Table 5.4: ID efficiency for ordinary PEM electrons obtained by using the Z^0 sample.

	# of events	Efficiency (%)
N_{tot}	410	
N_{TT}	0	
HAD/EM ≤ 0.1	410	100
$\chi^2(3 \times 3) \leq 3.0$	391	95.4±1.0
$VTX_{OCC} \geq 0.5$	384	93.7±1.2
Total (Ordinary PEM)	365	89.0±1.5

Using $J/\Psi \to ee$ Events

J/Ψ events were selected by requiring one CEM electron to pass the tight cuts ($E_{T1} \geq 7$ GeV, $P_{T1} \geq 4$ GeV/c). The other electron ($E_{T2} \geq 5$ GeV) does not need to pass any ID cuts from the low-P_T inclusive electron sample. Both electrons must pass $ISO \leq 2.0$ GeV. The invariant mass of two electrons should be between 3.0 and 3.2 GeV/c^2. The selection criteria for the tight cuts are : (1) $0.75 \leq E/p \leq 1.5$, (2) $LSHR \leq 0.2$, (3) HAD/EM ≤ 0.04, (4) $\chi^2_{strip} \leq 10.0$, (5) $\chi^2_{wire} \leq 15.0$, (6) $|\Delta x| \leq 1.5$ cm, (7) $|\Delta z| \leq 3.0$ cm.

We are left with only 107 CEM-CEM ($E_{T2} > 5$ GeV) J/Ψ events and very few CEM-CEM ($E_{T2} > 11$ GeV) and CEM-PEM ($E_{T2} > 5$ GeV) events. Therefore, we have no estimates for gold CEM ($E_{T2} > 11$ GeV) and ordinary PEM ($E_{T2} > 5$ GeV) electrons. The results for ordinary CEM electrons are shown in Table 5.5.

Table 5.5: ID efficiency for ordinary CEM electrons obtained by using J/Ψ sample.

	# of events	Efficiency (%)
N_{tot}	107	
N_{TT}	46	
#3D Tracks ≥ 1	107	100
$P_T \geq 2.0$ GeV/c	107	100
$E/p \leq 2.0$	107	100
$LSHR \leq 0.2$	101	96.1±1.6
HAD/EM $\leq 0.055 + 0.045 \times \frac{E}{100}$	101	96.1±1.6
$\chi^2_{strip} \leq 15.0$	100	95.4±1.7
$\|\Delta x\| \leq 3.0$ cm	107	100
$\|\Delta z\| \leq 5.0$ cm	106	99.4±0.7
Total (Ordinary CEM)	89	88.2±2.6

Summary of Electron ID Efficiency

We found the efficiencies for ordinary CEM electrons in the Z^0 and J/Ψ samples to be in good agreement. This supports the expectation that there is no significant E_T dependence in ID efficiency.

As for the low E_T PEM electrons, we checked the E_T dependence of the ID efficiency using another way. The HAD/EM is E_T dependence, but we applied a loose cut to neglect the E_T dependence. Thus, we can regard HAD/EM as E_T independence. The $VTX_{\rm OCC}$ is not E_T dependent but the luminosity dependence and the luminosity during the 1992-1993 run was not changed significantly. Thus, we need to estimate the E_T dependence of $\chi^2(3 \times 3)$. We roughly estimated it using the $\mu - e$ events from the heavy flavour($b\bar{b}, c\bar{c}$) production. We selected the $\mu-$PEM events with the missing $E_T < 15$ GeV in the low P_T inclusive muon sample. We selected the PEM electrons satisfied with the following cuts: $ISO < 1.8$GeV, HAD/EM<0.005, $VTX_{\rm OCC} > 0.88$, and matching between CTC track and EM cluster($\delta\phi < 0.02$rad and $\delta R < 1.0$cm). We estimated the $\chi^2(3 \times 3)$ efficiency for the PEM electrons passed the above cuts. The efficiency was 81.6% at $E_T < 10$GeV and 91.7% at $E_T > 15$GeV. We found the E_T dependence of 10% for the $\chi^2(3 \times 3)$ cut. The estimation was very rough rather than the estimation using Z^0 or J/Ψ event. And this dependence will make difference of only 2% in the SUSY trilepton event's acceptance. Thus, in the SUSY trilepton analysis, we can assume that the ordinary PEM efficiencies are not significantly E_T dependent.

In summary, the electron ID efficiencies depend on the electron E_T very weakly. Thus, we have used the efficiencies estimated from the Z^0 events for the SUSY trilepton analysis.

5.2.2 Muon ID Efficiency

Using $Z^0 \to \mu\mu$ Events

Z^0 events were selected by requiring one muon ($P_T > 20$ GeV/c) to pass the tight cuts defined below. The other muon does not need to pass any lepton ID cuts from the high-P_T central muon data sets [35]. Both muons must pass $ISO < 2.0$ GeV. The invariant mass of the two muons should be between 86 and 96 GeV/c^2. The selection criteria for the tight cuts are : (1) EM < 2.0 GeV, (2) HAD < 6.0 GeV, (3) EM+HAD > 0.1 GeV, (4) Impact parameter < 0.2 cm, (5) $|z_{track} - z_{vertex}| < 2.0$ cm, (6) CMU and CMP hit required, (7) CMU matching $\chi^2_x < 6$ and $\chi^2_z < 8$, (8) CMP matching $\chi^2_x < 6$.

The results are summarized in Tables 5.6, 5.7, 5.8, and 5.9, for gold CMU/CMP muons, ordinary CMU/CMP muons, ordinary CMX muons, and ordinary CMIO muons, respectively.

Table 5.6: ID efficiency for gold CMU/CMP muons obtained by using the Z^0 sample. The ID efficiencies for gold CMU*CMP or CMU-only outside CMP muons are also listed, which are used in Section 5.4.

	# of events	Efficiency (%)
N_{tot}	111	
N_{TT}	34	
EM $\leq$ 2.0 GeV	106	96.6±1.5
HAD $\leq$ 6.0 GeV	110	99.3±0.7
EM+HAD $\geq$ 0.1 GeV	110	99.3±0.7
Impact parameter $\leq$ 0.2 cm	111	100
Matching (CMU or CMP)	102	93.8±2.0
Total (Gold CMU/CMP)	97	90.3±2.5
Total (Gold CMU*CMP or CMU-only)	93	87.6±2.7

Table 5.7: ID efficiency for ordinary CMU/CMP muons obtained by using the Z^0 sample.

	# of events	Efficiency (%)
N_{tot}	111	
N_{TT}	34	
EM $\leq$ 2.0 GeV	106	96.6±1.5
HAD $\leq$ 6.0 GeV	110	99.3±0.7
EM+HAD $\geq$ 0.1 GeV	110	99.3±0.7
Impact parameter $\leq$ 0.5 cm	111	100
Matching (CMU or CMP)	102	93.8±2.0
(CMU Matching)	82/90	92.7±2.3
(CMP Matching)	77/77	100
Total (Ordinary CMU/CMP)	97	90.3±2.5
Total (Ordinary CMP only)	106	96.6±1.5

Table 5.8: ID efficiency for ordinary CMX muons obtained by using the Z^0 sample.

EM $\leq$ 2.0 GeV	65	97.0±2.1
HAD $\leq$ 6.0 GeV	67	100
EM+HAD $\geq$ 0.1 GeV	67	100
Impact parameter $\leq$ 0.5 cm	67	100
Matching (CMX)	65	97.0±2.1
Total (Ordinary CMX)	63	94.0±2.9

Table 5.9: ID efficiency for ordinary CMIO muons obtained by using the Z^0 sample.

	# of events	Efficiency (%)
N_{tot}	40	
N_{TT}	0	
EM $\leq$ 2.0 GeV	39	97.5±2.5
HAD $\leq$ 6.0 GeV	38	95.0±3.4
EM+HAD $\geq$ 0.1 GeV	40	100
Impact parameter $\leq$ 0.5 cm	40	100
Total (Ordinary CMIO)	37	92.5±4.2

Using $J/\Psi \rightarrow \mu\mu$ Events

J/Ψ events were selected by requiring one muon to pass the tight cuts defined below. The other muon does not need to pass any ID cuts from the J/Ψ-trigger sample. Both muons must pass $ISO < 2.0$ GeV. The invariant mass of the two muons must be between 3.0 and 3.2 GeV/c^2. The tight cut selection criteria are : (1) $P_T > 7$ GeV/c, (2) EM < 1.5 GeV, (3) HAD < 4.0 GeV, (4) EM+HAD > 0.1 GeV, (5) Impact Parameter < 0.2 cm, (6) $|z_{track} - z_{vertex}| < 2.0$ cm, (7) both CMP and CMU hits required, (8) CMU matching $\chi^2_x < 6$ and $\chi^2_z < 8$, (9) CMP matching $\chi^2_x < 6$. The criteria are much tighter than the ones for Z^0 events in order to remove the larger backgrounds. It should be noted that CMU and CMP muon tracks in the J/Ψ trigger were selected with CMU $\chi^2_x < 16$, CMU $\chi^2_z < 16$, and CMP $\chi^2_x < 16$.

Each cut efficiency is calculated in the same manner as in the Z^0 analysis. The results of the efficiencies for ordinary CMU/CMP muons and ordinary CMX muons are given in tables 5.10 and 5.11, respectively.

Summary of Muon ID Efficiency

The discrepancy in muon ID efficiencies for ordinary CMU/CMP and CMX between J/Ψ and Z^0 events (~97% vs. ~90%) can be explained by the CTC track - muon hit matching cut used in the J/Ψ trigger: CMU $\chi^2_x < 16$ and CMU $\chi^2_z < 16$, CMP $\chi^2_x < 16$. In fact, we obtained an efficiency of ~96% in Z^0 events when the ordinary CMU/CMP and CMX were preselected with these same matching cuts and then re-analyzed.

Table 5.10: ID efficiency for ordinary CMU/CMP muons obtained by using the J/Ψ sample.

	# of events	Efficiency (%)
N_{tot}	12494	
N_{TT}	9998	
EM $\leq$ 2.0 GeV	12281	99.05±0.06
HAD $\leq$ 6.0 GeV	12430	99.72±0.04
EM+HAD $\geq$ 0.1 GeV	12483	99.95±0.01
Impact parameter $\leq$ 0.5 cm	12463	99.86±0.02
Matching (CMU or CMP)	12154	98.49±0.08
(CMU Matching)	12215/12450	98.95±0.07
(CMP Matching)	11492/11605	99.48±0.05
Total (Ordinary CMU/CMP)	11862	97.13±0.11

Table 5.11: ID efficiency for ordinary CMX muons obtained by using the J/Ψ sample.

	# of events	Efficiency (%)
N_{tot}	3750	
N_{TT}	0	
EM $\leq$ 2.0 GeV	3700	98.67±0.19
HAD $\leq$ 6.0 GeV	3740	99.73±0.08
EM+HAD $\geq$ 0.1 GeV	3737	99.65±0.10
Impact parameter $\leq$ 0.5 cm	3746	99.89±0.05
Matching (CMX)	3690	98.40±0.20
Total (Ordinary CMX)	3625	96.67±0.29

In summary, the muon ID efficiencies depend on the muon P_T very weakly. We decided to use the efficiencies obtained from the Z^0 events for the SUSY trilepton analysis, since combining the J/Ψ and Z results is non-trivial unless we have accurately determined the χ^2 distributions from the data. Using the Z^0 efficiencies also provides a conservative estimate of the uncertainty.

5.3 Conversion Removal

By using $Z \to ee$ events, we obtained the conversion removal efficiencies for CEM and PEM electrons :

$$\left.\begin{array}{rcl} \epsilon_C^{conv} & = & 95.5 \pm 0.7\% \\ \epsilon_P^{conv} & = & 98.5 \pm 0.9\% \end{array}\right\} \tag{5.6}$$

As a reference, the efficiencies were also calculated by the Monte Carlo simulation program as:

$$\left.\begin{array}{rcl} \epsilon_C^{conv}(\mathrm{QFL}) & = & 98.3 \pm 0.3\% \\ \epsilon_P^{conv}(\mathrm{QFL}) & = & 97.7 \pm 0.9\% \end{array}\right\} \tag{5.7}$$

The Monte Carlo simulation values are slightly larger than the data values, as expected from the simplified tracking simulation used in Monte Carlo simulation.

5.4 Monte Carlo Simulation Correction

5.4.1 QFL - the event simulator at CDF

CDF provides two packages, QFL [36] and CDFSIM [37], for simulating events. We used the QFL simulation package for estimating the event acceptance. The purpose of the QFL simulation package is to provide a fast and reliable detector simulation for high statistics physics studies and acceptance calculations. The philosophy of the package is to parameterize detector response rather than derive the response from first principles. QFL produces higher level analysis banks rather than raw data, thus eliminating the need to run the complete reconstruction package on the simulation output. The QFL defaults have been designed to produce the banks needed by most users. We changed the QFL parameters with the TALK_TO commands in the Analysis_Control [38]. Other than that we used the default parameters of the QFL. The following is the input parameters list for QFL simulations.

```
ANA>>TALK QFLANA
BEAM 0.03 0.0 0.0036 0.0 0.0 0.0036
BFIELD -14.116
SIGMAZ 30. Z_OFFSET 0. Z_CUT 100.
CESE YES
BREMS YES
GAMMA YES
TRACKS SVXS YES
TRKS YES
       QTRK YES
       CTCS YES
       RETURN
DECAY YES
MOVE_GENP_DECAYS YES NO 1.29
MULT_SCATT YES
YEAR 1992
CPRD CPR_ON YES RETURN
MUONS
        ENABLE ON
        MU_ETA 1.5
        RETURN
RETURN
```

Other parameters that are not in the above list were the default values.

5.4.2 Monte Carlo Simulation Correction

The detector simulation with QFL V3.48 and offline analysis with Offline Version V7.10 were performed using ELES, CMUO, and CMIO banks. It is important to verify that the lepton simulation acceptance (due to geometry, shower simulation, clustering, tracking, muon hit simulation, and reconstruction) is reasonably accurate. Unfortunately, it was not clear that the MC code has been rigorously validated for leptons. Therefore, we have performed a simple cross-check of the validity of our lepton simulation, numerically correcting any discrepancies between MC and data, and assigning systematic uncertainties based on our findings.

Evaluation of the acceptance for each lepton type (CEM, PEM, CMU/CMP, CMX, and CMIO) was performed using W and Z events in the inclusive e and μ samples [34, 35]. The CDF W and Z cross sections are expressed by experimental quantities by the following formula :

$$\sigma_V^{CDF} = \frac{N_{event} - N_{BG}}{A_V \cdot \epsilon_V^{trig/ID} \cdot \epsilon^z \cdot \int \mathcal{L}_{INC} dt} \tag{5.8}$$

where

A_V = Geometrical/kinematical acceptance for the vector boson event;

$\epsilon_V^{trig/ID}$ = Combined trigger and ID (including ISO) efficiency;

ϵ^z = Efficiency for the event vertex cut;

$\int \mathcal{L}_{INC} dt$ = Integrated luminosity for the inclusive lepton sample.

N_{event} = Number of events with W and Z analysis cuts;

N_{BG} = Number of expected background events;

All numbers except A_V were determined from the real data. A_V was determined by a toy detector simulation which was known to have accurate detector geometry for electrons and muons. It should be noted that the luminosity mentioned above is the luminosity before including the efficiency for the event vertex cut $|z_{vertex}| < 60$ cm ($\epsilon^z = 95.6 \pm 1.1\%$ [39]).

The SUSY trilepton analysis is essentially the same as the W and Z analyses, but A is provided by QFL/OFFLINE. We emphasize that A is the event acceptance associated with the simulation and the offline reconstruction of ELES, CMUO, and CMIO banks via QFL/OFFLINE. We may evaluate the MC acceptance (due to geometry, shower simulation, clustering, tracking, muon hit simulation, and reconstruction) by repeating the W and Z analyses using our MC acceptance and comparing the MC cross section to the previously measured the cross sections [39], which we refer as "CDF cross section".

For technical reasons, we used the SUSY trilepton identification cuts in selecting Z and W events. In order to determine the correction factor for the MC acceptance, we compare the CDF cross section (σ^{CDF}) with the cross section using the MC acceptance (σ^{MC}) :

$$\sigma_V^{MC} \quad = \quad \frac{N'_{event} - N'_{BG}}{A_V^{MC} \cdot \epsilon_V^{trig/ID\prime} \cdot \int \mathcal{L}_{INC} dt} \tag{5.9}$$

where

N'_{event} = Number of events with our analysis cuts;

N'_{BG} = Number of expected background events with our analysis cuts;

A_V^{MC} = Event acceptance from QFL/OFFLINE;

$\epsilon_V^{trig/ID\prime}$ = Combined trigger and ID (including ISO) efficiency in our analysis.

We note that the QFL-simulated event containing electrons or muons must pass $|z_{vertex}|$ and isolation ($ISO < 4$ GeV) cuts. Thus, A^{MC} includes those efficiencies. Then, the correction factor for vector-boson events is defined by:

$$\alpha_V \quad = \quad \frac{\sigma^{MC}}{\sigma^{CDF}}. \tag{5.10}$$

By taking this ratio, N_{event} and $\epsilon^{trig/ID}$ cancel almost completely with N'_{event} and $\epsilon^{trig/ID\prime}$, while $\int \mathcal{L}_{INC} dt$ cancels completely. The correction factors for individual lepton types were calculated from the above formula as described below.

Correction Factors for CEM and PEM Using Z/W Events

The Z/W events were selected from the Run-1A inclusive electron (**ICE**) sample [34]. The sample contains 133,805 events. The integrated luminosity for the sample is 19.92 ± 7.2 pb^{-1} which is before including the efficiency for the event vertex at $|z_{vertex}| < 60$ cm ($\epsilon^z = 95.6 \pm 1.1\%$) [39].

Using $Z^0 \to ee$ Events The dielectron event should have the 1st lepton's leg to pass our tight ID cut ($ISO < 2$ GeV) with $E_T \geq 20$ GeV in the central region and the 2nd lepton's leg to pass our loose cut ($ISO < 2$ GeV) with $E_T \geq 20$ GeV (15 GeV) in the central (plug) region. The tight and loose lepton selection criteria, which are the same as in the SUSY trilepton analysis, are listed in Table 5.12.

Table 5.12: Selection criteria for CEM and PEM electrons in the SUSY trilepton analysis. FIDELE is used to check the fiducial area for electrons.

Lepton class	Gold	Ordinary	
Cut variables	Tight CEM	Loose CEM	Loose PEM
E_T (GeV)	≥ 11	≥ 5	≥ 5
ISO (GeV)	≤ 2	≤ 2	≤ 2
Conversion removal	Yes	Yes	Yes
Fiducial area	Yes	Yes	Yes
# 3D track	≥ 1	≥ 1	N/A
P_T (GeV/c)	≥ 2	≥ 2	N/A
E/p	≤ 2	≤ 2	N/A
HAD/EM	≤ 0.05	$\leq 0.055 + 0.045 \times \frac{E}{100}$	≤ 0.1
$\lvert\Delta x\rvert$ (cm)	≤ 3	≤ 3	N/A
$\lvert\Delta z\rvert$ (cm)	≤ 5	≤ 5	N/A
$LSHR$	≤ 0.2	≤ 0.2	N/A
χ^2_{strip}	≤ 10	≤ 15	N/A
$\chi^2_{3\times3}$	N/A	N/A	≤ 3
$VTX_{\rm OCC}$	N/A	N/A	≥ 0.5

The invariant mass of two electrons should be within the Z^0 mass region (66 - 116 GeV/c^2). After all the cuts, 383 CEM+CEM Z^0 and 444 CEM+PEM Z^0 events remained. The mass distribution is shown in figure 5.2(a).

The background is known to be small (1.6%) [39]. We simply assumed that the fraction

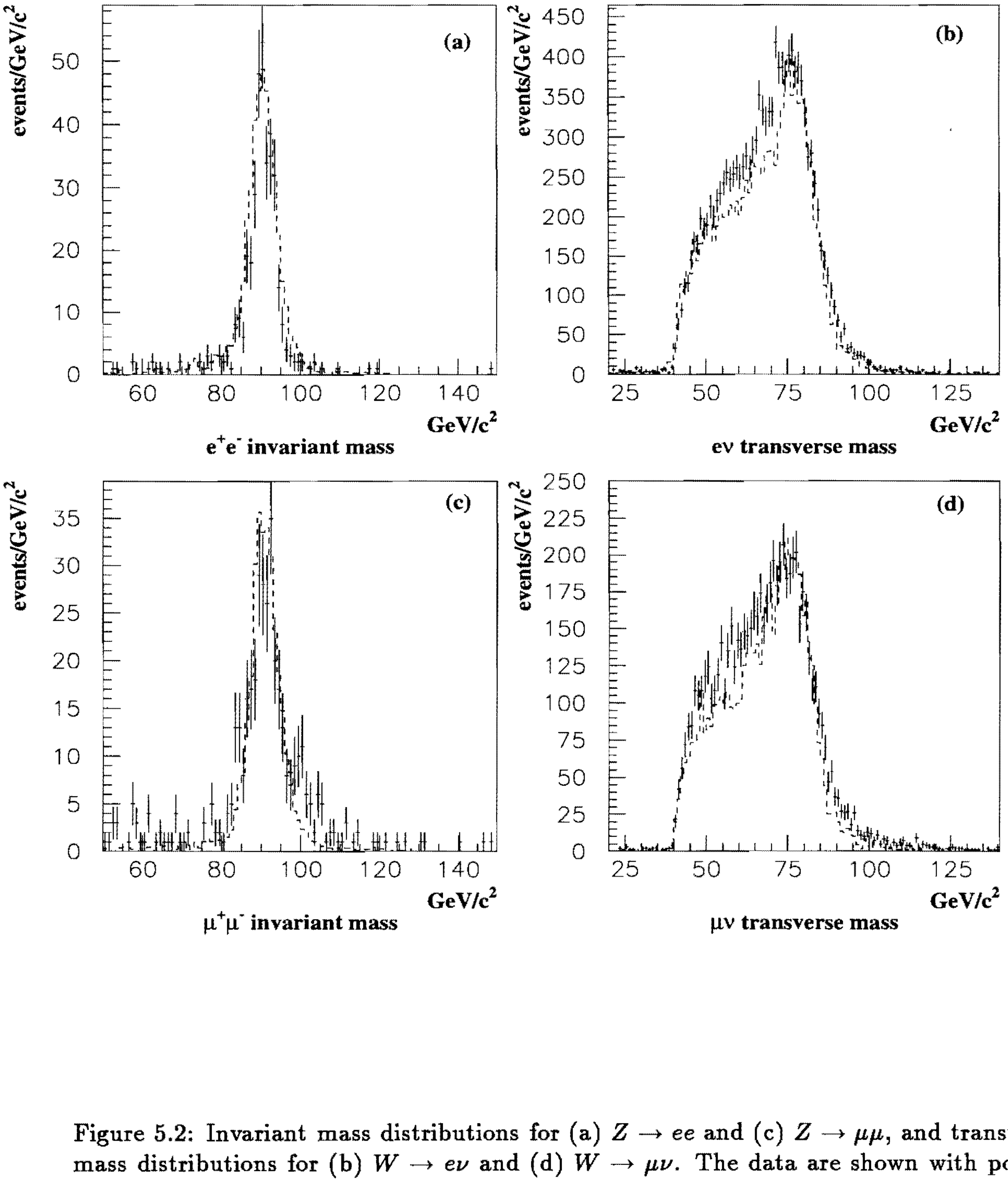

Figure 5.2: Invariant mass distributions for (a) $Z \rightarrow ee$ and (c) $Z \rightarrow \mu\mu$, and transverse mass distributions for (b) $W \rightarrow e\nu$ and (d) $W \rightarrow \mu\nu$. The data are shown with points, and MC (ISAJET V7.06 + QFL V3.48) simulation with dashed histograms.

of the background to the number of events (N'_{event}) to be the same as in Ref. [39], because we selected the events with the same mass region and the similar ID selection.

As for A^{MC}, 23,159 $Z^0 \rightarrow ee$ events (generated by ISAJET) were simulated with QFL. The event selection was done using the same analysis program used in the real data, but with $ISO < 4$ GeV and no lepton ID cuts. After these cuts, 2745 CEM+CEM Z^0 events and 3306 CEM+PEM Z^0 events remained.

The cross section for $Z^0 \rightarrow ee$ is:

$$\sigma_Z^{MC} = \frac{N'_{event} - N'_{BG}}{A_Z^{MC} \cdot \epsilon_Z^{trig/ID'} \cdot \int \mathcal{L}_{INC} dt} \tag{5.11}$$

where: N'_{event} is the number of Z^0 candidates; A_Z^{MC} is the acceptance (due to geometry, shower simulation, clustering, tracking, muon hit simulation, and reconstruction) of QFL/OFFLINE including mass cut, the $|z_{vertex}|$ cut and isolation cut; $\epsilon_Z^{trig/ID'}$ is the trigger and ID (with conversion removal) efficiency for two leptons. Here, A_Z^{MC} is given by

for CEM+CEM events;

$$A_{CC}^{MC} = A_{CC}^{gksr} \times (\epsilon_C^{ISO<4\text{ GeV}})^2 \times \epsilon^z \times \epsilon^{mass} \tag{5.12}$$

for CEM+PEM events;

$$A_{CP}^{MC} = A_{CP}^{gksr} \times \epsilon_C^{ISO<4\text{ GeV}} \times \epsilon_P^{ISO<4\text{ GeV}} \times \epsilon^z \times \epsilon^{mass} \tag{5.13}$$

where A^{gksr} is the efficiency due to geometrical/kinematical cuts, simulation, and reconstruction; ϵ^z is the $|z_{vertex}|$-cut efficiency; $\epsilon^{ISO<4\text{GeV}}$ is the isolation-cut efficiency for $ISO < 4$ GeV; ϵ^{mass} is the mass-cut efficiency.

Table 5.13 summarizes our measurement of the cross sections. The isolation efficiency for CEM (PEM) electron for $ISO < 4$ GeV is 99.0±0.4% (99.2±0.6%) for the real data, and 98.8±0.3% (99.2±0.3%) for QFL, as in Table 5.1. Both the data and the QFL values are consistent within the statistical errors. The DY correction [39] is ratio of the event from the Drell-Yan process within this mass region for the Z^0 events, which is necessary, because we could not reject these event using our analysis cuts. The conversion removal efficiencies for CEM+CEM Z^0 and CEM+PEM Z^0 events are 91.0±1.4% and 94.1±1.1%, respectively, from Eq. 5.6. These are included in $\epsilon^{ID'}$ in this analysis. Both CEM+CEM and CEM+PEM cross sections are larger than the CDF measurement of 231.4 ± 12.4 pb [39].

Table 5.13: $Z^0 \rightarrow ee$ cross sections obtained by using the MC (QFL/OFFLINE) event acceptance. The measured cross section with the standard cut for Z^0 (σ^{CDF}) is 231.4±12.4 pb [39].

	CEM+CEM Z^0	CEM+PEM Z^0
N'_{event}	383	444
Background Fraction (%) [39]	1.6	1.6
N'_{signal}	377	437
A^{MC}_{CC} or A^{MC}_{CP} (%)	12.27±0.021	14.88±0.26
$\epsilon(\epsilon^{trig}_{INC}, \epsilon^{ID'})$ (%)	62.7±1.84	49.0±2.2
$\int \mathcal{L}_{INC} dt$ (pb^{-1})	19.92±0.72	19.92±0.72
DY correction [39]	1.005±0.002	1.005±0.002
$\sigma(Z^0 \rightarrow ee)$ (pb)	247.2±17.7	302.4±23.1

Our numbers of CEM+CEM and CEM+PEM events (383 and 444) should be compared to the CDF published results of 529 ($N_{BG} = 1 \pm 1$) and 640 ($N_{BG} = 14 \pm 14$) events [40]. The discrepancy is explained by the difference in ϵ^{ID} resulting from the different ID criteria used in the two analyses. Therefore, the difference in the cross section comes from the deviation of the acceptance (due to geometry, shower simulation, clustering, tracking, muon-hit simulation, and reconstruction) of QFL/OFFLINE for the CEM and PEM electrons.

The correction factors for CEM and PEM electrons, α_C and α_P, can be obtained by solving

$$\sigma^{CDF} = \begin{cases} \dfrac{\sigma^{MC}_{CC}}{\alpha_C \cdot \alpha_C}, \\ \dfrac{\sigma^{MC}_{CP}}{\alpha_C \cdot \alpha_P}. \end{cases} \tag{5.14}$$

Thus,

$$\alpha_C = \sqrt{\frac{\sigma^{MC}_{CC}}{\sigma^{CDF}}} \tag{5.15}$$

$$\alpha_P = \frac{\sigma^{MC}_{CP}}{\sigma^{CDF}} \sqrt{\frac{\sigma^{CDF}}{\sigma^{MC}_{CC}}}. \tag{5.16}$$

With $\sigma^{CDF} = 231.4\pm12.4$ pb, we obtained

$$\alpha_C(Z) = 1.033 \pm 0.032 \tag{5.17}$$

$$\alpha_P(Z) = 1.265 \pm 0.074 \tag{5.18}$$

Using $W \rightarrow e\nu$ Events Similarly, we can also determine the correction factor for CEM using $W \rightarrow e\nu$ events, but not for PEM, because of the trigger bias in the **ICE** sample.

$W \rightarrow e\nu$ events were selected with $E_T^e \geq 20$ GeV and $\not{E}_T \geq 20$ GeV. The electron was identified with our gold electron selection criteria and $ISO \leq 2$ GeV. No cut was applied on the transverse mass of the electron and $\not{E}_T$. After all these cuts, 12,899 W events remained. The mass distribution is shown in figure 5.2(b). In this figure, the histogram of the MC simulation includes the $W \rightarrow e\nu$ events only. But the histogram of the real data includes $W \rightarrow e\nu$ events and its backgrounds and the background fraction was 12.3%. Therefore, the histogram of the real data didn't exactly agreement with the histogram of the MC simulation.

In order to find the event acceptance, 13,795 ISAJET W events were analyzed in the same manner as in the case for the Z QFL/OFFLINE analysis: we required $E_T^e \geq 20$ GeV, $ISO \leq 4$ GeV and $\not{E}_T \geq 20$ GeV. A total of 4,263 events were selected.

The obtained cross section, after the background subtraction, is listed in Table 5.14. The value of the CDF measurement for this cross section, after the background subtraction, is 2.508±0.122 nb [39]. We assumed that the background size and the shape in our analysis are similar to the CDF W analysis.

The number of W events (12,899) in our analysis should be compared to the CDF published result of 13,796 events [39, 40]. The discrepancy is explained by the difference in ϵ^{ID} resulting from the different ID criteria used in the two analyses. Therefore, the difference in the cross section comes from the deviation of the acceptance (due to geometry, shower simulation, clustering, tracking, muon-hit simulation, and reconstruction) of QFL/OFFLINE for the CEM electron.

Table 5.14: $W \rightarrow e\nu$ cross section using the MC (QFL/OFFLINE) acceptance. The CDF measurement for the cross section (σ^{CDF}) is 2.508±0.122 nb [39].

	CEM events
N'_{event}	12899
Background fraction (%)[39]	12.3
N'_{signal}	11312
A_W^{MC} (%)	31.43±0.42
$\epsilon(\epsilon_{INC}^{trig}, \epsilon^{ID'})$ (%)	70.1±1.4
$\int \mathcal{L}_{INC} dt$ (pb^{-1})	19.92±0.72
$\sigma(W \rightarrow e\nu)$ (nb)	2.577±0.114

The correction factor for CEM electrons is:

$$\alpha_C = \frac{\sigma_C^{MC}}{\sigma^{CDF}} . \tag{5.19}$$

With $\sigma^{CDF} = 2.508 \pm 0.122$ nb,

$$\alpha_C(W) = 1.028 \pm 0.037. \tag{5.20}$$

Summary of the Electron Correction Factors The two numbers of α_C from the Z and W samples are in a good agreement. We combined $\alpha_C(Z)$ and $\alpha_C(W)$ and obtained

$$\alpha_C = 1.031 \pm 0.024. \tag{5.21}$$

Then, we recalculated α_P using the combined value of α_C:

$$\begin{aligned} \alpha_P &= \left(\frac{\sigma_{CP}^{MC}}{\sigma^{CDF}}\right) \cdot \left(\frac{1}{\alpha_C}\right) \\ &= 1.268 \pm 0.079. \end{aligned} \tag{5.22}$$

Correction Factors for Muons Using Z/W Events

The Z/W events were selected from the Run-1A inclusive muon sample [35], which is comprised of four different streams : CMUO-CMUO dimuons, CMUO-CMIO dimuons, CMIO-CMIO dimuons, and CMUO single muons. The sample contains 83,051 events, corresponding to a total integrated luminosity of 18.83 ± 0.68 pb^{-1} before applying the event vertex cut $|z_{vertex}| < 60$ cm ($\epsilon^z = 95.6 \pm 1.1\%$) [39].

Using $Z^0 \rightarrow \mu\mu$ Events We required these events to have one gold CMU-only or CMU*CMP muon ($P_T > 20$ GeV/c) plus one ordinary CMUO/CMIO muon ($P_T > 20$ GeV/c). The selection criteria are the same as in Table 5.15, including a cut on $ISO < 2$ GeV for both muons. The dimuon mass must be between 66 and 116 GeV/c^2. A total of 333 $Z^0 \rightarrow \mu\mu$ events passed our selection criteria. The mass distribution is shown in figure 5.2(c) and the classifications of events with the 2nd leg muon's types are listed in Table 5.16.

Table 5.15: Selection criteria for CMUO and CMIO muons in the SUSY trilepton analysis. CMUSWM is used to check the fiducial area for muons.

Lepton class	Gold	Ordinary	
Cut variables	Tight CMUO	Loose CMUO	Loose CMIO
Hit region	CMU or CMP	CMU or CMP or CMX	CMIO
P_T (GeV/c)	≥ 11	≥ 4	≥ 10
ISO (GeV)	≤ 2	≤ 2	≤ 2
Fiducial area	Yes	Yes	Yes
EM (GeV)	≤ 2	≤ 2	≤ 2
HAD (GeV)	≤ 6	≤ 6	≤ 6
EM+HAD (GeV)	≥ 0.1	≥ 0.1	≥ 0.1
Impact para. (cm)	≤ 0.2	≤ 0.5	≤ 0.5
Matching (CMU)	$\|\Delta x\| \leq 2$ cm or $\chi_x^2 \leq 9$	$\|\Delta x\| \leq 2$ cm or $\chi_x^2 \leq 9$	N/A
Matching (CMP)	$\|\Delta x\| \leq 5$ cm or $\chi_x^2 \leq 9$	$\|\Delta x\| \leq 5$ cm or $\chi_x^2 \leq 9$	N/A
Matching (CMX)	N/A	$\|\Delta x\| \leq 5$ cm or $\chi_x^2 \leq 9$	N/A

Table 5.16: The number of $Z^0 \rightarrow \mu\mu$ events for various 2nd leg μ's types.

2^{nd} μ category		Events
CMU or CMP hit		142
	(CMU*CMP)	(82)
	(CMU only outside CMP)	(29)
	(CMU only inside CMP)	(7)
	(CMP only)	(24)
CMX hit		106
CMIO muon		85
Total		333

In order to obtain the QFL/OFFLINE acceptance (due to geometry, shower simulation, clustering, tracking, muon hit simulation, and reconstruction), we generated 60,028 $Z^0 \rightarrow \mu\mu$ events with ISAJET and simulated them using QFL. Dimuon events are selected with CMU only or CMU*CMP muon for the 1st leg and any muon type for the 2nd leg. We required $P_T \geq 20$ GeV/c and $ISO \leq 4$ GeV for the both legs. No other ID cuts are applied. After these cuts, 8861 $Z^0 \rightarrow \mu\mu$ events remained.

We calculated the cross sections for seven categories of $Z^0 \rightarrow \mu\mu$ events according to the 2nd leg muon type. Table 5.17 lists our results. In this study, we have assumed the background fractions for all categories of $Z \rightarrow \mu\mu$ events to be the same as in Ref. [39], since we selected events using the same mass region and similar ID cuts as in that analysis. If the total background of 1.3 events (= 333 × 0.004) were completely attributed to the 85 CMIO events (24 CMP events), the cross section would change by 1.5% (5.4%), where their statistically uncertainty of 10.8% (20.4%) is still dominant. Thus, our simple assumption should be acceptable.

Our number of Z events (333) should be compared to the CDF published result of 423 events [39, 40]. The discrepancy is explained by the difference in ϵ^{ID} resulting from the different ID criteria used in the two analyses. Therefore, the difference in the cross section comes from the acceptance (due to geometry, shower simulation, clustering, tracking, muon-hit simulation, and reconstruction) of QFL/OFFLINE for the CMUO and CMIO muons.

The ratio of the cross section in Table 5.17 to the CDF cross section (202.9±15.4 pb) provides the correction factor for the dimuon's acceptance. Since the 1st leg muon is always a CMU-only or a CMU*CMP muon, we have to divide the factors by α_1 when we calculate the correction factors for each category of muon (see Table 5.18). In this table, α_Z means the correction factor for $Z^0 \rightarrow \mu\mu$ events and the individual muon correction factors are indicated by α_i.

Using $W \rightarrow \mu\nu$ Events. We also performed the similar analysis for $W \rightarrow \mu\nu$ events using the inclusive hight-P_T muon data set from Run 1A. This data set was the same one we used for the $Z^0 \rightarrow \mu\mu$ study.

Table 5.17: $Z^0 \rightarrow \mu\mu$ cross sections using the MC (QFL/OFFLINE) event acceptance. The CDF cross section (σ^{CDF}) is 202.9±15.4 pb [39].

	CMU*CMP or CMU-only outside CMP	CMU-only inside CMP	CMP-only
N'_{event}	111	7	24
Background fraction (%) [39]	0.40	0.40	0.40
N'_{signal}	111	7	24
A_Z^{MC} (%)	3.830 ± 0.078	0.416 ± 0.026	2.041 ± 0.058
$\epsilon(\epsilon_{INC}^{trig}, \epsilon^{ID'})$ (%)	68.40 ± 3.82	60.50 ± 3.79	66.80 ± 3.46
$\int \mathcal{L}dt$ (pb^{-1})	18.83 ± 0.68	18.83 ± 0.68	18.83 ± 0.68
DY correction [39]	1.03 ± 0.01	1.03 ± 0.01	1.03 ± 0.01
$\sigma(Z^0 \rightarrow \mu\mu)$ (pb)	231.8 ± 27.4	152.1 ± 59.4	96.3 ± 20.7

	CMU or CMP	CMX	CMIO
$N_{event'}$	142	106	85
Background fraction (%) [39]	0.40	0.40	0.40
N'_{signal}	141	106	85
A_Z^{MC} (%)	6.287 ± 0.099	4.198 ± 0.082	4.276 ± 0.083
$\epsilon(\epsilon_{INC}^{trig}, \epsilon^{ID'})$ (%)	67.34 ± 3.14	65.00 ± 3.71	63.90 ± 4.23
$\int \mathcal{L}dt$ (pb^{-1})	18.83 ± 0.68	18.83 ± 0.68	18.83 ± 0.68
DY correction [39]	1.03 ± 0.01	1.03 ± 0.01	1.03 ± 0.01
$\sigma(Z^0 \rightarrow \mu\mu)$ (pb)	182.2 ± 18.9	212.5 ± 25.6	170.2 ± 22.8

Table 5.18: Muon acceptance correction factors using $\sigma^{CDF} = 202.9$ pb [39].

i	2^{nd} μ category	σ^{MC}	α_Z	α_i
1.	CMU only or CMU*CMP	231.8	1.142 ($= \alpha_1 \cdot \alpha_1$)	1.069 ± 0.062
2.	CMU only inside CMP	152.1	0.750 ($= \alpha_1 \cdot \alpha_2$)	0.702 ± 0.274
3.	CMP only	96.3	0.475 ($= \alpha_1 \cdot \alpha_3$)	0.444 ± 0.095
4.	CMU or CMP	182.2	0.898 ($= \alpha_1 \cdot \alpha_4$)	0.840 ± 0.077
5.	CMX only	212.5	1.047 ($= \alpha_1 \cdot \alpha_5$)	0.979 ± 0.099
6.	CMIO	170.2	0.839 ($= \alpha_1 \cdot \alpha_6$)	0.785 ± 0.092

We required $W \rightarrow \mu\nu$ events to have only one gold CMU-only (outside CMP) or CMU*CMP muon with $P_T \geq 20$ GeV/c and missing $E_T \geq 20$ GeV. The muons were required to pass $ISO \leq 2$ GeV. No transverse mass cut between the muon and the missing E_T was imposed. After all the cuts, 6179 $W \rightarrow \mu\nu$ events remained. The mass distribution is shown in figure 5.2(d). In this figure, the histogram of the MC simulation includes the $W \rightarrow \mu\nu$ events only. But the histogram of the real data includes $W \rightarrow \mu\nu$ events and its backgrounds and the background fraction was 13.2%. Therefore, the histogram of the real data didn't exactly agreement with the histogram of the MC simulation.

The event acceptance for muons with $P_T \geq 20$ GeV/c ($ISO \leq 4$ GeV) and $\not\!\!E_T \geq 20$ GeV is 15.71% (= 2961/18851). Table 5.19 shows the values used in our cross section calculation.

Table 5.19: $W \rightarrow \mu\nu$ cross section using the MC (QFL/OFFLINE) acceptance. The CDF cross section (σ^{CDF}) is 2.484±0.163 nb [39].

	CMU*CMP or CMU only outside CMP
N'_{event}	6179
Background fraction (%) [39]	13.2
N'_{signal}	5363
A_W^{MC} (%)	15.71 ± 0.27
$\epsilon(\epsilon_{INC}^{trig}, \epsilon^{ID\prime})$ (%)	72.5 ± 3.4
$\int \mathcal{L}_{INC} dt$ (pb^{-1})	18.83 ± 0.68
$\sigma(W \rightarrow \mu\nu)$ (nb)	2.501±0.158

Our W yield (6179 events) should be compared to the CDF published result of 6222 events [39, 40]. The difference is explained by the difference of ϵ^{ID} in the two analyses. Therefore, the difference in the cross section comes from the deviation of the acceptance (due to geometry, shower simulation, clustering, tracking, muon-hit simulation, and reconstruction) of QFL/OFFLINE for the CMUO muon.

Using the previously measured CDF cross section (2.484±0.163 nb [39]), we obtained the acceptance correction factor for the CMU-only or CMU*CMP muons to be 1.007 ± 0.062.

Summary of the Muon Correction Factors The α_1 (CMU*CMP or CMU only outside CMP muons) correction factors we obtained from Z and W events agreed within the statistical uncertainties. Thus, we combined these two numbers and recalculated the other correction factors. All results are summarized in Table 5.20.

Table 5.20: Summary of the muon acceptance correction factors (α_i). The combined α_i ($i = 2 \sim 6$) was re-calculated using $\alpha_1 = 1.038 \pm 0.043$.

	$Z^0 \to \mu\mu$	$W \to \mu\nu$	Combined α_i
1. CMU only outside CMP or CMU*CMP	1.069 ± 0.062	1.007 ± 0.062	1.038 ± 0.043
2. CMU only inside CMP	0.702 ± 0.274	—	0.723 ± 0.276
3. CMP only	0.444 ± 0.096	—	0.458 ± 0.094
4. CMU or CMP	0.840 ± 0.077	—	0.865 ± 0.071
5. CMX only	0.979 ± 0.099	—	1.009 ± 0.093
6. CMIO	0.785 ± 0.092	—	0.808 ± 0.089

The following values will be used in our trilepton analysis:

$$\alpha_{\text{CMU/CMP}} = 0.865 \pm 0.071 \tag{5.23}$$

$$\alpha_{\text{CMX}} = 1.009 \pm 0.093 \tag{5.24}$$

$$\alpha_{\text{CMIO}} = 0.808 \pm 0.089 \tag{5.25}$$

Comparison of W/Z Events with SUSY Trilepton Events

One final cross check was done to justify the validity of our lepton acceptance correction factors, determined using Z/W events, for SUSY trilepton events. We compared the pseudo-rapidity distributions of leptons in Z/W events to the distribution of SUSY events.

Figure 5.3 depicts the $\eta(\ell)$ distributions for $Z \to \ell\ell$ and $\tilde{\chi}_1^{\pm}\tilde{\chi}_2^0 \to 3\ell + X$ events, where $M_{\tilde{\chi}_1^{\pm}} = 45$ GeV/c^2. Since the two distributions are almost identical, the acceptance correction factors for $Z \to \ell\ell$ can be also used for the SUSY trilepton analysis.

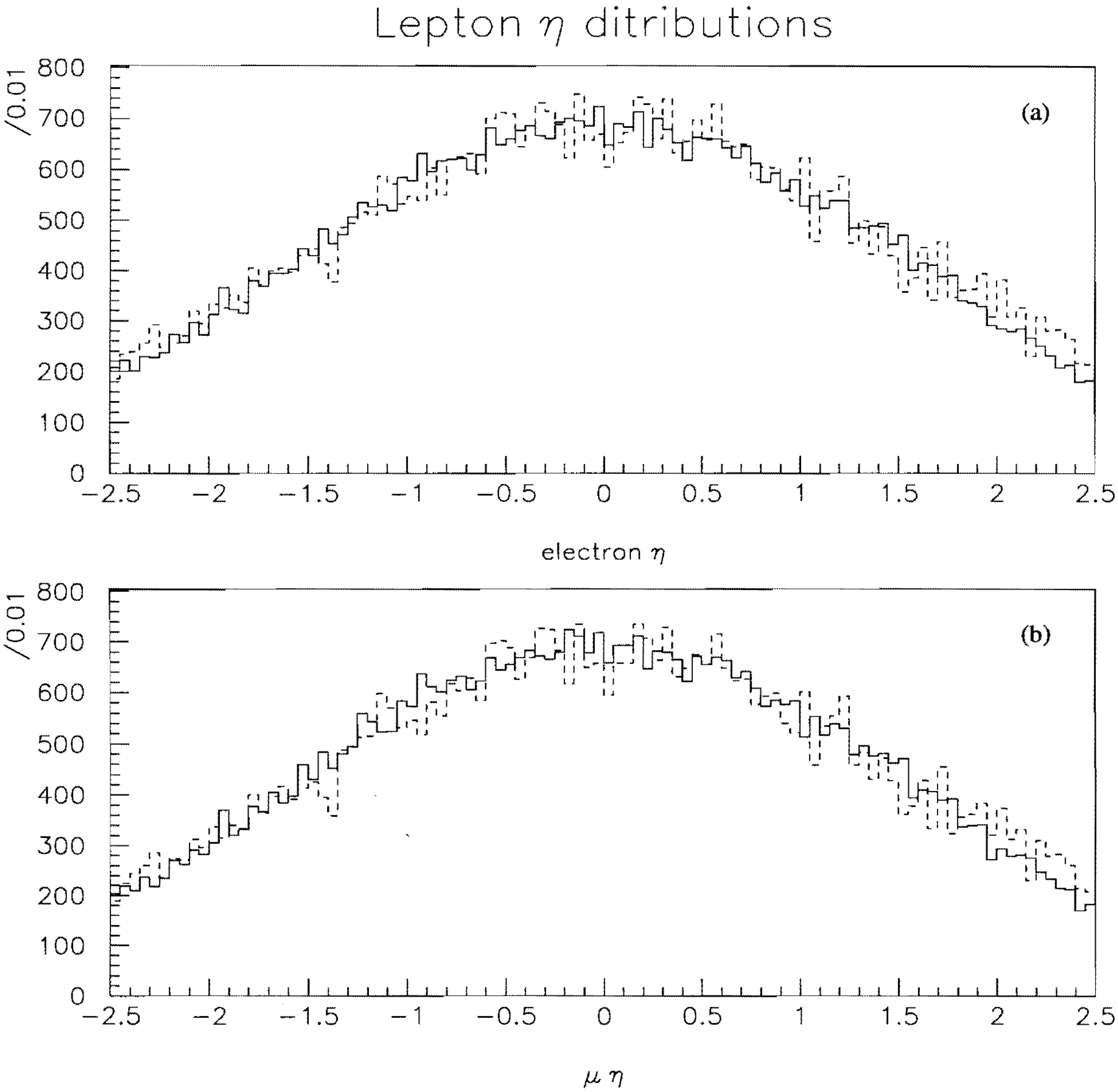

Figure 5.3: Pseudo-rapidity distributions for leptons in $Z \rightarrow \ell\ell$ (dashed line) and $\tilde{\chi}_1^{\pm}\tilde{\chi}_2^0 \rightarrow 3\ell + X$ (solid line) events, where (a) is for electrons and (b) is for muons.

5.5 Trigger efficiency

In this section, we estimate the trigger efficiency for trilepton events using the real data. This was done by using a sample of events which satisfied the trigger criteria other than the inclusive lepton trigger requirement. We then can look at detector hits which we believe to be genuine electrons or muons and see if the various inclusive lepton trigger bits (corresponding to those hits) had fired.

A few remarks are necessary before describing our trigger efficiency calculation. The figure 4.1, the result of the lepton's P_T distribution by the Monte Carlo simulation, revealed that the best CDF triggers for the trilepton event is single lepton triggers. Thus, if we assume that SUSY trilepton events were indeed being produced at CDF, these events will be tagged by the single trigger paths listed in table 5.21.

Since the trilepton analysis does not specifically select any particular trigger lines, it is possible that volunteer leptons may be accepted in the trilepton analysis.

Table 5.21: Possible single lepton triggers which may be satisfied by SUSY trilepton events.

Possible level 1 trigger lines	description
CMU_CMP_6PT0*	CMU*CMP, $P_T > 6$ (with or without BBC requirement)
L1_CALORIMETER_BBC*	PHA,FHA=25 single tower above threshold
Possible level 2 trigger lines	**description**
CMU_CMP_CFT_9_2*	CMU*CMP, $P_T > 9$,prereq. on CMU_CMP_6PT0_BBC
CMUNP_CFT_9_2_5DEG	CMU Only region, $P_T \geq 9.2$, TRL 5 degree match
CMUP_CFT_9_2_5DEG	CMU+CMP region, $P_T \geq 9.2$, TRL 5 degree match
CEM_9_SEED_9_SH_7_CFT_9_2*	CEM>9 GeV, CFT>9.2 (no prereq.)
Possible level 3 trigger lines	**description**
MUO1_CMU_CMP_7PT5*	Central muon + upgrade without CMX
MUO1_CMU_ONLY_15PT0*	Central muon with no upgrade
MUO1_CMP_ONLY_7PT5*	Upgrade only, no specific L1/L2 trigger req.
ELE1_CEM_8(9)_6	Inclusive electrons, $E_T > 8(9), P_T > 6$
ELE1_CEM_15_10	High-E_T, loose inclusive electrons

5.5.1 Muon trigger efficiencies

Since our GOLD muon P_T threshold was above 11 GeV/c and we required the GOLD muon to pass the muon triggers, we estimated the trigger efficiencies for $P_T > 11$GeV/c.

The level 1 muon trigger requires the hits on the CMU and the CMP with $P_T > 6$ GeV/c. This trigger efficiency was calculated by the events in the other trigger data sample which is unbiased for muon triggers and given $\epsilon = 94.99^{+0.74}_{-0.82}\%$ for muons with $P_T > 11$ GeV/c [41](figure 5.4).

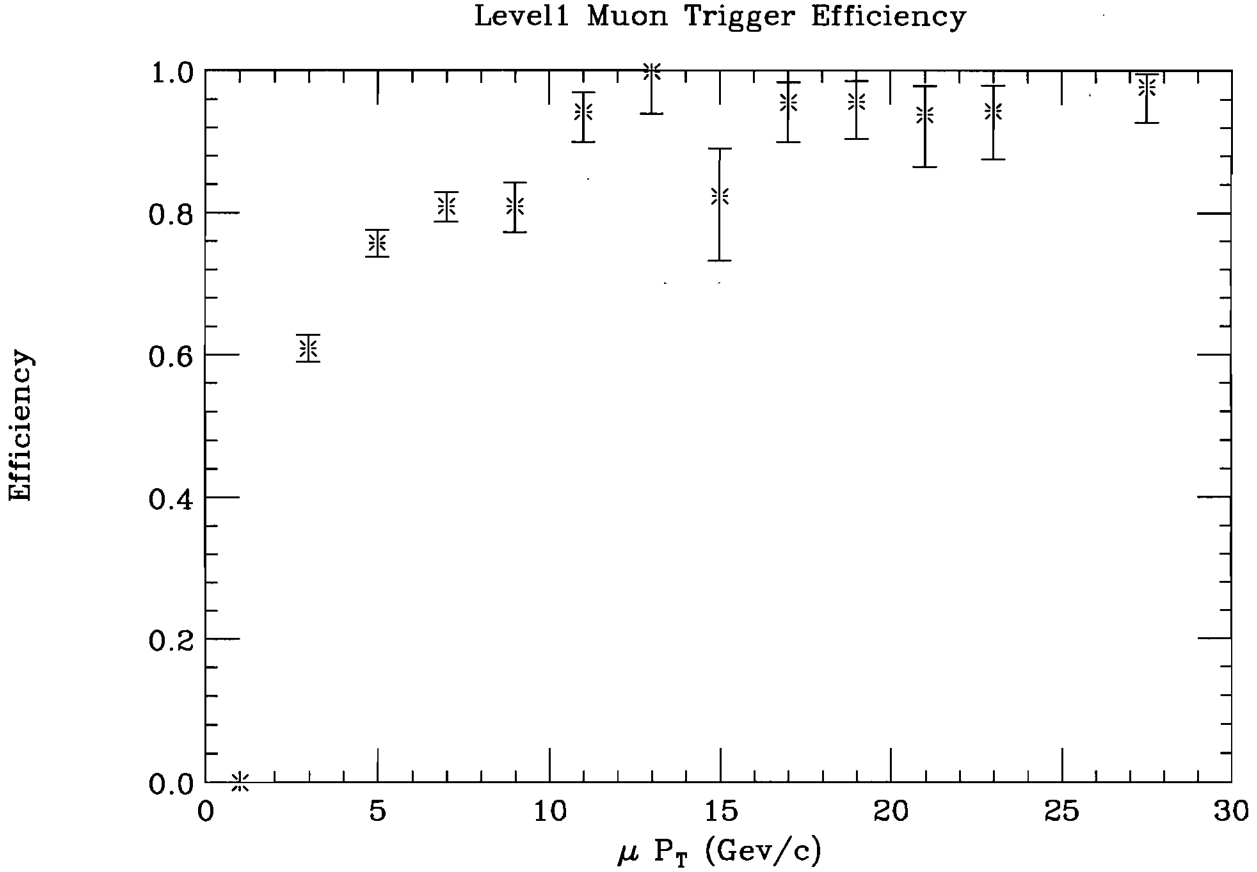

Figure 5.4: Level 1 muon trigger efficiency distribution

For level 2, a combined efficiency for the following three trigger lines was measured: CMU_CMP_CFT_9_2, CMUNP_CFT_9_2, and CMUP_CFT_9_2. The all triggers require the same P_T threshold on CFT but different hit requirement on the central muon chambers. The obtained value was $\epsilon = 90.23^{+1.35}_{-1.48}\%$, for muons with $P_T > 11$ GeV/c [41](figure 5.5).

To estimate the level 3 efficiency, the missing E_T data sample was used. This dataset was made by selecting events which satisfied either missing E_T or τ triggers. The both triggers are unbiased for muon triggers. Furthermore, in order to decouple the level

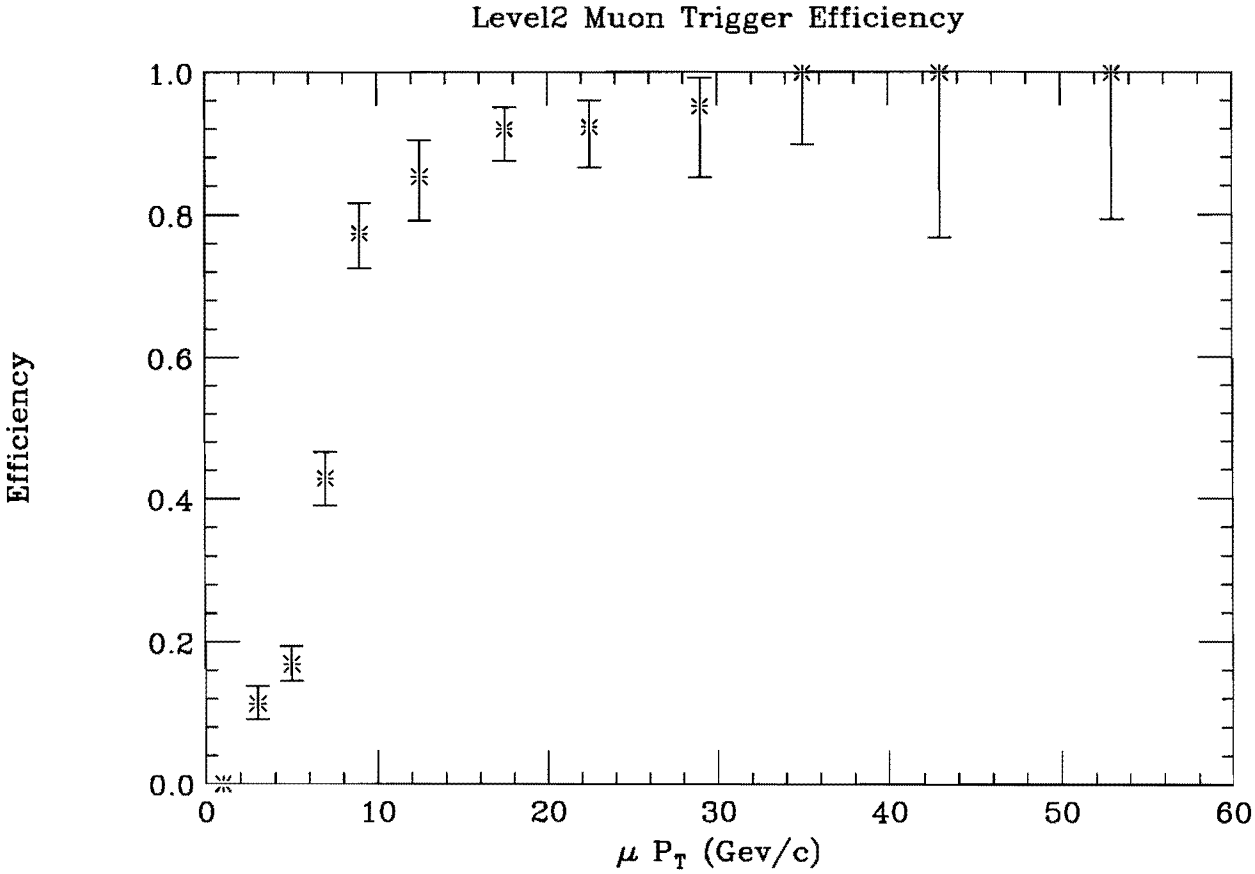

Figure 5.5: Level 2 muon trigger efficiency distribution

3 efficiency from the previously determined level 1 and level 2 efficiencies, events were selected which passed the level 1 and level 2 trigger lines listed above (of course, level 2 is a logical .OR. of the three possibilities). The event that passed the level 1 and level 2 muon triggers has at least one triggered muon. Then we require this muon to be a good muon and the good muon is guaranteed to pass the level 3 trigger. Good muons were identified using the following criteria:

- both CMU and CMP hits required
- EM energy < 1 GeV
- HAD energy < 6 GeV
- EM+HAD energy > 0 GeV
- $|DX| < 5.0$ cm
- energy(cone of radius 0.4 around muon) < 10 GeV

Having found an event containing a good muon, we then checked the level 3 trigger bits to see if the MUO1_CMU_CMP_7PT5* trigger line fired. The resulting efficiency distribution, plotted as a function of muon P_T, is shown in figure 5.6. Although the distribution appears to be flat for $P_T > 15$ GeV/c, we will make allowance for a small slope by assigning a systematic uncertainty of 2%. Thus, for muons $P_T > 11$ GeV/c, the efficiency is $\epsilon = 98.39 \pm 0.38 \pm 2.0\%$. Multiplying this result by the level 1 and level 2 efficiencies, and combining all errors in quadrature, we obtain a total muon trigger efficiency of $84.33 \pm 2.30\%$.

5.5.2 Electron trigger efficiencies

Since our GOLD electron E_T threshold was above 11 GeV and we required the GOLD electron to pass the electron triggers, we estimated the trigger efficiencies for $E_T > 11$GeV. The level 1 electron trigger efficiency was estimated using the events passed the level 1 and level 2 muon triggers. The obtained level 1 efficiency was $\epsilon = 99.2 \pm 0.1\%$ for electrons

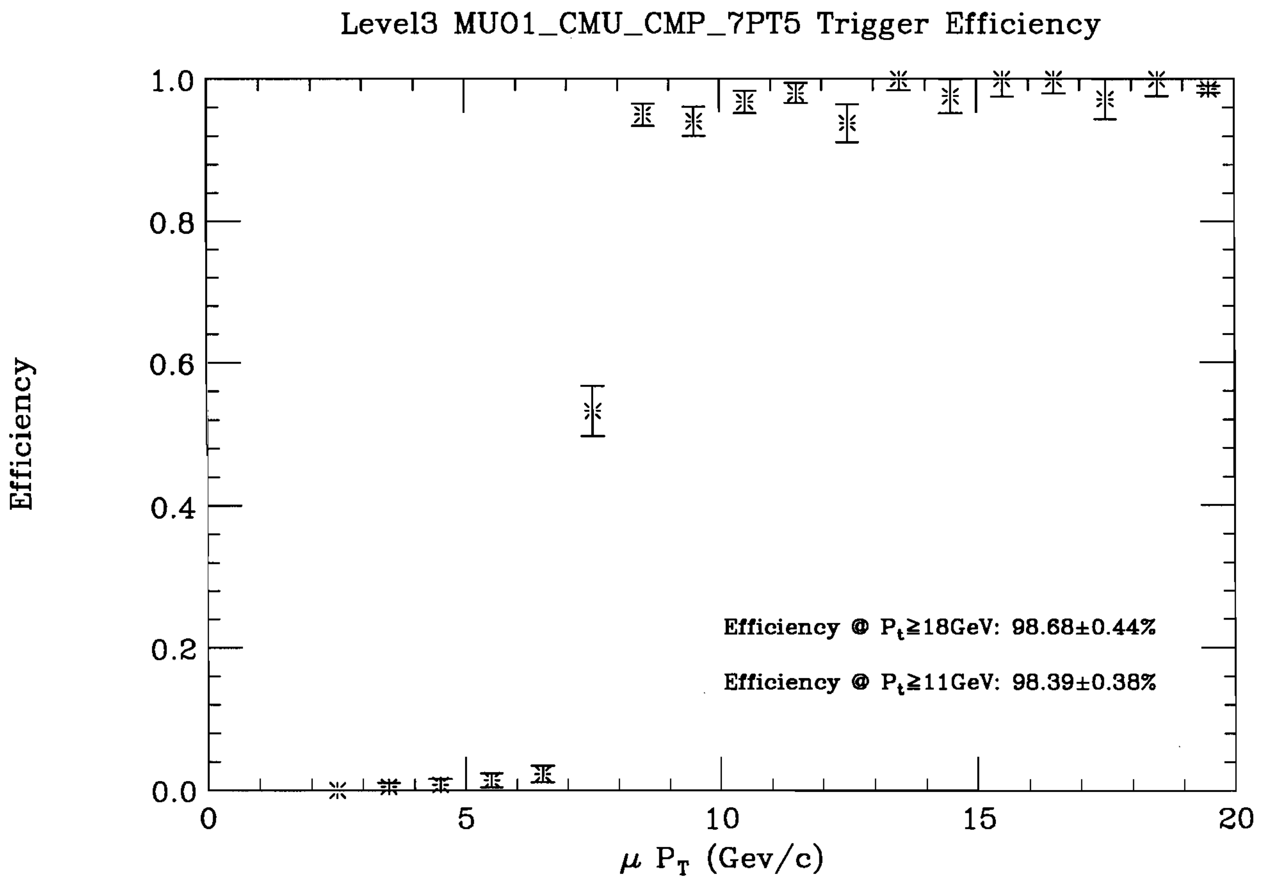

Figure 5.6: Level 3 muon trigger efficiency distribution

with $E_T > 11$ GeV[42] (figure 5.7). The level 2 electron trigger efficiency from [43] is $\epsilon = 92.9 \pm 0.7\%$ for electrons with $E_T > 11$ GeV (figure 5.8).

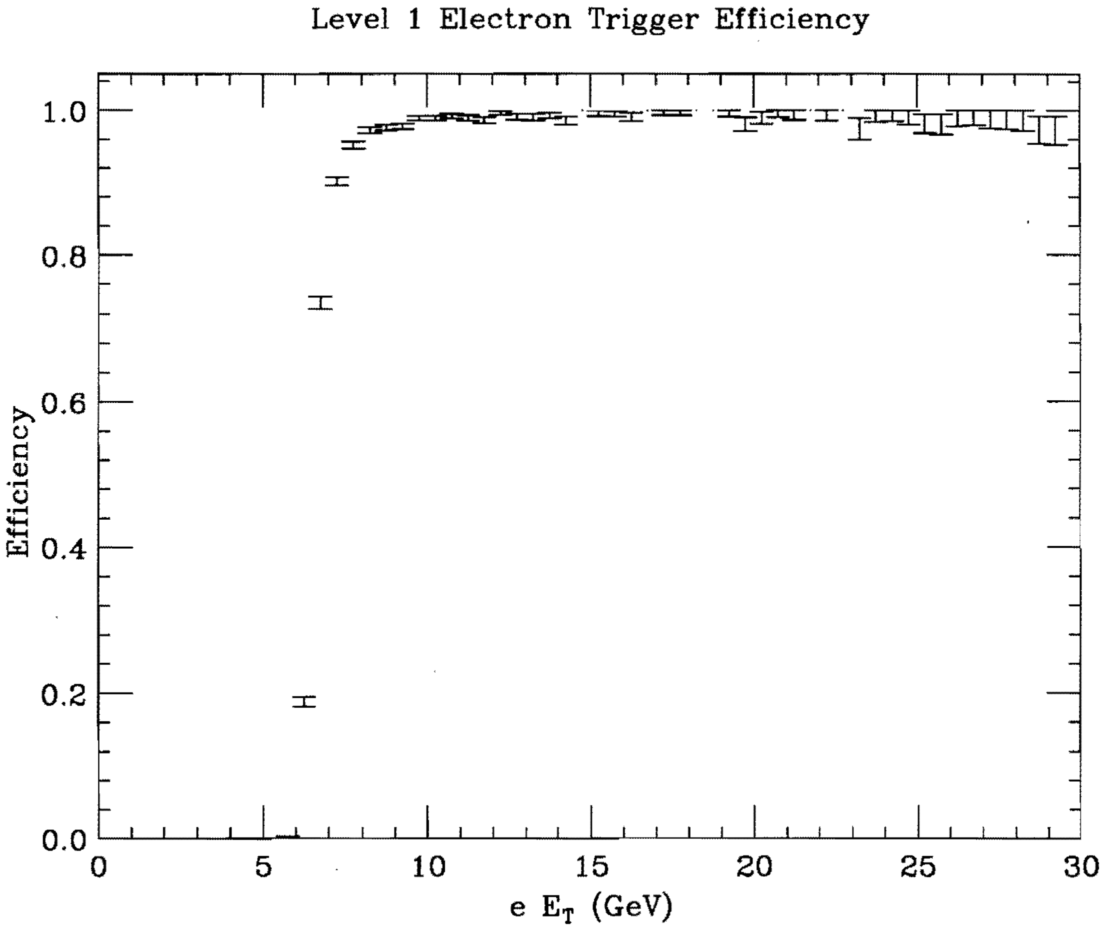

Figure 5.7: Level 1 calorimeter trigger efficiency distribution

To estimate the level 3 efficiency, we used the inclusive muon data sample. The missing E_T data sample used for the level 3 muon trigger efficiency estimation also can be used for this level 3 efficiency estimation, but it doesn't have enough inclusive good electron events to allow us to accurately determine the electron efficiency. The inclusive muon data sample should be unbiased for electrons. The way to estimate the electron efficiency is the same as the way for the muon efficiency. We define the mother sample as the events that passed level 1 and level 2 electron trigger's criteria listed table 5.21 and had one good electron. Good electrons are identified using the following criteria:

- $E/P < 2.0$

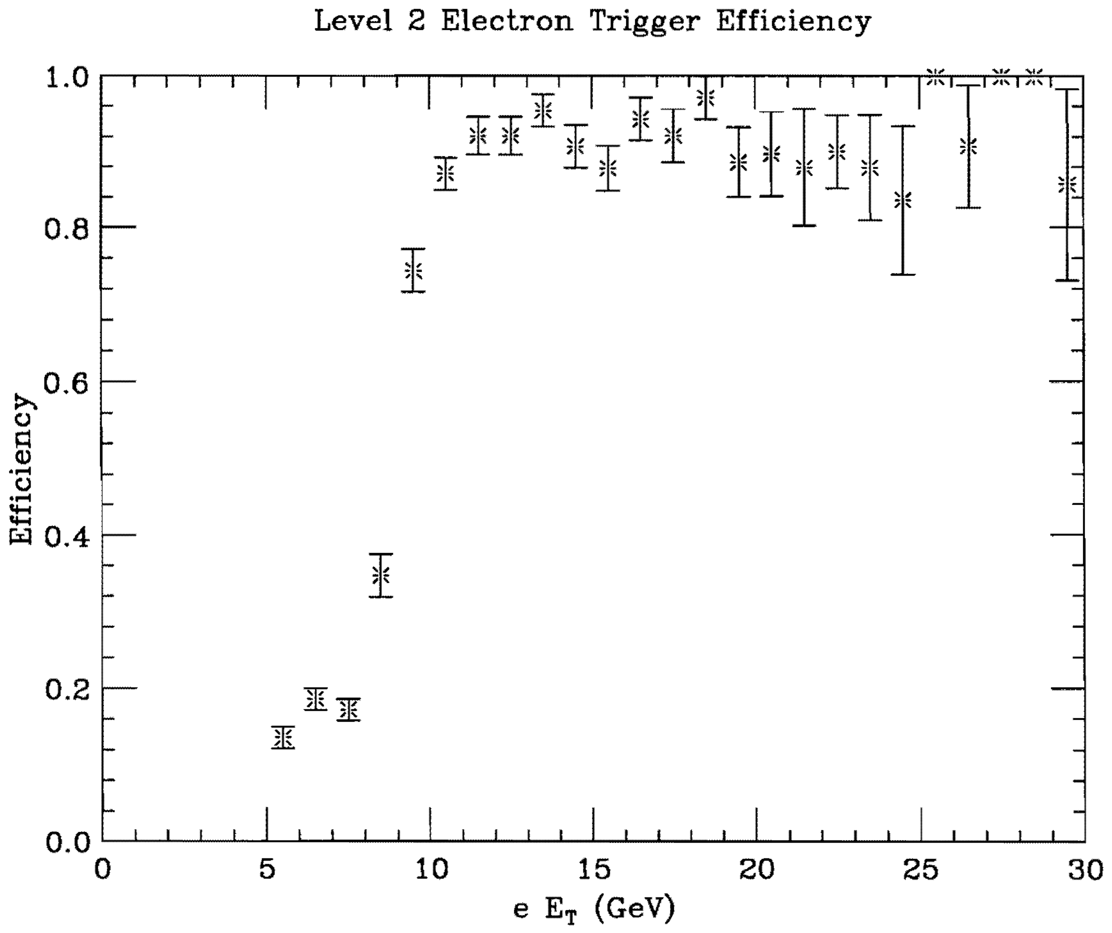

Figure 5.8: Level 2 electron trigger efficiency distribution

- HAD/EM $< 0.055 + 0.045 \times \frac{E}{100}$
- LSHR < 0.2
- $|\Delta X| < 3$ cm
- $|\Delta Z| < 5$ cm
- $\chi^2_{strip} < 10.0$
- Require the fiducial volume
- Not γ conversion

Events containing good electrons were then checked to see whether the ELE1_CEM_8(9)_6 or ELE1_CEM_15 trigger lines had fired. The resulting efficiency is shown in figure 5.9. This plot shows a sudden 3% increase at 16 GeV. Upon further investigation, it was determined that this bump is a real effect, not simply a statistical fluctuation. Figure 5.10 shows an efficiency plot for only the ELE1_CEM_8(9)_6 trigger line (ie., events which pass only ELE1_CEM_15 are rejected). The drop in efficiency around 15 GeV was determined to be due to a change in the ELE1_CEM_8(9)_6 trigger instituted during Run 1A. An additional cut of $\chi^2_{wire} < 15.0$ was imposed, presumably to reduce the background at low E_T. Unfortunately, electrons with $E_T \geq 15$ GeV have a high probability of radiating a photon. This process alters the direction of the electron and generates an another nearby EM shower, essentially widening the electron shower. Since this broadening occurs primarily in the azimuthal direction (ie., the direction measured by the wires), the wire position cut becomes less efficient at high E_T. Figure 5.10 demonstrates this behavior. If we change the criteria for a good electron to include $\chi^2_{wire} < 15.0$ and look at the probability of triggering the ELE1_CEM_8(9)_6 line only, the efficiency is flat above 15 GeV (Figure 5.11).

We decided not to include the $\chi^2_{wire} < 15.0$ in our definition of a good electron. Instead, we calculated separately the efficiencies for the two regions $11 < E_T < 16$ GeV and 11 GeV$< E_T$, then averaged these values and assign a systematic error of 1.5% (note that

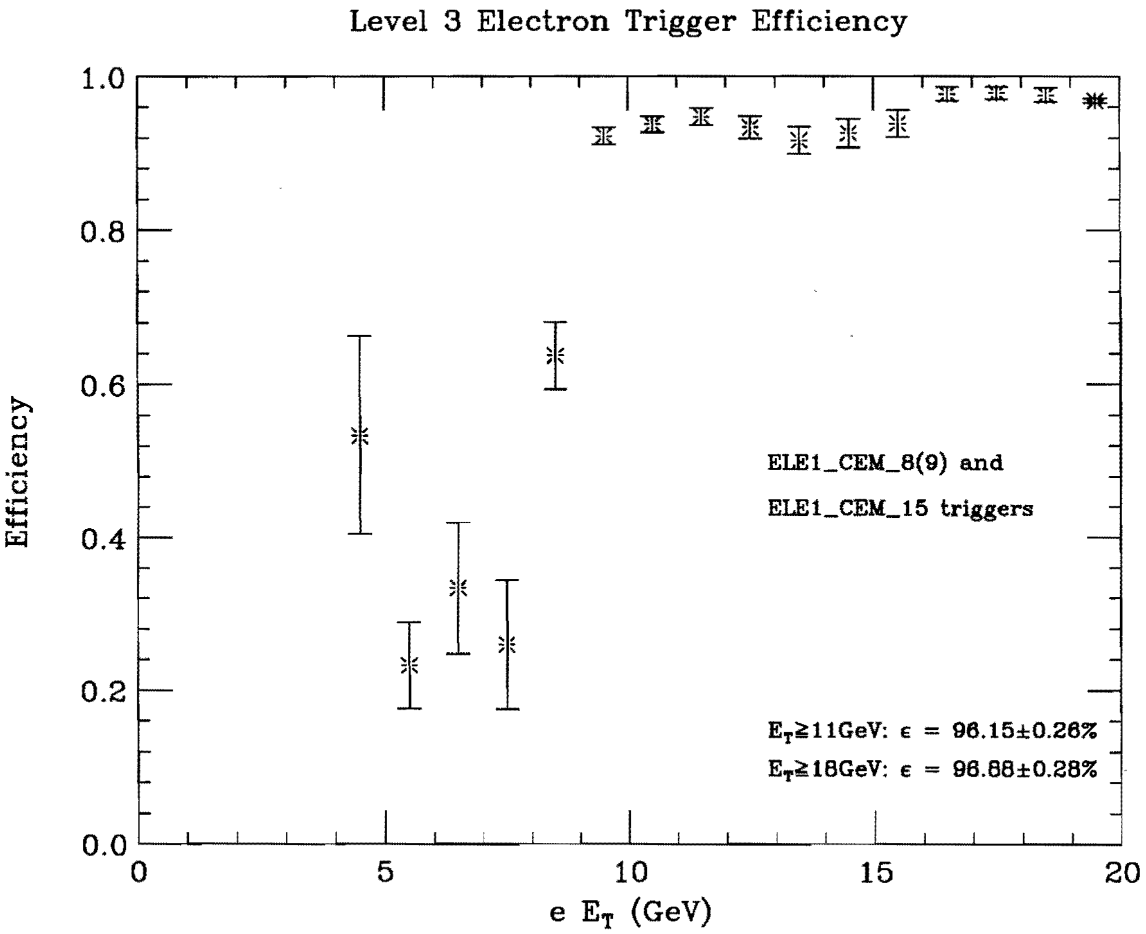

Figure 5.9: Level 3 electron trigger efficiency distribution (1)

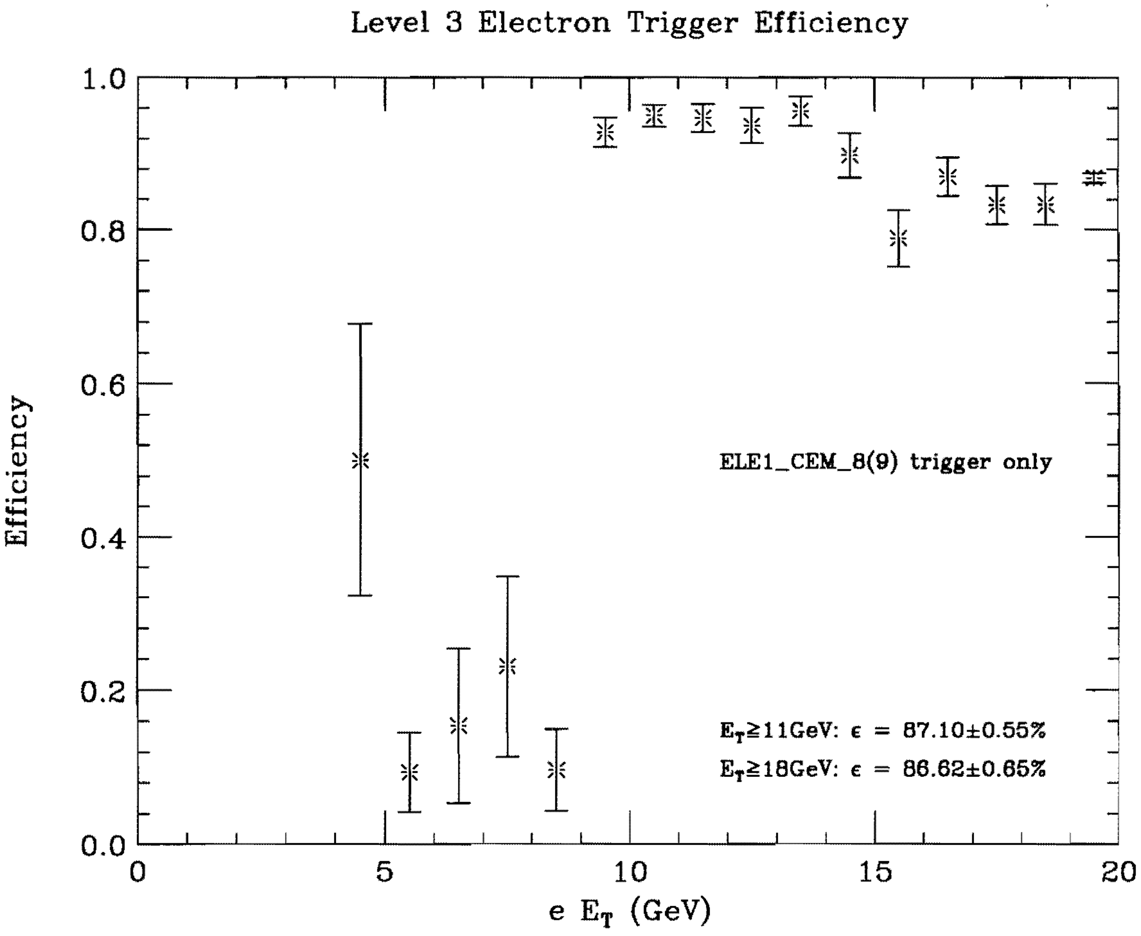

Figure 5.10: Level 3 electron trigger efficiency distribution (2)

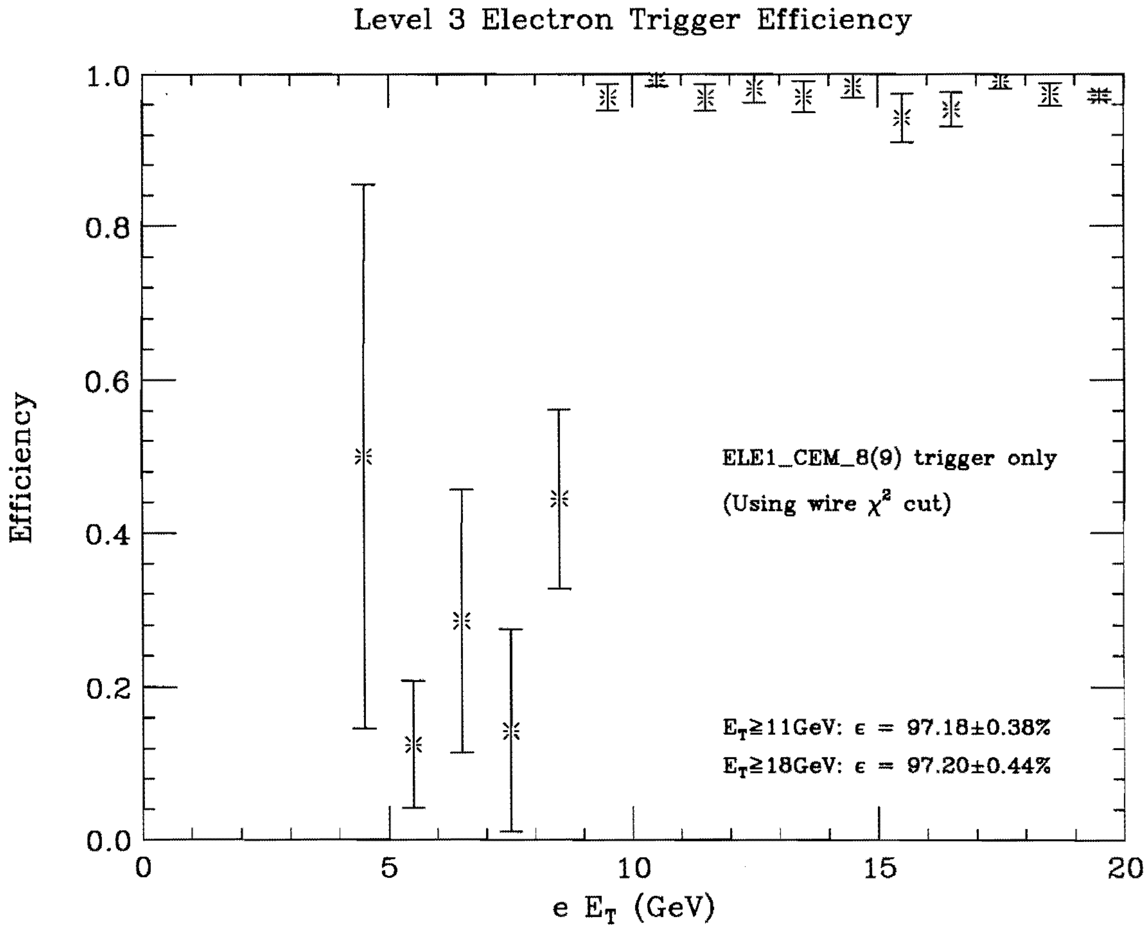

Figure 5.11: Level 3 electron trigger efficiency distribution (3)

the efficiency of 96.15% quoted in figure 5.11 is for the entire range $E_T > 11$ GeV). As a result, level 3 electron efficiency for the trilepton analysis (ie., electron $E_T > 11$ GeV) is 95.2% ±1.5%. By multiplying the Level 1, Level 2, and Level 3 efficiencies, and adding all errors in quadrature, we found the total electron trigger efficiency = 87.73±1.53%.

5.6 Systematic Uncertainties

The total detection efficiency for the trilepton event is affected by the systematic uncertainties associated with each of the efficiency factors. In this section, we describe the sources and the magnitudes of the systematic uncertainties.

5.6.1 Choice of Structure Functions

ISAJET is a leading-order generator, so that we could use either a leading order or a next-to-leading order structure function. We have used the CTEQ2L structure functions throughout the trilepton analysis. We now estimate the systematic uncertainty associated with using the following alternate structure functions: EHLQ set 1, MT, GRV, DO set 1, BM A, MRS S0', MRS D0-', CTEQ2MS, CTEQ2MF, and CTEQ2ML. All of these PDFs(parton distribution functions) are available in the CERN PDFlib library [44].

We have used four different gluino masses (140, 160, 200, and 240 GeV/c^2) for each structure function. These gluino masses correspond (approximately) to $M_{\tilde{\chi}_1^\pm} \approx 45$, 50, 60, and 70 GeV/$c^2$, respectively. Other SUSY parameters have been fixed to the following values: $\tan\beta = 4.0$, $M_{\tilde{q}} = 1.2 M_{\tilde{g}}$, $\mu = -400$ GeV. A summary of the study is presented in Table 5.22.

The maximum positive and negative deviations from ϵ^{tot}(CTEQ2L) do not seem to depend on the gluino mass (hence, the chargino mass). We averaged these deviations over the four gluino mass values and take these averages as the uncertainty of ϵ^{tot} due to the structure functions. Thus,

$$\left(\frac{\Delta\epsilon^{tot}}{\epsilon^{tot}}\right)_{SF} = \begin{cases} +8.17\% \\ -1.80\% \end{cases} \rightarrow \frac{\Delta\sigma}{\sigma} = \begin{cases} -7.6\% \\ +1.8\% \end{cases} \tag{5.26}$$

Table 5.22: Summary of the variation of ϵ^{tot} (%) due to the choice of structure function. The trilepton events were generated with $\tan\beta = 4.0$, $M_{\tilde{q}} = 1.2M_{\tilde{g}}$, and $\mu = -400$ GeV. The symbols H and L indicate the highest and lowest results obtained for a given gluino mass. The maximum positive and negative deviations from ϵ^{tot}(CTEQ2L) are listed at the bottom of the table.

	ϵ^{tot} (%)			
Struc. Func.	$M_{\tilde{g}} = 140$ GeV/c^2	160 GeV/c^2	200 GeV/c^2	240 GeV/c^2
CTEQ 2L (LO)	3.930	5.923	(L) 9.078	12.24
EHLQ set 1 (LO)	4.161	5.991	9.353	12.23
MT (LO)	4.139	6.010	9.383	12.32
GRV (LO)	4.195	(L) 5.776	9.598	12.15
DO set 1 (LO)	(H) 4.272	(H) 6.369	(H) 9.934	12.67
BM A (NLL)	4.162	6.011	9.308	(L) 11.88
MRS S0' (NLL)	4.055	6.209	9.341	12.61
MRS D-' (NLL)	4.152	6.121	9.670	12.28
CTEQ 2M (NLL)	4.041	6.115	9.281	12.39
CTEQ 2MS (NLL)	4.150	6.238	9.716	(H) 13.01
CTEQ 2MF (NLL)	4.018	6.200	9.752	12.29
CTEQ 2ML (NLL)	(L) 3.860	6.166	9.616	12.35
Average	4.095 ± 0.117	6.094 ± 0.160	9.503 ± 0.245	12.37 ± 0.286
RMS (%)	2.86	2.63	2.58	2.31
Upper Deviation (%)	8.70	7.53	9.43	7.03
Lower Deviation (%)	1.78	2.48	0.00	2.94

5.6.2 Systematic Uncertainties in Simulation Corrections

Since α_ℓ^{MC} was determined using ϵ_ℓ^{ISO} and ϵ_ℓ^{ID} as shown in Eqs. 5.9 and 5.10, the uncertainty in w_x (and, thus, in ϵ^{tot}) due to the uncertainties in ϵ_ℓ^{ID} and ϵ_ℓ^{ISO} is already contained in α_ℓ^{MC} (see Eq. 5.2). It is important to bear this in mind when calculating the total systematic error, in order to avoid double counting the contributions from ϵ_ℓ^{ID} and ϵ_ℓ^{ISO}. We now evaluate the uncertainty in ϵ^{tot} due to the uncertainties in ϵ_ℓ^{ID} and ϵ_ℓ^{ISO}.

MC events were analysed with the SUSY trilepton analysis program and the values of ϵ_ℓ^{ISO} and ϵ_ℓ^{ID} were each varied by 1σ. We found that the resulting change in ϵ^{tot} (Eq. 5.1) was only 0.03%. Therefore, we can ignore the lepton ID and ISO efficiencies as individual sources of systematic uncertainty in the cross section. To obtain a conservative estimate, however, we varied α_ℓ^{MC} by 1σ (including the uncertainties due to ϵ^{ID} and ϵ^{ISO}) and calculated the systematic uncertainty in ϵ^{tot} to be ±12.9%. Thus,

$$\left(\frac{\Delta\epsilon^{tot}}{\epsilon^{tot}}\right)_{MC} = \begin{cases} +12.9\% \\ -12.9\% \end{cases} \rightarrow \frac{\Delta\sigma}{\sigma} = \begin{cases} -11.4\% \\ +14.8\% \end{cases} \tag{5.27}$$

5.6.3 Uncertainty in Trigger Efficiency

The trigger efficiencies for single electrons and muons are described in the previous section. We found that the trigger efficiency for electrons (muons) above E_T (P_T) = 11 GeV (11 GeV/c) is flat. The averaged efficiencies for electrons and muons are

$$\epsilon_e^{trig} = 87.73 \pm 1.53\%, \tag{5.28}$$

$$\epsilon_\mu^{trig} = 84.33 \pm 2.30\%. \tag{5.29}$$

In trilepton event analysis, we have to consider the trigger efficiencies for multiple trigger-leptons. In SUSY trilepton events with chargino mass of 40-50 GeV/c^2, the 3rd lepton is very soft ($\approx$ 5 GeV), so that we only need to consider two categories of events: (a) one trigger lepton and (b) two trigger leptons.

In category (a), the worst scenario would be all trilepton events containing one trigger muon. This situation would give a trigger efficiency's uncertainty of 2.7%.

In category (b), the trigger efficiency for the event is:

$$\begin{aligned} \epsilon^{trig} &= 1-(1-\epsilon^{trig}_{\ell_1})\cdot(1-\epsilon^{trig}_{\ell_2}) \\ &= \epsilon^{trig}_{\ell_1}+\epsilon^{trig}_{\ell_2}-\epsilon^{trig}_{\ell_1}\cdot\epsilon^{trig}_{\ell_2} \end{aligned} \tag{5.30}$$

The worse scenario would arise, if all trilepton events have two trigger muons. Thus, with $\ell_1 = \ell_2 = \mu$ in the above equation, we obtain $\epsilon^{trig} = 97.54^{+0.67}_{-0.77}\%$.[1] The corresponding systematic uncertainty in the trigger efficiency is $^{+0.69}_{-0.79}\%$.

We obtain a conservative estimate of the trigger efficiency's uncertainty by assuming that all trilepton events are in case (a). Thus,

$$\frac{\Delta\epsilon^{trig}}{\epsilon^{trig}} = \left\{\begin{array}{l} +2.7\% \\ -2.7\% \end{array}\right. \rightarrow \frac{\Delta\sigma}{\sigma} = \left\{\begin{array}{l} -2.6\% \\ +2.8\% \end{array}\right. \tag{5.31}$$

5.6.4 Uncertainty in Luminosity Measurement

The uncertainty in the luminosity measurement in Run 1A is reported to be 3.6% [45]. Thus,

$$\frac{\Delta\int\mathcal{L}dt}{\int\mathcal{L}dt} = \left\{\begin{array}{l} +3.6\% \\ -3.6\% \end{array}\right. \rightarrow \frac{\Delta\sigma}{\sigma} = \left\{\begin{array}{l} -3.5\% \\ +3.7\% \end{array}\right. \tag{5.32}$$

5.6.5 Summary of Systematic Uncertainties

The summary of the uncertainties is shown in Table 5.23. The total systematic uncertainty was obtained as

$$\frac{\Delta\sigma}{\sigma} = \left\{\begin{array}{l} +15.6\% \\ -14.4\% \end{array}\right. \tag{5.33}$$

The upper limit in the cross section is obtained by adopting 15.6% as the total uncertainty.

---

[1] $99.76 \pm 0.14\%$ if the trilepton event have three trigger muons. The uncertainty is even smaller as the fraction of events is very small.

Table 5.23: Summary of the systematic uncertainties in $\sigma \cdot BR(\tilde{\chi}_1^{\pm}\tilde{\chi}_2^0 \rightarrow 3\ell + X)$.

Source	Uncertainty (%)
Structure Function	$^{+1.8}_{-7.6}$
Simulation Correction	$^{+14.8}_{-11.4}$
Trigger Efficiency	$^{+2.8}_{-2.6}$
Luminosity	$^{+3.7}_{-3.5}$
Total	$^{+15.6}_{-14.4}$

Chapter 6

Background study

The backgrounds for the SUSY trilepton events are expected from two categories of the standard model(SM) processes: (a) $WZ, ZZ, b\bar{b}/c\bar{c}, t\bar{t}$ and (b) Drell-Yan, Z, WW. Each mode in the category (a) can have three or four leptons in its leptonic or semileptonic decays. The modes in category (b) can directly produce only two leptons, but these events can be identified as "trilepton" events if there is an additional "fake" lepton in the event. We define a "fake" lepton as an any miss-identified non-leptonic object or a true lepton which is not originated from the primary processes in the Feynman diagrams.

In this chapter, we first describe the estimate of the fake-lepton's rate using clean W and J/Ψ samples. The background, expected in our sample, are then estimated using ISAJET V7.06 and QFL V3.48 with the MC correction factors determined in Chapter 5.

6.1 Fake Lepton's Rate

Non trilepton events can be classified as trilepton events with a presence of a fake lepton. For example, in a $p\bar{p} \rightarrow Z(\rightarrow \ell\ell) + X$ event, it can happen that we classify the event as a trilepton event, if we miss-identify a hadron or detect a real lepton from the decays of heavy flavour quarks (which were produced by gluon radiation and subsequent splitting as a 3rd lepton). In this scenario, we may thus erroneously identify this Z event as a SUSY trilepton event.

In order to estimate the fake's rate, we analyzed two data samples: $W \rightarrow \ell\nu$ and $J/\Psi \rightarrow \mu\mu$. The advantage of using W events is that the Q^2 values of W events are large enough to simulate the high Q^2 environment expected in high mass DY, Z, and diboson events. We can also check the fake's rate for lower Q^2 events (*e.g.*, $b\bar{b}/c\bar{c}$ events) using J/Ψ events.

In the following two subsections, we present our estimate of the fake's rate from the two samples.

6.1.1 Fake Lepton's Rate using $W \rightarrow \ell\nu$ sample

Our $W^{\pm} \rightarrow \ell^{\pm}\nu$ sample is a subset of the inclusive high-P_T lepton data (50,850 events) from Run 1A express data set. We selected well identified W's by requiring a good lepton with $P_T > 20$ GeV/c, $\not{E}_T \geq 20$GeV, and the transverse mass of the lepton-$\not{E}_T$ system to be between 40 and 100 GeV/c^2.

The selection criteria for good high-P_T muons are:

- CTC track matched with the CMU or CMP hit,
- $P_T > 20$ GeV/c,
- Impact parameter $\delta_0 < 0.2$ cm,
- $|Z_{vertex} - Z_{track}| < 5.0$ cm,
- E(EM tower) < 2 GeV,
- E(HAD tower) < 6 GeV,
- E(EM+HAD) > 0.1 GeV,
- CMU $|\Delta X| < 2.0$ cm or CMP $|\Delta X| < 5.0$ cm.

The selection criteria for good high-E_T electrons are:

- EM cluster within a fiducial volume of the CEM detector with a 3-D CTC track,
- $E_T > 20$ GeV,
- $P_T > 13$ GeV/c,

Table 6.1: Events in clean W sample used for the study of the fake lepton's rate

Category	# of events
# of analyzed events	50850
# of W candidate events	21266
# of $W \rightarrow e\overline{\nu}_e$	13272
# of $W \rightarrow \mu\overline{\nu}_\mu$	7994
# of $W^- \rightarrow e^-\overline{\nu}_e$	6795
# of $W^+ \rightarrow e^+\nu_e$	6477
# of $W^- \rightarrow \mu^-\overline{\nu}_\mu$	3902
# of $W^+ \rightarrow \mu^+\nu_\mu$	4092

- $E/P < 1.5$,
- E(HAD tower)/E(EM tower) < 0.05,
- $LSHR < 0.2$,
- $\chi^2_{strip} < 10.0$,
- $|dx| < 1.5$ cm,
- $|dz| < 3.0$ cm,
- $ISO(0.4)/E_T < 0.1$,
- Not a conversion (using C$ELE:CONVERT).

If the event has additional leptons, the invariant mass of the any pairs of the leptons(ee or $\mu\mu$) was calculated. If the mass is within the Z^0 mass window (75-105 GeV/c^2), we removed the event from this sample. The total number of W events was 21,266 events (13,272 $W \rightarrow e\nu$ and 7,994 $W \rightarrow \mu\nu$). Our W events are summarized in Table 6.1.

The fake's rate is defined as:

$$f_\ell = \frac{\text{Number of leptons other than the } W \text{ leptons found in the } W \text{ Sample}}{\text{Number of } W \text{ events}}$$

where the additional lepton must pass our loose quality cuts (*i.e.*, ordinary lepton cuts) with $P_T > 4$ GeV/c for muons and $E_T > 5$ GeV for electrons. In order to reduce the

Table 6.2: Summary of fake's lepton rates from the W sample.

Event Type	Fake Type	# of Events	Fake's Rate (%)
$W^- \to e^- \overline{\nu}_e$	CMUO μ^-	2/6795	0.0294±0.0208
$W^- \to e^- \overline{\nu}_e$	CMUO μ^+	9/6795	0.1325±0.0401
$W^+ \to e^+ \nu_e$	CMUO μ^-	1/6477	0.0154±0.0154
$W^+ \to e^+ \nu_e$	CMUO μ^+	0/6477	<0.0463 (95% CL)
$W^- \to \mu^- \overline{\nu}_\mu$	CMUO μ^-	1/3902	0.0256±0.0256
$W^- \to \mu^- \overline{\nu}_\mu$	CMUO μ^+	9/3902	0.2307±0.0768
$W^+ \to \mu^+ \nu_\mu$	CMUO μ^-	9/4092	0.2199±0.0732
$W^+ \to \mu^+ \nu_\mu$	CMUO μ^+	2/4092	0.0489±0.0346
$W^\pm \to (e\nu_e$ or $\mu\nu_\mu)$	Total CMUO	33/21266	0.1552±0.0270
$W^\pm \to (e\nu_e$ or $\mu\nu_\mu)$	Total CMIO	1/21266	0.0047±0.0047
$W^- \to e^- \overline{\nu}_e$	CEM e^-	0/6795	<0.0442 (95% CL)
$W^- \to e^- \overline{\nu}_e$	CEM e^+	3/6795	0.0442±0.0235
$W^+ \to e^+ \nu_e$	CEM e^-	5/6477	0.0772±0.0345
$W^+ \to e^+ \nu_e$	CEM e^+	0/6477	<0.0463 (95% CL)
$W^- \to \mu^- \overline{\nu}_\mu$	CEM e^-	0/3902	<0.0769 (95% CL)
$W^- \to \mu^- \overline{\nu}_\mu$	CEM e^+	2/3902	0.0513±0.0362
$W^+ \to \mu^+ \nu_\mu$	CEM e^-	0/4092	<0.0733 (95% CL)
$W^+ \to \mu^+ \nu_\mu$	CEM e^+	1/4092	0.0244±0.0244
$W^\pm \to (e\nu_e$ or $\mu\nu_\mu)$	Total CEM	11/21266	0.0517±0.0156
$W^\pm \to (e\nu_e$ or $\mu\nu_\mu)$	Total PEM	13/21266	0.0611±0.0169
$W^\pm \to (e\nu_e$ or $\mu\nu_\mu)$	Total e or μ	58/21266	0.2727±0.0358

contaminations from undetected $Z \to \ell\ell$ events (where one of the leptons can be outside the detector fiducial volume), we do not include the muons (electrons) with $P_T > 20$ GeV/c ($E_T > 20$ GeV) in our fake lepton's sum.

The fake rates have been determined for each lepton type, as shown in Table 6.2.

A few remarks about our results are:

- The fake's rate for CMIO is negligible because the P_T cut is 10 GeV/c.
- PEM electrons were selected without any determination of the electric charge because of the poor tracking performance in the plug region.
- Some charge and flavor correlations are evident. For example, larger fake rates are

obtained in the case of unlike sign ee or $\mu\mu$ pairs (*e.g.*, $W^+ \to e^+\nu$ plus CEM e^-), compared to same sign pairs. These could be explained by contamination from other SM processes (Z, Drell-Yan, WW, WZ, ZZ, *etc.*). If the fake-lepton's rate were estimated only from same-sign and/or opposite-flavor pairs, the fake's rate would be substantially reduced. However, we have taken a more conservative approach by simply comparing the number of all fake leptons found to the total number of W events. The total fake rate is, thus, 0.273±0.036%.

6.1.2 Fake Lepton's Rate using $J/\Psi \to \ell\ell$ sample

The estimate of the fake lepton's rate in the $J/\Psi \to \ell\ell$ events was essentially the same as in the $W \to \ell\nu$ events. Our J/Ψ events are selected such that two leptons (e^+e^- or $\mu^+\mu^-$) pass our tight cuts and the invariant mass of the two leptons must be between 2.9 and 3.3 GeV/c^2.

The selection criteria for the tight electrons are:

- EM cluster within a fiducial volume of the CEM detector with a 3-D CTC track,
- $0.75 < E/P < 1.5$,
- $E(\text{HAD tower})/E(\text{EM tower}) < 0.04$,
- $LSHR < 0.2$,
- $\chi^2_{strip} < 10.0$,
- $|dx| < 1.5$ cm,
- $|dz| < 3.0$ cm,
- Not a conversion (using C$ELE:CONVERT)

The selection criteria for the tight muons are:

- CTC track matched with the CMU or CMP hit,
- Impact parameter $\delta_0 < 0.2$ cm,

Table 6.3: Fake lepton's rates in the $J/\Psi \rightarrow \mu\mu$ events.

Fake type	# of events	Fake's rate (%)
CMUO μ	142/62912	0.226±0.019
CMIO μ	3/62912	0.0048±0.0028
CEM e	11/62912	0.0175±0.0053
PEM e	22/62912	0.0350±0.0075
Total e or μ	178/62912	0.283±0.021

- $|Z_{vertex} - Z_{track}| < 2.0$ cm,
- E(EM tower) < 1.5 GeV,
- E(HAD tower) < 4.0 GeV,
- E(EM+HAD tower) > 0.1 GeV,
- CMU $\chi^2_x < 6.0$ and $\chi^2_z < 8.0$,
- CMP $\chi^2_x < 6.0$.

A total of 62,912 $J/\Psi \rightarrow \mu\mu$ and 58 $J/\Psi \rightarrow ee$ events were found. We used only the $J/\Psi \rightarrow \mu\mu$ events for this study because of the poor statistics in the $J/\Psi \rightarrow ee$ sample.

We then searched for additional leptons in the J/Ψ events. The leptons must pass our ordinary lepton cuts with $ISO < 2.0$ GeV, as in the study with the W sample. We found the fake lepton's rate in the J/Ψ events to be 0.283±0.021% (see Table 6.3). It should be noted that this rate is consistent with the fake's rate estimated using the W sample. Thus, the fake's lepton rates are same for the events in two different Q^2 regimes.

6.1.3 Summary of the Fake-rate Study

We have determined the fake-lepton's rate using well identified $W \rightarrow \ell\nu$ and $J/\Psi \rightarrow \mu\mu$ events. The fake's rates are measured to be $0.273 \pm 0.036\%$ and $0.283 \pm 0.021\%$ for the W and J/Ψ samples, respectively. It should be noted that these numbers are consistent with each other. Therefore, we concluded that the fake's rate is independent of the physics process. Our combined fake rate is then 0.280±0.018%.

6.2 Monte Carlo Background Studies

The size of the SM background has been estimated using Monte Carlo simulation. The events were generated with ISAJET V7.06 [17] with CTEQ 2L structure functions [44], and the top quark mass was set to 170 GeV/c^2. The detector simulation was performed with QFL V3.48 in the offline version 7.10. We have performed extensive tests of the QFL-simulated analysis variables and determined the correction factors for lepton acceptance. For example, the distributions of ISO in data and simulation are similar but not identical. The data and simulation's lepton efficiencies are consistent for $ISO < 4$ GeV, but the efficiencies for $ISO < 2$ GeV are not. Thus, we have performed event selection using an $ISO < 4$ GeV cut in our simulations, and later apply a correction to obtain the efficiency for $ISO < 2$ GeV (which is the cut we used for the real data). In particular, the PEM isolation distribution in QFL/OFFLINE was markedly different from that in the real data.

6.2.1 Drell-Yan process

Drell-Yan events ($p\overline{p} \rightarrow \gamma^* \rightarrow \ell^+\ell^-$) were generated for $15 < M_{\gamma^*} < 120$ GeV/c^2, without the inclusion of higher order terms. Decreasing the lower limit of M_{γ^*} did not change our results. Z^0 events were generated for $50 < M_{Z^0} < 130$ GeV/c^2.

The background expectation in 19.11 pb^{-1} is expressed in the formula:

$$N_{\text{DYor }Z} = \sigma_{\text{DYor }Z} \cdot BR \cdot \epsilon_{\ell\ell}^{tot} \cdot f_\ell \cdot \int \mathcal{L}dt$$

where, ($\epsilon_{\ell\ell}^{tot}$) is the dilepton detection efficiency and (f_ℓ) is our estimate of the fake-lepton's rate. The production cross sections are given by the previous CDF measurements $\sigma \cdot BR(p\overline{p} \rightarrow Z^0 \rightarrow e^+e^-) = 231$ pb [39] and $\sigma(p\overline{p} \rightarrow \gamma^* \rightarrow e^+e^-) = 400$ pb [46] (within the mass range $25 < M_{e^+e^-} < 120$ GeV/c^2).

The total detection efficiency ($\epsilon_{\ell\ell}^{tot}$) for dilepton events is defined in the same manner as in our trilepton analysis, namely, the event weight was calculated on an event by event basis:

$$\epsilon_{\ell\ell}^{tot} = \frac{\sum_x w_x \mathcal{A}_x^{MC}}{N_{gen}}.$$

However, the definitions of w_x and $\mathcal{A}_x^{MC}$ are different from the trilepton case:

$$\begin{aligned} w_x &= \text{weight for } x\text{-th event } = \alpha_{\ell\ell}^{MC} \cdot \epsilon_{\ell\ell}^{ISO} \cdot \epsilon_{\ell\ell}^{ID} \cdot \epsilon_{\ell\ell}^{trig} \\ \mathcal{A}_x^{MC} &= 1 \text{ if the dilepton event is accepted (0 otherwise)} \end{aligned}$$

where

$$\begin{aligned} \alpha_{\ell\ell}^{MC} &= \text{Correction factor to the MC acceptance for dileptons} \\ \epsilon_{\ell\ell}^{ISO} &= \text{Isolation efficiency } (ISO < 2 \text{ GeV}) \text{ for dileptons} \\ \epsilon_{\ell\ell}^{ID} &= \text{Lepton ID Efficiency for dileptons} \\ \epsilon_{\ell\ell}^{trig} &= \text{Trigger efficiency for dileptons} \end{aligned}$$

In the $\gamma^*/Z^0 \to \tau\tau$ events, we forced each τ to decay into an e or μ before the detector simulation. The branching ratio, $BR(\tau \to \ell;\ \ell = e \text{ or } \mu)$, was set to 0.355. We summarize the total detection efficiency for each mode below.

Process	Decay Mode	BR	N_{gen}	ϵ^{tot}	f_ℓ	# events
$\gamma \to \ell^+\ell^-$		1	20031	1.38×10^{-2}	2.80×10^{-3}	0.591
$\gamma \to \tau\tau$	$\tau\tau \to \ell^+\ell^-$	0.126	8816	1.49×10^{-3}	2.80×10^{-3}	4.02×10^{-3}
$Z^0 \to \ell^+\ell^-$		1	23903	3.91×10^{-3}	2.80×10^{-3}	9.67×10^{-2}
$Z^0 \to \tau\tau$	$\tau\tau \to \ell^+\ell^-$	0.126	10253	2.70×10^{-2}	2.80×10^{-3}	4.20×10^{-2}
Total						0.734

It should be noted that the value of $\epsilon_{\ell\ell}^{tot} \cdot f_\ell$ is slightly overestimated for the probability of seeing trilepton events from Drell-Yan and Z events, because the $\Delta R_{\ell\ell}$ and $|\mathrm{Q}_1+\mathrm{Q}_2+\mathrm{Q}_3|$ cuts used in the trilepton analysis are not applied for the 3rd lepton. We take these conservative numbers as our final estimate.

6.2.2 Diboson Events

Diboson events are generated with ISAJET V7.06 ($10 < P_T^{W \text{ or } Z} < 300$ GeV/c). For $Z^0 \to \tau\tau$ and $W \to \tau\nu$ events, we force each τ to decay into an e or μ before the detector simulation. The branching ratio, $BR(\tau \to \ell;\ \ell = e \text{ or } \mu)$, is set to 0.355.

$Z^0 + W$ event

The topology of $W + Z^0 \to \ell^\pm\nu\ell^\pm\ell^\mp$ events is expected to be similar to that of SUSY trilepton events ($\tilde{\chi}_1^\pm\tilde{\chi}_2^0$): three isolated leptons with minimal jet activity. We have one

$WZ^0 \rightarrow eee$ event candidate in Run 1A data. Figure 6.1 shows the event display and figure 6.2 shows the lego plot for the CDF $Z^0W \rightarrow eee$ event. We rejected most of this background by vetoing events with an unlike-sign dilepton mass in the Z^0 mass window (75-105 GeV/c^2).

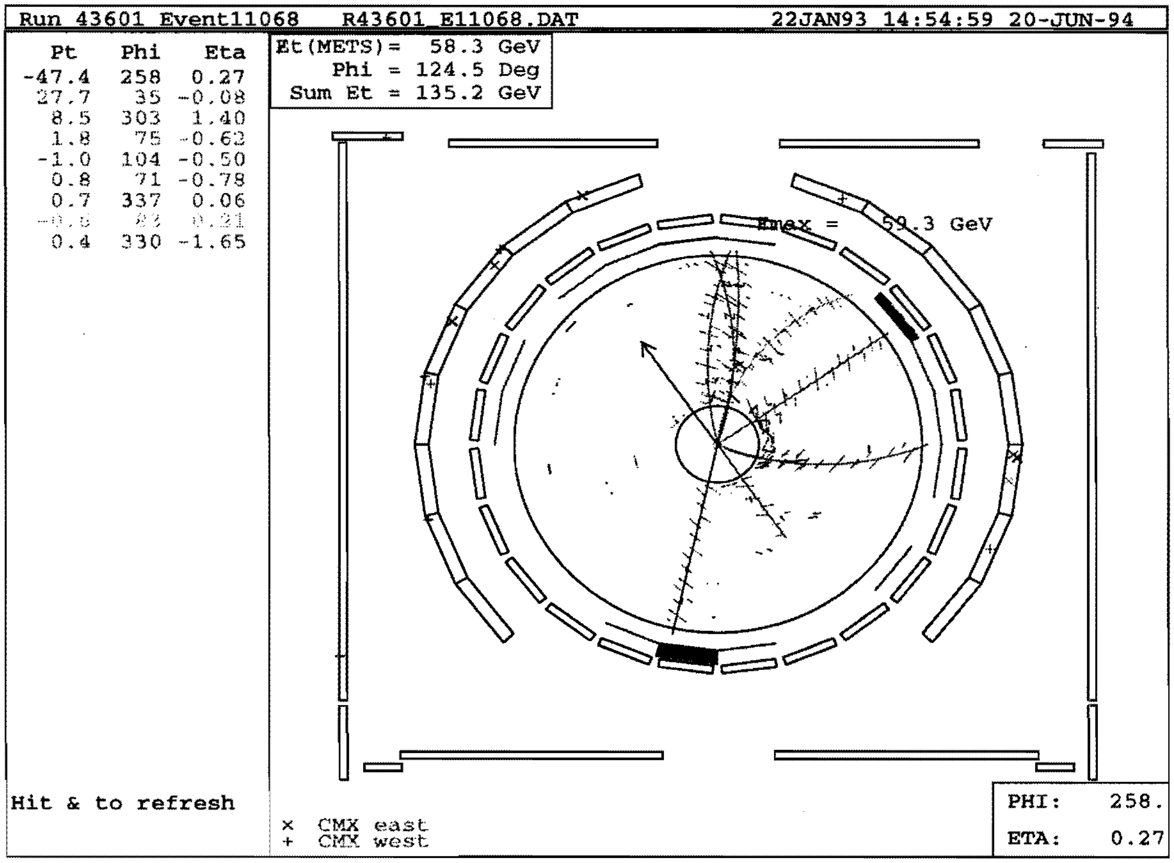

Run 43601 Event11068 R43601_E11068.DAT 22JAN93 14:54:59 20-JUN-94

Pt	Phi	Eta
-47.4	258	0.27
27.7	35	-0.08
8.5	303	1.40
1.8	75	-0.62
-1.0	104	-0.50
0.8	71	-0.78
0.7	337	0.06
-0.6	83	0.21
0.4	330	-1.65

Et(METS) = 58.3 GeV
Phi = 124.5 Deg
Sum Et = 135.2 GeV

Hit & to refresh

PHI: 258.
ETA: 0.27

Figure 6.1: The event display of the $Z^0W \rightarrow eee$ event in Run 1A

The background contribution in 19.11 pb^{-1} was calculated as follows:

$$N_{WZ} = \sigma_{WZ} \cdot BR \cdot \epsilon_{3\ell}^{tot} \cdot \int \mathcal{L}dt.$$

The production cross section for WZ^0 was taken as 2.5 pb [47, 48], and the total detection efficiency ($\epsilon_{3\ell}^{tot}$) was calculated in the same manner as in the SUSY trilepton analysis.

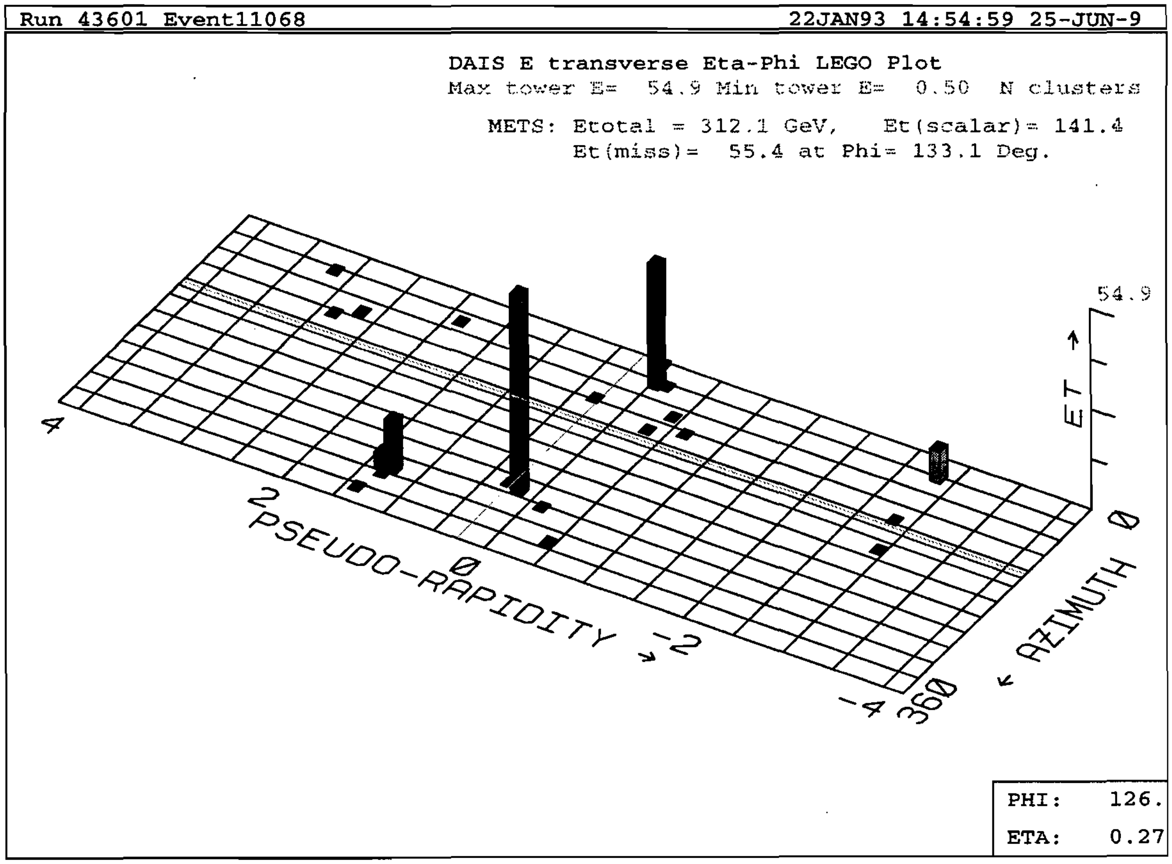

```
Run 43601 Event11068                              22JAN93 14:54:59 25-JUN-9

                        DAIS E transverse Eta-Phi LEGO Plot
                        Max tower E=  54.9 Min tower E=  0.50  N clusters

                          METS: Etotal = 312.1 GeV,   Et(scalar)= 141.4
                                Et(miss)=  55.4 at Phi= 133.1 Deg.

                                                           PHI:    126.
                                                           ETA:    0.27
```

Figure 6.2: The lego plot of the $Z^0W \rightarrow eee$ event in Run 1A

The efficiencies and yields for all possible WZ^0 background modes are listed below:

Process	Decay Mode	BR	N_{gen}	ϵ^{tot}	# events
WZ^0	$\ell\nu_\ell\ell^+\ell^-$	1.40×10^{-2}	31053	3.31×10^{-3}	2.21×10^{-3}
WZ^0	$\tau\nu_\tau\ell^+\ell^- \rightarrow \ell\ell\ell$	2.51×10^{-3}	51705	2.18×10^{-3}	2.61×10^{-4}
WZ^0	$\ell\nu_\ell\tau^+\tau^- \rightarrow \ell\ell\ell$	8.79×10^{-4}	7706	3.49×10^{-2}	1.47×10^{-3}
WZ^0	$\tau\nu_\tau\tau^+\tau^- \rightarrow \ell\ell\ell$	1.57×10^{-4}	9848	2.72×10^{-2}	2.04×10^{-4}
Total					4.15×10^{-3}

$Z^0 + Z^0$ event

Production and decay of $p\bar{p} \rightarrow Z^0 + Z^0 \rightarrow \ell^+\ell^-\ell^+\ell^-$ events can also be a source of trilepton background. Thus, we have studied Z^0Z^0 events in the same manner as in the WZ^0 analysis: we required the dilepton mass to be outside the Z^0 mass window. A Z^0Z^0 production cross section of 1.0 pb [47, 48] was used in our calculations.

The total detection efficiency was determined in the same manner as in the SUSY analysis. We found:

Process	Decay Mode	BR	N_{gen}	ϵ^{tot}	# events
Z^0Z^0	$\ell^+\ell^-\ell^+\ell^-$	4.46×10^{-3}	52901	5.28×10^{-3}	4.50×10^{-4}
Z^0Z^0	$\ell^+\ell^-\tau^+\tau^- \rightarrow \ell\ell\ell\ell$	2.79×10^{-4}	6617	4.28×10^{-2}	2.28×10^{-4}
Z^0Z^0	$\tau^+\tau^-\tau^+\tau^- \rightarrow \ell\ell\ell\ell$	1.75×10^{-5}	3216	8.64×10^{-2}	2.89×10^{-5}
Total					7.07×10^{-4}

$W + W$ event

$W + W \rightarrow \ell\nu_\ell\ell\nu_\ell$ events can also be a background in the SUSY trilepton analysis if two isolated leptons from the W decays are detected, along with a 3rd fake-lepton. The production cross section for WW was taken to be 9.5 pb [47, 48]. The following three modes of WW events were analyzed in the same manner as in the DY/Z^0 analysis: $WW \rightarrow \ell\nu_\ell\ell\nu_\ell$, $WW \rightarrow \ell\nu_\ell\tau\nu_\tau$, and $WW \rightarrow \tau\nu_\tau\tau\nu_\tau$.

The estimation of the total dilepton detection efficiencies and trilepton yields for these modes are shown below:

Process	Decay Mode	BR	N_{gen}	ϵ^{tot}	f_ℓ	# events
WW	$\ell\nu_\ell\ell\nu_\ell$	4.41×10^{-2}	3551	1.70×10^{-1}	2.80×10^{-3}	3.81×10^{-3}
WW	$\ell\nu_\ell\tau\nu_\tau \rightarrow \ell\ell$	8.21×10^{-3}	5372	1.05×10^{-1}	2.80×10^{-3}	4.38×10^{-4}
WW	$\tau\nu_\tau\tau\nu_\tau \rightarrow \ell\ell$	1.47×10^{-3}	7628	7.47×10^{-2}	2.80×10^{-3}	5.58×10^{-5}
Total						4.30×10^{-3}

Summary of Diboson Events:

The total expected number of background trilepton events from diboson production in 19.11 pb^{-1} is 9.2×10^{-3}.

6.2.3 $b\bar{b}$ and $c\bar{c}$ event

Rejection of leptons from semileptonic b or c decays depends heavily on the isolation cut. While in the ISO distribution, two major sources of backgrounds are: (a) underlying particles/detector noise and (b) fragmentation and decay products from b/c-decays.

We have looked into the ISO distribution for (a) in Section 5.1. QFL does not agree with the data for the PEM isolation distribution below 2 GeV. The QFL efficiency for $ISO < 2$ GeV is higher than the data (see Table 5.1), which was most likely caused by the PEM detector's noise in the real data. The efficiency for $ISO < 0.5$ GeV in the QFL for the PEM was 83.4%, which it was almost the same as the efficiency for $ISO < 2$ GeV in the data (79.2%). Thus, analysing QFL events with $ISO < 2$ GeV will give us an overestimate of the PEM electron detection efficiency, hence, an overestimate of the background.

As for (b), the ISAJET fragmentation was checked with and without the CLEO QQ Monte Carlo. We found no significant difference in the energy flow distribution around the lepton from the b decay. Thus, our MC sample was generated without CLEO QQ in order to save CPU time.

A huge MC sample of $b\bar{b}/c\bar{c}$ events was generated for background studies in SUSY analyses [49]. The events were generated and simulated with ISAJET and QFL for three different processes: direct production, initial state gluon splitting, and final state gluon splitting (in three different P_T ranges). Each event in the MC sample contains at least two leptons (either muon or electron). One lepton must have $P_T > 9.0$ GeV/c in $|\eta| < 1.5$, and the other lepton must have $P_T > 2.8$ GeV/c in $|\eta| < 3.0$. These cuts guarantee full efficiency for gold leptons (≥ 11 GeV/c) and ordinary leptons (≥ 4 GeV/c).

The $b\bar{b}/c\bar{c}$ events were analyzed by imposing $ISO < 2$ GeV instead of $ISO < 4$ GeV (as was used in the trilepton analysis of the real data). It should be noted that we set

$\epsilon_\ell^{ISO} = 1$ for all lepton types (CEM, PEM, CMU/CMP, CMX, CMIO).

Below is a summary of the expected contribution from $b\bar{b}/c\bar{c}$ events in 19.11 pb^{-1}. The total expected $b\bar{b}/c\bar{c}$ contribution was 1.15 events.

Process	p_T range (GeV/c)	$\sigma(b\bar{b}/c\bar{c} \to \ell\ell)$ (pb)	$\int \mathcal{L}dt$ (pb^{-1})	ϵ^{tot}	# events
Direct	10 - 25	1278.0	51.76	8.268×10^{-6}	0.202
	25 - 50	1125.7	106.6	6.096×10^{-6}	0.131
	50 - 500	190.3	105.1	0.0	0.0
Initial state	10 - 25	765.1	104.6	0.0	0.0
	25 - 50	105.5	757.1	0.0	0.0
	50 - 500	120.2	167.0	0.0	0.0
Final state	15 - 25	242.1	82.6	0.0	0.0
	25 - 50	1647.3	86.2	2.236×10^{-5}	0.704
	50 - 500	914.9	109.3	6.358×10^{-6}	0.111
Total					1.15

6.2.4 $t\bar{t}$ event

The $t\bar{t}$ event could be a background in the SUSY trilepton analysis if we detect two leptons from W boson decays and another lepton from b decays. Since the CDF measurement of the top-quark mass is $176 \pm 8 \pm 10$ GeV/c^2 and the production cross section is $6.8^{+3.6}_{-2.4}$ pb [50], we used $M_{top} = 170$ GeV/c^2 and $\sigma_{t\bar{t}} = 7$ pb in our study.

A total of 20000 $t\bar{t}$ MC events were generated for the background studies in SUSY analysis [49]. The events were generated and simulated by ISAJET and QFL.

We took the two ways for the background estimation. One was the same way as for the Drell-Yan process and the another is same as the $b\bar{b}/c\bar{c}$. And we required either two leptons or three leptons in the events in both methods. Since the leptons in $t\bar{t}$ events are made from W decays and the heavy quark decays, we considered the both effects. The detection efficiencies from the both estimations are,

- From the Drell-Yan estimation.
  - 3 leptons required in the event: $\epsilon^{tot} = 1.97 \times 10^{-4}$
  - 2 leptons and a fake lepton required in the event: $\epsilon^{tot} = 7.45 \times 10^{-3}$

- From the $b\bar{b}/c\bar{c}$ estimation.
  - 3 leptons required in the event: $\epsilon^{tot} = 3.64 \times 10^{-5}$
  - 2 leptons and a fake lepton required in the event: $\epsilon^{tot} = 6.09 \times 10^{-3}$

From the above, the ϵ^{tot}'s from the both methods are similar for the 2 leptons + a fake lepton in the event. Since the two leptons from W in top decays are well isolated, these leptons can be survived from the both selections. We found there was no difference between the Drell-Yan estimation and the $b\bar{b}/c\bar{c}$ estimation for the lepton from the boson decay. Since one lepton out of three in the $t\bar{t}$ event comes from b-quark decay, we took the $t\bar{t}$ background rate as the value from the $b\bar{b}/c\bar{c}$ estimation with the 3 leptons required.

The total acceptance for $t\bar{t}$ trilepton events and the total number of background events expected in 19.11 pb^{-1} were calculated in the same manner as in the SUSY trilepton analysis:

Process	Decay Mode	N_{gen}	ϵ^{tot}	# events
$t\bar{t}$	All	20000	3.64×10^{-5}	4.87×10^{-3}

6.2.5 Summary of background study

The grand total of all expected Standard Model backgrounds in 19.11 pb^{-1} was 1.9 events (see Table 6.4). This estimate is consistent with our observation of zero events.

The main background source is $b\bar{b}/c\bar{c}$ event. Since the isolation distribution of the lepton from the heavy quark decay is different from other leptons, the isolation cut efficiency for the heavy quark lepton is overestimated for our analysis. Thus, our estimation of the Standard Model background for SUSY trilepton events was less than 1.90 events.

Table 6.4: Expected SUSY trilepton backgrounds in Run 1A data sample (19.11 pb^{-1}). All τ's are forced to decay to e or μ.

Physics Process	σ [pb]	BR	ϵ^{tot}	Fake Rate	# events
DY $\gamma \to \ell\ell$	800	1.0	1.38×10^{-2}	2.80×10^{-3}	5.91×10^{-1}
DY $\gamma \to \tau\tau$	400	1.26×10^{-1}	1.49×10^{-3}	2.80×10^{-3}	4.02×10^{-3}
DY $Z^0 \to \ell\ell$	462	1.0	3.91×10^{-3}	2.80×10^{-3}	9.67×10^{-2}
DY $Z^0 \to \tau\tau$	231	1.26×10^{-1}	2.70×10^{-2}	2.80×10^{-3}	4.20×10^{-2}
$WZ \to \ell\nu_\ell\ell^+\ell^-$	2.5	1.40×10^{-2}	3.31×10^{-3}	–	2.21×10^{-3}
$WZ \to \tau\nu_\tau\ell^+\ell^-$	2.5	2.51×10^{-3}	2.18×10^{-3}	–	2.61×10^{-4}
$WZ \to \ell\nu_\ell\tau^+\tau^-$	2.5	8.79×10^{-4}	3.49×10^{-2}	–	1.47×10^{-3}
$WZ \to \tau\nu_\tau\tau^+\tau^-$	2.5	1.57×10^{-4}	2.72×10^{-2}	–	2.04×10^{-4}
$ZZ \to \ell^+\ell^-\ell^+\ell^-$	1.0	4.46×10^{-3}	5.28×10^{-3}	–	4.50×10^{-4}
$ZZ \to \ell^+\ell^-\tau^+\tau^-$	1.0	2.79×10^{-4}	4.28×10^{-2}	–	2.28×10^{-4}
$ZZ \to \tau^+\tau^-\tau^+\tau^-$	1.0	1.75×10^{-5}	8.64×10^{-2}	–	2.89×10^{-5}
$WW \to \ell\nu\ell\nu$	9.5	4.41×10^{-2}	1.70×10^{-1}	2.80×10^{-3}	3.81×10^{-3}
$WW \to \tau\nu\ell\nu$	9.5	8.21×10^{-3}	1.05×10^{-1}	2.80×10^{-3}	4.38×10^{-4}
$WW \to \tau\nu\tau\nu$	9.5	1.47×10^{-3}	7.47×10^{-2}	2.80×10^{-3}	5.58×10^{-5}
$b\bar{b}, c\bar{c}$ direct					3.33×10^{-1}
$b\bar{b}, c\bar{c}$ initial gluon					0.0 (negligible)
$b\bar{b}, c\bar{c}$ final gluon					8.15×10^{-1}
$t\bar{t}$	7.0		3.64×10^{-5}		4.87×10^{-3}
Total					1.90

Chapter 7

Results

We found zero trilepton event as a result of our analysis in the Run 1A. Then we estimated the systematic errors and the number of expected background events in the previous chapters.

Based on the observation of zero trilepton event, we set a 95% confidence level (CL) upper limit of 3.11 events on the mean number of events after the total systematic uncertainty of 15.6% was convoluted (as a Gaussian smearing) with a Poisson distribution. We can exclude the regions in the MSSM parameter space, if:

$$\sigma \cdot BR(\tilde{\chi}_1^{\pm}\tilde{\chi}_2^0 \rightarrow 3\ell + X) \cdot \epsilon^{tot} \cdot \int \mathcal{L}dt \quad > \quad N_{95\%\mathrm{CL}} \tag{7.1}$$

where $N_{95\%\mathrm{CL}} = 3.11$.

Then, we can place the mass limits on $\tilde{g}$, $\tilde{q}$, $\tilde{\chi}_1^{\pm}$, and $\tilde{\chi}_2^0$, in the specific MSSM parameter space. In this chapter, we describe the result of the MSSM parameter scanning and the estimation of the excluded region in the MSSM space.

7.1 Search for the Effective MSSM space in the Analysis

The combination of 5 parameters (μ, $\tan\beta$, $\mathrm{m}_{\tilde{g}}$, m_H, m_t) forms the MSSM space in ISAJET v7.06. It is un-realistic to scan the whole space formed by them. Since we have the $\int \mathcal{L}dt = 19.11 pb^{-1}$ data in the $p\overline{p}$ collisions at $\sqrt{s} = 1.8$ TeV, there is a little space that we can explore at this time in this huge space. Hence, we selected the most effective regions in the space for our exploring.

To determine the exclude region, we needed to estimate the production cross-section, the branching ratio, and the detection efficiency for the $p\overline{p} \rightarrow \tilde{\chi}_1^{\pm}\tilde{\chi}_2^0 \rightarrow 3\ell$ process at a particular point in the MSSM space. These variables are strongly dependent on the MSSM parameters. Specially, the detection efficiency depends on $M_{\tilde{\chi}_1^{\pm}}$, $M_{\tilde{\chi}_1^0}$, and $M_{\tilde{\chi}_2^0}$. Because a momentum of lepton is determined by the relations between them. In MSSM, the relation between them is $M_{\tilde{\chi}_1^{\pm}} \simeq M_{\tilde{\chi}_2^0} \simeq 2M_{\tilde{\chi}_1^0}$. But this relation is broken at a specific region in the space and a small fluctuation has a significant effect on the detection efficiency. Then we estimated the detection efficiency in the MSSM space using Monte Carlo simulation.

We picked up several sets of $\tan\beta$ and $M_{\tilde{q}}/M_{\tilde{g}}$ and estimated $\sigma(p\overline{p} \rightarrow \tilde{\chi}_1^{\pm}\tilde{\chi}_2^0)$ and $\mathrm{BR}(\tilde{\chi}_1^{\pm}\tilde{\chi}_2^0 \rightarrow 3\ell + X)$ for these parameters using ISAJET event generator. The $M_{\tilde{g}}$ is sensitive for $M_{\tilde{\chi}_1^{\pm}}$. And $\sigma \cdot BR(\tilde{\chi}_1^{\pm}\tilde{\chi}_2^0 \rightarrow 3\ell X)$ is very sensitive for $M_{\tilde{\chi}_1^{\pm}}$. Then we set the $M_{\tilde{g}}$ value which makes $M_{\tilde{\chi}_1^{\pm}}$ to be within 45±0.6 GeV/c^2 for each set of the parameters. Because the region that we can explore the limit of $\mathrm{M}_{\tilde{\chi}_1^{\pm}}$ is around 46 GeV/c^2 in the Run 1A data.

7.1.1 $\mathrm{m}_{\tilde{q}}/\mathrm{m}_{\tilde{g}}$ dependence for $\sigma \cdot BR(\tilde{\chi}_1^{\pm}\tilde{\chi}_2^0 \rightarrow 3\ell X)$

For given chargino/neutralino masses, the branching ratio of $BR(\tilde{\chi}_1^{\pm}\tilde{\chi}_2^0 \rightarrow 3\ell X) = BR(\tilde{\chi}_1^{\pm} \rightarrow \tilde{\chi}_1^0\ell\nu) \cdot BR(\tilde{\chi}_2^0 \rightarrow \tilde{\chi}_1^0\ell\ell)$ depends on the squark/gluino masses, because they determine the slepton and sneutrino masses according to eq. 2.17

We first look at $\sigma \cdot BR(\tilde{\chi}_1^{\pm}\tilde{\chi}_2^0 \rightarrow 3\ell X)$ as a function of the ratio of $M_{\tilde{q}}$ to $M_{\tilde{g}}$ (=1.0, 1.001, 1.01, 1.1, 1.2, 1.3, 1.4, 1.5, 1.6, 1.7, 1.8, 1.9, 2.0, 3.0, and 4.0) at $M_{\tilde{\chi}_1^{\pm}} \approx 45$ GeV/c^2. The $\tilde{\chi}_2^0$ mass is the same as the $\tilde{\chi}_1^{\pm}$ mass within 0.4 GeV/c^2. The $\tilde{\chi}_1^0$ mass is 21.0 ± 0.3 GeV/c^2. The gluino mass is around 150 GeV/c^2 because of the relation in eq. 2.8. The other parameters are fixed: $\mu = -400$ GeV, $\tan\beta = 4.0$. The $\tilde{\chi}_1^{\pm}$ and $\tilde{\chi}_2^0$ masses are determined by the above parameters and were calculated in ISAJET(ISASUSY) generator.

We generated 500 $\tilde{\chi}_1^{\pm}\tilde{\chi}_2^0$ events with ISAJET generator and obtained $\sigma(p\overline{p} \rightarrow \tilde{\chi}_1^{\pm}\tilde{\chi}_2^0)$ and $BR(\tilde{\chi}_1^{\pm}\tilde{\chi}_2^0 \rightarrow 3\ell X)$. Table 7.1 shows the results. The maximum trilepton production occurs when $M_{\tilde{q}}/M_{\tilde{g}} = 1.2$. We picked $M_{\tilde{q}}/M_{\tilde{g}} = 1.0$, 1.2, and 2.0 as the three values to be used in our scanning of the MSSM parameter space.

Table 7.1: Dependence of $\sigma \cdot BR(\tilde{\chi}_1^{\pm}\tilde{\chi}_2^0 \rightarrow 3\ell X)$ on $M_{\tilde{q}}/M\tilde{g}$, where $BR(\tilde{\chi}_1^{\pm}\tilde{\chi}_2^0 \rightarrow 3\ell X)$ is the branching ratio for the four trilepton modes to which we are sensitive. $BR(\tilde{\chi}_1^{\pm})$ and $\tilde{\chi}_2^0$ are the semi-leptonic branching ratios (e or μ). The unit of mass is in GeV/c^2.

$M_{\tilde{q}}/M_{\tilde{g}}$	$M_{\tilde{g}}$	$M_{\tilde{\chi}_1^{\pm}}$	$BR(\tilde{\chi}_2^0)$	$BR(\tilde{\chi}_1^{\pm})$	$BR(\tilde{\chi}_2^0\tilde{\chi}_1^{\pm})$	σ (pb)	$\sigma \cdot BR$ (pb)
1.0	140	44.47	4.98×10^{-4}	7.04×10^{-4}	3.50×10^{-7}	67.82	2.37×10^{-5}
1.001	141	44.75	3.74×10^{-4}	5.56×10^{-4}	8.33×10^{-8}	63.50	5.29×10^{-6}
1.01	142	44.98	0.0133	0.3237	0.0172	62.84	1.081
1.1	145	45.69	0.2322	0.4581	0.1063	60.76	6.459
1.2	145	44.84	0.3074	0.3467	0.1066	67.06	7.149
1.3	148	45.29	0.3389	0.2876	0.0975	65.46	6.382
1.4	150	45.50	0.3446	0.2574	0.0887	61.62	5.466
1.5	150	45.17	0.3415	0.2417	0.0825	66.82	5.513
1.6	150	44.88	0.3337	0.2327	0.0776	69.88	5.423
1.7	150	44.60	0.3228	0.2273	0.0734	78.32	5.749
1.8	152	44.90	0.3066	0.2237	0.0686	75.60	5.163
1.9	152	44.66	0.2915	0.2217	0.0646	79.20	5.069
2.0	155	45.26	0.2683	0.2202	0.0591	68.82	4.067
3.0	160	44.85	0.1016	0.2193	0.0223	81.12	1.809
4.0	165	44.96	0.0488	0.2204	0.0108	77.60	0.838

7.1.2 *tanβ* dependence for $\sigma \cdot BR(\tilde{\chi}_1^{\pm}\tilde{\chi}_2^0 \rightarrow 3\ell X)$

There are theoretical limits on $\tan\beta$ [51]:

- Lower bound = 1: This condition must be satisfied in all models where radiative electroweak breaking is required (this is the case of all supergravity models). The MSSM with or without the GUT hypothesis does not require this.

- Upper bound = 50-60: Required in all GUT models (including supergravity models), to give sensible Yukawa couplings for bottom quark.

In the ISAJET V7.06 code, however, the allowed range of $\tan\beta$ values is $1 < \tan\beta < 10$ [52].

We have studied the $\sigma \cdot BR$ dependence of $\tan\beta$ for the following values: $\tan\beta$=1.5, 1.6, 1.8, 2.0, 2.2, 2.4, 2.8, 3.0, 3.2, 3.8, 4.0, 4.2, 4.5, 5.0, 8.0, 10.0. We performed this study at $M_{\tilde{\chi}_1^{\pm}} \approx 45$ GeV/c^2, and set $\mu = -400$ GeV, $M_{\tilde{q}}/M\tilde{g} = 1.2$. We generated 500

$\tilde{\chi}_1^{\pm}\tilde{\chi}_2^0$ events with the ISAJET generator and estimated $\sigma \cdot BR(p\bar{p} \rightarrow \tilde{\chi}_1^{\pm}\tilde{\chi}_2^0 \rightarrow 3\ell + X)$. Table 7.2 is a summary of the results.

Table 7.2: $\tan\beta$ dependence of $\sigma \cdot BR(\tilde{\chi}_1^{\pm}\tilde{\chi}_2^0 \rightarrow 3\ell X)$, where $BR(\tilde{\chi}_1^{\pm}\tilde{\chi}_2^0 \rightarrow 3\ell X)$ is the branching ratio for four trilepton modes to which we are sensitive. $BR(\tilde{\chi}_1^{\pm})$ and $BR(\tilde{\chi}_2^0)$ are the semi-leptonic decay branching ratios (e or μ). The unit of mass is in GeV/c^2.

$\tan\beta$	$M_{\tilde{g}}$	$M_{\tilde{\chi}_2^0}$	$M_{\tilde{\chi}_1^{\pm}}$	$BR(\tilde{\chi}_2^0)$	$BR(\tilde{\chi}_1^{\pm})$	$BR(\tilde{\chi}_2^0\tilde{\chi}_1^{\pm})$	σ (pb)	$\sigma \cdot BR$ (pb)
1.5	121	46.94	45.12	0.4544	0.3230	0.1467	48.92	7.177
1.6	122	46.75	45.02	0.4440	0.3210	0.1426	41.24	7.307
1.8	125	46.61	45.08	0.4254	0.3176	0.1351	52.54	7.098
2.0	127	46.23	44.88	0.4080	0.3168	0.1292	56.08	7.246
2.2	130	46.18	45.00	0.3934	0.3160	0.1243	57.12	7.100
2.4	132	45.92	44.89	0.3796	0.3174	0.1205	61.06	7.358
2.8	137	45.90	45.11	0.3580	0.3206	0.1148	60.00	6.888
3.0	138	45.57	44.87	0.3476	0.3248	0.1129	63.78	7.201
3.2	140	45.57	44.96	0.3392	0.3280	0.1112	63.84	7.099
3.5	142	45.59	45.08	0.3266	0.3354	0.1095	63.80	6.986
3.8	145	45.60	45.18	0.3184	0.3402	0.1083	62.54	6.773
4.0	146	45.50	45.13	0.3120	0.3454	0.1078	62.86	6.776
4.2	147	45.44	45.11	0.3064	0.3508	0.1075	64.74	6.960
4.5	148	45.25	44.97	0.2984	0.3596	0.1073	67.50	7.243
5.0	150	45.15	44.94	0.2874	0.3742	0.1075	68.08	7.319
8.0	158	45.13	45.11	0.2490	0.4592	0.1143	69.04	7.891
10.0	160	44.93	44.94	0.2350	0.5026	0.1182	72.88	8.614

Since $\tan\beta$ is one of the several parameters involved in the mixing which produces the two chargino and four neutralino weak eigenstates, $M_{\tilde{\chi}_2^0}$ changes with $\tan\beta$. The mass differences $M_{\tilde{\chi}_2^0} - M_{\tilde{\chi}_1^{\pm}}$, at $\tan\beta = 1.5$, 3.0, and 10.0 are +1.82GeV/c^2, +0.61GeV/c^2, and -0.01GeV/c^2, respectively. The behavior of $BR(\tilde{\chi}_1^{\pm} \rightarrow 1\ell + X)$ and $BR(\tilde{\chi}_2^0 \rightarrow 2\ell + X)$ are quite different when $\tan\beta$ is increased. The $BR(\tilde{\chi}_1^{\pm})$ will be increased, while $\tan\beta$ and the $BR(\tilde{\chi}_2^0)$ will be decreased.

The value of $\sigma \cdot BR$ seems to be almost constant. We picked three values to use in our MSSM parameter space scanning: $\tan\beta = 2.0$, 4.0, and 10.0.

7.1.3 μ Parameter

The lower bound on μ can be set from the LEP result that the most of the kinematically accessible domain is excluded for the "higgsino" mass, μ, value not too large compared to the Z mass: $|\mu| < \mathcal{O}(100 \text{ GeV})$. The result was obtained by assuming the GUT hypothesis in the framework of the MSSM.

Although there is no theoretical input on the upper bound of μ in the MSSM, we expect that all SUSY parameters (including μ) should not be too large compared to the SUSY scale.

Thus, we set our scanning range on μ to be 200GeV$< |\mu| <$ 100GeV.

7.1.4 Summary of the Scanning MSSM Parameter Space

The MSSM parameters that we scanned are;

- $\tan\beta = 2.0, 4.0, 10.0$
- $M_{\tilde{q}}/M_{\tilde{g}} = 1.0, 1.2, 2.0$
- 200 GeV $< |\mu| <$ 1000 GeV
- $M_{\tilde{g}} = 120 \sim 250$ GeV/c^2

Other parameters used, in the ISAJET V7.06 input, are pseudo-scalar Higgs boson mass(500 GeV/c^2) and M$_t$(170 GeV/c^2).

7.2 Total Detection Efficiency

Figures 7.1, 7.2, 7.3, 7.4, 7.5, and 7.6 show ϵ^{tot} vs. $M_{\tilde{\chi}_1^\pm}$ for all scanning points. Similarly, the plots of ϵ^{tot} vs. $M_{\tilde{\chi}_2^0}$ are shown in figures 7.7, 7.8, 7.9, 7.10, 7.11, and 7.12.

The efficiency tends to increase linearly with the chargino and neutralino mass in the mass region we scanned. Our event selection for the trilepton event is mainly determined by the lepton qualities, and a high momentum lepton tends to have higher quality. Since the $\tilde{\chi}_1^\pm$ and $\tilde{\chi}_2^0$ with high mass decay to high momentum leptons, the efficiency is high.

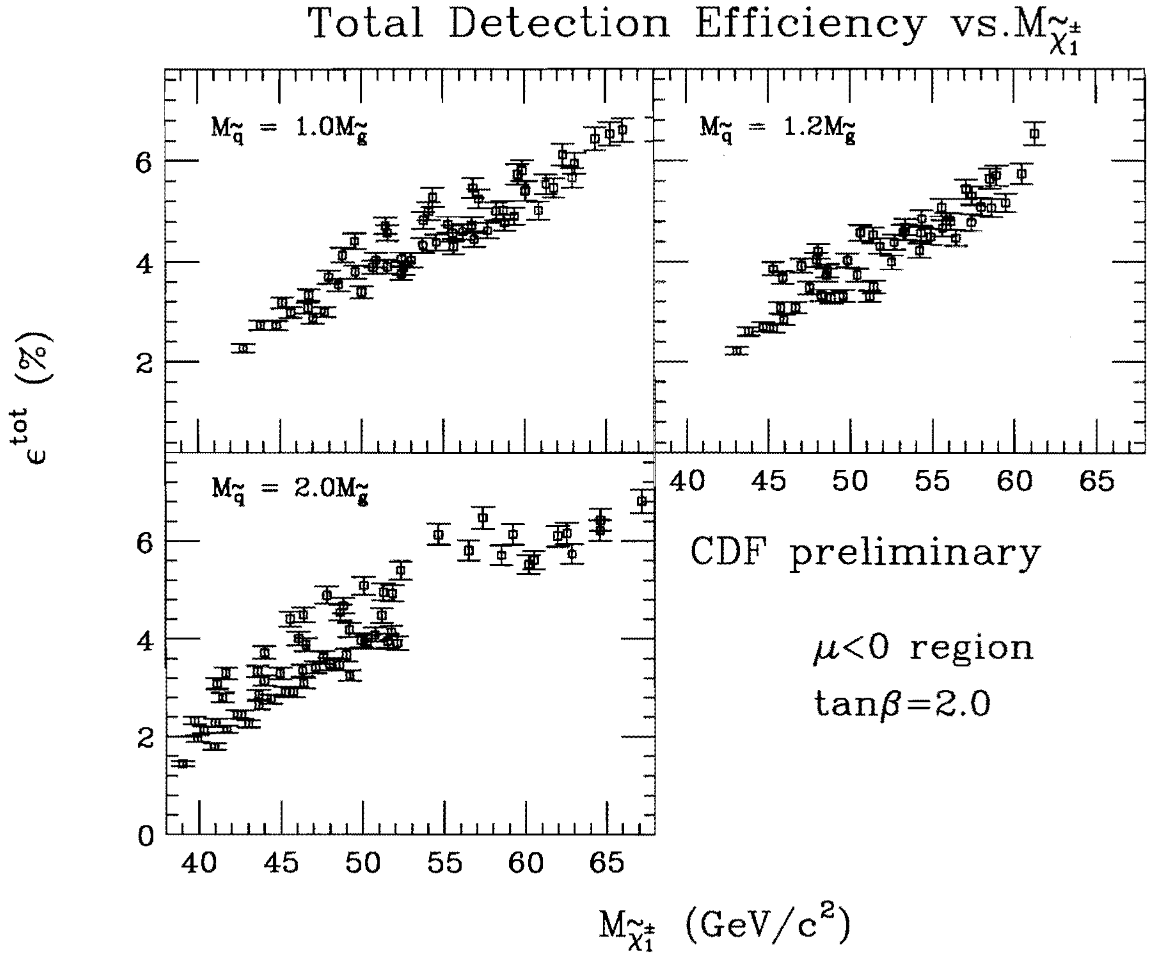

Figure 7.1: Total detection efficiency as a function of $M_{\tilde{\chi}_1^\pm}$.

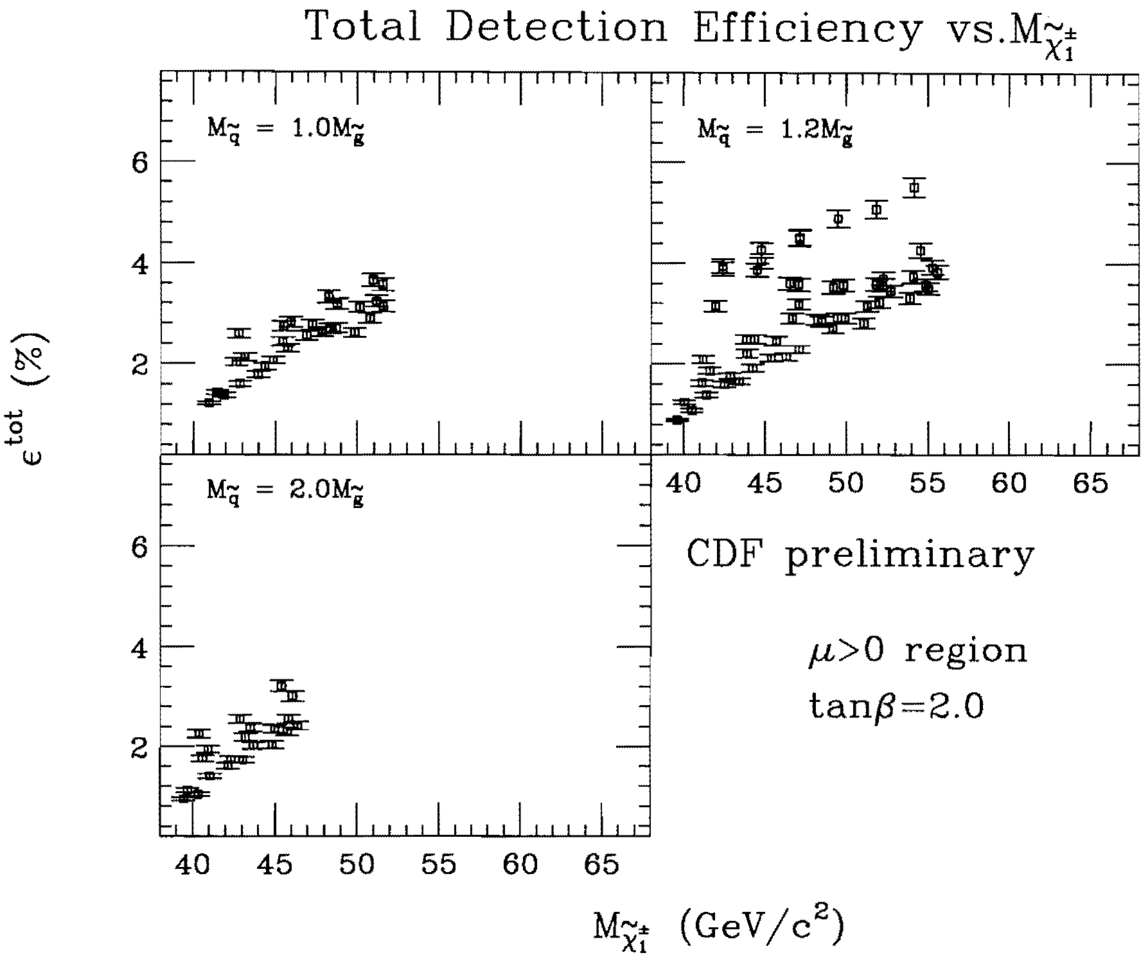

Figure 7.2: Total detection efficiency as a function of $M_{\tilde{\chi}_1^\pm}$.

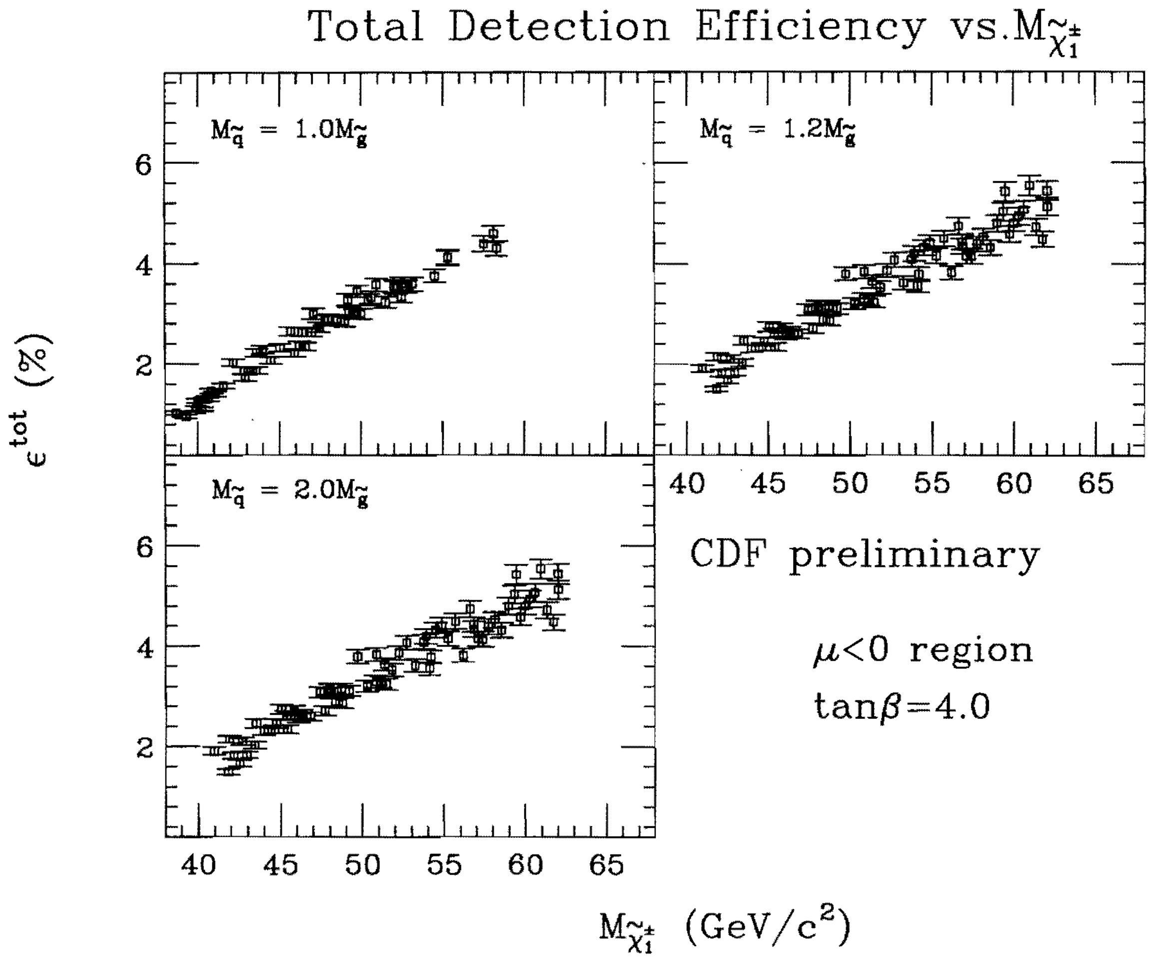

Figure 7.3: Total detection efficiency as a function of $M_{\tilde{\chi}_1^\pm}$.

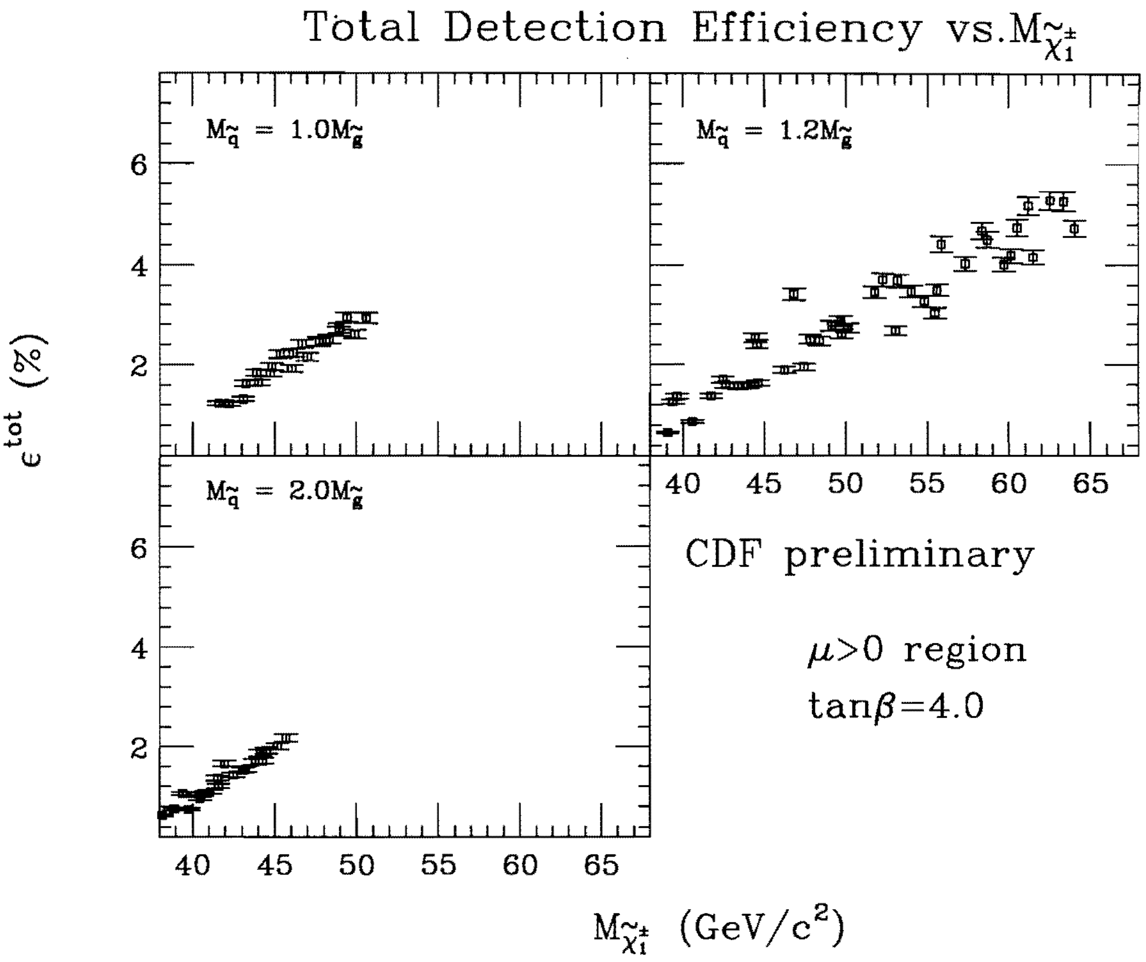

Figure 7.4: Total detection efficiency as a function of $M_{\tilde{\chi}_1^\pm}$.

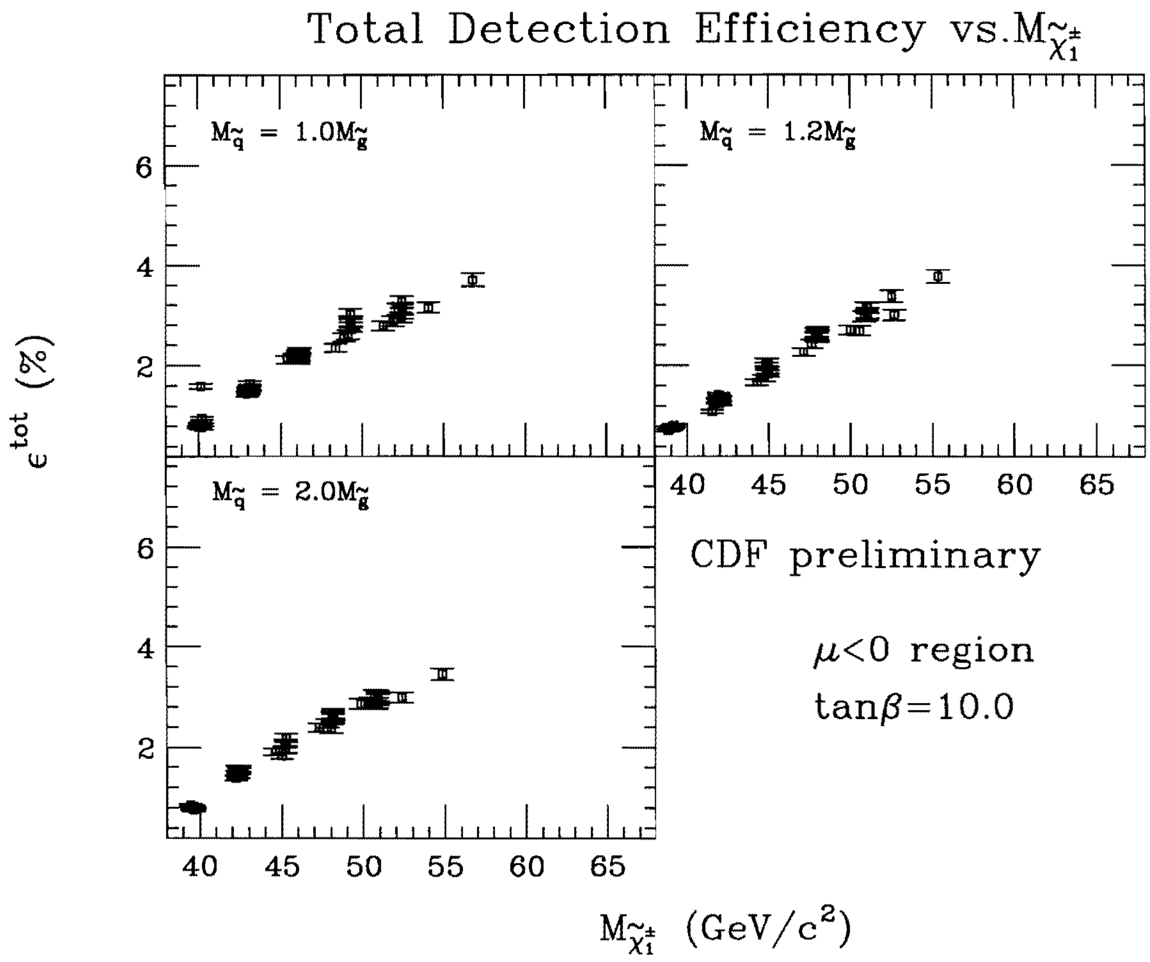

Figure 7.5: Total detection efficiency as a function of $M_{\tilde{\chi}_1^\pm}$.

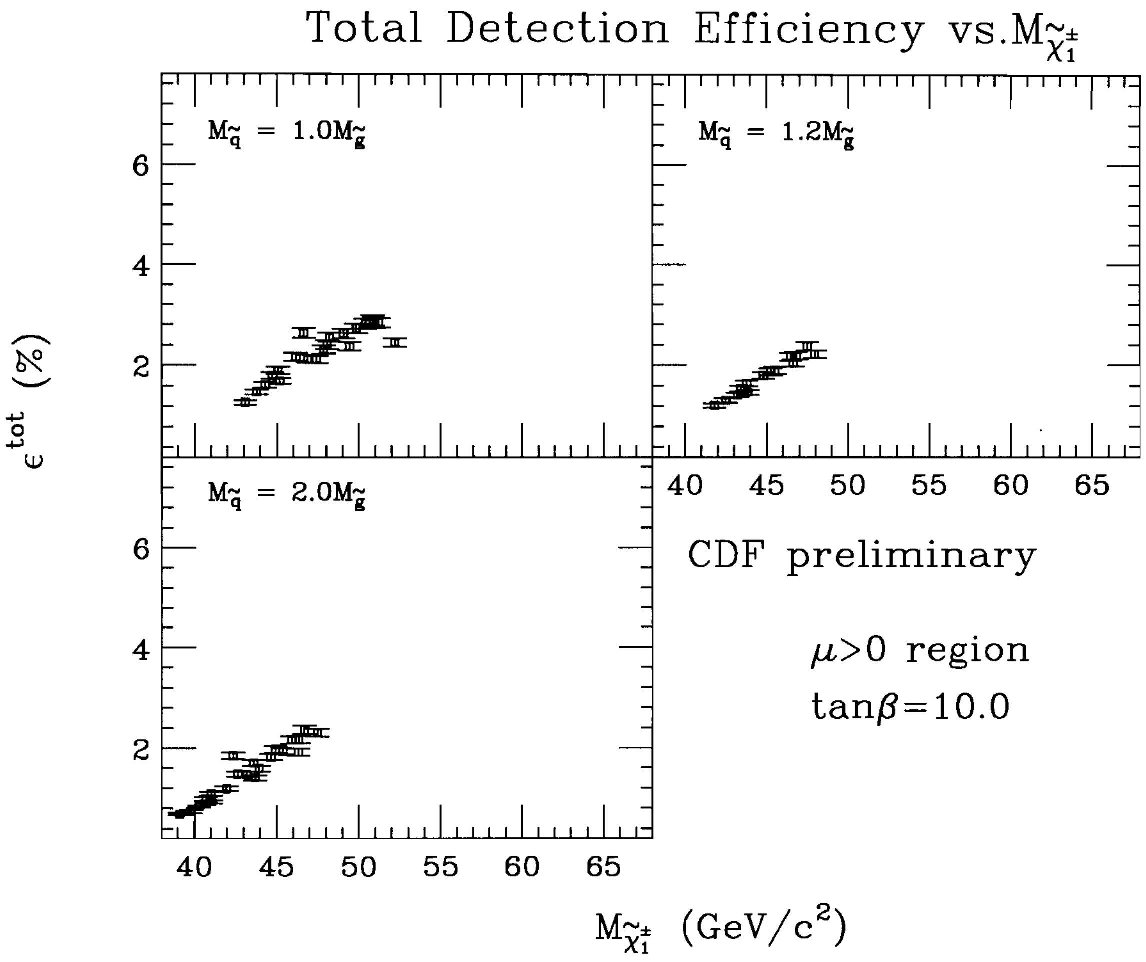

Figure 7.6: Total detection efficiency as a function of $M_{\tilde{\chi}_1^\pm}$.

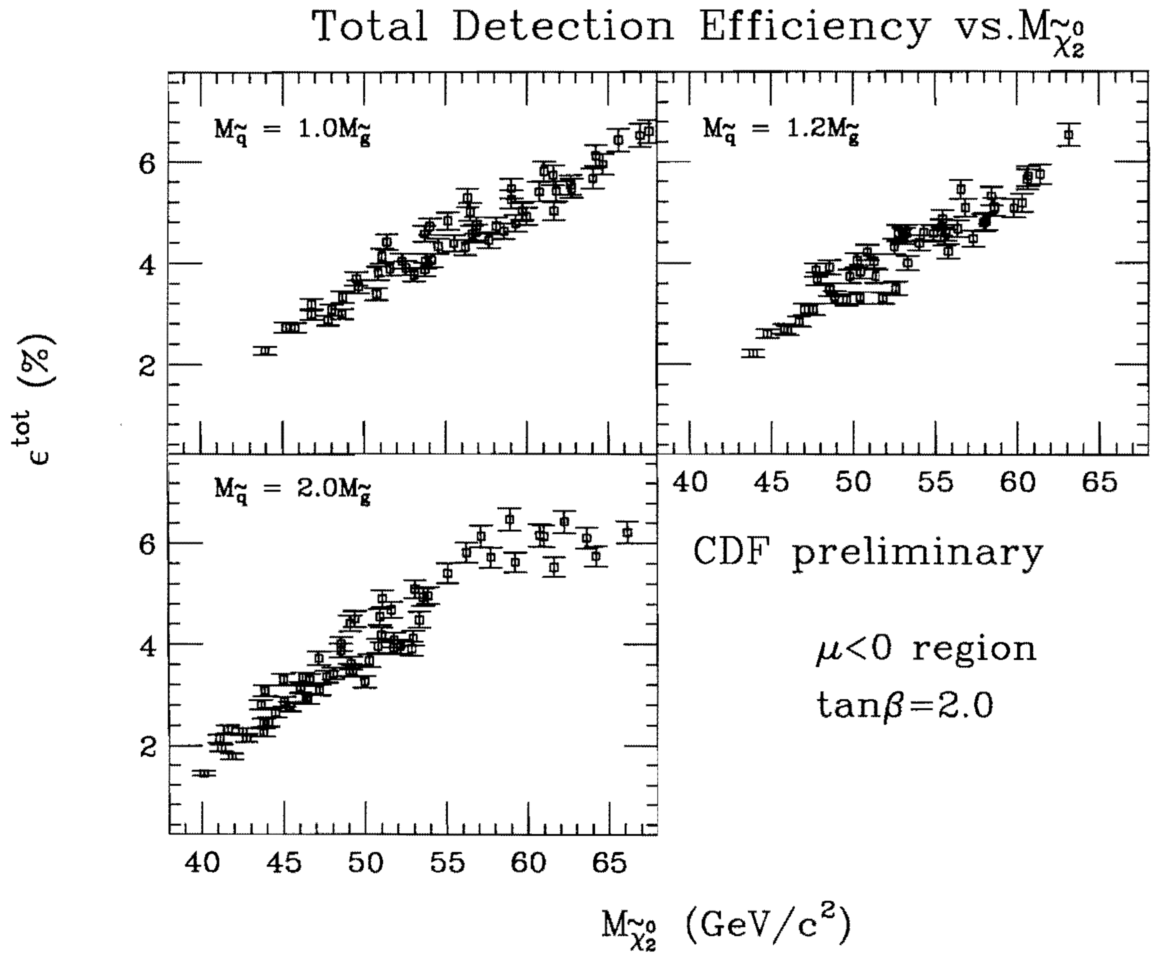

Figure 7.7: Total detection efficiency as a function of $M_{\tilde{\chi}_2^0}$.

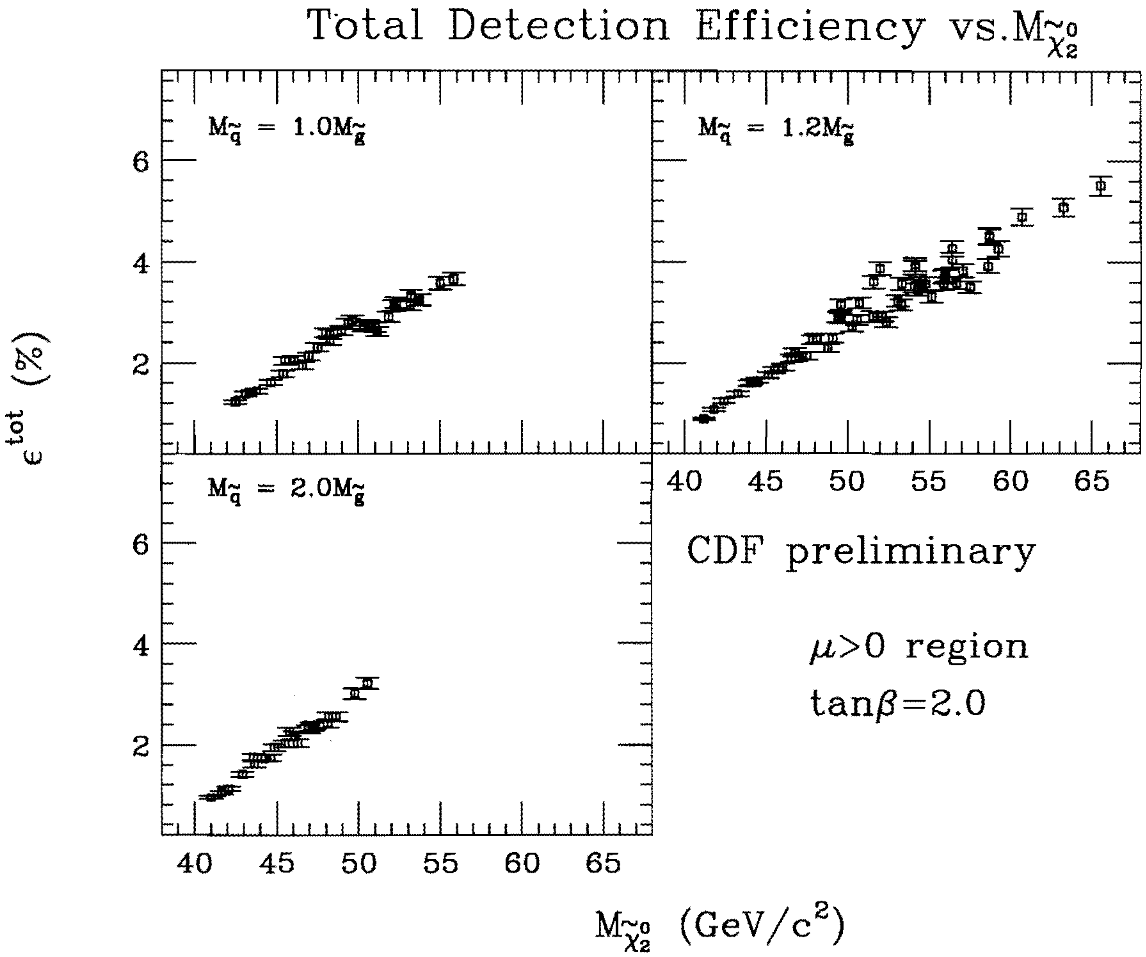

Figure 7.8: Total detection efficiency as a function of $M_{\tilde{\chi}_2^0}$.

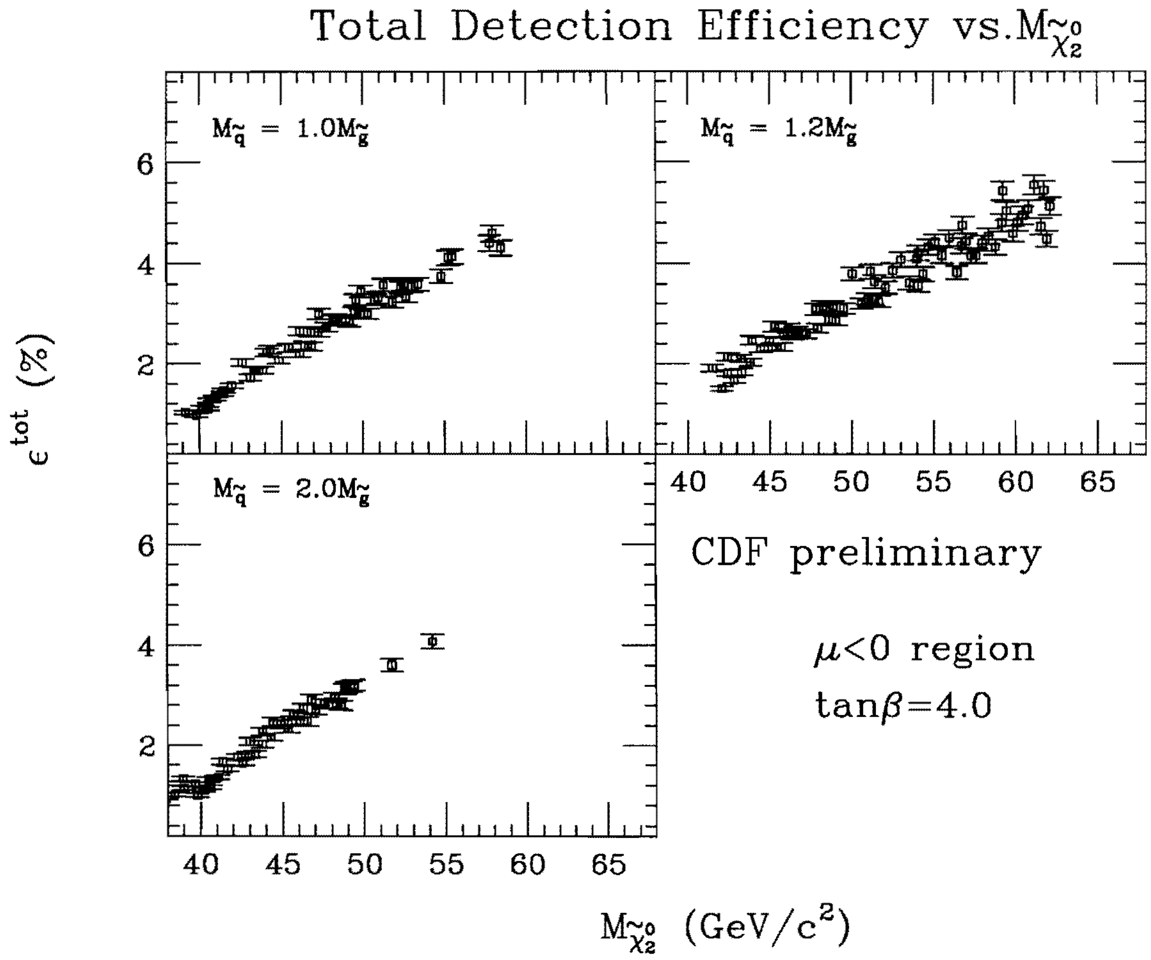

Figure 7.9: Total detection efficiency as a function of $M_{\tilde{\chi}_2^0}$.

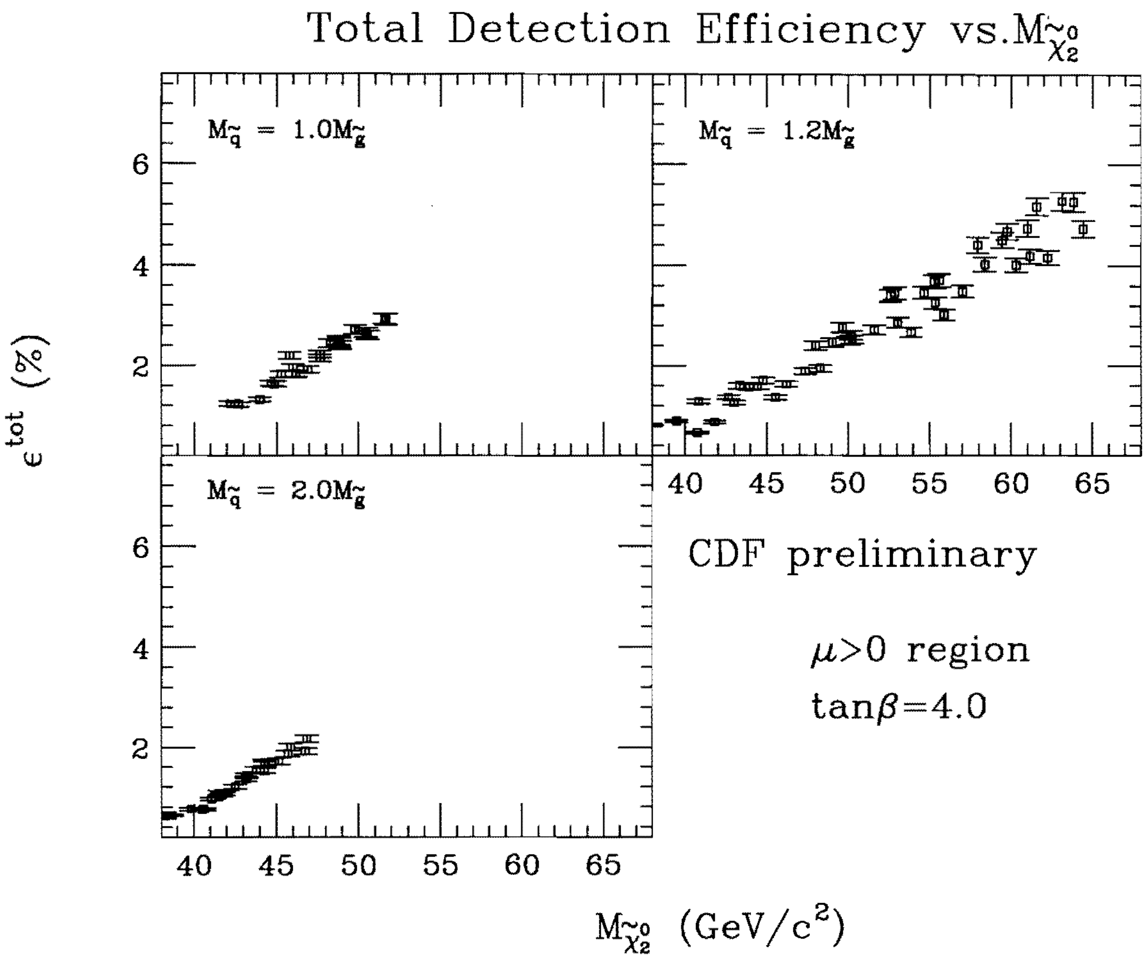

Figure 7.10: Total detection efficiency as a function of $M_{\tilde{\chi}_2^0}$.

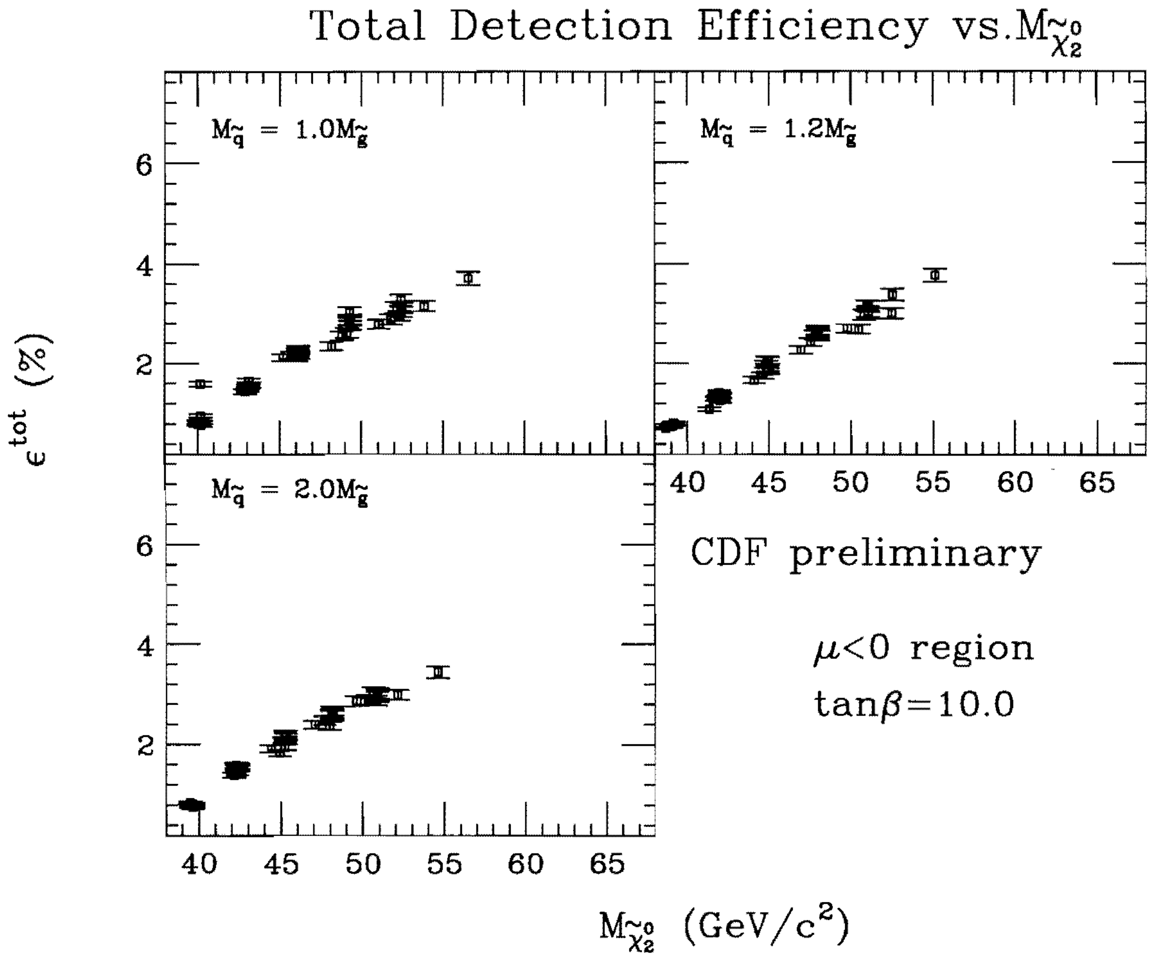

Figure 7.11: Total detection efficiency as a function of $M_{\tilde{\chi}_2^0}$.

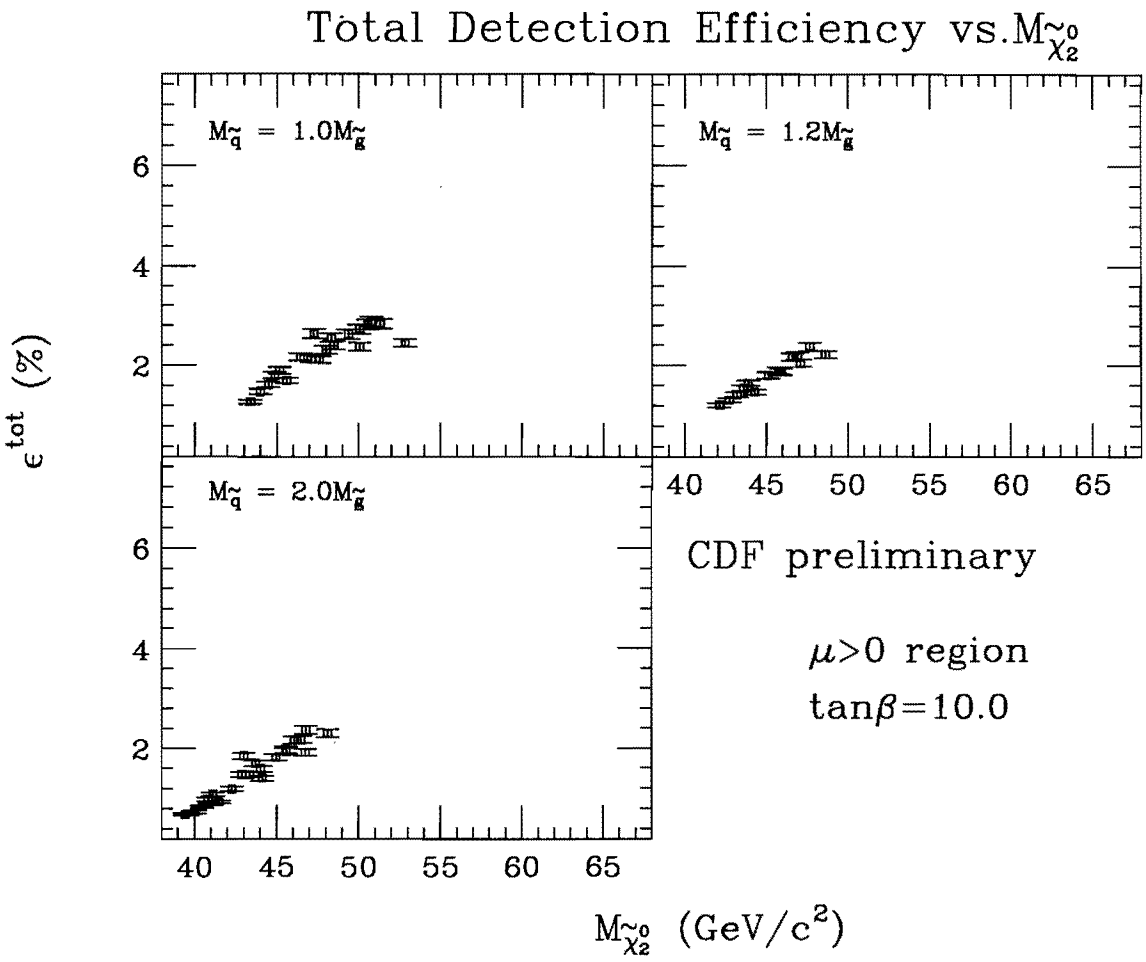

Figure 7.12: Total detection efficiency as a function of $M_{\tilde{\chi}_2^0}$.

There is no significant difference of the tendency of the efficiency between the positive μ and the negative μ regions in the MSSM space. But there are some higher efficiency points at a positive μ region in $\tan\beta = 2.0, M_{\tilde{q}}/M_{\tilde{g}}$ space in figure 7.2. The higher efficiency points exist at the region where $M_{\tilde{\chi}_1^\pm}$ is lighter than $M_{\tilde{\chi}_2^0}$ about 10 GeV/c^2 and at small positive μ value($\mu < 200$ GeV). The efficiency depends on the lepton's P_T in the event and these lepton's P_T depend on the $\tilde{\chi}_1^\pm$ and $\tilde{\chi}_2^0$ masses. Since $\tilde{\chi}_2^0$ decays into two leptons and $\tilde{\chi}_1^\pm$ decays into one lepton, the efficiency is determined by the $\tilde{\chi}_2^0$ mass if the $\tilde{\chi}_2^0$ mass is higher than $\tilde{\chi}_1^\pm$ mass. Thus these point's efficiencies are higher than the others at the same $\tilde{\chi}_1^\pm$ mass.

We conclude the event acceptance is in proportion to $\tilde{\chi}_2^0$ and $\tilde{\chi}_1^\pm$ over our scanning range.

7.3 Mass limits

Figure 7.13 is a plot of $\sigma \cdot BR(\tilde{\chi}_1^\pm\tilde{\chi}_2^0 \to 3\ell + X)$ versus $M_{\tilde{\chi}_1^\pm}$ for all points we scanned in the MSSM parameter space. Here $BR(\tilde{\chi}_1^\pm\tilde{\chi}_2^0 \to 3\ell + X)$ is the branching ratio for four trilepton modes to which we are sensitive. The points excluded by 95% CL are indicated by diamond marks, while points which are not excluded are indicated by **x**'s.

A similar plot for the neutralino mass ($M_{\tilde{\chi}_2^0}$) is shown in figure 7.14. The maximum reaches in mass (cross section times branching ratio) is about 48 GeV/c^2 and 5 pb.

Figure 7.15 and figure 7.16 show the 95% CL limit of $\sigma \cdot BR(\tilde{\chi}_1^\pm\tilde{\chi}_2^0 \to 3\ell + X)$ for the $M_{\tilde{\chi}_1^\pm}$ and $M_{\tilde{\chi}_2^0}$ respectively. In the figure 7.15, the 95% limit at one MSSM parameter set($\tan\beta = 2.0$, M($\tilde{q}$)/M($\tilde{g}$) = 1.2, $\mu = -400$ GeV) is 1.4 pb, 0.6 pb, and 0.4 pb for $\tilde{\chi}_1^\pm$ of 45, 70 and 100 GeV/c^2.

The regions excluded by CDF can be presented in the $M_{\tilde{\chi}_1^\pm}$-μ plane. Figure 7.17 shows the excluded regions for $\tan\beta = 2.0$, 4.0, and 10.0, respectively, for $M_{\tilde{q}}/M_{\tilde{g}} = 1.2$. Figure 7.18 is the same as figure 7.17, but at $M_{\tilde{q}}/M_{\tilde{g}} = 2.0$.

It should be noted that we didn't scan $\mu < -600$ GeV at $\tan\beta = 2.0$ because the top-squark ($\tilde{t}$) becomes lighter than the lightest neutralino ($\tilde{\chi}_1^0$) in this region of the parameter space. The LEP limit of 47 GeV/c^2 (if $M_{\tilde{\chi}_1^0} < 40$ GeV/c^2) [53] is shown by a dashed line.

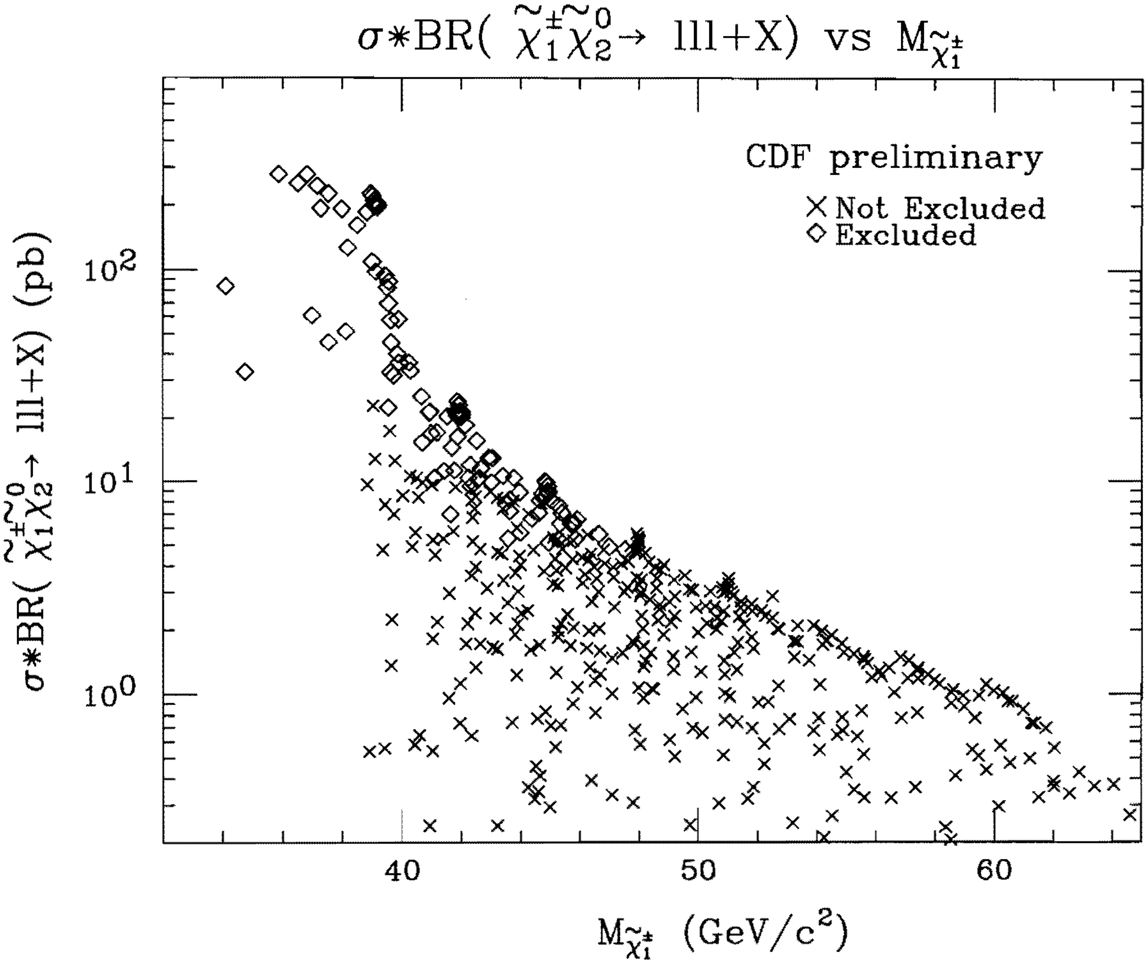

Figure 7.13: Plots of $\sigma \cdot BR(\tilde{\chi}_1^{\pm}\tilde{\chi}_2^0 \rightarrow 3\ell + X)$ versus $M_{\tilde{\chi}_1^{\pm}}$ for all points scanned in the MSSM parameter space. $BR(\tilde{\chi}_1^{\pm}\tilde{\chi}_2^0 \rightarrow 3\ell + X)$ is the branching ratio for the four trilepton modes to which we are sensitive. Points excluded by this analysis are indicated by diamond symbols.

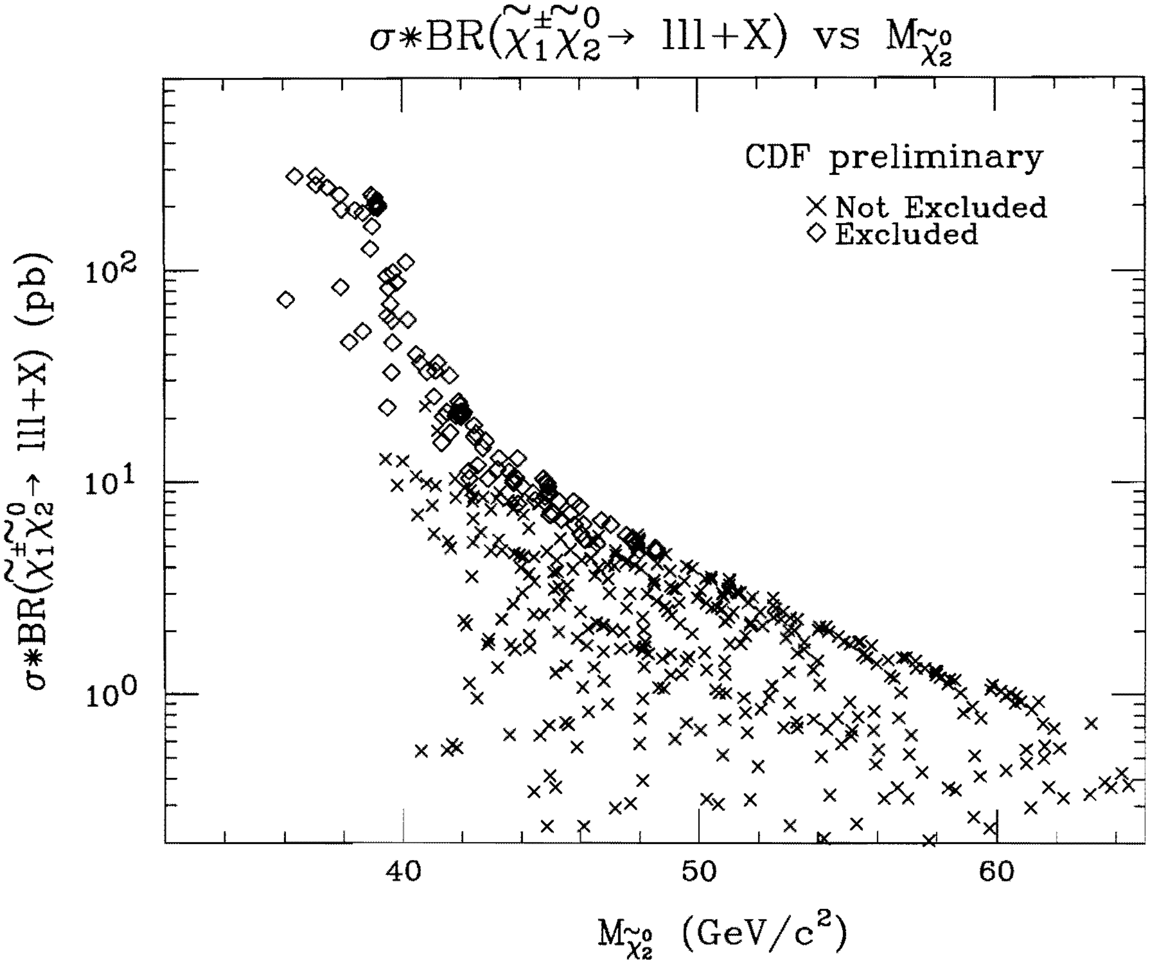

Figure 7.14: Plots of $\sigma \cdot BR(\tilde{\chi}_1^{\pm}\tilde{\chi}_2^0 \rightarrow 3\ell + X)$ versus $M_{\tilde{\chi}_2^0}$ for all points scanned in the MSSM parameter space. $BR(\tilde{\chi}_1^{\pm}\tilde{\chi}_2^0 \rightarrow 3\ell + X)$ is the branching ratio for the four trilepton modes to which we are sensitive. Points excluded by this analysis are indicated by diamond symbols.

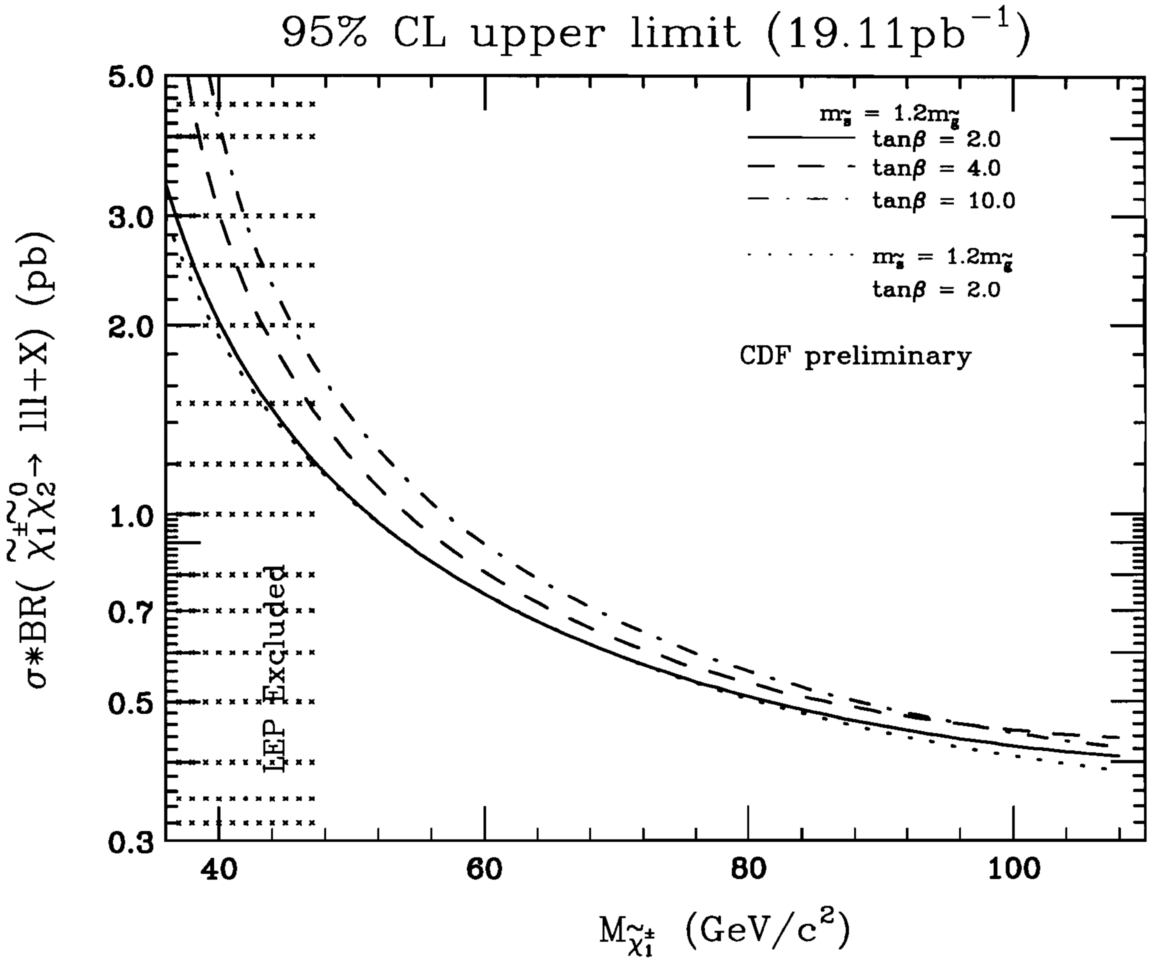

Figure 7.15: The 95% CL limit of $\sigma \cdot BR(\tilde{\chi}_1^{\pm}\tilde{\chi}_2^0 \rightarrow 3\ell + X)$ for the $M_{\tilde{\chi}_1^{\pm}}$

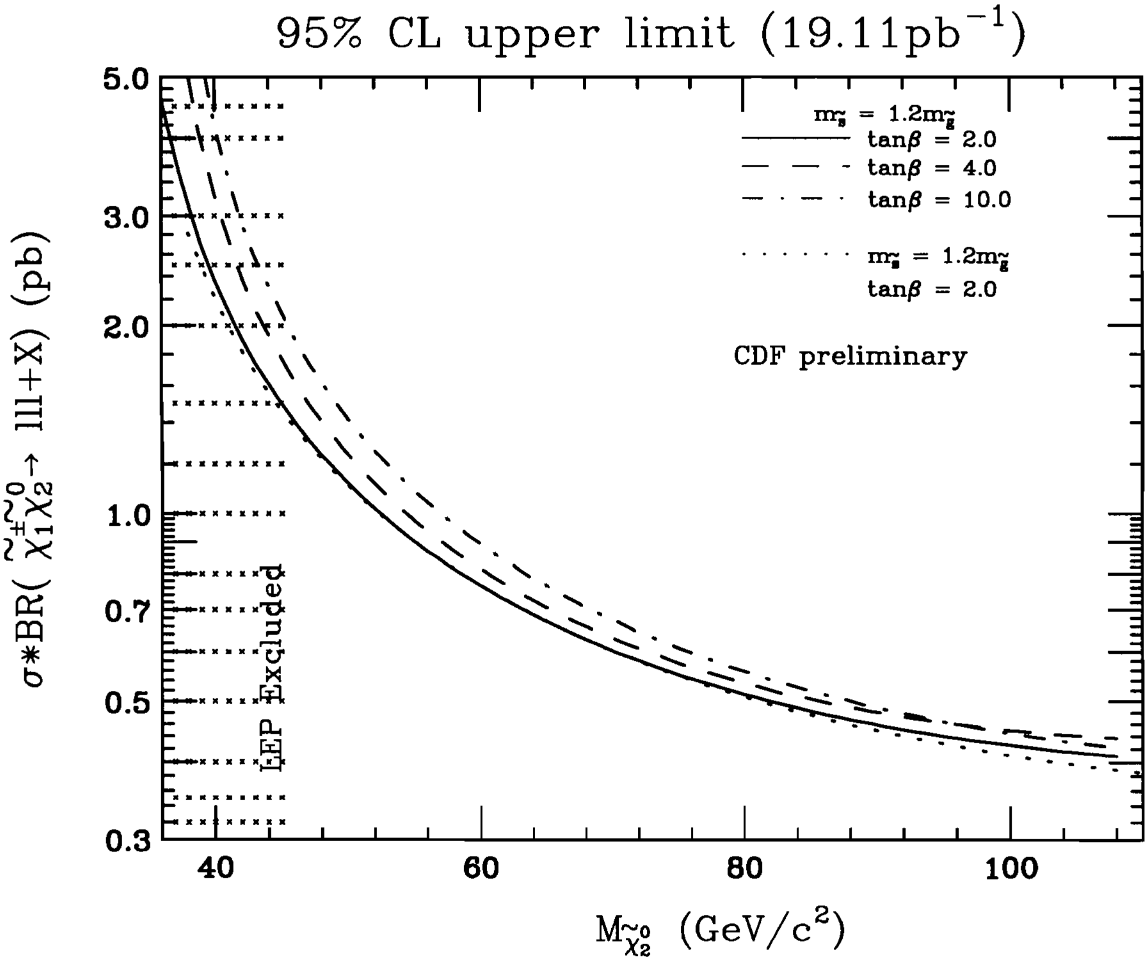

Figure 7.16: The 95% CL limit of $\sigma \cdot BR(\tilde{\chi}_1^{\pm}\tilde{\chi}_2^0 \to 3\ell + X)$ for the $M_{\tilde{\chi}_2^0}$

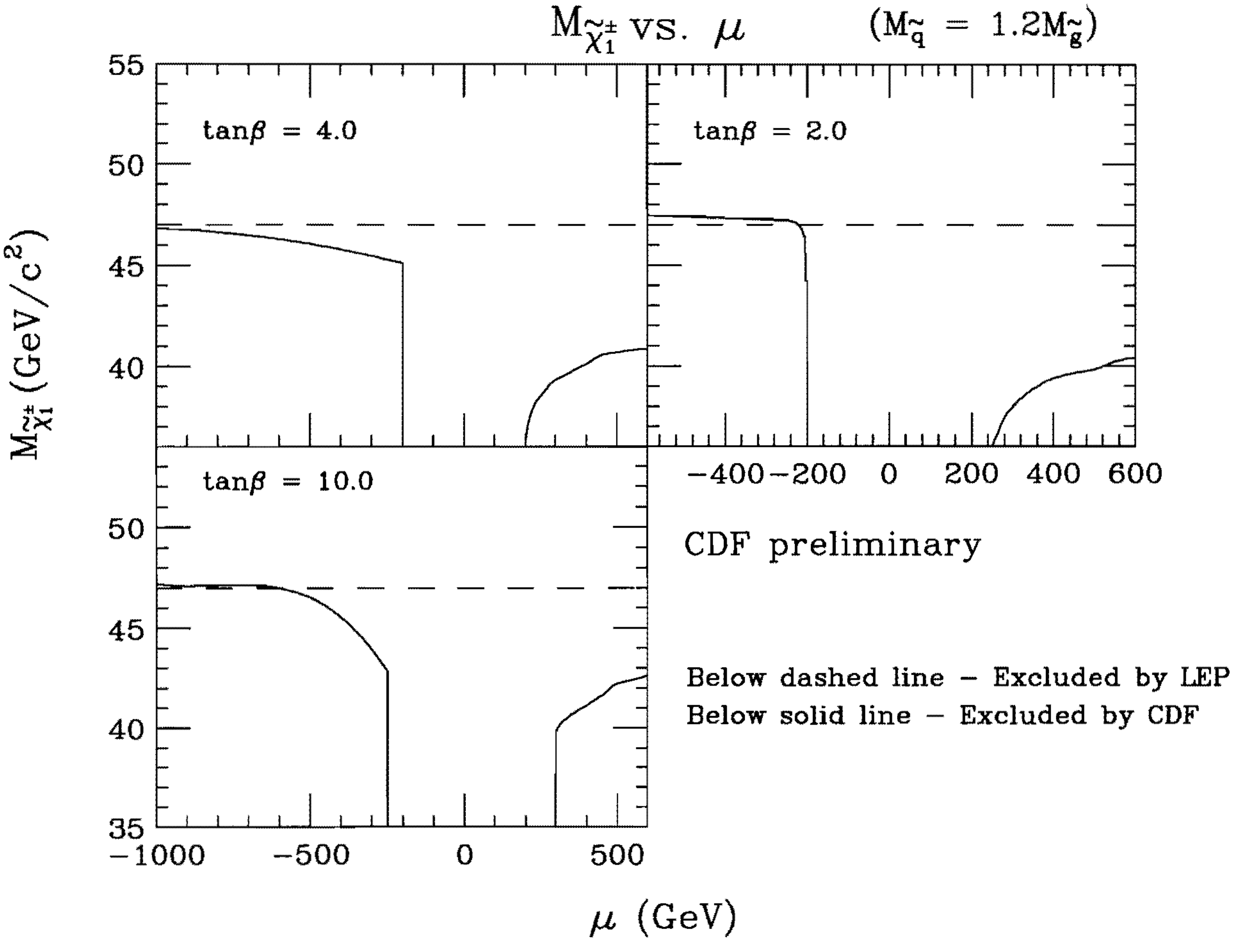

Figure 7.17: The excluded region in the $M_{\tilde{\chi}_1^\pm}$-μ plane for $M_{\tilde{q}}/M_{\tilde{g}} = 1.2$.

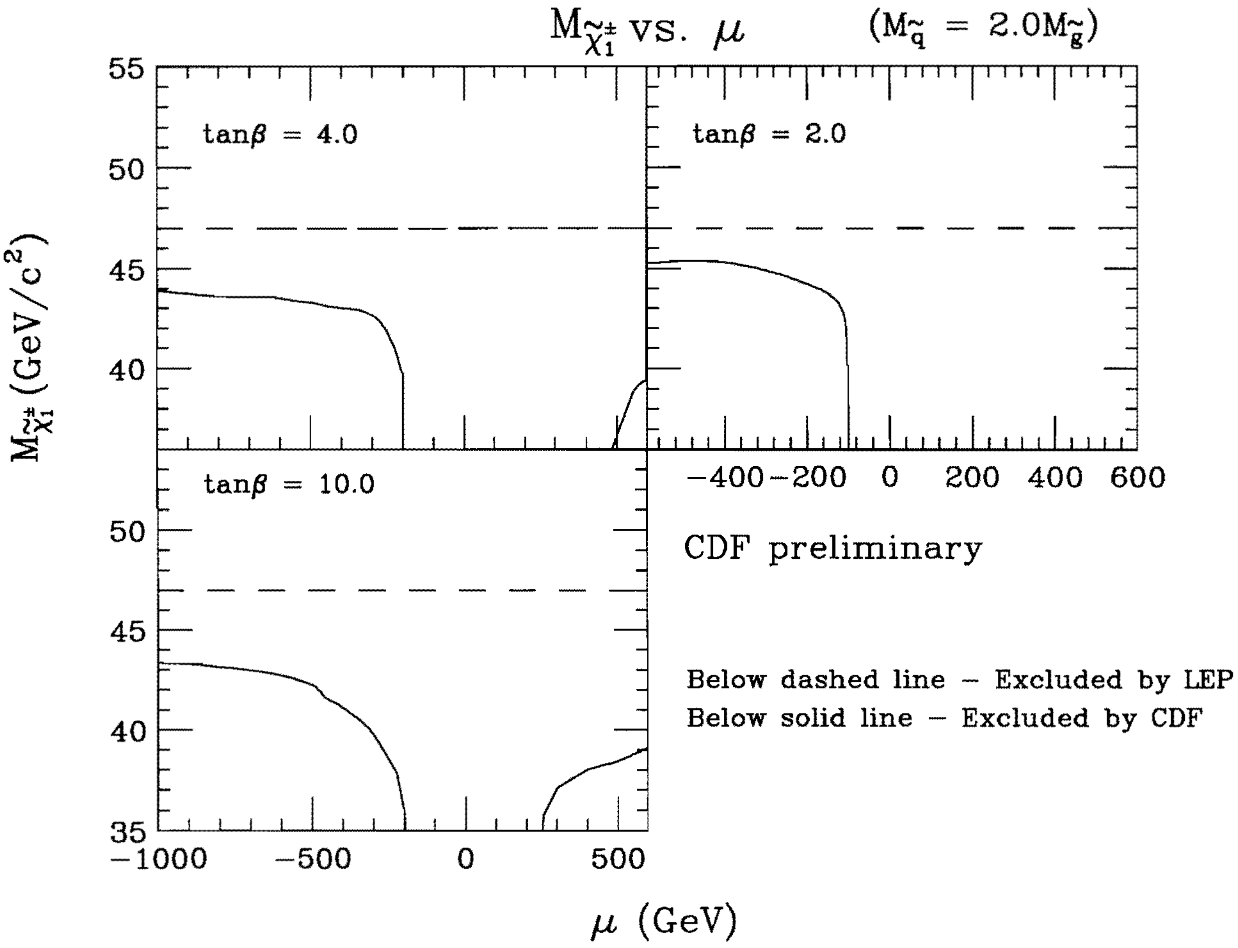

Figure 7.18: The excluded region in the $M_{\tilde{\chi}_1^\pm}$-μ plane for $M_{\tilde{q}}/M_{\tilde{g}} = 2.0$.

We do not show the limits at $M_{\tilde{q}}/M_{\tilde{g}} = 1.0$, because our reach there is well below the LEP limit, due to the small leptonic branching ratio.

Similarly, figures 7.19 and 7.20 show the CDF excluded regions in the $M_{\tilde{\chi}_2^0}$-μ plane for $M_{\tilde{q}}/M_{\tilde{g}} = 1.2$ and 2.0, respectively.

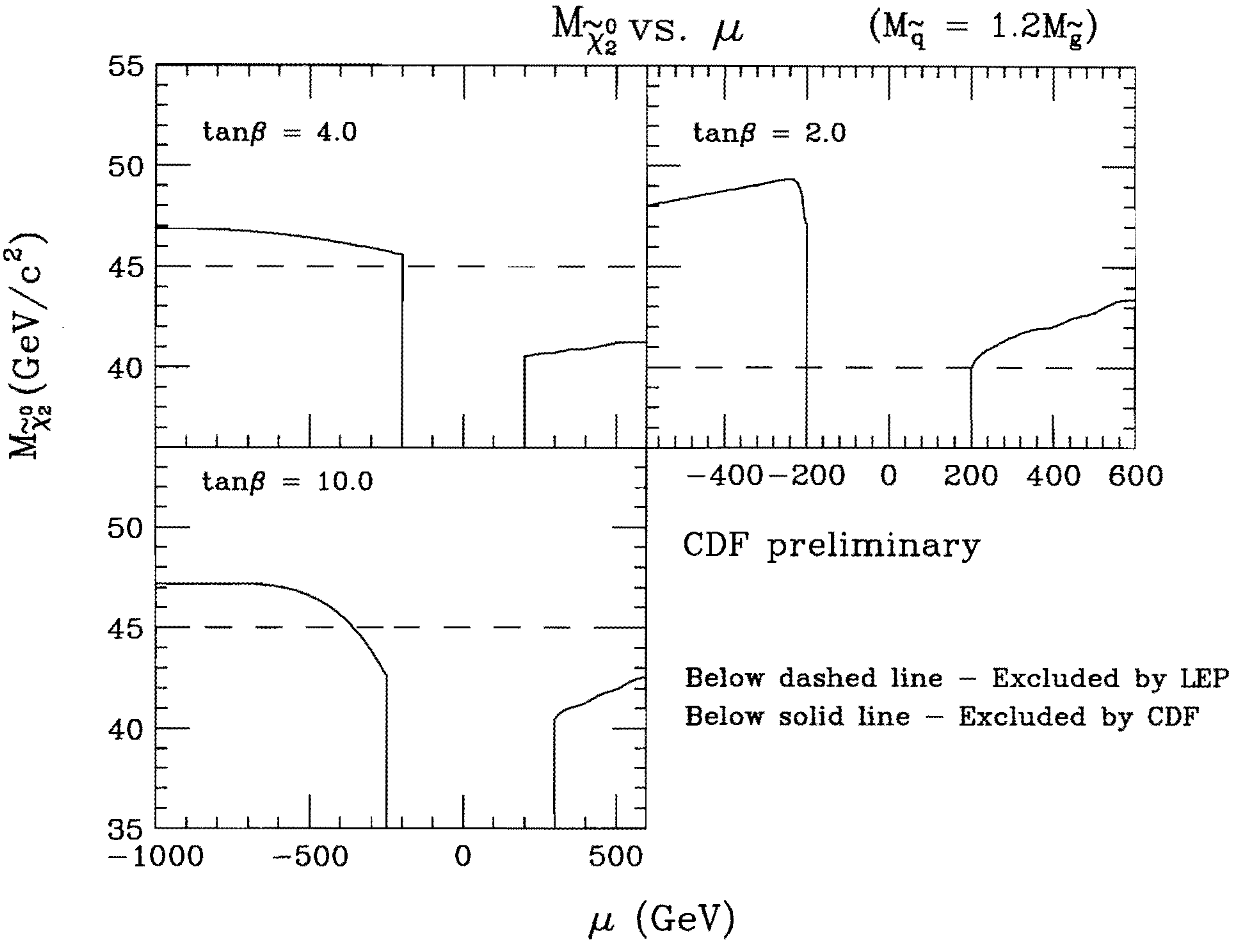

Figure 7.19: The excluded region in the $M_{\tilde{\chi}_2^0}$-μ plane for $M_{\tilde{q}}/M_{\tilde{g}} = 1.2$.

The LEP limits of 40 GeV/c^2 (if $\tan\beta = 2.0$) and 45 GeV/c^2 (if $\tan\beta > 3.0$) [53] are shown by dashed lines.

In general, we do not observe any sensitivity beyond the LEP result in $\mu > 0$ region. The maximum reach on chargino mass is obtained at $\tan\beta = 2.0$ and $M_{\tilde{q}}/M_{\tilde{g}} = 1.2$: 47 GeV/$c^2$ in $-600 < \mu < -200$ GeV. We can, however, slightly exceed the LEP limit (40 GeV/c^2) for $M_{\tilde{\chi}_2^0}$ at $\tan\beta = 2.0$. The CDF limit is 49 GeV/c^2 (46 GeV/c^2) for the region

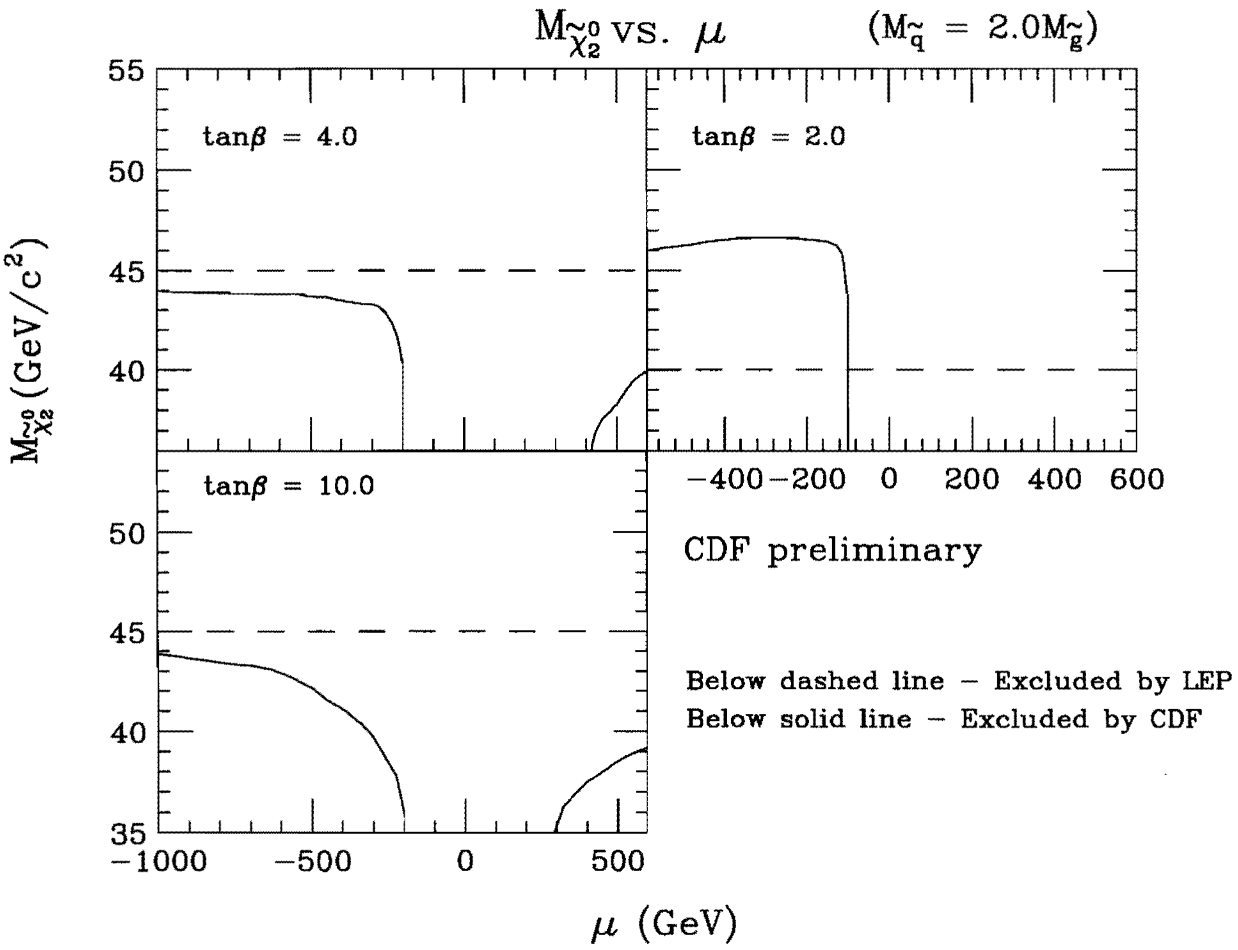

Figure 7.20: The excluded region in the $M_{\tilde{\chi}_2^0}$-μ plane for $M_{\tilde{q}}/M_{\tilde{g}} = 2.0$.

$-600 < \mu < -200$ GeV at $M_{\tilde{q}} = 1.2 \times M_{\tilde{g}}$ ($2.0 \times M_{\tilde{g}}$).

Since gluino mass excluded by the multi-jets plus $\not{E}_T$ search ($\mu = -400$ GeV and $\tan\beta = 4.0$) is $M_{\tilde{g}} > 160$ GeV/c^2 for arbitrary $M_{\tilde{q}}$, and $M_{\tilde{g}} > 220$ GeV/c^2 for $M_{\tilde{q}} = M_{\tilde{g}}$ [54, 55], it is interesting to plot our results in the $M_{\tilde{g}}$-μ plane by assuming a GUT assumption which relates the chargino/neutralino masses to the gluino mass. The region excluded by LEP is also calculated using the ALLOW program [56]. Figures 7.21 and 7.22 show the CDF excluded region compared to the LEP excluded region. At $\mu = -400$ GeV and $\tan\beta = 4.0$, we set a lower limit of $M_{\tilde{g}} > 150$ GeV/c^2 for $M_{\tilde{q}} = 1.2 \times M_{\tilde{g}}$ (145 GeV/c^2 for $M_{\tilde{q}} = 2.0 \times M_{\tilde{g}}$). These are weaker limits, but consistent with multi-jets plus $\not{E}_T$ search.

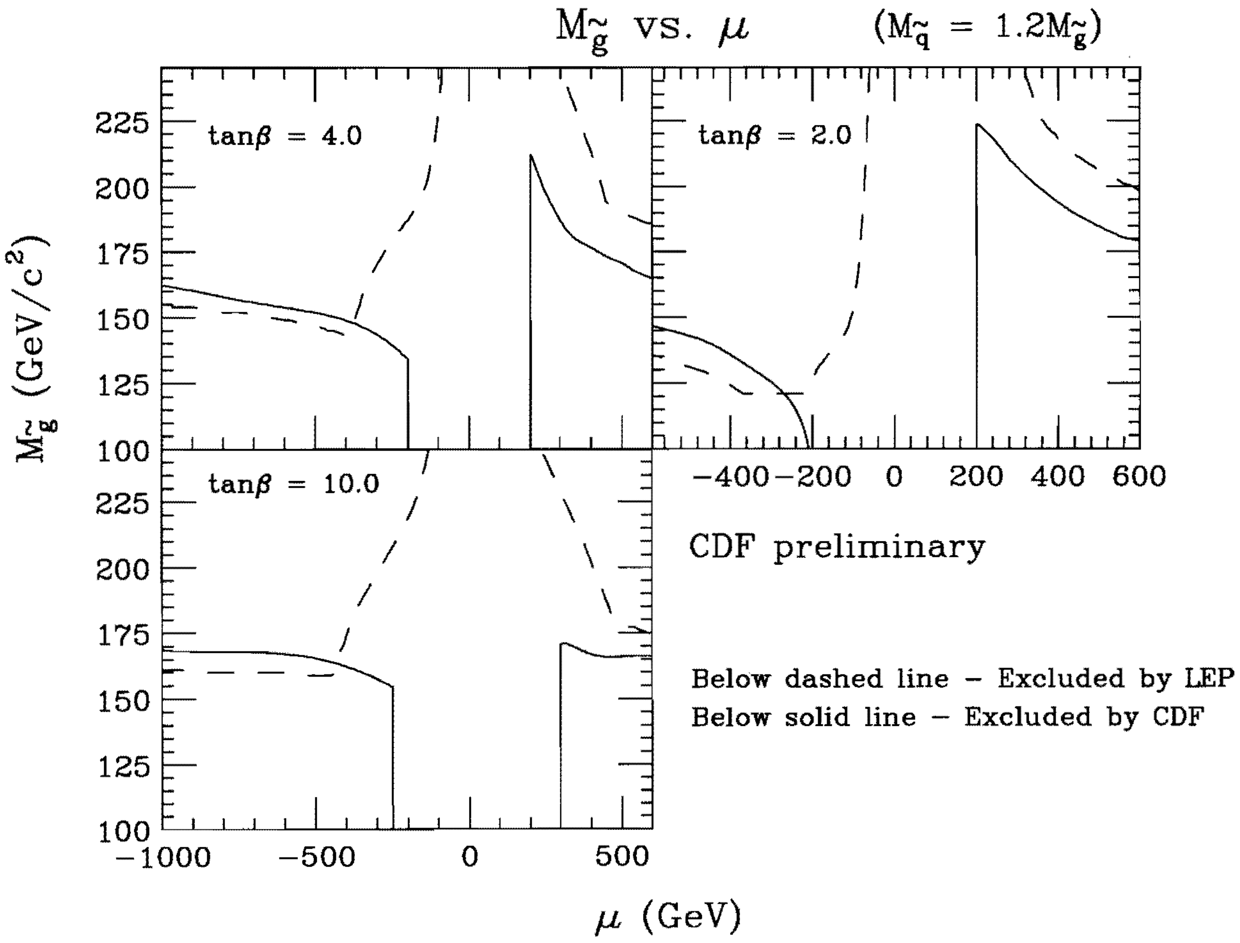

Figure 7.21: The excluded region in the $M_{\tilde{g}}$-μ plane for $M_{\tilde{q}}/M_{\tilde{g}} = 1.2$.

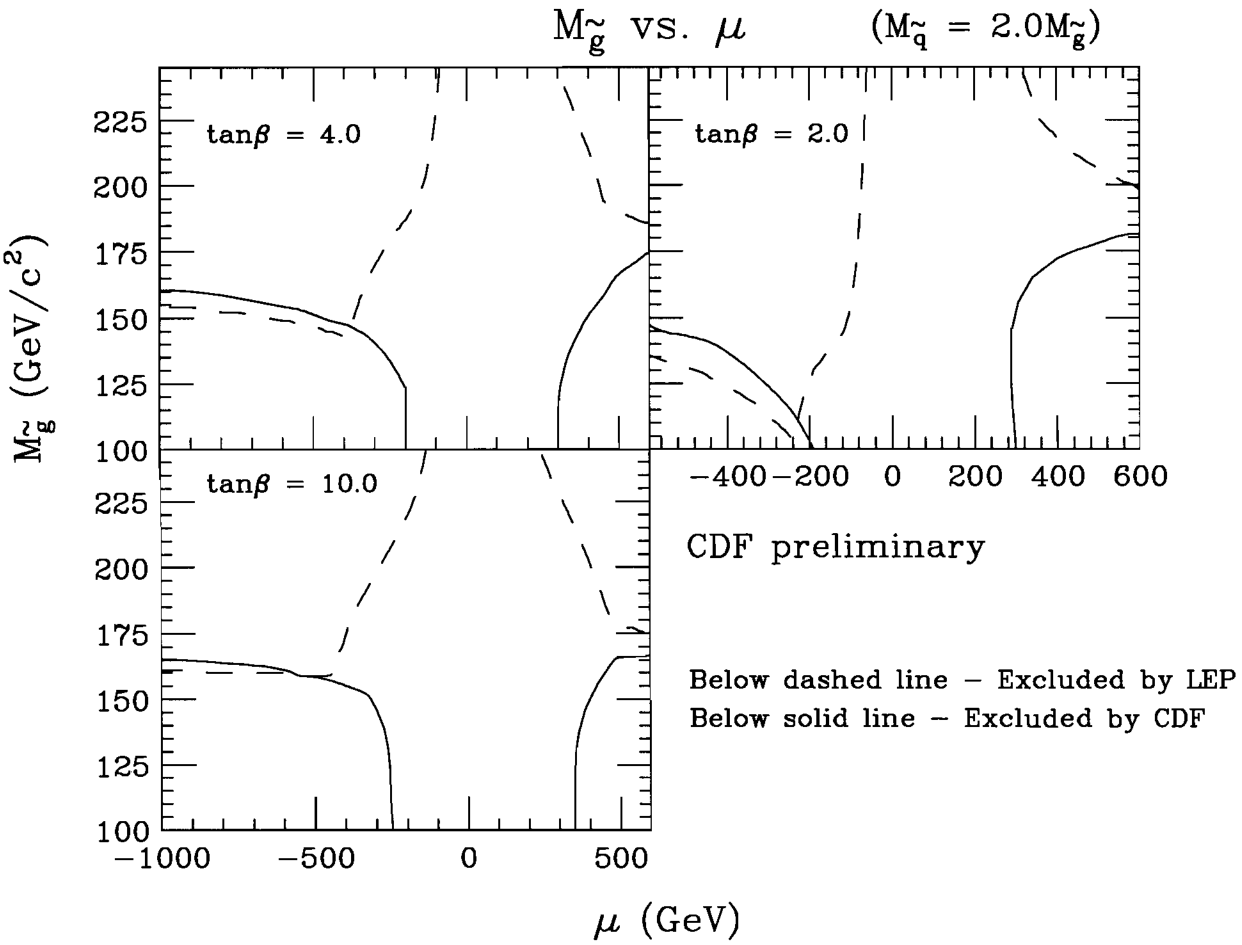

Figure 7.22: The excluded region in the $M_{\tilde{g}}$-μ plane for $M_{\tilde{q}}/M_{\tilde{g}} = 2.0$.

Chapter 8

Conclusion

The Minimal Supersymmetric Standard Model (MSSM) is a very well motivated extension to the Standard Model. Although it is true that there is currently no high energy physics data which is in serious conflict with any Standard Model prediction, this is also true for the MSSM, in a large portion of its parameter space. In addition, the MSSM provides a solution to the fine-tuning problem, it accommodates the coupling constant unification at high energies, and suggests a natural dark-matter candidate. Thus, it is imperative that SUSY searches be performed at high energy physics experiments until either a discovery is made or the entire MSSM parameter space is excluded.

Chargino-neutralino ($\tilde{\chi}_1^{\pm}\tilde{\chi}_2^0$) pair production and decay to a three-lepton final state has long been suggested as a promising supersymmetry (SUSY) discovery channel at the Tevatron.

We have conducted a SUSY search using trilepton events in $p\overline{p}$ collisions at $\sqrt{s} =$ 1.8 TeV. In the channels of all possible combinations of electrons and muons, we observed no events in 19.11 pb^{-1} data using our trilepton selection criteria.

Assuming the GUT hypothesis and mass relations between slepton/sneutrino and gluino/squarks within the framework of the MSSM, the maximal excluded region is found to be

$$M_{\tilde{\chi}_1^{\pm}} < 47 \text{ GeV}/c^2 \text{ (LEP: 47 GeV/c}^2\text{)} \tag{8.1}$$

$$M_{\tilde{\chi}_2^0} < 49 \text{ GeV}/c^2 \text{ (LEP: 40 GeV/c}^2\text{)} \tag{8.2}$$

for $-600 < \mu < -200$ GeV at $\tan\beta = 2.0$ and $M_{\tilde{q}} = 1.2 \cdot M_{\tilde{g}}$. We also exclude $M_{\tilde{\chi}_2^0} < 46$

GeV/c^2 (LEP: 40 GeV/c^2) at $\tan\beta = 2.0$ and $M_{\tilde{q}} = 2.0 \cdot M_{\tilde{g}}$. The limits are weaker for different $\tan\beta$ values (4.0 and 10.0) and $M_{\tilde{q}}/M_{\tilde{g}}$ ratios (1.0 and 2.0). Though, we have no additional sensitivity beyond the LEP result for $\mu > 0$, their search channel is different from us and the results should be presented in parallel. In the hadronic channel, using trilepton events from cascade decays of chargino-neutralino pair production, the results in this thesis set the highest limits on the $M(\tilde{\chi}_1^{\pm})$ and $M(\tilde{\chi}_2^0)$.

Bibliography

[1] S.L. Galshow Nucl.Phys.**22**, 579(1961);
S. Weinberg, Phys. Rev. Lett. **19**, 1264(1967);
A Salam, in *Elementary Particle Theory: Relativistic Groups and Analyticity (Nobel Symposium No.8)*, edited by N. Svatholm (Almqvist and Wiksell, Sweden, 1968), p.367.

[2] J. Illopoulos, S.L. Galshow, L. Maiani Phys. Rev. D, 2(7), 1285(1970)

[3] The Review of Particle Properties, Phys. Rev. D45(1992)

[4] U. Amaidi, W. de Boer, and H. Fürstenau. Phys. Lett. **B260** 447(1991)

[5] F. Abe *et al.* (CDF collaboration), Phys. Rev. Lett. **69**, 3439(1992)

[6] H. E. Haber G. L. Kane, Phys. Rep. **117**, 75(1985)

[7] P. Nath R. Arnowitt, Mod. Phys. Lett. **A2**, 331(1987); R. Arnowitt, R. Barnett, P. Nath, F. Paige, Int. J. Mod. Phys. **A2**, 1113(1987)

[8] J. Wess, B. Zumino, Nucl. Phys. **B70**, 39(1972); Phys. Lett. **49B**, 52(1974)

[9] D. Volkov, V. P. Akulov, JETP Lett. **16**, 438(1972)

[10] G. Farrar, P. Fayet, Phys. Lett. **76B**, 575(1988)

[11] J. Ellis, J.S. Hagelin, D.V. Nanopoulos, K. Olive, M. Srendnicki, Nucl. Phys. **B238**, 453(1984)

[12] Y. Oaka, M. Yamaguchi, T. Yanagida, Phys. Lett. **262B**, 54(1991)

[13] K. Inoue, A. Kakuto, H. Komatsu, H. Takashita, Prog. Theor. Phys. **68**, 927(1982)

[14] P. Fayet Phys. Lett. **125B**, 178(1983)

[15] H. Baer, X. Tata Phys. Rev. **D47**, 2739(1993)

[16] M. Dress, M. Nojiri, Nucl. Phys. **B369**, 54(1992)

[17] H. Baer, F. Paige, S. Protopopescu, X. Tata, FSU-HEP-930329 (1993)

[18] G.Fox, S. wolfram, Nucl. Phys. **B168**, 285(1980); T. Gottschalk, Nucl. Phys. **B277**, 700(1986)

[19] R. Field, R. Feynman, Nucl. Phys. **B136**, 1(1978)

[20] F.Abe *et al.* (CDF collaboration), Nucl.Inst.and Meth. **A 271**,387(1988)

[21] Fermilab-Pub-94/024-E, submitted to Nucl.Instrum.Methods Phys. res.

[22] F.Bedeschi *et al.*, Nucl.Inst.and Meth. **A 268**,50(1988)

[23] L.Balka *et al.*, Nucl.Inst.and Meth. **A 267**,272(1988)

[24] S.Bertolucci *et al.*, Nucl.Inst.and Meth. **A 267**,301(1988)

[25] Y.Fukui *et al.*, Nucl.Inst.and Meth. **A 267**,280(1988)

[26] G.Brandenburg *et al.* Nucl.Inst.and Meth. **A 267**,257(1988)

[27] S.Cihangir *et al.* Nucl.Inst.and Meth. **A 267**,249(1988)

[28] G.Ascoli *et al.*, Nucl.Inst.and Meth. **A 268**,33(1988)

[29] T.J.LeCompte, V.Papadimitriou CDF note 2238(1994)

[30] K.Byrum *et al.*, Nucl.Inst.and Meth. **A 268**,46(1988)

[31] G.W.Foster *et al.* A Fast Hardware Track-Finder for the CDF Central Tracking Chamber. Nucl.Inst.and Meth. **A 269**, 93(1988)

[32] F.Abe *et al.* (CDF collaboration), Phys. Rev. Lett. **64**,142(1990)
F.Abe *et al.* (CDF collaboration), Phys. Rev. **D43**, 664 (1991)

[33] T.A. Fuess and C. Wendt, "Search for WW, WZ, ZZ Production," CDF Note 2501(1994).

[34] D. Saltzberg, CDF Note 2213(1993).

[35] M. Krasberg, CDF Note 2326(1993).

[36] M. Shapiro, A. Bhatti, J. Benlloch, R. Harris, T. Rodrigo, P. Sphica, T. Westhusing, CDF note 1810(1992)

[37] S. Behrends, S. Kuhlmann, CDF note 684(1988)

[38] M. Shapiro, D. Quarrie, CDF note 384(1987)

[39] W.F. Badgett, "Measurement of W and Z Boson Production and Extraction of the W Width and Branching Ratios," Proceedings of the 8th Meeting of Division of Particles and Fields of the American Physical Society, p.431, ed. S. Seidel, The University of New Mexico, Albuquerque, N.M., August 2-6, 1994; also in CDF Note 2741(1994).

[40] F. Abe *et al.* (CDF Collaboration), "Measurement of the Ratio $\sigma \cdot B(p\bar{p} \to W \to e\nu)/\sigma \cdot B(p\bar{p} \to Z^0 \to ee)$ in $p\bar{p}$ Collisions at $\sqrt{s} = 1800$ GeV," Fermilab-Pub-95/025-E (1995), submitted to Phys. Rev. D; also in CDF Note 2812(1995).

[41] Tom LeCompte, Tony Liss, Andrew Martin, CDF note 2367(1993)

[42] Sacha E. Kopp, CDF note 2391(1993)

[43] Jinsing Wang, Xin Wu, Milciades Contreras, Allan Clark, CDF note 2435(1994)

[44] H. Plothow-Besh, PDFLIB: Nucleon, Pion and Photon Parton Density Functions and α_s calculations, W5051(1993)

[45] S. Belforte, P. Derwent, J. Marriner, C. Pilcher, CDF note 2361(1994)

[46] F. Abe *et al.* (CDF Collaboration), Phys. Rev. Lett. **67**, 2418(1991).

[47] K. Hagiwara, J. Woodside, and D. Zeppenfeld, Phys. Rev. **D41**, 2113(1990).

[48] J. Ohnemus, Phys. Rev. **D44**, 1403(1991); J.Ohnemus and J.F. Owens, Phys. Rev. **D43**, 3626(1991); J. Ohnemus, Phys. Rev. **D44**, 3477(1991).

[49] S. Lammel, CDF Note 2889(1994).

[50] F.Abe *et al.* (CDF collaboration), Phys. Rev. D**50**, 2966(1994)

[51] J.L. Lopez, private communication.

[52] H.Baer, private communication; The allowed range of $\tan\beta$ in the current version of ISAJET is $1 < \tan\beta < 10$. For much larger values of $\tan\beta$, the splitting in the bottom-squark and tau-slepton sectors become important because there is large mixing for sbottom and stau sector. This can cause frequently $\tilde{\chi}_2^0 \rightarrow \tau + \tilde{\tau}$ and $\tilde{\chi}_1^\pm \rightarrow \tilde{\tau} + \nu_\tau$, which would completely disrupt the trilepton signal.

[53] ALEPH Collaboration, Phys. Lett. **B244**, 541 (1990) and Phys. Rep. **216C**, 253 (1992); DELPHI Collaboration, Phys. Lett. **B247**, 157 (1990); L3 Collaboration, Phys. Lett. **B233**, 530 (1989) and Phys. Rep. **236**, 1 (1993); OPAL Collaboration, Phys. Lett. **B240**, 261 (1990) and Phys. Lett. **B248**, 211 (1990). For review, see G. Giacomelli and P. Giacomelli, Riv. Nuovo Cim. **16**, 1 (1993).

[54] F. Keyvan, J. Hauser, and S. Lammel, "Search for Supersymmetry in the Missing E_T plus Multijet Channel," CDF Note 3044(1995).

[55] J. Hauser (CDF Collaboration), "Search for SUSY by CDF," Proceedings of 10th Topical Workshop on Proton-Antiproton Collider Physics, Fermilab, Batavia, IL., May 9-13, 1995; also in CDF Note 3210(1995)

[56] H. Baer and X. Tata, private communication; The ALLOW program, a part of ISASUSY code, calculates the LEP excluded region. We obtain the LEP excluded region with the following constraints (CERN-PPE/94-188): (a) $2M_{\tilde{\chi}_1^\pm} < M_Z$, (b) Anomalous Z branching ratio $< 10^{-5}$, (c) $\Delta\Gamma_Z < 23$ MeV, (d) $\Delta\Gamma_Z^{invisible} < 7.6$ MeV, (e) $BR(Z \to Z^* + h) < BR(Z \to Z^* + H_{\rm SM})$, (f) $BR(Z \to h + H_A) < 10^{-5}$. Here the LEP results (CERN-PPE/94-187) are $M_Z = 91.1888 \pm 0.0044$ GeV/c^2, $\Gamma_Z = 2.4974 \pm 0.0038$ GeV, $\Gamma_Z^{invisible} = 499.8 \pm 3.5$ MeV, $M_{H_{\rm SM}} > 64.5$ GeV/c^2, and $\alpha_3 = 0.126 \pm 0.005 \pm 0.002$. Since our scanning had started with $\alpha_3 = 0.12$ before the updated value (= 0.126) became available, we kept 0.12 for α_3 in ALLOW program.